TECHNISCHE UNIVERSITÄT DRESDEN

Technische Universität Dresden
Bereich Mathematik und Naturwissenschaften
Institute für Kern- und Teilchenphysik

Dissertation
zur Erlangung des akademischen Grades
Doctor rerum naturalium

Pulse shape simulation and search for rare decays with the COBRA extended demonstrator

vorgelegt von
Yingjie Chu

Eingereicht am 19.03.2024, Disputation am 15.08.2024

First reviewer:	Prof. Dr. Daniel Bemmerer
Second reviewer:	Dr. Habil. Ivan Stekl
Supervisor:	Prof. Dr. Kai Zuber

Abstract

Double beta decay is a powerful tool to investigate the properties of the neutrino and of the weak interaction. Studying characteristics of this decay is very challenging because of its long half-life and interfering natural backgrounds. One experiment aiming to investigate double beta decay is the COBRA experiment located at the Gran Sasso Underground Laboratory. COBRA uses room temperature CdZnTe semiconductor detectors that intrinsically contain multiple double beta decay candidates. The previous COBRA Demonstrator had a relatively high background level and thus is not competitive for double beta decay searches. With the objective of reducing the background as well as increasing the signal sensitivity, the experiment was upgraded using large CdZnTe detectors with a novel electrode design.

This work focuses on the study of the new detectors. A pulse shape simulation based on COMSOL and Monte Carlo is developed with the goal of characterizing the new detectors. This simulation framework is also part of a newly developed pulse shape discrimination to suppress background.

Applying those analysis cuts the background index improves by a factor of 23 compared to the previous setup. Furthermore, the $2\nu\beta\beta$-decay of ^{116}Cd is investigated using data with an exposure of 0.18 kg·yr. The potential for measuring the excited state transition of this decay is also explored.

Apart from the double beta decay investigations, a study of the charge non-conserving decay of ^{113}Cd will be presented. The new half-life limit helps to constrain the theoretical presumptions for this exotic decay process.

Contents

1. Introduction

Neutrinos are the most numerous particles in the universe, second only to photons. They travel through space almost at the speed of light and hardly ever interact with matter. Neutrinos are created through various processes. Some were already created in the Big Bang, and others are produced in space and on Earth, from supernova explosions, and nuclear reactions inside stars, to reactions in nuclear power plants and naturally occurring radioactive decays.

The history of the neutrino can be traced back to the theoretical postulation about the continuous β-spectrum. Neutrino was assumed to be an electrically neutral and massless elementary particle. Only after decades of its postulation, neutrino was detected.

Neutrinos belong to the Lepton family in the Standard Model of particle physics. Unlike electrons, which are also leptons, neutrinos have no electric charge and come in three flavors (types). These flavors can be determined by observing the lepton produced from neutrinos' interaction. The original Standard Model requires that neutrinos are massless. If neutrinos do have mass, they can change from one flavor to another, the so-called neutrino oscillation. The discovery of neutrino oscillation has been ground-breaking for particle physics and was awarded the Nobel Prize in 2015. This phenomenon provides direct evidence for physics beyond the Standard Model. However, direct mass measurement is difficult because neutrinos only participate in the weak interaction.

The questions about the neutrino mass, the neutrino nature, and possible charge parity violation in leptons have become important research topics in neutrino physics. One possible way to answer these questions is the neutrinoless double beta decay. It is a second-order β-decay process without emitting neutrinos, as the name says. The decay mode violates the lepton number conservation and is thus forbidden in the Standard Model. Its observation will reinforce physics beyond the Standard Model. The neutrinoless double beta decay is expected to be extremely rare with half-lives beyond 10^{26} yr and has been searched for decades worldwide. Currently, many large-scale low-background experiments are being built.

The Cadmium Zinc Telluride 0-Neutrino Double Beta Research Apparatus (COBRA) experiment is one of the modern double beta decay experiments. It was proposed in 2001 [1]. The experimental setup is located at the Gran Sasso Underground Laboratory in Italy. It uses room temperature CdZnTe semiconductor detectors which contain several double beta decay candidates. The most promising candidate is ^{116}Cd because of its high Q-value. CdZnTe crystal has been investigated for decades to improve the detector performance, and significant progress has been made so far. The detector also allows pulse shape discriminations for background suppression.

The previous long-term operation has demonstrated the success of the experimental concept and design. Recently, the setup has been upgraded with larger CdZnTe detectors. The goal is to measure the two-neutrino mode of double beta decay of ^{116}Cd using the new large CdZnTe

detectors. COBRA also aims to measure or search for other rare decays, like the fourfold forbidden non-unique single β-decay of ^{113}Cd, and a possible charge non-conserving β-decay.

The main goal of this thesis is to evaluate the properties of new detectors and develop pulse shape discriminations to improve the background level. The second goal is to investigate the potential of searching for rare nuclear decays.

This work is organized in the following chapters. In Chapter 2, theoretical aspects of neutrino physics and related experiments are presented. The COBRA experiment and the CdZnTe detectors are introduced in Chapter 3. Detector characterizations, including pulse shape simulation and event reconstruction, are discussed in Chapter 4. Chapter 5 evaluates the long-term stability of the upgraded setup. The following chapter gives details of the development of pulse shape analysis which is a powerful approach to reducing backgrounds. Chapter 7 presents measurements of the two neutrino double beta decay of ^{116}Cd and potentials for excited state searches. Finally, the charge non-conserving β-decay of ^{113}Cd is discussed in Chapter 8. Chapter 9 summarizes this work.

2. Neutrino physics and double beta decay

The existence of neutrinos was first populated by Pauli in order to explain energy conservation in β-decays. Pauli's hypothesis was indirectly proved by the electron capture (EC) of ^{7}Be measured in 1942 [2, 3]. Later in 1956, the neutrino's existence was confirmed by detecting antineutrinos from a nuclear reactor [4]. Since the discovery of neutrinos, the understanding of neutrino properties and interactions has been greatly improved in the past decades. However, there is still far more to be understood, including the neutrino mass scale, charge parity (CP) violation, and possible additional neutrino species. For detailed discussions, see Refs. [5–7]. To address these open questions, experiments in particle physics, nuclear physics, and cosmology are investigating neutrinos from various sources like the Sun, the atmosphere, accelerators, reactors, or outer space.

A further process that is extremely important for probing the fundamental character of neutrinos is neutrinoless double beta decay. It is regarded as the most sensitive way for studying the possible Majorana nature that neutrino could be its own antiparticle. This decay process can also constrain the absolute neutrino mass scale. Multiple double beta decay experiments have been operated dedicatedly to search for this decay.

This chapter will first introduce the neutrino properties within the Standard Model in Section 2.1. Then, the phenomenon of neutrino oscillations is introduced in Section 2.2. The following section discusses the potential mechanisms of nonzero neutrino mass. Afterwards, double beta decay is presented in Section 2.4 regarding theory and Section 2.5 for experiments.

2.1. Neutrino within the Standard Model

The Standard Model of particle physics describes the fundamental particles and interactions via the electromagnetic, weak, and strong forces based on the gauge invariance of symmetry groups. In the Standard Model, neutrinos have zero electric and color charges. The neutral charge makes them hard to detect. However, neutrinos can interact weakly with other elementary particles through the exchange of massive $W^{\pm}$ bosons and Z^{0} boson. The force carriers $W^{\pm}$ bosons are responsible for the charged current (CC) interaction, and in the neutral current (NC) interaction Z^{0} boson is responsible.

Neutrinos have three types of flavors, electron neutrinos (ν_e), muon neutrinos (ν_μ), and tau neutrinos (ν_τ), corresponding to the three charged leptons. Each flavor has its respective antineutrino.

A fundamental electroweak process to study is the neutrino-electron scattering via CC and NC interactions. The CC and NC interactions have played an important role in detecting solar neutrinos [8]. For ν_e, both interactions are involved, while for ν_μ and ν_τ only NC is possible in the energy range of solar neutrinos.

Besides, neutrino-nucleon interactions are crucial for neutrino and weak interaction studies in nuclei. These interactions can take place via the CC process, like the inverse β-decay $\bar{\nu}_e + p \rightarrow e^+ + n$, or be mediated by the weak NC interaction as the coherent scattering process $\nu + \mathrm{N} \rightarrow \nu + \mathrm{N}$, where ν can be any flavor. The coherent neutrino-nucleus scattering was predicted to have a large cross-section in the Standard Model compared to other neutrino interactions. However, it is hard to observe due to tiny nuclear recoil energies of a few keV or even lower. With the technological breakthroughs of low background experiments and low energy thresholds, this interaction was first detected by the COHERENT experiment using energetic pulsed neutrinos from a spallation neutron source [9]. In the long run, a precise measurement can help to address the questions of nuclear structure.

Another investigated interaction is the coherent neutrino-neutrino scattering process essential to the oscillations of supernova neutrinos. Standard Model predictions and experimental measurements for the cross-section of those mentioned physics processes can provide valuable information on the electroweak parameters.

For most fermions in the Standard Model, particles and antiparticles can be discriminated by their electric charge. If the particle and antiparticle are not identical, the fermion is called a Dirac particle. The Dirac particle has four independent components. The Dirac mass term can be written in its chiral components,

$$\mathcal{L}_{\mathrm{D}} = m_D(\bar{\psi}_L\psi_R + \bar{\psi}_R\psi_L), \tag{2.1}$$

where ψ is a spinor field of the fermion and can be expressed as $\psi = \psi_L + \psi_R$, a sum of the left and right-handed components. $\bar{\psi}$ is its Hermitian conjugation. Eq. 2.1 requires that the fermion has both the left and right-handed chiral component of the spinor field. However, it has been observed that all neutrinos are left-handed, and all antineutrinos are right-handed. There is no right-handed neutrinos. Hence, Eq. 2.1 cannot be used to describe neutrinos unless the mass term is zero, which leads to massless neutrinos.

With the massive neutrinos described in the following section, the right-handed neutrino singlets can be forced to be incorporated into the Standard Model particles to produce masses or in another way, for example, using Higgs triplets (see Section 2.3).

2.2. Neutrino oscillations

In quantum physics a particle with a given mass is described by a wave function with a certain frequency. The flavor eigenstates ν_e, ν_μ, and ν_τ of the weak interaction are non-trivial superpositions of the respective neutrino mass eigenstates. Thus their flavor contents oscillate as they propagate through space and time. Therefore, the probability of which neutrino flavor varies from one location to another.

The observation of neutrino oscillations in solar neutrino deficit, atmospheric neutrino anomaly, and the followed reactor, accelerator neutrino experiments has marked a great breakthrough in particle physics [10]. It proved that neutrinos are massive. A theoretical description of neutrino oscillations and a summary of experimental results are given in this section. A thorough review is found in [8, 11].

2.2.1. Theoretical formalism

Neutrinos are produced and detected as flavor states. A neutrino with flavor $|\nu_\alpha\rangle$, where $\alpha = e, \mu$ or τ, is a mixture of different mass eigenstates $|\nu_k\rangle$ with $k = 1, 2, 3$

$$|\nu_\alpha\rangle = \sum_{k=1}^{3} U^*_{\alpha k}|\nu_k\rangle, \quad |\nu_k\rangle = \sum_{k=1}^{3} U_{\alpha k}|\nu_\alpha\rangle, \tag{2.2}$$

where U is a unitary matrix. The mass eigenstate is described by plane wave functions,

$$|\nu_k\rangle = e^{-i\frac{m_k^2 L}{2E}}|\nu_k(0)\rangle \tag{2.3}$$

with $L = ct$ being the neutrino flight length between the neutrino source and detector. E is the energy carried by neutrinos, and $\frac{m_k^2}{2E}$ determines the wave frequency. So, each neutrino mass state propagates with its specific frequency. As the flavor eigenstate is a superposition of the mass eigenstates as described by Eq. 2.2, the frequency differences cause interferences for flavor contents at each position.

The probability of a neutrino flavor changing states can be calculated. Considering two neutrino flavors, for instance, ν_μ and ν_τ oscillation, which is approximately the case for atmospheric neutrinos, two mass eigenstates are involved. The oscillation probability can be simplified as [11]

$$p(\nu_\mu \to \nu_\tau) = \sin^2 2\theta \ \sin^2(1.27\frac{\Delta m^2 L}{E}) \tag{2.4}$$

with Δm^2 the difference in squared mass of the mass eigenstates. The neutrino flavor changes periodically with the distance L, hence oscillating. The mixing angle $\sin^2 2\theta$ determines the amplitude of the oscillation, and Δm^2 influences the oscillation strength.

Assuming three neutrino flavors, the mixing of neutrino states is described by the Pontecorvo-Maki-Nakagawa-Sakata (PMNS) matrix that is parametrized as

$$\begin{aligned} U_{\text{PMNS}} &= \begin{pmatrix} 1 & 0 & 0 \\ 0 & c_{23} & s_{23} \\ 0 & -s_{23} & c_{23} \end{pmatrix} \begin{pmatrix} c_{13} & 0 & e^{-i\delta}s_{13} \\ 0 & 1 & 0 \\ -e^{i\delta}s_{13} & 0 & c_{13} \end{pmatrix} \begin{pmatrix} c_{12} & s_{12} & 0 \\ -s_{12} & c_{12} & 0 \\ 0 & 0 & 1 \end{pmatrix} \\ &= \begin{pmatrix} c_{12}c_{13} & s_{12}c_{13} & e^{-i\delta}s_{13} \\ -s_{12}c_{23} - c_{12}s_{23}s_{13}e^{i\delta} & c_{12}c_{23} - s_{12}s_{23}s_{13}e^{i\delta} & s_{23}c_{13} \\ s_{12}s_{23} - c_{12}c_{23}s_{13}e^{i\delta} & -c_{12}s_{23} - s_{12}c_{23}s_{13}e^{i\delta} & c_{23}c_{13} \end{pmatrix}, \end{aligned}$$

where $c_{ij} = \cos\theta_{ij}$ and $s_{ij} = \sin\theta_{ij}$. δ is the phase factor relevant for CP violation in the neutrino sector. In total, there are six parameters to describe neutrino oscillations, including three mixing angles (θ_{12}, θ_{23}, θ_{13}), two squared mass differences (Δm^2_{12}, $\Delta m^2_{23(13)}$) and the phase factor. These parameters can be obtained from experimental measurements. For instance, measuring $p(\nu_\mu \to \nu_\tau)$ of atmospheric neutrinos gives θ_{23}, and the mass difference of $\Delta m^2_{23} = \Delta m^2_{\text{atm}}$ [12].

The above discussion applies to neutrino oscillations in a vacuum. When neutrinos pass through matter, as in the Sun or the Earth, the oscillation probabilities are modified due to

the Mikheyev-Smirnov-Wolfenstein (MSW) effect. The MSW mechanism is a result of the weak interactions of ν_e in matter differing from those of ν_μ and ν_τ. It can have large effects on neutrino oscillations through resonance enhancement depending on the electron density and the neutrino energy. For the solar neutrinos, the matter effects break the degeneracies of Δm^2_{21} and θ_{12}, probing the hierarchy in the neutrino mass state 1-2. This is because when $\Delta m^2_{21} > 0$ and $\theta_{12} < \pi/4$, the high energetic neutrino oscillation shows a resonance.

However, the sign of Δm^2_{23} remains unknown, which leads to the different ordering of neutrino mass states, the normal mass ordering ($m_1 < m_2 \ll m_3$) and the inverted mass ordering ($m_3 \ll m_1 < m_2$).

2.2.2. Experimental status

All mixing angles and the absolute values of the neutrino mass squared differences have been measured or constrained within the three-flavor neutrino oscillations framework in the past decades. Various detection techniques have been used.

The neutrino oscillation measurements can be performed in an appearance mode by looking for neutrino flavors different from those emitted by the source. For example, Super-Kamiokande, a water Cherenkov detector located about 1000 m underground, has observed that atmospheric ν_μ are converted into ν_τ through the elastic scattering reaction [13]

$$\nu_\alpha + e^- \to \nu_\alpha + e^-. \tag{2.5}$$

Alternatively, one can measure the reduced flux of a certain neutrino flavor. One of the reactor experiments, KamLAND, was designed to measure the disappearance of $\bar{\nu}_e$ using a liquid scintillator [14]. $\bar{\nu}_e$ is detected through the inverse beta decay

$$\bar{\nu}_e + p \to e^+ + n. \tag{2.6}$$

The event signature is a coincident measurement of the 511 keV photons associated with positron annihilation and a neutron capture reaction a few µs later. The results show a good agreement with the solar neutrino measurements.

Despite the great achievement, whether ν_3 is the heaviest remains unknown and must be measured. Furthermore, discovering CP violation could profoundly impact our understanding of the leptogenesis and baryon asymmetry of the universe. If CP is violated in neutrino oscillations, the probabilities of oscillating from ν_μ to ν_e and from $\bar{\nu}_\mu$ to $\bar{\nu}_e$ will not be identical. The upcoming experiments aim to improve the precision of mixing parameters and to measure the neutrino mass ordering, as well as explore the potential of the CP violation. Several experiments are under construction, like the medium-baseline experiment JUNO, long-baseline experiments DUNE and Hyper-Kamiokande where matter effects will increase with the distance [15, 16].

2.3. Neutrino mass mechanism

The discovery of neutrino oscillation has shown neutrino properties beyond the Standard Model, which implies that the Standard Model itself is incomplete. Many theories are for-

mulated to explain the origin of the neutrino mass. The most popular theory, known as the seesaw mechanism, ascribes the tiny mass of the left-handed neutrino to the exchange of heavy particles, such as right-handed singlet neutrinos or triplet Higgs.

The key to the seesaw mechanism is to add new particles into the Standard Model without loss of the gauge symmetry and Lorentz invariance. As the neutrino does not carry electrical charge or color, it could be identical to its antiparticle, $\nu = \bar{\nu}$. The lepton number conservation would be violated. In this case, neutrinos are referred to as Majorana neutrinos. The Majorana mass term becomes possible by connecting the neutrino to its charge conjugate term.

In addition to the Dirac neutrinos, the seesaw mechanism also includes the Majorana neutrinos. The Lagrangian is then generalized by

$$\begin{aligned}\mathcal{L} &= m_D(\bar{\psi}_L\psi_R + \bar{\psi}^c_L\psi^c_R) + m_L\bar{\psi}_L\psi^c_R + m_R\bar{\psi}^c_L\psi_R + h.c. \\ &= \begin{pmatrix}\bar{\psi}_L & \bar{\psi}^c_L\end{pmatrix}\begin{pmatrix}m_L & m_D \\ m_D & m_R\end{pmatrix}\begin{pmatrix}\psi^c_R & \psi_R\end{pmatrix},\end{aligned}$$

where the spinor field of $\bar{\nu}$, ψ^c, follows $\psi^c_{L,R} = (\psi^c)_{R,L} = (\psi_{R,L})^c$. m_D is the Dirac mass term. m_L and m_R are the left and right-handed Majorana mass terms. By assuming $m_R \gg m_D$ and $m_L = 0$, the mass eigenvalues are obtained with

$$m_1 = \frac{m_D^2}{m_R} \approx 0, \quad m_2 = m_R(1 + \frac{m_D^2}{m_R^2}) \approx m_R. \tag{2.7}$$

As can be seen, one is light, while the other is heavy. This is the essence of the seesaw mechanism. The tiny mass is compensated by the heavy neutrino with an opposite chirality. For more details about seesaw mechanisms, see Ref. [17].

Since neutrino oscillation experiments can only probe the differences of squared neutrino mass eigenvalues Δm^2_{ij}, the absolute mass scale of neutrinos remains unknown. Its measurement would help answer the open questions of the origin of neutrino masses. There are three feasible ways to probe the neutrino mass.

KATRIN is the most promising direct mass search experiment independent of the physics model [18]. It is designed to reach a $\langle m_\nu \rangle$ sensitivity of $0.2\,\mathrm{eV/c^2}$. The experiment uses a high vacuum spectrometer to measure the precise shape of the tritium β-decay spectrum in the vicinity of its endpoint at 18.6 keV, as the electron neutrino mass changes the spectrum shape in the region. Other direct mass measurements are also being carried out. For example, the ECHO experiment is built with calorimeters to investigate the EC of ^{163}Ho with a Q-value at 2.8 keV and to probe the sub-eV sensitivity on the mass of the electron neutrino [19, 20].

Despite the smallness of their masses, neutrinos play a crucial role in the evolution of large-scale structures in the universe due to their high abundance. In this respect, one may constrain the absolute neutrino mass scale from cosmological observations with underlying assumptions. Currently, cosmology gives the strongest limit of 0.12 eV on the sum of the neutrino mass $\sum = m_1 + m_2 + m_3$ [21].

Furthermore, if massive neutrinos are Majorana particles, it is possible to determine the neutrino mass by observing the neutrinoless double beta decay. The observation can also

help to probe the neutrino mass ordering. Fig. 2.1 illustrates the effective Majorana neutrino mass, $\langle m_{\beta\beta} \rangle$, as a function of the lightest neutrino mass, with $\langle m_{\beta\beta} \rangle$ being $\mid \sum_{i=1}^{3} m_i U_{ei}^2 \mid$. The shaded areas correspond to the 3σ regions due to the propagation of uncertainties from the oscillation parameters. The detection of $\langle m_{\beta\beta} \rangle$ will not be sufficient to determine the mass ordering if the lightest neutrino mass is above 40 meV. It can also be seen that only a limit on $\langle m_{\beta\beta} \rangle$ below 10 meV could be used to rule out the inverted ordering case.

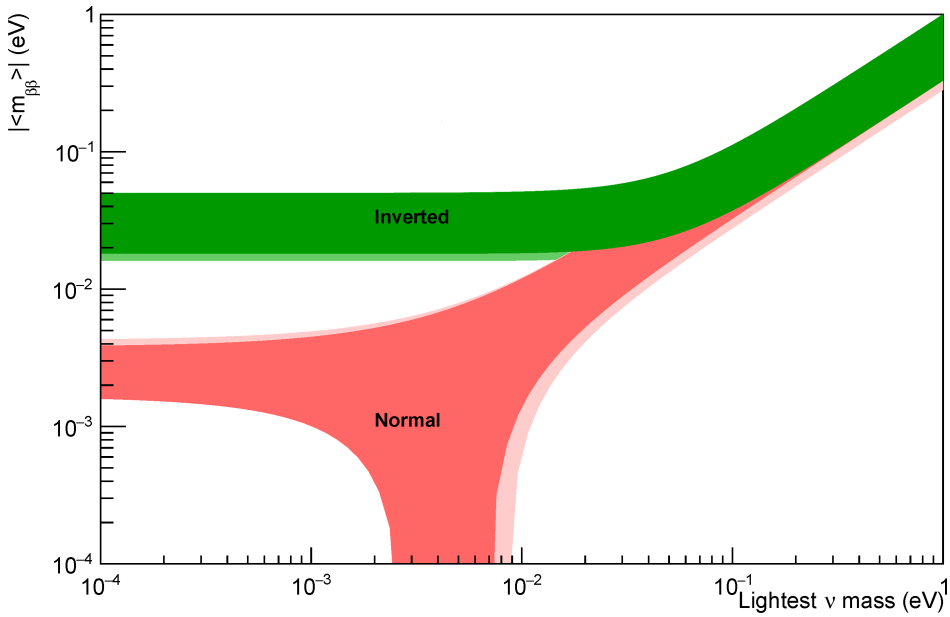

Figure 2.1.: Allowed regions of the effective Majorana mass, $\langle m_{\beta\beta} \rangle$, as a function of the lightest neutrino mass for inverted and normal mass ordering [22]. The uncertainties on the neutrino oscillation parameters are taken into account.

2.4. Double beta decay

Double beta decay is a type of radioactive decay in which two protons are simultaneously transformed into two neutrons, or vice versa, inside an atomic nucleus. It only occurs for certain even-even nuclei for which beta decay is energetically forbidden or highly suppressed by the large involved angular momenta [5]. As this process is a second-order effect, the half-lives are very long.

There are 35 double beta decay emitters. Several isotopes listed in Table 2.1 are being investigated. An ideal isotope should have characteristics of high natural abundance, high Q-value, and be possible to produce in large quantities so that the detection probability will be high. In reality, there is no ideal isotope. For instance, ^{48}Ca has a Q-value larger than the highest γ line at the 2615 keV produced from the natural Thorium decay chain. This means that the region of interest (ROI) will not be affected by the natural γ background. However,

Table 2.1.: Commonly used double beta decay nuclides [5].

isotope	Nat. ab. [%]	Q [keV]
^{48}Ca	0.187	4263
^{76}Ge	7.8	2039
^{82}Se	8.7	2998
^{96}Zr	2.8	3348
^{100}Mo	9.8	3035
^{116}Cd	7.5	2813
^{130}Te	34.08	2527
^{136}Xe	8.9	2459
^{150}Nd	5.6	3371

the most challenging part of investigating ^{48}Ca is how to enrich the isotope effectively. One has to make compromises in order to look for an optimal choice.

2.4.1. Two neutrino double beta decay

The two neutrino double beta ($2\nu\beta\beta$) decay is in the form of [23],

$$(A, Z) \rightarrow (A, Z+2) + 2e^- + 2\bar{\nu}_e. \tag{2.8}$$

The total kinetic energy is shared among the four leptons as the recoil energy of the daughter nucleus is negligible. The lepton number is conserved, and therefore this process is allowed in the Standard Model. Equivalent decay modes are the $\beta^+\beta^+$ decay which is always accompanied by EC/EC or β^+/EC decays. A simultaneous decay of two nucleons in the same nucleus is extremely unlikely. Therefore, the observed $2\nu\beta\beta$-decay usually has a typical long half-life $T^{2\nu}_{1/2}$ larger than 10^{19} yr [24].

The decay rate for the second-order weak decay is deduced from the Fermi golden rule and can be expressed as a product of independent factors depending on the atomic physics and nuclear structure

$$\left(T^{2\nu}_{1/2}\right)^{-1} = G^{2\nu}(Q, Z)|M^{2\nu}|^2. \tag{2.9}$$

The phase space factor, $G^{2\nu}(Q, Z)$, accounts for the influence of the Coulomb field of the daughter nucleus on the emitted electrons or positrons. It is determined based on the electron wave functions and is considered to be known with good precision [25]. The dependence of $G^{2\nu}(Q, Z)$ on the Q-value is known as $G^{2\nu}(Q, Z) \propto Q^{11}$. Therefore, the larger the Q-value is, the more probable is the decay.

The nuclear matrix element, $M^{2\nu}$, describes the transition probability from the initial state to the final state of a nucleus, including an initial state in the nucleus (A, Z) to an intermediate state of $(A, Z+1)$ and then the transition from this intermediate state to the final state of daughter nucleus $(A, Z+2)$. $M^{2\nu}$ can be derived experimentally from the measured $2\nu\beta\beta$-decay rate. For the $2\nu\beta\beta$-decay, Gamow-Teller (GT) transitions are favored by the selection

rules, whereas Fermi transitions are strongly suppressed. The $M^{2\nu}$ is given by the sum of the products of $M^{2\nu}_{\mathrm{GT}}$ via the intermediate GT state with the energy denominator. A detailed evaluation of the $M^{2\nu}$ can provide references for theoretical calculations and will be crucial for studying the neutrinoless double beta decay. A comprehensive review can be found in Ref. [26].

2.4.2. Neutrinoless double beta decay

Theories beyond the Standard Model predict that the double beta decay may also occur without the emission of neutrinos or antineutrinos and thus lead to a lepton number violation by two units. The neutrinoless double beta ($0\nu\beta\beta$) decay is expressed as

$$(A, Z) \rightarrow (A, Z + 2) + 2e^{-}. \tag{2.10}$$

The decay can be assumed that the right-handed $\bar{\nu}_e$ emitted from the first neutron decay is absorbed as a left-handed ν_e by the second neutron. Hence, the remaining parts in the final state are the daughter nucleus and two electrons.

The most commonly considered mechanism for the $0\nu\beta\beta$-decay to occur is the light Majorana neutrino exchange [27]. In this case, the $0\nu\beta\beta$-decay rate depends on the effective Majorana neutrino mass $\langle m_{\beta\beta}\rangle$

$$\left(T^{0\nu}_{1/2}\right)^{-1} = G^{0\nu} g_A^4 |M^{0\nu}|^2 \left(\frac{\langle m_{\beta\beta}\rangle}{m_e}\right)^2. \tag{2.11}$$

The observable parameter in this decay is the $T^{0\nu}_{1/2}$. In order to extract the mass term, the phase space factor $G^{0\nu}$, weak axial-vector coupling strength g_{A} and nuclear matrix element $M^{0\nu}$ have to be calculated precisely. It is known that $G^{0\nu}$ is proportional to the Q^5 and is determined to a sufficient precision. However, g_{A} is observed to be reduced from its free nucleon value of 1.27 in β-decays. A quenched g_{A} implies a longer $T^{0\nu}_{1/2}$. The nuclear matrix element, $M^{0\nu}$, adds large uncertainties to the derivation of the effective neutrino mass $\langle m_{\beta\beta}\rangle$, because its calculation is very sensitive to the descriptions of nuclear structure. It is worth noting that the $T^{0\nu}_{1/2}$ is suppressed by $\langle m_{\beta\beta}\rangle^2$ divided by the electron mass m_e. This is one reason why $T^{0\nu}_{1/2}$ is so large compared to that of the $2\nu\beta\beta$-decay.

Independent of any possible mechanism leading to the $0\nu\beta\beta$-decay, the observation of the $0\nu\beta\beta$-decay will prove that neutrinos are Majorana particles. In addition, the discovery of the $0\nu\beta\beta$-decay would provide information about conservation laws, like lepton number, CP violation, and Lorentz symmetry. However, the experimental search for this decay is extremely challenging and has not yet been successful despite all previous attempts.

The $0\nu\beta\beta$ signal is limited in sensitivity by signal statistics and by the present background. The sensitivity S is the half-life limit that can be set for a decay process if no signal is observed. At a certain confidence level (C.L.), it is estimated as

$$S = \ln(2) \cdot \epsilon \cdot \frac{1}{n_\sigma} \cdot \frac{a \cdot N_A}{M} \cdot \sqrt{\frac{m \cdot t}{B \cdot \Delta E}}, \tag{2.12}$$

where ϵ denotes the detection efficiency, a is the natural abundance, N_A is Avogradro's constant. The background follows a Poisson distribution, and its fluctuation is $\sqrt{N_\mathrm{B}}$, which is usually quoted from the background index B in units of cts/(keV·kg·yr). n_σ is 1.64 at 90% C.L.. ΔE is the width of the energy window over the ROI, usually based on the energy resolution. M is the molar mass. $m{\cdot}t$ is the accumulated exposure in kg·yr.

If an experiment can reach a background index of less than $1{\times}10^{-3}$ cts/(keV·kg·yr), it is said to be background-free. For a background-free environment, the sensitivity is linearly proportional to the data exposure as $S \propto m \cdot t$, which can be significantly improved.

2.5. Double beta decay experiments

In recent years, the $0\nu\beta\beta$-decay process has become of great interest due to the discovery of neutrino oscillations. While the total energy of the two electrons produced in the $2\nu\beta\beta$-decay is a continuum, the $0\nu\beta\beta$-decay emits electrons with the summed energy at the Q-value and shows a peak in the energy spectrum, as shown in Fig. 2.2, probably smeared by the detector's energy resolution. This signature is being searched for experimentally, and then the potentially measured half-life can be used to derive the effective Majorana neutrino mass via Eq. 2.11.

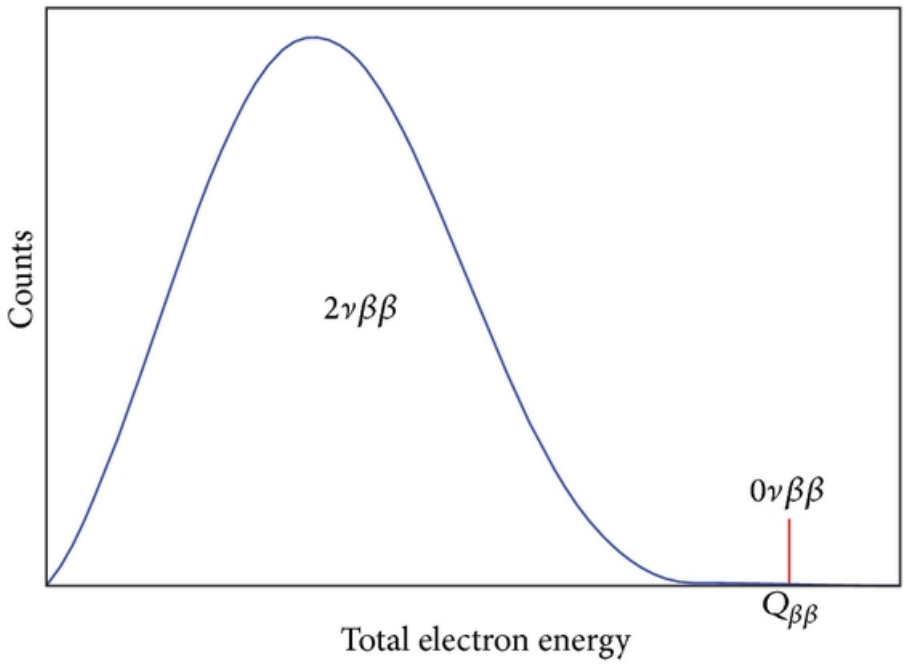

Figure 2.2.: Signal shapes of the double beta decays. The $2\nu\beta\beta$ events display a continuous spectrum, while the $0\nu\beta\beta$ signal shows a peak at the Q-value [28].

A good energy resolution is vital for double beta decay searches as shown in Eq. 2.12 and

also for separating the $0\nu\beta\beta$ signal from the irreducible backgrounds like the $2\nu\beta\beta$-decay.

As the double beta decay rates are expected to be extremely low, the signal efficiency has to be as high as possible. Meanwhile, ultra-low backgrounds are crucial for such rare event searches. For this reason, the experiments have to be operated in underground laboratories. Multiple shielding layers and pulse shape analyses are necessary to suppress the background events. In recent years, machine learning algorithms have also been incorporated into the analysis to improve the signal to background ratio.

Moreover, if an experiment has the ability to scale up to a larger one, this will shorten the time duration for observing such events.

2.5.1. Detector technology

In general, double beta decay experiments can be divided into two classes. One uses the "detector=source" approach, where the detector material includes the candidate nuclei. This approach can maximize the intrinsic detection efficiency. When the source and the detector are separate, trajectories and angular distributions of the two electrons can be measured. However, self-absorption in the source will degrade the energy deposition of the detector. Based on the two approaches, various detector technologies are explored.

Semiconductor detectors are preferably used because of their good energy resolution compared to other types of detectors. ^{76}Ge-enriched HPGe detectors are well suited for $\beta\beta$ searches due to the intrinsic purity of Ge, the well-developed enrichment technology, and excellent energy resolution. The GERDA and MAJORANA experiments have used such enriched HPGe detectors [29, 30]. An energy resolution of 2.53 keV at the $Q_{\beta\beta}$ value has achieved [30]. Advanced pulse shape discriminations are employed to distinguish single energy depositions (possibly signal events) and multiple ones caused by background events.

Large solid or liquid scintillator detectors can load isotopes of interest. It also follows the idea that the source and the detector are identical. The energy resolution of scintillator detectors is worse than that of semiconductor detectors. However, the main advantage is its scalability for future operations. One experiment is the SNO+ being conducted by 780 tonnes of liquid scintillator loaded with 3.9 tonnes of natural Tellurium, corresponding to 1.3 tonnes of ^{130}Te [31].

Tracking calorimeters can also search for the $0\nu\beta\beta$-decay of nuclide candidates. For this technique, the detector and source are separate from each other. A thin layer of $\beta\beta$ emitting candidates can be sandwiched between trackers and surrounded by calorimeters. This technique has the capability of particle identification. Based on the 3D track characteristics, $\beta\beta$-like signals can be distinguished from events entering the detector from outside. The calorimeters help to identify events with the energy of a $0\nu\beta\beta$-decay and to reject the dominant background stemming from $2\nu\beta\beta$ events. The SuperNEMO experiment, a successor to the NEMO-3 with larger source mass, improved energy resolution, and reduced background level, is under construction [32].

Some double beta decay isotopes can also be made as cryogenic calorimeters. Those bolometers work at temperatures of mK with good energy resolution and high detection efficiency. A highly sensitive thermometer measures the heat induced by interacting particles in the absorber and converts the thermal fluctuation to a voltage signal. The bolometer absorbers can

be made from various crystals, including TeO_2, $CdWO_4$, and so on. The CUORE experiment has shown the validity and scalability of the bolometric technique to the ton scale using 988 of $5\times5\times5\,cm^3$ TeO_2 crystals hosted in a cryostat. The detector energy resolution has achieved (7.7 ± 0.5) keV at the Q-value of the ^{130}Te $0\nu\beta\beta$-decay, which is comparable to semiconductor detectors [33].

Furthermore, the time projection chamber can be used where the double beta decay emitter is in the detection medium. For instance, the EXO-200 experiment uses a cylindrical time projection chamber filled with enriched ^{136}Xe. The chamber is divided into two drift regions by one cathode in the center. Near the two ends are the anodes consisting of two crossed-wire planes for ionization signal collection and photodetectors behind the wire planes for scintillation light collection. Each event is reconstructed by grouping the charge and the light signals into energy deposits. The energy resolution at the Q-value reaches 1.15% [34]. The chamber is capable of reconstructing a 3D position that allows for strong background rejection by developing a fiducial volume cut. Moreover, the ionization-to-scintillation ratio can be used for particle identifications.

2.5.2. Future experiments

Double beta decay experiments have steadily improved their sensitivity using different isotopes and techniques. At present, the most stringent limits on $\langle m_{\beta\beta}\rangle$ derived from the $0\nu\beta\beta$ investigations are $\langle m_{\beta\beta}\rangle <$ 79-180 meV for ^{76}Ge, $\langle m_{\beta\beta}\rangle <$ 75-350 meV for ^{130}Te and $\langle m_{\beta\beta}\rangle <$ 61-165 meV for ^{136}Xe.

Based on the knowledge from neutrino oscillations, the mass regions to be explored are about 15-45 meV in the case of the inverted hierarchy and 1.5-4 meV in the normal hierarchy. The $0\nu\beta\beta$ half-lives expected for these regions are well above 10^{26-27} yr. To achieve a better sensitivity, a larger quantity of source nuclei will be required, while the background in the ROI has to be reduced. The amount of nuclei necessary for such experiments is on an order of multiple tons, depending on the nuclear matrix elements and the phase space factors.

Several large-scale double beta decay experiments are already under construction. One experiment, LEGEND, will investigate the $0\nu\beta\beta$-decay of ^{76}Ge using infrastructures and designs from the GERDA and MAJORANA experiments. The aim is to reach sensitivities on the $0\nu\beta\beta$-decay to 10^{28} yr and probe an effective Majorana mass of around 10 meV. The CUPID experiment will also be built from its predecessors and allow for a future zero-background study of the $0\nu\beta\beta$-decay of ^{100}Mo [35]. The sensitivity is expected to reach $T^{0\nu}_{1/2} > 1\times10^{27}$ yr, corresponding to $\langle m_{\beta\beta}\rangle <$ 10-20 meV [36]. Another ton-scale experiment nEXO aims for a sensitivity of 10^{28} yr for ^{136}Xe.

Although the COBRA experiment is not comparable with the mentioned large-scale experiments in size, it has produced fruitful physics results in double beta decay studies for the last decades [37–39]. The experiment has unique features and advanced technologies intrinsic to the CdZnTe detectors, which will be discussed in the following chapters. With the progress expected to be made in manufacturing the CdZnTe crystals in the future, COBRA will be able to be scaled up with a reasonable financial cost.

3. COBRA experiment

The COBRA experiment uses CdZnTe (CZT) crystals as both the detector and the source for rare event searches. The "detector=source" approach allows for a high detection efficiency. An experimental benefit of CZT is the property of being a room-temperature semiconductor. No complicated cooling equipment is required. And since it is a semiconductor detector, a good energy resolution can be achieved.

A low background level is essential to search for rare decays. To reduce the background from cosmic rays, the experiment is located at the Gran Sasso Underground Laboratory. The laboratory is shielded against cosmic rays by 1400 m of rock with a water equivalent of 3800 m. The muon flux from cosmic rays is reduced to $(3.41\pm0.01)\times10^{-4}\,(\mathrm{m}^2\cdot\mathrm{s})^{-1}$ [40].

To date, the collaboration has built two experimental setups. The first phase is the COBRA Demonstrator, which comprises 64 CZT detectors, each with a size of $1\,\mathrm{cm}^3$. The main objectives of the Demonstrator are to investigate the long-term operational stability of the CZT detectors under an ultra-low background environment and to identify potential background sources.

Following the successful operation of the Demonstrator, the COBRA collaboration has recently upgraded the setup to the next stage, the eXtended DEMonstrator (XDEM), by using nine additional CZT detectors. To increase the detection efficiency, large detectors with a size of $6\,\mathrm{cm}^3$ are used. The large detector has a comparatively reduced surface to volume ratio, which decreases potential surface contaminations. XDEM aims to collect high-quality data with an exposure of $1\,\mathrm{kg}\cdot\mathrm{yr}$. Meanwhile, the background index is expected to be reduced by more than one order of magnitude compared to the previous setup. By reaching the required data exposure, the half-life sensitivity of the ^{116}Cd $0\nu\beta\beta$-decay of the Demonstrator will be surpassed by more than one order of magnitude.

This chapter will describe the technical aspects of the COBRA setup installed at the Laboratori Nazionali del Gran Sasso (LNGS). An overview of the experimental design and major hardware components are given in Section 3.1. The characteristics and the basic working principles of the CZT detectors used in the Demonstrator are discussed in Section 3.2. The status of the Demonstrator in Section 3.3 motivates the application of the new CZT detectors presented in Section 3.4. Finally, the upgrade of the XDEM setup is shown in Section 3.5.

3.1. Shielding and electronics of the COBRA setup

The Demonstrator and XDEM have been built with a similar operational concept. Both setups include arrays of CZT detectors, shieldings, auxiliary infrastructure, and the data acquisition (DAQ) system. In comparison to the Demonstrator, the main difference of the XDEM is using large detectors and a novel electrode configuration. In the Demonstrator, the

small CZT detectors employ a coplanar grid (CPG) readout, while the new detectors use a quad-CPG design. More details about the new electrode will be given in Section 3.4.

Fig. 3.1 presents the layout of the experimental instruments in the COBRA setup. The detector modules and the first stage of the readout electronics are located on the ground floor. To protect the detectors from the waste heat produced by electronics, the rest of the readout electronics are situated on the second floor. Detailed descriptions of the setup are shown elsewhere [41–44]. A summary is given here regarding the shieldings and electronics.

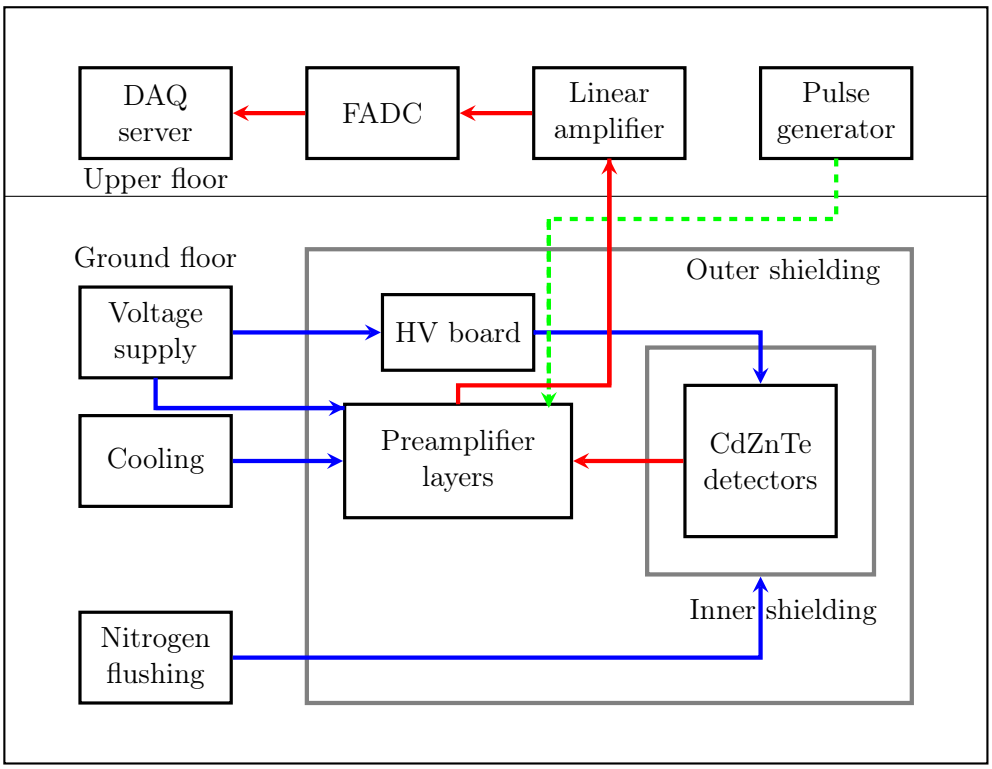

Figure 3.1.: Sketch of the COBRA setup. Red lines indicate the signal flow. The voltage supply and the slow control are shown in blue lines. The green dashed line shows that artificial pulses produced from a pulse generator are injected into the preamplifier.

Despite the rock coverage, the experiment can be affected by various background sources. A multi-layer shielding is thus used to protect the detectors from radiation created underground. The shielding layer is built in the way that an outer shielding surrounds an inner shielding and preamplifiers.

One background source is neutrons. They can be produced by muons or spontaneous fission of ^{238}U. α particles emitted from the natural decay chains can also produce neutrons via the (α, n) reaction. ^{113}Cd intrinsic to the detector has a large cross-section for neutron capture, and the reaction can emit γ-rays as $^{113}\mathrm{Cd}(n, \gamma)^{114}\mathrm{Cd}$. Therefore, a neutron shield lies in

the outermost layer, as shown in Fig. 3.2. The shield is made of borated polyethylene plates with a thickness of 7 cm, which can slow down and absorb neutrons entering the setup. The following layer uses 2 mm thick iron sheets to prevent electromagnetic interferences (EMI) from coupling to the signals.

Another background source is the Radon that can diffuse through the outer shielding. Its decay products are also radioactive and have relatively short half-lives. So, the inner shielding starts with an air-tight sealed acrylic glass box, keeping Radon out. The 15 mm thick box is under overpressure by constantly flushing it with evaporated and purified Nitrogen, reducing the Radon content inside the box and keeping the humidity at a reasonably low level to prevent condensation.

Inside the Radon shield, a $60\times60\times70\,\mathrm{cm}^3$ Lead castle is placed to prevent γ-rays from entering the setup. However, the standard Lead contains radioactive ^{210}Pb that can contribute to the background. A layer of ultra-low activity (ULA) Lead with a thickness of 5 cm is enclosed by the normal Lead to shield against the decay product of ^{210}Pb. The ULA Lead has a ^{210}Pb activity of less than 3 Bq/kg. The innermost layer is made of oxygen-free high conductivity (OFHC) electroformed Copper with a thickness of 5 cm. The Copper can shield remaining backgrounds and Bremsstrahlung or characteristic X-rays from Lead. The material is extremely pure. Then, the detector arrays of the XDEM and the Demonstrator are placed inside separately.

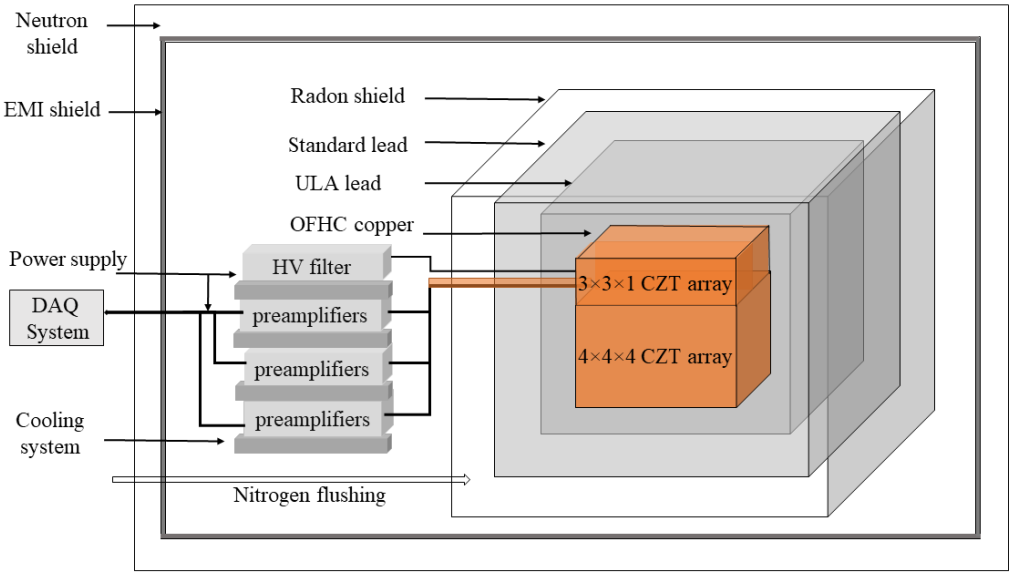

Figure 3.2.: CZT detector arrays surrounded by layers of shieldings are shown in the illustration. The Copper shield hosting the XDEM (3×3×1 CZT array) is on top of the according part of the Demonstrator (4×4×4 CZT array), as shown in orange color. Three preamplifier modules are used in XDEM [44]. A picture is given in Fig. A.1.

The electronic signal is recorded by the DAQ system, as illustrated in Fig. 3.1, for offline

analysis. The induced charges are usually too small to be processed by digitizer. Thus, charge signals are amplified. These signals are transmitted to the preamplifiers and converted into differential voltage signals. The differential signal ensures a robust and stable transmission, as it minimizes external disturbances, such as EMI, noise, and crosstalk. The preamplifiers are close to the detectors to limit noise interferences. Then, the voltage signals are amplified by linear amplifiers and converted to single-ended signals. The following Flash Analog to Digital Converter (FADC)s digitize signals with a resolution of 12 bits and a sampling frequency of 100 MHz. Finally, the discrete signals are stored with a pulse length of 10.24 µs in steps of 10 ns, which amounts to 1024 samples. Besides saving signals from detectors, artificial events are injected into the same DAQ system and recorded for electronic diagnostics.

As these analog electronics generate thermal waste, cooling devices are used in order to reduce the resulting thermal noise. A cooling unit (JULABO FL 601) is installed next to the preamplifiers to cool down them. Also, the detectors are cooled slightly because of the vicinity to the cooling device, allowing them to be operated at an optimal temperature of around 10 °C. In addition, a newly installed air-conditioning handles the waste heat produced by electronics on the upper floor.

To ensure the stable operation of the electronics and the central infrastructure, uninterruptible power supply (UPS) units were installed in case of a power breakdown or any significant voltage fluctuations.

The setup is designed to be operated remotely, including a cooling system, voltage control, and data-taking. Its stability can also be monitored and diagnosed in real-time. For more details, see Chapter 5.

3.2. CdZnTe detectors

The CZT detector contains multiple double beta decay emitters. These candidates are listed in Table. 3.1, together with their current half-life limit. Among the five $\beta\beta$ nuclides, ^{116}Cd is being investigated because of its high Q-value of 2813.5 keV, which is above the highest energetic γ-line at 2615 keV from natural decay chains so that the $0\nu\beta\beta$ signal region is not contaminated by γ-rays. The study of β^+/β^+, β^+/EC, and EC/EC decay modes is also possible. Four candidates are capable of these decay modes. ^{106}Cd is the most promising one with a high Q-value and relatively high abundance compared to the other three nuclides. ^{113}Cd is also an isotope of particular interest for studying the double beta decay.

As the source, the high radiopurity of the CZT crystal is beneficial for a low background experiment. As for a detector, the compound has high atomic numbers and a wide band gap (1.57 eV), allowing for efficient detection at room temperatures. This is a practical advantage for COBRA as an extra cooling system is likely to introduce backgrounds.

When an ionizing particle interacts with the semiconductor, a number of electrons and holes proportional to the deposited energy are produced. Driven by an electric field, these charge carriers move to the respective electrode and induce charges in the course of the drift. However, the electrons and holes can be trapped by defects or recombination centers in the crystal, leading to the loss of charge carriers. The transport of charge carriers is described by the mobility μ, the lifetime τ, and their product $\mu\tau$. In CZT materials, the $\mu\tau$ for holes is two

Table 3.1.: Decay modes, Q-values, and natural abundances of double beta decay candidates intrinsic to the CZT detector. The present half-life limits on the $0\nu\beta\beta$ (β^+/EC) decays (at 90% C.L.) are also listed.

Isotope	Decay modes	Q [keV]	Nat.ab. [%]	$T^{0\nu}_{1/2}$ limit [yr]
^{64}Zn	β^+/EC	1096.3	48.6	1.2×10^{22} [45]
	EC/EC			2.6×10^{21} [46]
^{70}Zn	$\beta^-\beta^-$	1001	0.62	1.6×10^{21} [45]
^{106}Cd	$\beta^+\beta^+$	2771	1.25	1.2×10^{21} [47]
	β^+/EC			5.0×10^{21} [48]
	EC/EC			1.0×10^{21} [47]
^{108}Cd	EC/EC	272	0.88	1.0×10^{18} [49]
^{114}Cd	$\beta^-\beta^-$	534	28.7	1.6×10^{21} [37]
^{116}Cd	$\beta^-\beta^-$	2813.5	7.5	2.2×10^{23} [50]
^{120}Te	β^+/EC	1722	0.1	2.9×10^{22} [51]
	EC/EC			2.1×10^{17} [52]
^{128}Te	$\beta^-\beta^-$	868	31.7	2.2×10^{24} [53]
^{130}Te	$\beta^-\beta^-$	2526.97	33.8	2.2×10^{25} [54]

orders of magnitudes smaller than for electrons. This means that slow-moving holes cannot travel far and are very likely to get trapped, whereas electrons contribute to the signal. This will make the signal detection depth dependent if conventional planar electrodes are used.

Several single-polarity charge sensing techniques have already been developed to overcome the severe trapping effect of holes. For instance, CPG electrodes, pixelated anodes, and virtual Frisch-grid have made the CZT-based detectors applicable when high efficiency and good energy resolution are required [55–57]. Nowadays, CZT detectors have been widely used in hard X-ray and γ-ray astronomy, medical imaging, and rare nuclear decay searches.

3.2.1. Coplanar grid principle

The detection technique used by COBRA is the CPG readout. The idea is similar to the Frisch grid in gas chambers, which overcomes the problem of the slow drift of ions. The principle was first implemented for semiconductor detectors by Luke [58, 59]. Further technological improvements have been made in the past years.

One CZT detector with the CPG readout is illustrated on the left graph of Fig. 3.3. The anode is segmented into two interlocking grids and set to different electric potentials. One anode, called the collecting anode (CA), is grounded. The other anode, non-collecting anode (NCA), is set to a negative potential in a magnitude of 60 V to 80 V. On the opposite side, the cathode is implemented as a planar electrode. If the detector has a thickness of 1 cm, the cathode is usually biased around -1.2 kV. The high voltage leads to an electric field expected to be homogeneously distributed in most regions except near the anode. When charge carriers propagate through the electric field, holes are probably trapped before reaching the cathode.

On the other hand, electrons move towards the anode, and the electric field between the grid will guide them to the CA and be collected.

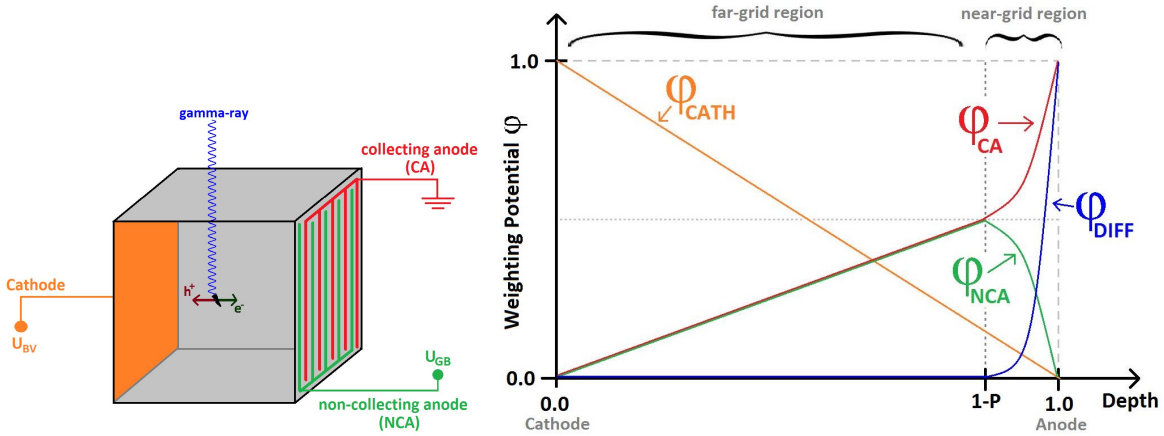

Figure 3.3.: Schematic drawing of the electrode configuration for a coplanar grid detector (left). The anodes consist of alternating parallel strips, forming two independent sets of grid electrodes. The red anode is the CA, while the green is referred to as the NCA. The opposite side is a planar cathode (orange color). The right graph illustrates the weighting potential for each electrode along the depth between the cathode and the anodes. The CA and NCA weighting potentials diverge approximately near the grid, where P is the distance between two neighboring anode lanes. The difference between φ_{CA} and φ_{NCA}, φ_{DIFF}, is shown in a blue line. Taken from [60].

The Shockley-Ramo theorem allows one to calculate the induced charge on an electrode more efficiently compared to the traditional method [61, 62]. One caveat is that the theorem is based on the movement of the charge carriers towards an electrode, not the number of collected charges. The equation for determining ΔQ is given as

$$\Delta Q = \int_{x_i}^{x_f} qE_v \cdot dx = -q[\varphi(x_f) - \varphi(x_i)], \tag{3.1}$$

where the charge cloud q drifts from its initial point x_i to the final position x_f. The E_v corresponds to the weighting field of the given electrode. The weighting potential φ is a normalized quantity defining the amount of induced charges. It is calculated by setting the electrode's potential to unity and the potentials of all other electrodes to zero and solving the Laplace equation $\bigtriangledown^2\varphi = 0$ when the space charge within the device is negligible.

Fig. 3.3 also shows the φ distribution of each electrode along a trajectory intersecting with one strip of the CA. The distribution can be divided into far and near-grid regions. In the far-grid region, due to the symmetrical configuration of the two anodes, the weighting potential of the CA and the NCA, φ_{CA} and φ_{NCA}, are nearly equal and rise with a slope of $\frac{1}{2}$ from the cathode reaching the anode. Near the grid region, φ_{CA} increases sharply to unity while φ_{NCA} drops to zero. As a result, the difference weighting potential $\varphi_{\mathrm{DIFF}} = \varphi_{\mathrm{CA}}$ - φ_{NCA} is rising to unity in the vicinity of the anodes and ideally zero elsewhere throughout the detector. Thus,

using φ_{DIFF} can eliminate the charges induced by the slow-moving holes in the far-grid region, and only electrons drifting through the grid contribute to the signal.

Assuming electron trapping is negligible, the number of the induced charges is determined by the following expressions according to Eq. 3.1,

$$\Delta Q_{\mathrm{CA}} = ne[\varphi_{\mathrm{CA}}(z=0) - \varphi_{\mathrm{CA}}(z=z_0)], \tag{3.2}$$

$$\Delta Q_{\mathrm{NCA}} = ne[\varphi_{\mathrm{NCA}}(z=0) - \varphi_{\mathrm{NCA}}(z=z_0)], \tag{3.3}$$

where ΔQ_{CA} and ΔQ_{NCA} are the induced anode signals. n is the number of electrons drifting to the anodes. z is referred to as the interaction depth. It is normalized by the length between the cathode and anode. The anode is defined as $z = 0$, while the cathode is $z = 1$, as opposed to the actual depth shown in Fig. 3.3. z_0 is the distance between the interaction point and the anode. The $\varphi_{\mathrm{CA}}(z = 0)$ is one as electrons are collected by the CA, whereas $\varphi_{\mathrm{NCA}}(z = 0) = 0$.

The difference signal, $\Delta Q_{\mathrm{DIFF}} = Q_{\mathrm{CA}}$ - $Q_{\mathrm{NCA}} = ne$, is the difference of the anode signals. In principle, it is independent of the interaction depth and proportional to the energy E.

The CPG technique also allows for reconstructing the interaction depth. As the cathode is a planar electrode, φ_{CATH} is linear as a function of the depth. So, the cathode signal is proportional to the total charge and the depth of the interaction. By eliminating the induced charges ne, the interaction depth, z_0, is obtained by the ratio of the cathode signal ΔQ_{CATH} to the difference signal ΔQ_{DIFF},

$$z_0 = \frac{\Delta Q_{\mathrm{CATH}}}{\Delta Q_{\mathrm{DIFF}}} = \frac{\Delta Q_{\mathrm{CA}} + \Delta Q_{\mathrm{NCA}}}{\Delta Q_{\mathrm{CA}} - \Delta Q_{\mathrm{NCA}}}. \tag{3.4}$$

However, electron trapping in CZT detectors has a strong effect that leads to position dependence of the signal and energy resolution degradation. The corresponding corrections have been investigated to compensate for the electron trapping effect. One way is to apply an optimal weighting factor ω on the NCA signal. The corrected signal is reconstructed as

$$\Delta Q_{\mathrm{ADIFF}} = Q_{\mathrm{CA}} - \omega \cdot Q_{\mathrm{NCA}}. \tag{3.5}$$

The parameter ω is empirically determined for each detector as charge transport properties vary with crystals. Such a correction has significantly improved the energy resolution and will be discussed in detail for the new detectors in Chapter 4.

Assuming a mean trapping length λ for electrons drifting in the CZT crystal, the resulting anode signals are calculated. The trapping corrected depth z_{tc} is obtained from

$$z_{tc} = \lambda \ln\left(1 + \frac{1}{\lambda}\frac{\Delta \mathrm{Q}_{\mathrm{CATH}}}{\Delta \mathrm{Q}_{\mathrm{DIFF}}}\right). \tag{3.6}$$

λ can be calculated from the weighting factor via $\lambda = \frac{1+\omega}{1-\omega}$ [63].

Apart from the electron trapping, several other factors have limited the performance of CPG detectors. These include material non-uniformity, weighting potential distortions, and electronic noise [64, 65]. In recent years, manufacturing technology has made good progress with the crystal quality. The CPG configuration has been further optimized to balance the weighting potential [66, 67]. Details about the electronic noise will be discussed in Section 5.4.

However, there are still issues intrinsically related to the CPG technique. For instance, it is known that the CA and NCA weighting potentials differ significantly near the anode. Consequently, there are reconstruction artifacts for interactions occurring in this region. Moreover, it is not practical to completely eliminate the hole's contributions. If an interaction happens near the anode, the generated holes can be collected by the NCA, which will then double the reconstructed energy. These issues will be dealt with accordingly in the analysis.

3.2.2. Energy resolution

The energy resolution at a certain γ peak is often used as one of the quantities evaluating the detector performance. It is quoted as the full width at half maximum (FWHM) in keV or FWHM(E_γ)/E_γ in percent. To extract the FWHM from a γ peak, a two-sided Gaussian function plus a linear Compton background is used to fit the full energy peak (FEP). The fitting function is expressed as

$$f(x) = A \cdot e^{-\frac{1}{2}\frac{(x-\mu)^2}{\sigma_{\mathrm{L,R}}}} + a \cdot x + b, \tag{3.7}$$

where σ_{L} and σ_{R} are the standard deviations for the left and right sides, respectively. μ is the mean value of the peak.

The FWHM is derived via

$$\mathrm{FWHM} = 2\sqrt{2\ln(2)}\frac{\sigma_{\mathrm{L}} + \sigma_{\mathrm{R}}}{2}. \tag{3.8}$$

The lower the FWHM is, the better the detector will be at resolving closely spaced γ lines.

The energy resolution in terms of FWHM (keV) as a function of the energy E is parameterized as the convolution of three factors

$$\mathrm{FWHM}(E) = \sqrt{p_0^2 + p_1^2 \cdot E + p_2^2 \cdot E^2}. \tag{3.9}$$

The first term, p_0, accounts for a constant noise contribution. p_1 describes the statistical fluctuations of electron-hole pairs. As the charge carrier production follows a Poisson distribution, this term is proportional to $\sqrt{E/\epsilon}$, where ϵ is the minimum energy to create one electron-hole pair. The third factor, p_2, describes the effect of the incomplete charge collection and scales linearly with the incident energy. Compared to Germanium and Silicon semiconductors, CZT has a larger ϵ. Hence, the relative statistical fluctuation of the number of charge carriers is larger for CZT.

3.3. The COBRA Demonstrator

The previous section has discussed the working principles for CZT detectors with a CPG design. In the Demonstrator, 64 of such detectors are arranged in four layers inside Delrin holders. Each detector has an approximate mass of 5.9 g. A picture of one layer with 4×4 detectors is shown in the left of Fig. 3.4.

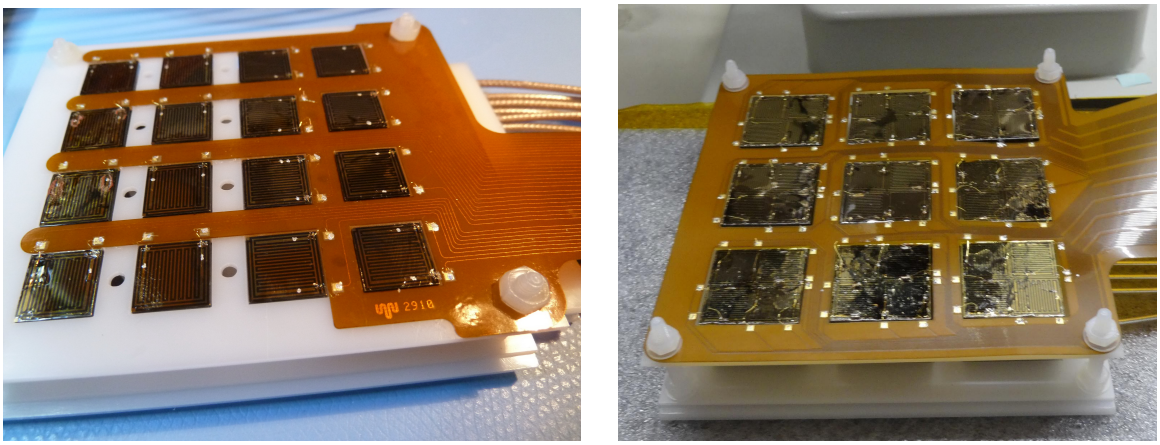

Figure 3.4.: Pictures of one Demonstrator layer holding 16 CZT detectors (left) and the new XDEM layer consisting of nine large detectors (right) taken from the anode side. The cathode is on the opposite side. The detector shown on the left has a size of $1\times1\times1\,\mathrm{cm}^3$, and each XDEM detector has a dimension of $2\times2\times1.5\,\mathrm{cm}^3$. The detectors are supported by the Delrin holder in white color. The electrical contact is achieved with gold wires connecting the detectors to coaxial cables on the cathode and a Kapton ribbon cable (orange color) on the anode side. The contact procedures used for small detectors differ from those used in XDEM. Details are discussed in the text.

In total, 61 out of the 64 detectors are functional. The three detectors suffer from faulty electrical contacts. A mean energy resolution of $(1.7\pm0.1)\%$ at 2615 keV was achieved [38]. Fig. 3.5 shows the accumulated exposure as a function of time. Periods without data-taking were caused by on-site shifts, Nitrogen flushing failures, and the XDEM installation. High-quality data with an exposure of 533.3 kg·d have been collected.

For the Demonstrator operation, the dominant backgrounds for double beta decays are identified. At low energies, events originating from the fourfold forbidden non-unique single β-decay of ^{113}Cd dominate. Noise events are also present. The main background component at high energies is α particles emitted from detector surface contaminations and Radon decays. High energetic γ photons produced from radioisotopes can also enter and interact with the detectors. These events need to be suppressed in order to set a robust half-life limit on $\beta\beta$-decays. For this purpose, pulse shape discriminations were developed to reject backgrounds as well as to optimize the detector performance [39].

Remarkable results have been achieved with the Demonstrator [37]. Analyses are ongoing to develop a background model and produce a more sensitive search for $0\nu\beta\beta$ decays with more exposure than the previous work. Apart from the $\beta\beta$ searches, the fourfold forbidden non-unique single β-decay of ^{113}Cd has been investigated to evaluate the quenched value of the axial-vector coupling strength g_A [38]. An accurate g_A is crucial when the potentially measured $0\nu\beta\beta$-decay half-life is converted into a Majorana neutrino mass. This parameter strongly depends on the β spectrum shape and will be investigated further at low energies.

The Demonstrator proves that CZT detectors have been operated stably under ultra-low

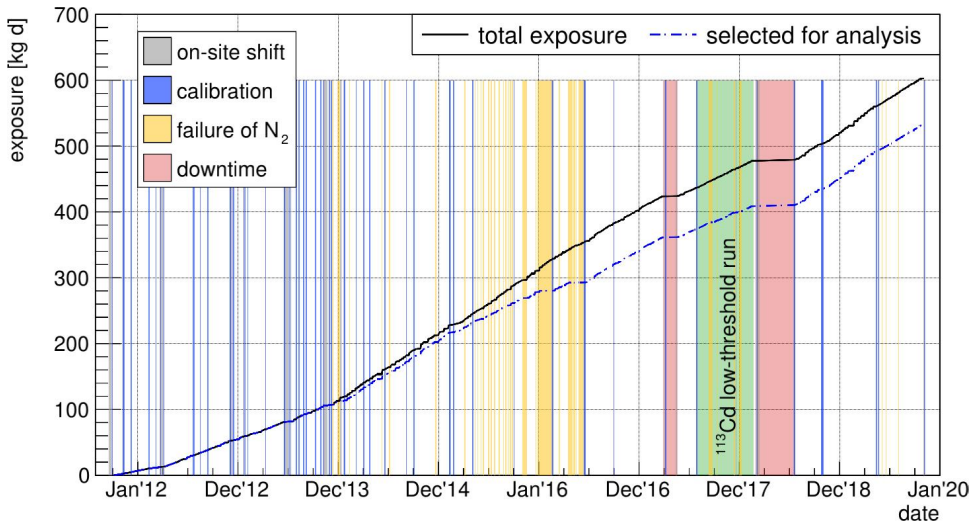

Figure 3.5.: Accumulated exposure for the Demonstrator at the LNGS [39]. Data-taking is affected by on-site shifts, calibrations, Nitrogen flushing failures, and XDEM installation.

background conditions over a time scale of several years [68]. In order to improve the signal sensitivity, the Demonstrator has to be scaled up to obtain more exposure. However, it was found that its background level is 1.2 cts/(kg·keV·yr) in the ROI of the ^{116}Cd $0\nu\beta\beta$-decay [39], which is too high to see $\beta\beta$ signals. Hence, minimizing backgrounds is the priority of the following upgrade.

3.4. Quad coplanar grid CdZnTe detectors

One efficient solution for suppressing the prominent α contaminations is to ground a boundary electrode surrounding the CPG, the so-called guard ring. In this way, the charge clouds produced near the lateral surfaces of the crystal are collected mainly by the guard ring instead of the CA. This strategy is applied to the new detectors [69].

Another drawback of the Demonstrator is the smallness of the individual CZT crystals. According to a Geant4 simulation [68, 70], the small volume limits the detection efficiency to about 63% at the Q-value of the ^{116}Cd $0\nu\beta\beta$-decay. In comparison, larger detectors will be favorable because they substantially improve the detection efficiency, which is especially important in double beta decay experiments. Using larger CZT crystals also minimizes the number of readout channels and auxiliary components per detector volume.

Large volume CZT detectors have existed for several years but with limited availability and performance [71–73]. One of the restrictions is that it is time-consuming to select highly uniform crystals capable of efficient charge transport [74]. This is because defects are unavoidably generated and increase with the crystal size, which is limited by the current manufacturing technologies. Defects like grain boundaries, large-scale Te-inclusions, and prismatic dislocations are particularly detrimental, as they are known to trap charge carriers [75–78]. The charge loss can be so significant that it cannot be corrected without introducing new problems.

As a result, the energy resolution and detection efficiency are degraded by charge transport non-uniformities.

The non-uniform electric field also limits the detector volume, as it leads to various drift paths of charge carriers and thus causes fluctuations of induced charges [78]. This non-uniformity is possibly associated with the accumulation of positive space charges. It is also correlated with the content of crystal strains and defects [76]. Furthermore, the electric field can also vary laterally because of the surface conductivity that defines boundary conditions for the electric potential. Consequently, the so-called edge effect leads to charge loss near the detector edges [79–81].

3.4.1. Quad coplanar grid principle

Thanks to the considerable progress achieved in crystal growth in recent years, comparatively large CZT crystals are commercially available now [82–84]. Meanwhile, different electrode configurations are investigated, and significant variations in spectral performance have been observed [78, 85–87]. It turns out that simply scaling the grid electrodes results in poor performance. This is because the capacitance and the leakage current will also scale with the grid size, contributing to the overall detector noise and deteriorating the spectral performance.

Instead, the quad coplanar grid (qCPG) design is conceptualized for the large detector, as illustrated in Fig. 3.6. The anode consists of four CPGs rotated by 90° against each other on a single crystal, while the cathode is patterned as a planar electrode on the bottom. The guard ring (GR) surrounds the four CPGs. The volume under each CPG is called a sector. The outer rail of the CPG is the collecting anode (CA), while the inner rail is the non-collecting anode (NCA). By employing this configuration, the NCA potential in the central acts as a virtual steering grid. It is thus possible to reduce the potential charge-sharing effect among different sectors. The charge-sharing effect indicates that a portion of the electron cloud gets collected by multiple sectors. It happens when an event occurs in the vicinity of the CPGs' border, where the non-uniformity of the weighting potential of any grid is the worst.

The signals from all the CPGs and GR are read out independently, while the cathode signal is not read out. Each sector can be analyzed individually. The detector granularity also allows for the discrimination of multi-sector events in which an incident particle deposits its energy in more than one sector [88]. These multi-sector events are mostly caused by multiple scattered γ-rays. So, the discrimination intrinsically reduces γ backgrounds.

Furthermore, the grounded GR is not only to suppress events from lateral surfaces but also beneficial for the overall detector performance. This is because the grounded GR can absorb surface leakage currents so that they will no longer contribute to noise. A relatively high bulk voltage can be applied, and thus a better charge collection efficiency is expected. Moreover, the GR minimizes the weighting potential distortions of the CPG, especially near the anode [67]. However, it is worth noting that suppressing the lateral surface events comes at the cost of reducing the effective area of the detector, leading to a lower detection efficiency.

In short words, with this electrode configuration, the leakage current and the capacitance between the grids have been reduced. The detector achieves a good energy resolution with low energy thresholds.

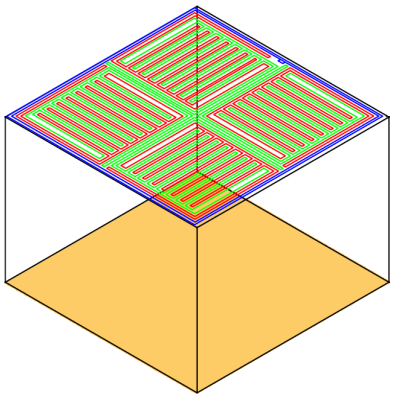

Figure 3.6.: Sketch of one CZT detector with the qCPG readout. Four CPG pairs with interleaved CA (red color), NCA (green color), and an outer GR (blue color) are patterned on the top. The common planar cathode (orange color) is metalized on the bottom. The cathode surface area is $2\times2\,\mathrm{cm}^2$, and the crystal thickness is 1.5 cm.

3.4.2. Working point determination

As stated earlier, CZT detectors require voltage supplies to drive charge carriers to the respective electrode. The bulk voltage (BV) refers to the high voltage between the cathode and anode, while the grid bias (GB) represents the voltage between the CA and NCA. The voltage should be high enough so that charge carriers can move fast. On the other hand, the electronic noise attributed to the leakage current should also be minimized. Since both the BV and the GB affect the electric field distribution, the detector performance depends on their interplay.

In this section, two qCPG prototype detectors are characterized with working point measurements. The working point is the combination of the BV and the GB, under which the detector has the optimal performance. One detector is from manufacturer eV Products, and the other is from Redlen Technologies. Unlike the installed XDEM detectors, the prototypes employ a slightly different electrode configuration, where the GR is not instrumented. This difference has negligible effects on the results presented here.

In principle, large detectors require higher voltages than small ones to obtain comparable electric fields. However, due to the limitations of cables and connectors used at TU Dresden, high voltage can only be set to a maximum of 1700 V. Therefore, the BV was adjusted from 900 V to 1700 V in steps of 100 V by a power supply unit ISEG SHQ 226L, and the GB was ranged from 25 V to 125 V in steps of 5 V. The CA is grounded, and the applied BV is negative in order to drive electrons to the anode. For each combination of the BV and GB, the detectors were irradiated with a 250 kBq ^{137}Cs source. The measurements were already performed previously [39, 89]. This section focuses on the data analysis that follows a similar procedure as for small detectors.

At the working point, the detector would have the best energy resolution at the 661.7 keV γ peak. A weighting factor ω is introduced for each combination of the BV and GB to

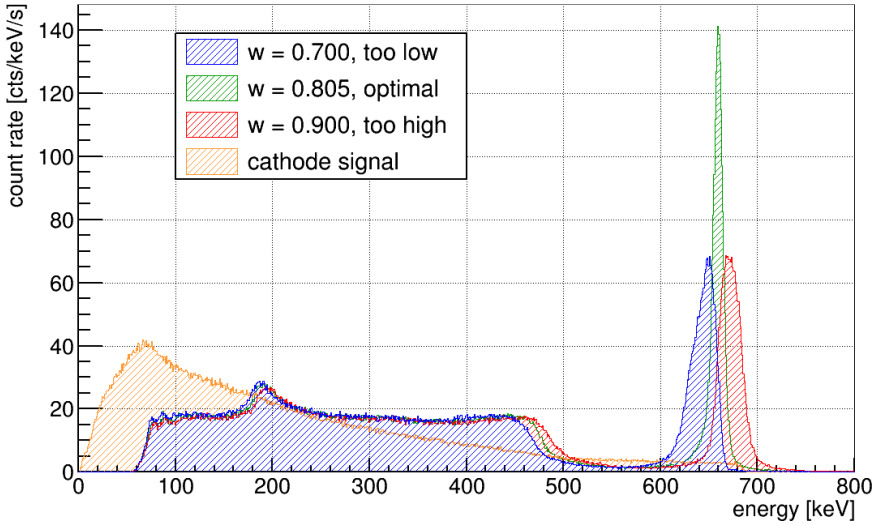

Figure 3.7.: The energy spectra of ^{137}Cs applied with different weighting factors [39]. The energy resolution varies significantly. The detector performs the best with an optimal ω.

compensate for electron trapping. In the ideal case that electrons are not trapped, ω will be one. A smaller ω would indicate that electron trapping is more severe. Fig. 3.7 shows the spectral performance varying with ω. The correlation of the energy resolution and ω can be modeled by a parabola function. The optimal ω lies at the minimum of the function.

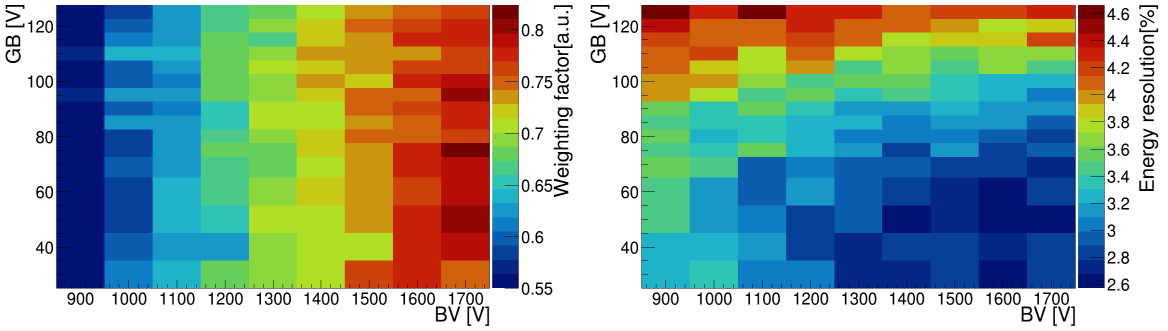

Figure 3.8.: The weighting factor (left) and the relative energy resolution (right) of a sector from one qCPG detector (eV Products) are calculated for each BV and GB combination. The other three sectors show similar behavior.

Fig. 3.8 demonstrates the weighting factor and the relative energy resolution as a function of the applied voltage. When detectors work under a low bias, it is said that the polarization effect[1] becomes noticeable and can distort the electric field distribution [90], which explains

[1]Polarization is usually characterized by progressive degradation of the energy resolution or low energy shifts of γ peaks. It is related to a detector's bias voltage, radiation flux, and temperature [90].

small weighting factors and degraded energy resolutions. The weighting factor is seen increasing with BV. This is because the drift velocity of electrons rises with the voltage and reduces the electron trapping and drifting path variations. A better detector performance is achieved. Once the bias approaches a critical value, increasing the voltage further will degrade the detector performance due to increased electronic noise.

A similar mechanism also applies to the GB, which should steer all electrons toward the CA. However, charge sharing events[2] are observed with a low GB. The incomplete charge collection causes a low energy tail at the γ peak. With a higher GB applied, the leakage current between the anodes increases and leads to electronic noise.

Each detector has a specific working point depending on its physical properties. A BV of -1700 V and a GB of -50 V for the eV Products detector shown in Fig. 3.8, and a BV of -1300 V as well as a GB around -100 V for the Redlen prototype are determined.

Extensive characterizations for the new detectors were carried out at TU Dortmund, where the high voltage reaches over 3000 V [43]. The optimal working points are listed in Table A.1. The BV is from -2000 V to -2600 V, which results in the drift velocity of electrons comparable with small detectors. The Redlen detectors are operated under relatively low voltages and thus produce smaller leakage currents. All sectors of a qCPG detector are supplied with the same GB that has a typical value of -60 V to -80 V.

It is only practical to perform working point measurements above ground as they are very time-consuming. However, being operated underground at a temperature of 10 °C decreases thermal excitations of valence electrons. The detector generates a reduced leakage current, which allows for high biasing and improves the charge collection efficiency. Nevertheless, adjusting the working point is expected to produce comparable results and is not considered in this work.

3.4.3. Electric field uniformity

A constant lateral electric field in CZT detectors is expected to ensure uniform efficiency in charge collection over the entire device down to the edges. However, as mentioned in Section 3.4, the electric field distribution is mostly not uniform due to the surface conductivity, which is likely to cause incomplete charge collection. To measure the electric field strength, the drift velocity of electrons is used.

In order to quantify the electron velocity at different locations, the scanning data measured before are analyzed [91]. Any inhomogeneity would indicate a non-uniform charge transport. The plane parallel to the anodes is referred to as the xy plane, and the perpendicular direction is z. The scanning device can point to all detector sides with a collimated source except for the bottom. The detector is irradiated with a collimated ^{137}Cs source with 90 MBq placed along the xy plane. A stepper motor moves along the detector at a distance of 1 mm so that the detector is irradiated homogeneously. The irradiated area is about 1 mm^2. In total, 22×22 points were scanned.

[2] In this context, charge sharing means charge clouds are partially collected by the NCA, and the CPG working principle cannot be applied properly.

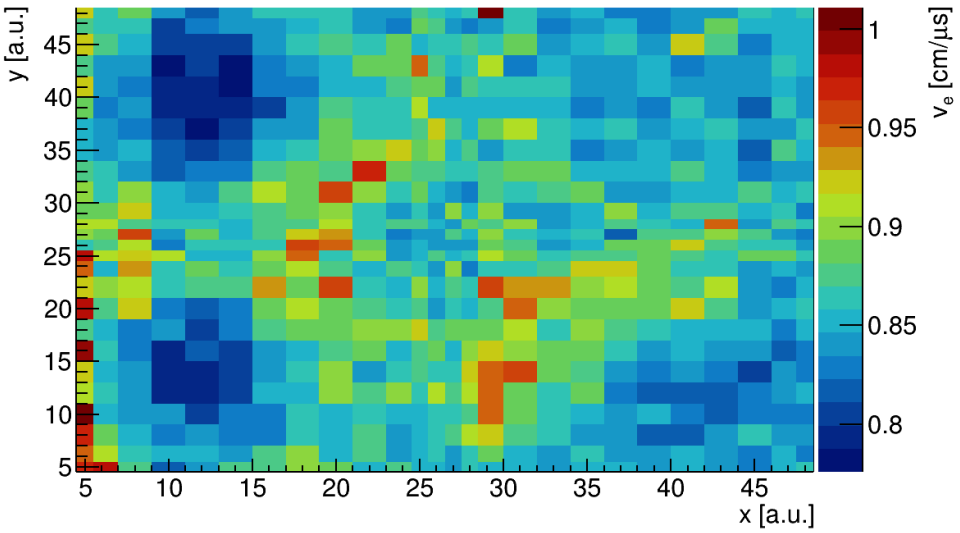

Figure 3.9.: Spatial variations of the electron drift velocity for the Redlen detector. The velocity is estimated as the interaction depth divided by the drift time. The anode side (xy plane) is irradiated by a ^{137}Cs source. Only events within the full energy peak at 661.7 keV and the normalized depth region of 0.75 to 0.95 are considered.

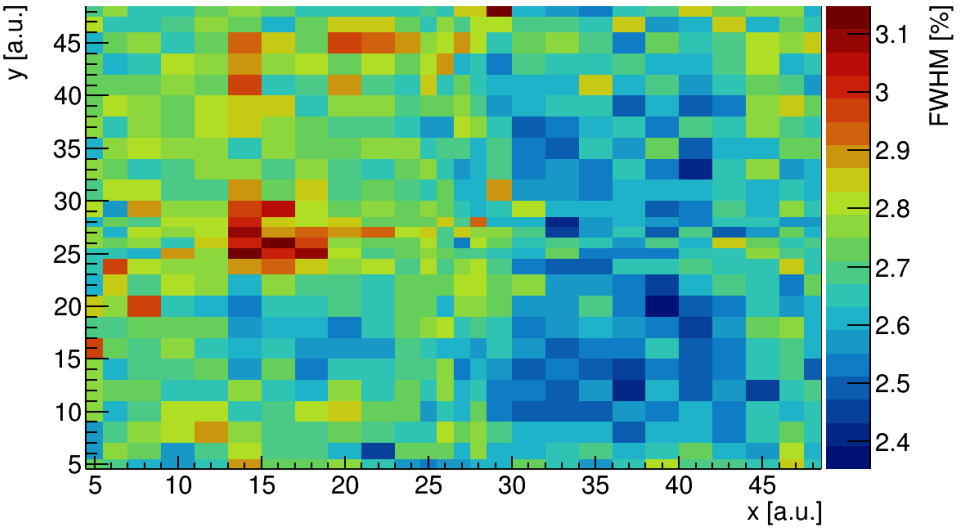

Figure 3.10.: The relative energy resolution of the scanning points irradiated from the anode of the Redlen detector. Only events within the full energy peak and the normalized depth region of 0.75 to 0.95 are considered.

The velocity is calculated from the z position divided by the drift time. The depth reconstruction discussed in Section 4.7 gives the normalized depth z, and then z is scaled to the actual drift depth. As for the drift time, it is extracted from the rising slope of the cathode pulse, which will be discussed in Section 6.7.

Fig. 3.9 shows the drift velocity plotted as a 2D map representing the overall detector response. The interaction depth is selected in the region of $z = 0.75$ to $z = 0.95$ near the cathode to ensure enough statistics. The graph shows that the velocity is not uniform. A high velocity indicates an increased electric field. This result agrees with the measurements shown in Ref. [81]. Around the sector borders, the velocity is relatively large. Similar phenomena are observed for the eV prototype detector. Nevertheless, this non-uniformity causes a negligible impact on the overall spectral response because the energy resolution is not degraded, as can be seen in Fig. 3.10.

3.5. Upgrade to the COBRA extended demonstrator

The previous study shows that the new detectors fulfill low background operation requirements [88]. The detector batches provided by the two manufacturers were installed at the LNGS in March 2018.

The goal of the XDEM is to increase the signal sensitivity and reach a reduced background level. Achieving this goal requires increasing the sensitive volume and lowering background contaminations. The total mass of 315.1 g nearly doubles the detector volume. A low background level relies on sufficient shieldings, radiopure material selections, and careful handling procedures during the assembly. Those measures are taken to reduce intrinsic and extrinsic radioactive backgrounds. Meanwhile, the cosmogenic activation of critical components is also minimized. The basic infrastructure and the controlling system used before still apply to the XDEM.

Rebuilding the shieldings is necessary to include the new detector layer. On the other hand, it is beneficial to keep the original shieldings as comparatively long-lived radioisotopes produced through cosmogenic activation have already decayed. Before installation, all the new shield parts were stored in the Felsenkeller underground laboratory shielded by 45 m of rock overburden. They were cleaned extensively in an ultrasonic bath with cleaning agents and ultrapure water at the LNGS to reduce potential surface contaminations. All components inside the Lead shield were screened using Inductively Coupled Plasma Mass Spectrometry (ICP-MS), alpha spectroscopy, and gamma-ray spectrometry to estimate background contributions.

Furthermore, materials used to construct the detector components have to be radiopure. For example, all detectors are coated with lacquer to prevent performance degradation from potential exposure to moisture or oxygen. The coating material used for the detectors from Redlen is an Epoxy-based resin. It has a specifically reduced ^{40}K content. The eV Products detector batch is offered with a Glyptal resin.

The electrode metalization also uses materials containing less α contaminations than the Demonstrator. The procedure for electrical contact has also been improved to reduce possible contaminations. A silver-based conductive epoxy, TRA-DUCT 2902, was introduced instead

of using old materials with a high contamination level. The material has a high radiopurity and mechanical strength, making it suitable for low background applications..

Gold wires connect anodes to a Kapton ribbon cable for the signal transmission. The Kapton cable also supplies detectors with the grid bias. The bulk voltage is supplied from a custom-made high voltage filter via coaxial cables on the cathode. The filter ensures a stable transmission of the optimal voltage to the detector array. Unlike the previous setup, the high voltage supply lanes have been separated from the preamplifier modules to prevent any adverse effect, such as crosstalk from micro discharges inside the module.

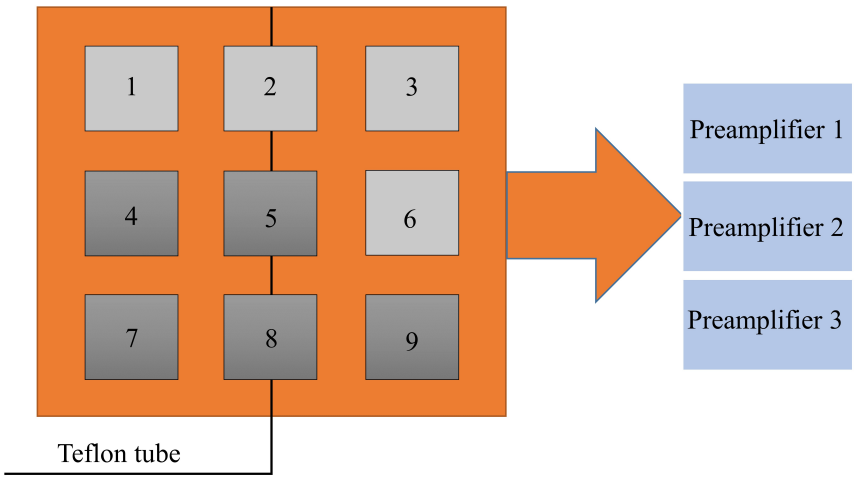

Figure 3.11.: Schematics of the detector designations in the XDEM. Color coding indicates the detectors from two manufacturers. The light grey ones are from eV Products, and the dark grey ones are from Redlen. Preamplifier module 1 operates detectors one, two, and three, and module 2 works for seven, eight, and nine. A Teflon tube guides the calibration source to the bottom of the detector layer.

Finally, nine encapsulated and metalized CZT detectors were framed as a 3×3 layer by a Delrin support holder, as already shown on the right Fig. 3.4. Fig. 3.11 shows the layout of detectors and preamplifier modules. Each module connects three detectors. The cooling unit is expanded to cool down the XDEM preamplifiers as well. Eleven linear amplifiers are hosted in a multi-channel NIM crate that allows for the stable operation of the amplifiers despite the high power consumption. Each FADC reads out signals from the four sectors of a qCPG detector, while two additional FADCs digitize the guard ring signals. The FADC gets triggered as soon as one of the CA channels is above the threshold.

This chapter has given an overview of the COBRA experimental setup. The working principles and characterizations of the CZT detector were also discussed. The prominent α contaminations found in the previous setup and γ-rays are expected to be reduced significantly with the innovative readout and the improved handling procedures.

4. Event reconstruction for the qCPG CdZnTe detector

The previous detector characterizations show that the qCPG readout works well enough for the large CZT crystal to build up XDEM. However, several aspects of the new device design are not yet fully understood. In order to gain a better understanding, pulse shape simulations are developed. They can give insights into how the new electrode affects the detector performance [92–94]. With a good understanding of the detector response, event reconstruction can be updated and expanded.

The pulse shape construction is based on the Shockley-Ramo theorem. In this work, the simulation framework is built with COMSOL [95] for obtaining the electric field and the weighting potential distribution inside the crystal, as well as Geant4 for modeling the physical processes involved with radiation interactions through matter. The developments for the pulse shapes are explained in detail from Section 4.1 to Section 4.4. The following sections will discuss the energy and position reconstructions, including a correction for electron trapping.

4.1. COMSOL simulations

COMSOL is a finite element package that can be used to solve partial differential equations numerically. It is suitable for obtaining the potential profile within a device. The simulations are performed in a series of steps detailed in the block diagram given by Fig. 4.1.

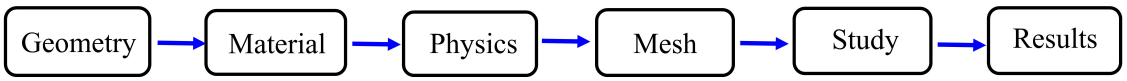

Figure 4.1.: Block diagram displaying steps for COMSOL simulations.

A precise description of the detector geometry is vital for the simulation. The first step is to model a $2\times2\times1.5\,\mathrm{cm}^3$ detector employing the current electrode, as illustrated in Fig. 3.6. The geometry is created using AutoCAD, a computer-aided design software [96]. Then, the material properties available in COMSOL are assigned for each component. The following step is to add physics lists. Various physics modules are available. For our purpose, the "Electrostatics" module is used with the corresponding parameters and equations defined. The finite element method is based on solving meshes on the defined geometry. So, the whole geometric detector is meshed into many small elements, as shown in Fig. 4.2.

The computation can start after completing the mesh process. To mitigate the computational time while maintaining precision, the Adaptive Mesh Refinement implemented in

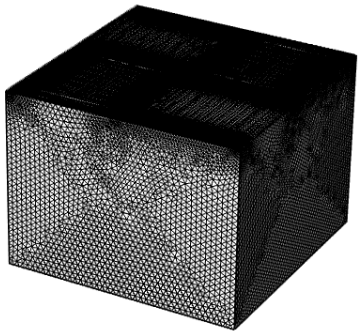

Figure 4.2.: Meshing the CZT detector in COMSOL. The electrode (on top) is meshed intensively because it contains many geometric details.

COMSOL is applied. The refinement is to re-mesh the geometry with finer elements in the region where the resulting error is large. With this refined mesh, the solution tends to be more accurate than before. The level of mesh refinement is controllable. This feature is well-suited for modeling problems involving high gradients.

The approximate solutions to differential equations are obtained at discrete points defined by the mesh. The last step is to visualize and analyze the computed results.

4.1.1. Electric field distribution

The electric potential $\Phi(x, y, z)$ of the detector is obtained by solving the following equation

$$\frac{\partial^2\Phi(x,y,z)}{\partial x^2} + \frac{\partial^2\Phi(x,y,z)}{\partial y^2} + \frac{\partial^2\Phi(x,y,z)}{\partial z^2} = 0 \tag{4.1}$$

using the multi-grid solver implemented in COMSOL. The boundary conditions are set automatically by voltage settings. The bulk voltage (BV) is set to 2600 V and the grid bias (GB) to 80 V, based on the optimal working point given in Section 3.4.2.

The electric field is defined as the gradient of the electric potential,

$$E_x = - \bigtriangledown \Phi(x), \tag{4.2}$$

where E_x is the electric field in the direction of x, and $\Phi(x)$ is the electric potential. The electric field strengths are stored in a histogram and later used to calculate the charge transport.

As mentioned earlier, the solutions are represented as discrete data points. Since charge carriers can propagate to any random position, interpolation will be necessary. The interpolation generally requires known values from neighboring points. Various algorithms are available in which high gradients can be averaged out. The electric field at the boundary changes significantly. As this change is crucial to the drift of charge carriers, the boundary value cannot be interpolated.

It turns out that the optimal working point lies at a lower GB than that expected from simulations. When the same GB is applied, the charge sharing effect is still noticeable in the

simulation but not in the measurement. The same phenomenon is also found in Ref. [97]. In other words, a comparatively low GB is enough to reduce the charge sharing effect so that the moving electrons are guided to the CA and not to the NCA.

4.1.2. Weighting potential distribution

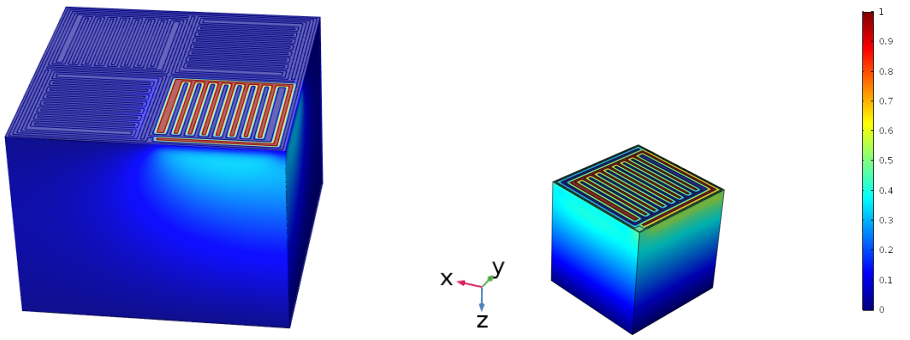

Figure 4.3.: Weighting potentials distributed from zero to one by setting one CA to a unit potential. Left: one qCPG detector installed for the XDEM. Right: one small CPG detector used in the Demonstrator.

As already explained before, the weighting potential determines the charges induced on an electrode by moving charge carriers. It is independent of the applied voltage. Fig. 4.3 shows the weighting potential distribution with an XDEM detector and one Demonstrator detector, respectively. The weighting potential is obtained by setting one CA to a unit potential, grounding the rest of the electrodes, and solving the Laplace equation.

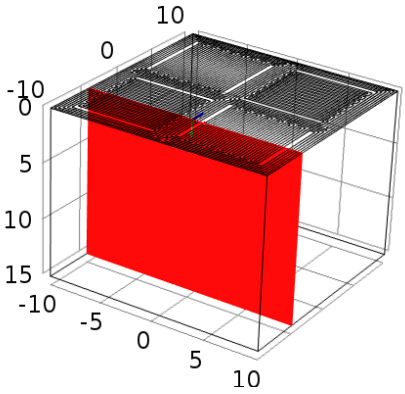

Figure 4.4.: The 2D cutting plane used for calculating the field distribution. It will also be used to determine the charge carrier drift and charge induction. The plane intersects the middle of the two front sectors. The detector size is in the unit of mm.

It can be seen that the weighting potential distribution of the new detector is not as uniform as the previous generation and even extends to the neighboring sectors. Similarly, to simulate

weighting potentials and determine the charges induced on NCA, the NCA is set to a unit potential, and the other electrodes are kept at zero.

The finer the mesh size is, the more accurate the field calculation will be. Hence, an extremely fine mesh configuration is used. Concerning intensive computations with the extremely fine mesh, it is possible to exploit the symmetric geometry of the detector and transform the 3D model into a 2D. The 2D projection of the geometry reduces the computation power significantly and allows an even finer mesh size compared to the 3D. Fig. 4.4 shows the cutting plane used for the projection.

Like the electric field interpolation, the weighting potential is also interpolated. And values at the boundary are excluded from the interpolation, as they are crucial to the precise estimation of induced charges and cannot be smoothed out.

4.2. Pulse shape development

With the obtained electric field and the weighting potential, the first attempt of the pulse shape simulation concentrates on the single charge carrier drift. It simulates how one electron induces a charge on the readout electrodes.

Table 4.1.: Parameters used in the pulse shape simulation are listed.

parameter	value
BV [V]	2600
GB [V]	80
μ_e [cm^2/(V·s)]	1000
Δt [ns]	1

Since holes move much slower than electrons in the CZT crystal, we assume that the hole remains stationary during the period of the electron drift. The electron generated at one initial position (x_0, y_0) moves to the anode driven by the electric field. Its drift path is calculated via

$$x = x_0 + \sum \Delta x = x_0 + \sum v_x \Delta t = x_0 + \sum \mu_e E_x \Delta t, \tag{4.3}$$

where v_x is the drift velocity in the direction of x. It is determined from the product of the electron mobility μ_e and the electric field strength E_x. The electron mobility depends on the electric field and stays nearly constant under the applied field strength [98, 99]. For more discussions about μ_e, see Section 6.7.2. A similar calculation was done for the y dimension. In a simplified case, a constant average velocity can also be used as the electric field is distributed uniformly in most regions [100].

The trajectory of the charge carrier is calculated for each time step Δt. Instead of the FADC digitizing rate of 10 ns, a time step of 1 ns was used for a more detailed development. Then, the according weighting potentials of the CA and the NCA are extracted from each position. Based on the Shockley-Ramo theorem described in Section 3.1, the charge signals induced

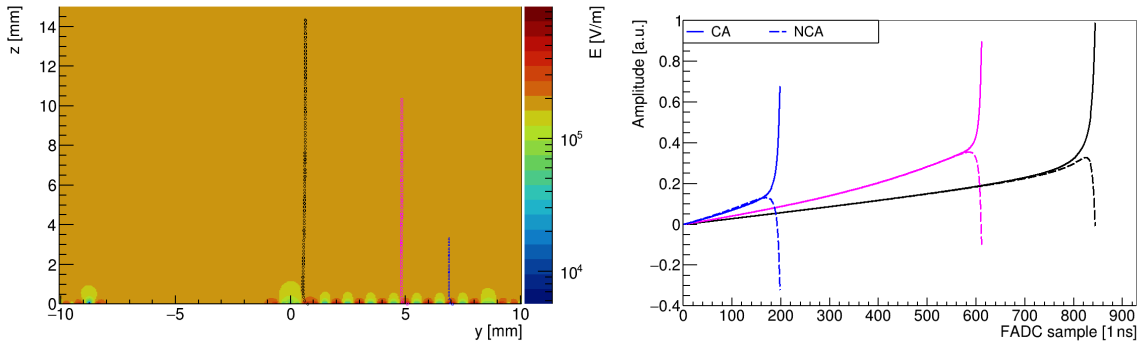

Figure 4.5.: Left: The electric field distribution in the detector. The trajectories for the three single electrons are determined from the electron transport calculation and are shown in different colors. These electrons start from different positions. Right: Calculated pulse shapes for the single electrons drifting within the CZT detector, including CA pulses (in solid lines) with the rising slope and NCA pulses (in dashed lines) with the dropping slope. The color coding indicates the respective trajectory shown on the left.

on the respective electrode are determined by adding the weighting potentials' difference between the current and previous positions. This process continues till the electron reaches the endpoint. The resulting pulse shapes are saved to ROOT, a data analysis software based on C++ [101]. The trapping effect is not considered in the course of the drift. Parameters used in the simulation are summarized in Table 4.1.

An example of pulse shapes induced by single electrons with various initial positions is given in Fig. 4.5. The left figure shows that the field strength is constant throughout the detector except in the vicinity of the anodes. At each time step of the charge trajectory, the electron induces charges on the two anodes simultaneously when moving towards them. Due to the voltage difference between the two anodes, electrons are steered towards the CA and eventually collected by it. That is when the induced charges on the CA reach the maximum, while the NCA signals drop, as shown on the right graph of Fig. 4.5.

The total charge resulting from the subtraction of the two anode pulses will be constant, as $Q_{\mathrm{DIFF}} = Q_{\mathrm{CA}} - Q_{\mathrm{NCA}}$. It is independent of the initial position of the electron. This is because only charge carriers drifting through the grid contribute to the final signal. As only one electron is considered, $Q_{\mathrm{DIFF}} = e$.

Fig. 4.6 highlights the trajectories of single electrons near the anodes. These electrons from different initial positions are eventually driven to the CA. It is worth noting that electrons traveling underneath the NCA exhibit pulse shapes slightly different from those developed by events originating from the CA side. As shown in the right Fig. 4.6, there is a dip in the CA pulse and a bump on the NCA pulse as a result of the relatively long time staying close to the NCA. Hence, this bump indicates events are from the NCA side and can be used for pulse shape discriminations.

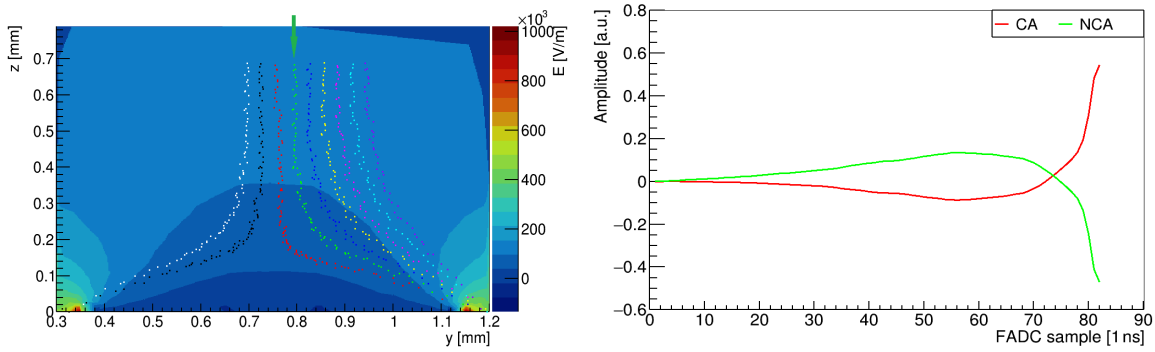

Figure 4.6.: Left: The electric field zoomed in near the NCA. The trajectories of the single electrons from different initial positions are determined from the transport calculations and are shown in different colors. Right: Calculated pulse shapes for the single electron with the trajectory in green color denoted with an arrow on the left, including the CA pulse with the rising slope and the NCA pulse with the dropping slope. A dip is found in the CA pulse and a bump in the NCA pulse, compared to Fig. 4.5.

4.3. Monte Carlo simulations

Instead of single electrons, a number of charge carriers are usually generated by radiation interacting with the detector, and the amount is proportional to the deposited energy. The following step is to convert the pulse shape of a single charge to multiple charge carriers. For this purpose, a Monte Carlo simulation is performed to obtain the detailed energy deposition and position information.

The Monte Carlo simulation models the particle tracks and the corresponding energy losses within the crystal. The program used here is Geant4, a C++ toolkit for simulating the passage of particles through matter. It has been widely used in many experiments at different scales of energies. The probabilities and interactions between particles and the detector material are considered.

In the simulation, the detector is regarded as an ideal calorimeter. A particle takes steps along its trajectory until an end condition is met. Each step carries information about the starting and ending points of that step and the energy loss between the two points. It is also possible to obtain the total energy deposition and the exact trajectory of the particle. For constructing pulses, the step information is stored.

4.3.1. Geant4 rdecay02 package

The framework is first developed based on the rdecay02 package (Geant4.10.06). This package is available in the extended examples of the Geant4 installation. rdecay02 has radioactive decay physics implemented and provides the interface for saving data in ROOT files. Changes are made to adapt to this work. First of all, the detector geometry is modified to a single CZT detector. Secondly, the position and the energy information of each step are stored

accordingly. For the original code, if a decay goes to the excited state of its daughter nucleus, the de-excitation energy converts to kinetic energy instead of photons. This issue is corrected by including the physics lists of $FTFP\_BERT$ and $G4RadioactiveDecayPhysics$.

4.3.2. COBRA simulation toolkit - VENOM

Although the revised rdecay02 simulates interactions with single detectors, a more advanced Monte Carlo toolkit, VENOM, simulates with the whole experimental geometry based on Geant4 [102]. The physics module includes the *Shielding* list with all the relevant physics processes suitable for low background experiments. This tool is interfaced with several event generators to produce primary particles, such as the Geant4's particle gun, the decay chain generator (*chaingen*), the $\beta\beta$-decay generator (*Decay0*), and so on [103].

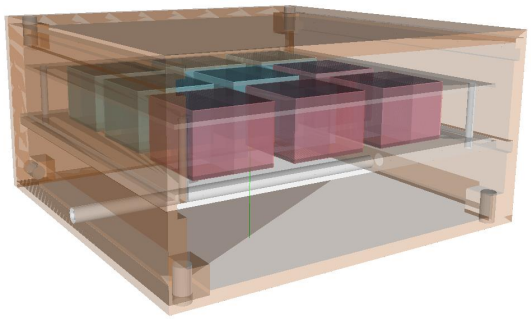

Figure 4.7.: VENOM visualization of the nine detectors framed by Delrin holders (white color) and hosted inside an electroformed Copper (orange color) [104]. Color coding indicates different detector manufacturers. A calibration source can be inserted into the Teflon tube (white color) placed at the bottom of the Copper shield.

VENOM supports the so-called Geometry Description Markup Language (GDML) files for describing geometries [105]. GDML files are independent of the source code and can be modified without affecting the rest part of the VENOM. Following the upgrade of XDEM, the detectors, as well as the surrounding materials, including Delrin holders, coating lacquer, cables, shielding layers, and calibration tube, have been incorporated previously [43, 104]. The detector module surrounded by an electroformed Copper is visualized in Fig. 4.7.

To gain a good understanding of the new setup and validate the simulation software, the energy deposition of a calibration source is simulated and compared with the measured data. For the simulation, the radioactive source is modeled as a cylinder with a size of $1.0\times1.0\,\mathrm{mm}$, enclosed by an Aluminum container with a dimension of $1.0\times1.0\times3.5\,\mathrm{mm}^3$. The container is to shield electrons emitted from the source. The source is placed in a Teflon cube located at the bottom of the Copper shield, close to the detector's cathode.

Primary particles are generated by an event generator, *bkggen*, which can also confine the source within the calibration tube. Fig. 4.8 compares the simulated total energy deposition with ^{228}Th and the measured spectrum at the LNGS. The simulated energy is smeared with an average energy resolution function discussed in Section 5.5. One can see that the simulated

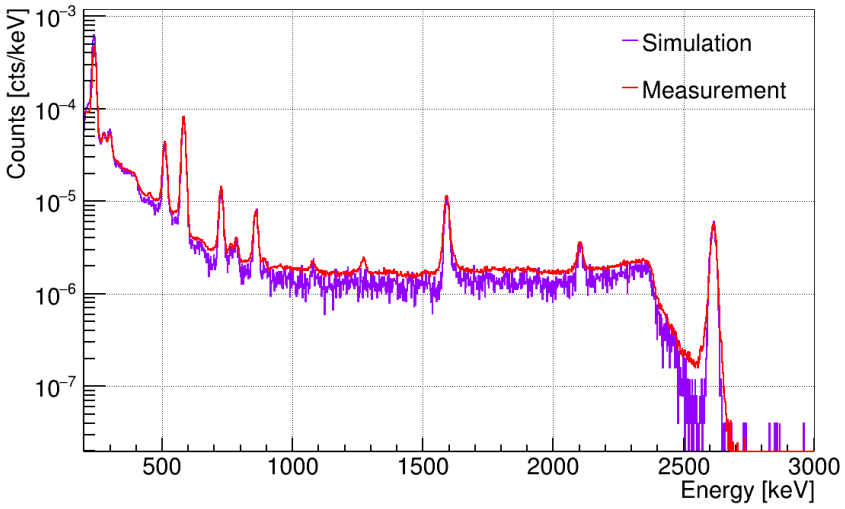

Figure 4.8.: Comparison of the normalized energy spectra of ^{228}Th obtained from the simulation and the measurement. A combined experimental dataset from different periods is used. The simulation is smeared with an average energy resolution function. A threshold of 200 keV is applied in the simulation to approximate the energy threshold in calibrations.

γ lines are consistent with those in the measurement, except that a slightly low energy tail is present at high energies for the measurement. This tail is probably due to the incomplete charge collection, as the simulation does not take the loss of charge carriers into account.

4.4. Final pulse shapes

Based on the previous descriptions of how a single charge induces pulses and how to obtain the energy loss along the particle trajectory, the framework is applied to multiple charge carriers to construct final pulses. Hardware effects can be added so that one can make a comparison of the simulation and data. A similar simulation framework is also developed for the Demonstrator.

4.4.1. Signal pulses construction

The pulse shape of a complete event is constructed by the step information obtained from the Monte Carlo simulation. The energy deposited at each step is assumed to be equivalent to the number of electron-hole pairs created at that step. For each step, a pulse is developed. The total signal of a simulated event is composed of several interactions and is a sum of pulses from every step. The thermal diffusion and the Coulomb expansion of charge clouds are not considered here. Therefore, charge carriers are point-like instead of creating a charge cloud.

Also, to match the coordinates of the cutting plane shown in Fig. 4.4 and extract weighting potentials from them, each detector's position in XDEM has been corrected accordingly.

4.4.2. Mirror pulses and guard ring pulse construction

For an XDEM detector, besides the primary sector where an event deposits its energy, the neighboring sectors are also taken into account. This is because the electrodes on these sectors also sense the movement of charge carriers and create the so-called mirror pulses.

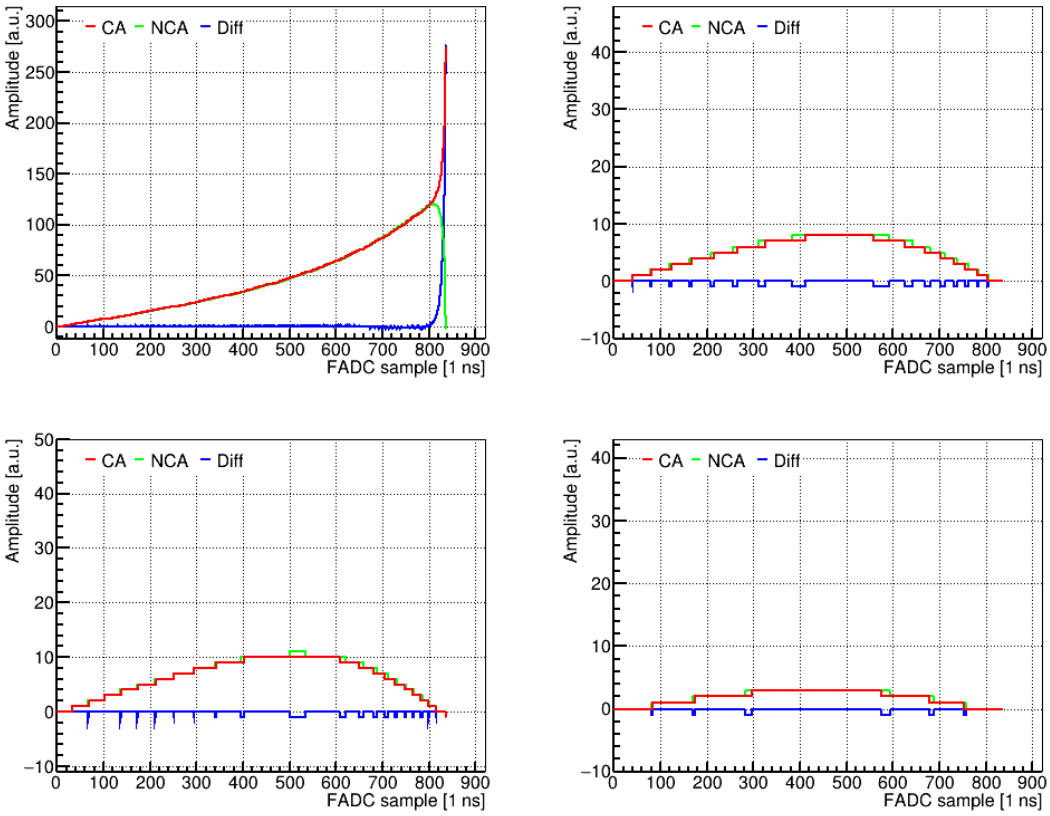

Figure 4.9.: Simulated signal and mirror pulses for one event from the calibration source ^{22}Na. The difference pulse is from the subtraction of a CA pulse and a NCA pulse. The first canvas shows signal pulses from the primary sector, and the rest plots display mirror pulses from the right neighbor sector, the bottom neighbor sector, and the diagonal sector.

The mirror pulses are simulated in a way similar to the signal pulses. The only difference is that the weighting potentials are extracted from the symmetric trajectory mirrored in neighboring sectors by the drift trajectory of the primary sector. Fig. 4.9 shows the simulated signal and mirror pulses from one event. The mirror pulses of the CA and the NCA are identical, and the resulting difference pulse will be approximately zero. The amplitude of mirror pulses is usually low and easily affected by noise.

Charges are also induced on the guard ring (GR). To simulate the GR pulse, the corresponding weighting potential is extracted along the drift trajectory when the GR is set to a unit potential, as illustrated in Fig. 4.10. One example of the GR pulse depicted in Fig. 4.11

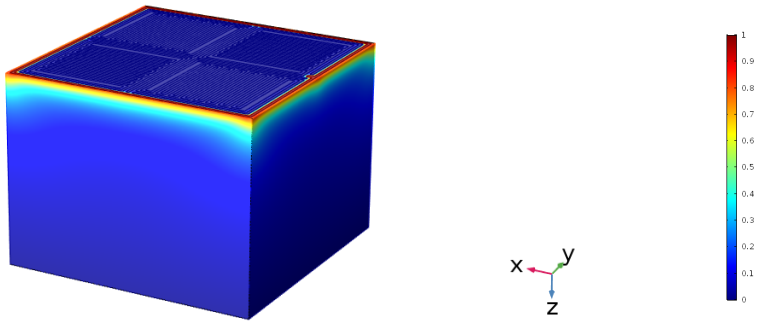

Figure 4.10.: The weighting potential distribution when the GR is set to a unit potential, and the other electrodes are set to zero.

is from the same event shown in Fig 4.9. For this event, the energy deposition on the GR is zero, indicating that the charge carriers are not collected by the GR. On the other hand, the electric field between the GR and the cathode can cause electrons to be driven towards the GR and collected by it. In this case, the energy deposition will be above zero.

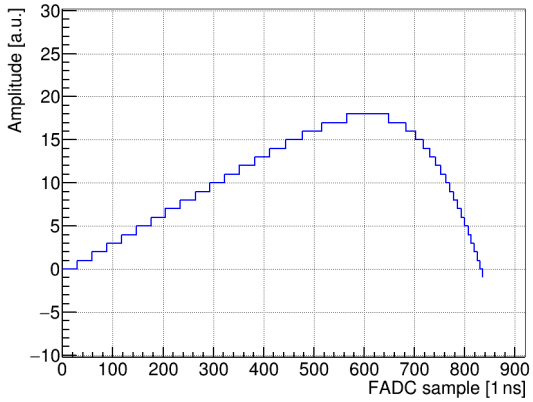

Figure 4.11.: The GR pulse from the same event shown in Fig. 4.9.

The total energy of an event is proportional to the charges induced on the qCPG and the GR, as expressed by

$$E \propto Q_{\mathrm{DIFF}} = \left(\sum_{i=1}^{i\leq 4} Q^{i}_{\mathrm{CA}} - \sum_{i=1}^{i\leq 4} Q^{i}_{\mathrm{NCA}} + Q_{\mathrm{GR}} \right), \tag{4.4}$$

where $i = 4$ denotes the four sectors of one detector. In the case of a single sector hit, i will be one. For multi-sector hits, i is larger than one. Pulses collected from each CA are added to the total CA signal pulse. Likewise, pulses recorded from NCAs are summed up as the total NCA signal. The GR signal is independent of the CPG principle.

Another event information, the interaction depth describing the normalized interaction

position in z direction, as explained in Section 3.2, is given

$$z = \frac{Q_{\mathrm{CATH}}}{Q_{\mathrm{DIFF}}} = \frac{\sum_{i=1}^{4} \left(Q^i_{\mathrm{CA}} + Q^i_{\mathrm{NCA}}\right) + Q_{\mathrm{GR}}}{Q_{\mathrm{DIFF}}}, \tag{4.5}$$

where Q_{CATH} is the sum of all pulses.

4.4.3. Simulation verification

We have now acquired simulated signal, mirror, and GR pulses. The simulation framework will be verified in terms of the energy deposition and the interaction depth.

Fig. 4.12 compares the energy spectra of ^{228}Th obtained from the simulation and the measurement for XDEM. The spectra are in good agreement, and γ peaks match well. This result demonstrates that the partitioning of energy loss within each step into individual charge clusters is simulated accurately.

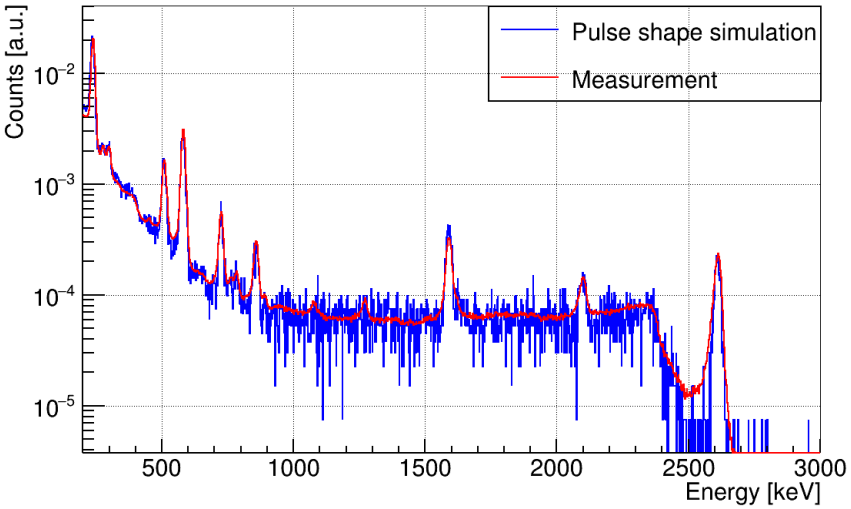

Figure 4.12.: Energy spectra reconstructed from simulated pulses and measured events with the calibration source ^{228}Th in XDEM. The simulated energy is smeared.

One way to test the depth distribution is the fourfold non-unique single β-decay of ^{113}Cd. Events are expected to be distributed uniformly in most part of the crystal, as the decay has a low Q-value of (322.2±1.2) keV. Fig. 4.13 shows the depth distribution of simulated ^{113}Cd β-decay events for the Demonstrator and XDEM detectors, which is constant as expected.

The simulation verification is also specifically investigated for the Demonstrator. The 2D map of the energy versus depth in Fig. 4.14 is reconstructed from simulated pulses of ^{22}Na for small detectors. The simulated energy is not smeared with the energy resolution. It is worth noting that the width of γ peaks increases near the anodes, as also observed in measurements. The XDEM detectors show a similar response illustrated in Fig. A.2. One can conclude that the near anode distortion is intrinsic to the CPG readout, which is caused by the differing weighting potential of the CA and NCA, as discussed in Section 3.2.

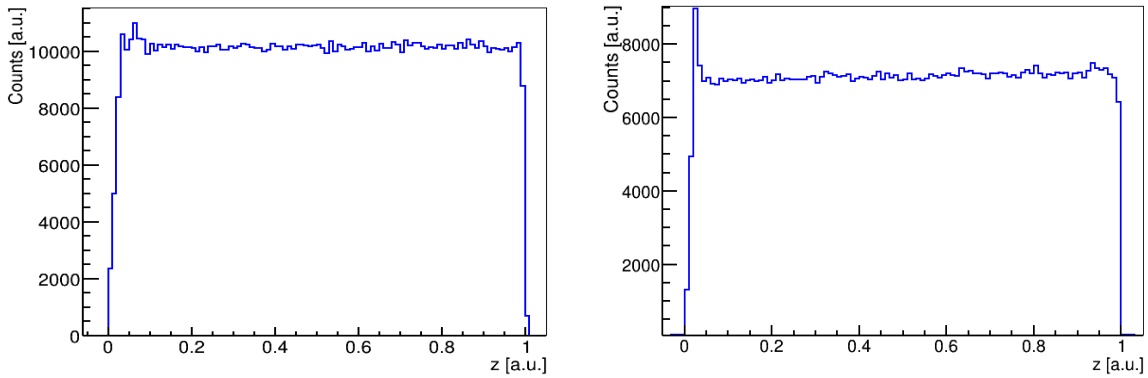

Figure 4.13.: Depth reconstructed from the simulated pulses of ^{113}Cd β-decay in the Demonstrator (left) and in the XDEM (right). The constant distribution is due to homogeneously distributed ^{113}Cd atoms in the detectors and most of the low energy β particles depositing energies inside. The anode is at $z = 0$, while the cathode is at $z = 1$.

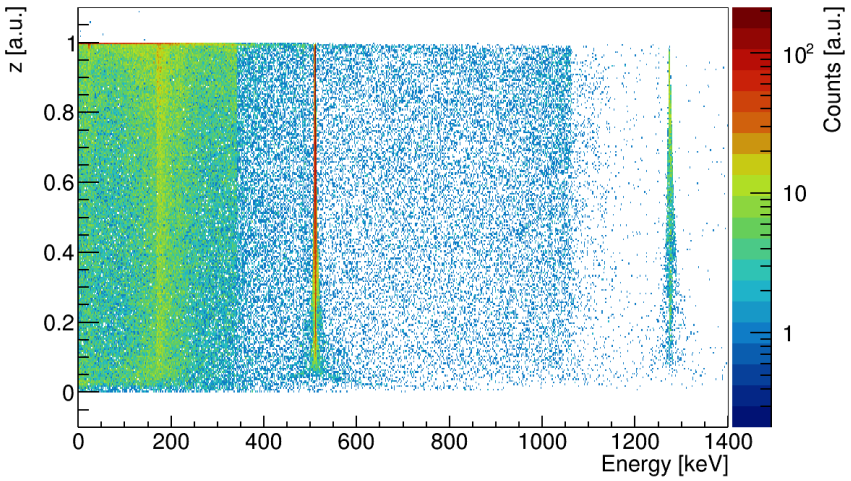

Figure 4.14.: Energy versus depth distribution reconstructed from the simulated pulses of ^{22}Na for the Demonstrator. The energy is not smeared. At around $z = 0$, the near anode distortion is visible.

4.4.4. Electronic response convolution

The previous section verifies the simulation framework. The last block of the pulse shape simulation outlined in Fig. 4.15 is to couple electronic responses to the "clean" pulses developed in previous sections. This step is to compare the simulation to the real data.

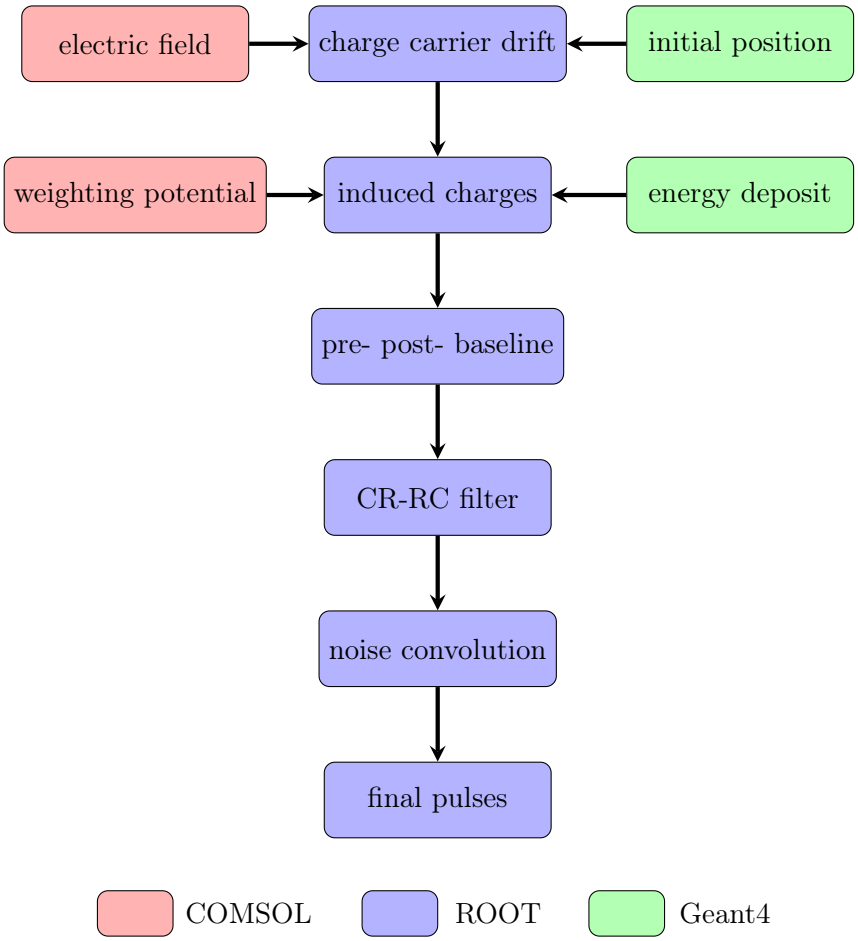

Figure 4.15.: The flowchart displays steps of the pulse shape simulations for CZT detectors. Color coding indicates modules processed with different software. Electric field and weighting potential are obtained from the COMSOL simulation. The initial position and the energy deposition are based on the Geant4 simulation. The rest parts are processed with ROOT.

Firstly, the simulated pulses are converted from a time step of 1 ns to 10 ns. The pre and post-baselines[1] are then added so that sample numbers in the simulation and the data are the same. This is done by setting a threshold value at a chosen time stamp. This threshold

[1]The baselines are the voltages that a FADC records when no signal is detected. The pre-baseline is the recorded voltage before the charge cloud moves towards the respective electrode. The post-baseline is the voltage after the charge cloud is collected by an electrode.

also accounts for the actual trigger, like in measurements. If a pulse's amplitude is above the threshold, the pulse will be recorded by a FADC.

The detector system consists of multiple capacitors and resistors. These components basically work as digital filters to limit the bandwidth and thus reduce noise input. They form RC integrators or CR differentiators, which are seen as the low pass and high pass filters in the frequency domain, respectively.

The high pass filter is responsible for the post-baseline attenuation. This happens when a capacitor in preamplifier chips is discharged through a resistor, which leads to a signal fall with a time of τ_{fall}. The response function of the high pass filter is formulated as

$$Q_i = \frac{\tau_{\text{fall}}}{-\Delta t}(\Delta Q_i - \Delta q_i), \tag{4.6}$$

where Q_i is the output of the filter, and ΔQ_i is the difference of Q_i and the previous output Q_{i-1}. Δq_i is the increment of the induced charges within the time step of Δt. The decay time is equal to the product of the resistance and the capacitance of the DAQ electronics with $\tau_{\text{fall}} = RC$. It is set to 140 µs in accordance with the datasheet of preamplifier chips [100].

The low pass filter will modify the rise structure of a pulse. The output is given as

$$Q_i = q_i - \tau_{\text{rise}}\frac{\Delta Q_i}{\Delta t}, \tag{4.7}$$

where Q_i is the output. q_i is the output from the previous high pass filter and is taken as the input here. A rise time τ_{rise} of 35 ns is found to match experimental pulses well and will be used to convolve with the simulated pulses [100].

Lastly, random noise is added. The noise is extracted from the baseline of the injected pulses mentioned in Section 3.1. Fig. 4.16 compares the resulting pulse shapes for one simulated event and one measured event selected by specific pulse properties. The main pulse features agree well for the two events. One thing to notice is that the rising slope of the measured pulse is smoother, probably due to the accumulative effects of the charge cloud. On the other hand, charge carriers are assumed to be point-like in the simulation. That is why the simulated pulse shows a sharp turn.

The difference pulse obtained from the subtraction of the two anode pulses is also shown. It has a time delay with respect to that of anode pulses. This delay is due to electrons traveling from their creation point to the vicinity of the grid.

In summary, pulse shape simulations have been established for the CZT detectors, and the result agrees well with the measurements. A slight discrepancy is likely the result of the charge cloud modeling. This simulation enables us to gain a detailed understanding of the detector's response. A direct application of this framework will be the investigation of the pulse shape analysis discussed in Chapter 6.

Simulations usually do not require any corrections regarding hardware responses and material properties. However, in reality, these factors have limited the performance of the CZT detectors. Therefore, corrections are made during the event reconstruction to improve the overall detector performance and obtain precise event information. The following sections will focus on compensating for the amplification imbalance and electron trapping based on the measured data.

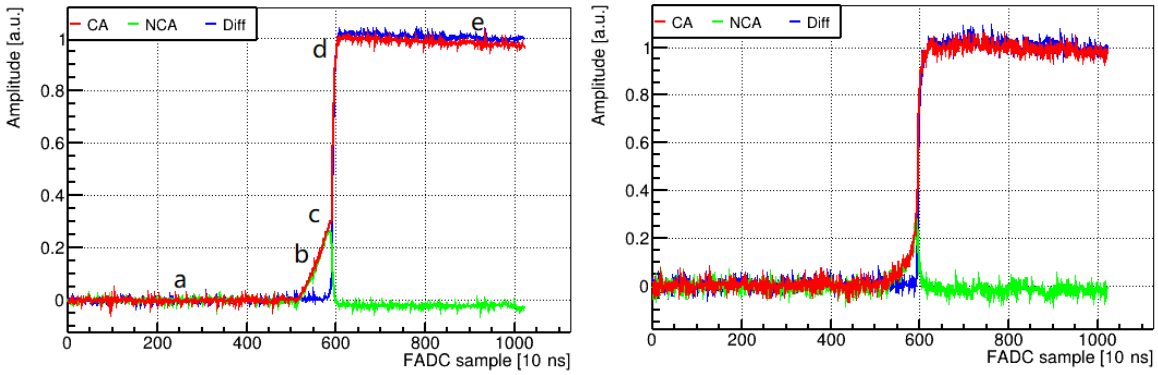

Figure 4.16.: Comparison of signal pulses from one simulated event (left) and one measured event (right) with similar energy deposition and interaction depth. The pulses are normalized by the height of the difference pulse. The main pulse features include (a) the pre-baseline before trigger, (b) the common rise of CA and NCA signals due to the bias voltage, (c) the diverging point of anode signals caused by the grid bias, (d) when charges collected by the CA, and (e) an exponential decrease of the final pulse height.

4.5. Gain correction

The amplification imbalance arises from the variations of amplifier chips and capacitors. It causes pulses from various channels to be amplified differently. As the cathode signal involves pulses from all four sectors, such an imbalance directly affects the reconstructed cathode signal and thus will contribute to the uncertainty of the depth reconstruction. Therefore, a gain correction factor g is introduced.

Ideally, the rising edges of the CA and NCA pulses should be equal for the same event. However, due to the amplification imbalance, the actual pulses rise differently. This difference can be corrected by g with

$$Q_{\mathrm{DIFF}} = Q_{\mathrm{CA}} - g \cdot Q_{\mathrm{NCA}}. \tag{4.8}$$

The g value will be one if the CA and the NCA have the same amplification. It can be estimated by the ratio of the rising slopes of CA and NCA pulses. However, the rising slope is sensitive to noise.

The solution is to calculate g by the amplitude variations of artificial pulses. As already mentioned, these pulses are injected into the electronic channels with a certain amplitude. Various amplitudes indicate different amplifications. g is thus expressed as

$$g = g_{\mathrm{ca}} \cdot g_{\mathrm{nca}}, \tag{4.9}$$

where g_{ca} is the factor to correct the imbalance among sectors, which makes $g_{\mathrm{ca}} = \frac{\overline{A_{\mathrm{CA}}}}{A^i_{\mathrm{CA}}}$. $\overline{A_{\mathrm{CA}}}$ is the pulse amplitude of the CA which will be used as the reference channel. A^i_{CA} is the CA pulse amplitude of the respective sector i. g_{nca} is to correct the imbalance between the reference CA channel and the NCA of the respective sector, which leads to $g_{\mathrm{nca}} = \frac{\overline{A_{\mathrm{CA}}}}{A^i_{\mathrm{NCA}}}$. A^i_{NCA}

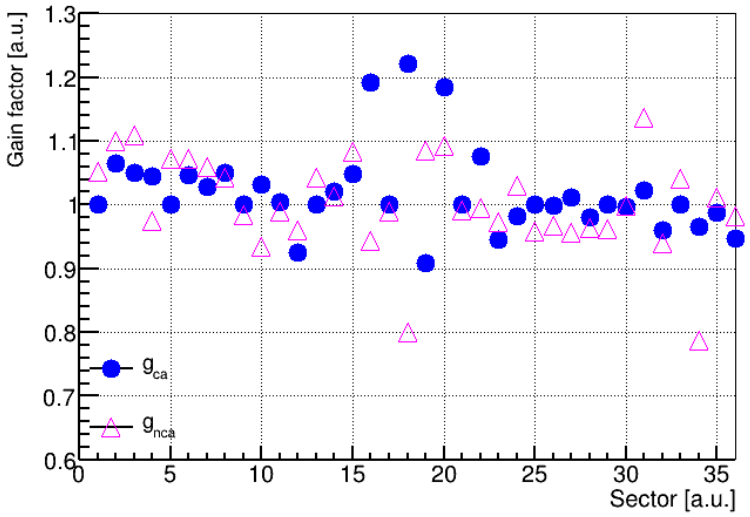

Figure 4.17.: The gain values extracted from the injected pulses. The g_{ca} corrects the amplifications among sectors, and the g_{nca} is to correct the imbalance between the CA and the NCA for the respective sector. Statistical uncertainties are too small to be seen.

is the NCA pulse amplitude of the individual sector. One thing to notice is that the injected pulse cannot reflect the detector's response and can only correct the electronic characteristics.

Fig. 4.17 shows the obtained gain corrections for all sectors using injected pulses. The g value is mainly in the range from 0.90 to 1.20, which agrees with that determined from the pulse rising slopes. Comparing g values with other operational periods as shown in Appendix A.3, the factors stay stable over time.

4.6. Energy reconstruction

Even though the CPG principle minimizes the effect of trapped holes, the electron trapping is not negligible in the CZT detectors. In this section two different methods, depth-sensing [55] and differential gain [59], are investigated to compensate for the electron trapping.

4.6.1. Zeroth-order energy reconstruction

Firstly, the so-called zeroth-order reconstruction is used, which does not apply any electron trapping correction. We now consider the energy deposition on the CPGs without including the guard ring (GR) signal. The deposited energy is proportional to the height of the difference pulse, which is obtained from a subtraction of the pre and post-baseline. A moving average filter (see Section 6.1.1) is employed to smooth pulse fluctuations so that the pulse height can be accurately determined.

According to the pulse shape simulation, as shown in Fig. 4.9, the difference between the CA and NCA mirror pulses is mostly zero. Since the measured mirror pulses are coupled

with noise, which will introduce additional uncertainties to the pulse height, they are not considered for the energy reconstruction.

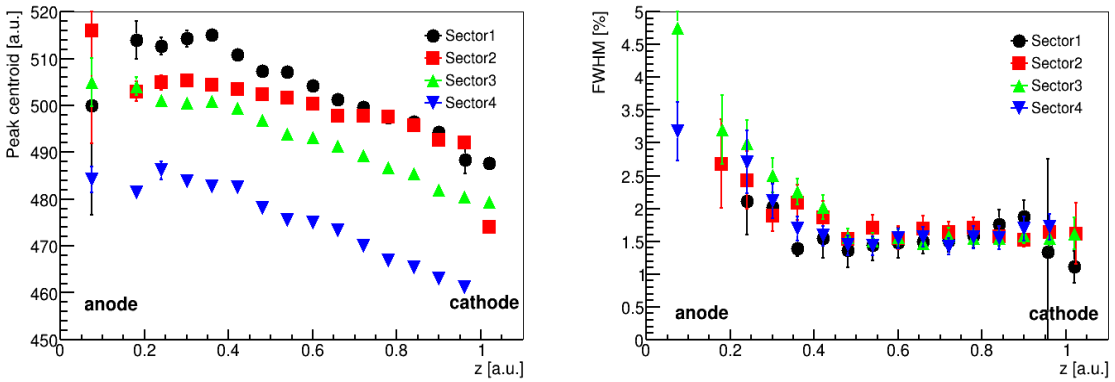

Figure 4.18.: The peak centroid (left) and the relative energy resolution (right) at the 1274.5 keV γ-line obtained from the zeroth-order reconstruction as a function of depth. The calibration was performed with a ^{22}Na source for detector three (manufacturer: eV Products) at the LNGS.

Ideally, CPG readout allows the deposited energy to be independent of the depth. In practice, electrons are trapped on the drifting path to the anode. Consequently, the pulse height is reduced depending on the traveling distance with which the total trapping centers increase.

Fig. 4.18 shows the peak centroid of the full energy peak and the corresponding energy resolution at the 1274.5 keV γ-line as a function of the interaction depth (see Section 4.7). The plot shows four sectors of detector three with the ^{22}Na calibration performed at the LNGS. The physical depth is normalized and sliced into 16 layers. Since the detector is irradiated from the cathode side with the calibration source, fewer events are detected near the anode than the cathode. Therefore, the first layer ranges from 0 to 0.15 to compensate for the low statistics near the anodes. The following layers have a depth interval of 0.06 from 0.15 to 1.05. As the current depth reconstruction is not sensitive to multi-sector hits, only single-sector events are considered.

For events near the anode, the trapping effect is less severe than for those away from the cathode. According to the left graph, the depth dependency of electron trapping in this detector varies by sector. The variation implies that the trapping effect depends on the charge transport properties of the respective sector. The right figure shows the detector has the worst performance near the anode and performs well away from it. The reason is that events originating from the anode are affected by the inhomogeneities of the weighting potential and the charge sharing effect.

The deviation of the peak centroid degrades the overall energy resolution. Therefore, the electron trapping effect has to be corrected accordingly for each sector.

4.6.2. Electron trapping correction

There are two possibilities to correct for the trapping of electrons. The goal is to improve the energy resolution. The depth-sensing method introduces correction factors to modify the pulse height depending on the interaction depth, as given by

$$E \propto c_k \cdot Q^k_{\mathrm{DIFF}}, \tag{4.10}$$

where Q^k_{DIFF} is the pulse height of an event from the depth layer k. c_k is the correction factor for the same layer. It is defined as the ratio of the peak centroid at each depth layer to a reference value. The reference value is the peak centroid taken from events near the anode, which are less affected by electron trapping. c_k is determined for each sector separately. The left Fig. 4.19 shows that the corrected peak centroid is nearly constant over the entire depth range except near the anode region.

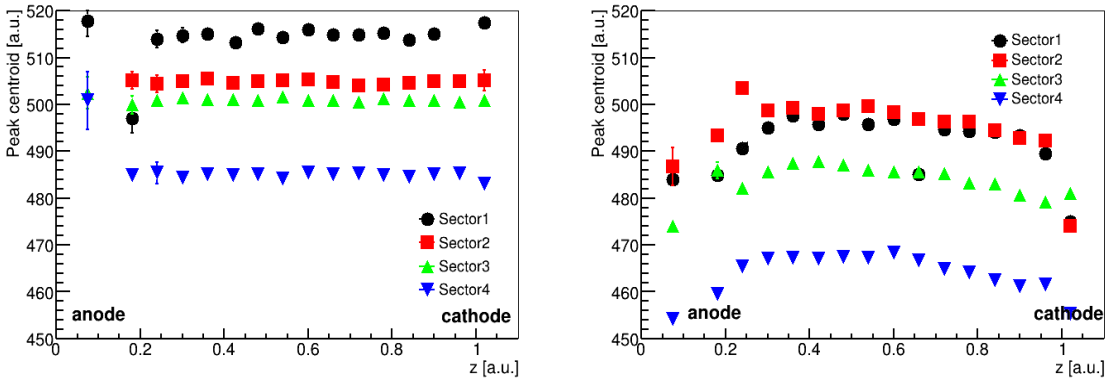

Figure 4.19.: The peak centroid shown in Fig. 4.18 is corrected with the depth-sensing method (left) and the differential gain method (right) at the 1274.5 keV γ-line.

Alternatively, the so-called differential gain correction compensates for electron trapping, assuming good material uniformity. Each sector has a weighting factor introduced. With ω_i applied to the NCA pulse of sector i, the corrected energy is formulated as

$$E \propto \sum_{i=1}^{i\leq 4} Q^i_{\mathrm{CA}} - \sum_{i=1}^{i\leq 4} \omega_i \cdot Q^i_{\mathrm{NCA}}. \tag{4.11}$$

Each ω is optimized with the ^{22}Na calibration to achieve the optimal performance and the detection efficiency at the 1274.5 keV γ peak. In principle, ω is less than unity so that signals hardly affected by trapping are reduced to be comparable with the trapped signals. The detector response is thus weighted to be homogeneous. As shown in the right Fig. 4.19, the centroids are effectively balanced with minimized deviations.

Using one global ω leads to a general deterioration of the achievable energy resolution. This is because there will be regions in the detector where the correction is far from the optimum.

Table 4.2.: The achievable energy resolution at the 1274.5 keV γ-line for the four sectors shown in Fig. 4.19. The energy reconstruction with the zeroth-order, depth-sensing, and differential gain methods are listed. Corresponding weighting factors used in the differential gain method are also shown.

sector	zeroth-order [%]	depth-sensing [%]	differential gain [%]	ω
1	4.37±0.16	1.82±0.06	2.43±0.07	0.87
2	2.89±0.08	1.85±0.05	2.27±0.06	0.95
3	4.39±0.12	1.82±0.04	2.20±0.05	0.86
4	5.08±0.18	1.82±0.05	2.50±0.07	0.84

Note that pulses with high-level noise usually cause uncertainties on ω. The affected sector will be cross-checked.

Table. 4.2 shows the energy resolution at the 1274.5 keV γ-line for all four sectors of detector three based on different reconstructions. The weighting factor of each sector agrees well with the respective trapping characteristics shown on the left plot of Fig. 4.18. It is close to one if the trapping curve above a depth of 0.2 is relatively flat. While this detector is from the manufacturer eV, detectors from Redlen are also studied, and one example is shown in Appendix A.4.

Both trapping correction methods significantly improve the spectral response. The differential gain approach turns out to be beneficial for the depth reconstruction (see Section 4.7). Hence, it is established as the primary method for the qCPG detectors.

4.6.3. Calibration procedures

The detector measures the charge signal as a voltage amplitude. However, the energy scale is more commonly used. Calibrations are performed to convert the voltage into the energy. For this purpose, measurements with calibration sources ^{22}Na, ^{228}Th, and ^{152}Eu are carried out.

The calibration overview is displayed in Fig. 4.20. In the first step, raw pulses are processed by the Multiple-Analysis Toolkit for the COBRA Experiment (MAnTiCORE). Pulse properties, including pulse height, rising slope, maximum range, and so on, are determined [106]. Subsequently, the pulse height is corrected by the gain factor g that accounts for the amplification imbalance between the CA and the NCA. The following weighting factor ω compensates for the electron trapping effect. After a second processing with these correction factors, the corrected pulse height is histogramed and modeled with the two-sided Gaussian function shown in Eq. 3.7.

The energy calibration is then performed by a linear fit between the determined peak positions (pulse heights) with uncertainties included and the γ lines known from calibration sources, as shown in Fig. 4.21. Calibration parameters are extracted from the fit. Finally, the data are processed for a third time with the calibration parameters to obtain the final energy spectra. Events detected by different sectors can be combined for enough statistics.

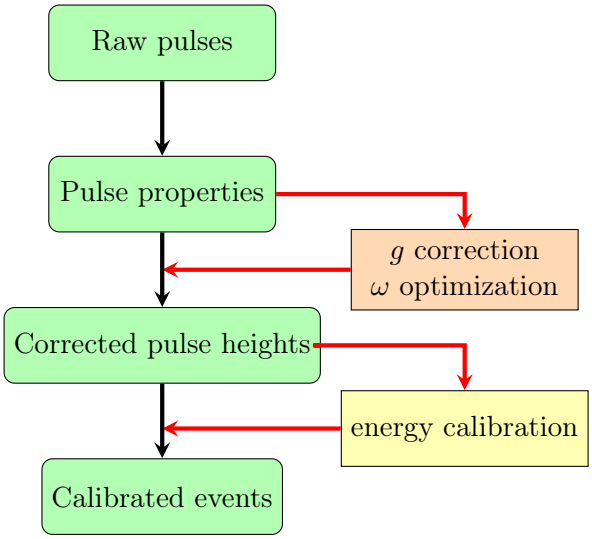

Figure 4.20.: Block diagram displaying energy calibration procedures. The black arrows denote steps processed with MAnTiCORE. The red arrows show the required input parameters. Individual steps are briefly explained in the text.

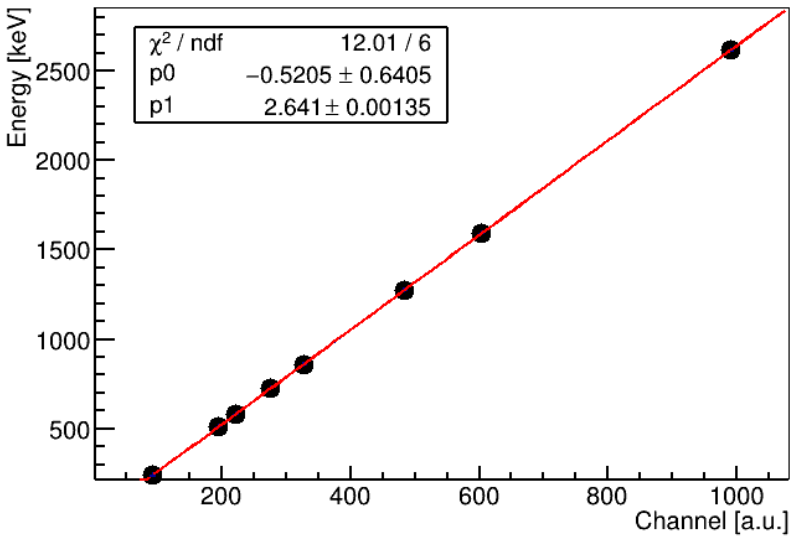

Figure 4.21.: A linear fit to convert the pulse height into the energy scale for one sector. The known γ lines of the ^{22}Na, ^{228}Th sources are used. p_0 is the offset, and p_1 represents the slope. Error bars are too small to be visible.

4.6.4. Energy deposition on the CPGs and the guard ring

Although typical double beta decays are expected to lose all the energy carried by the two electrons inside a single sector, the total energy deposition inside a crystal, including the four sectors, is still of particular interest to characterize backgrounds.

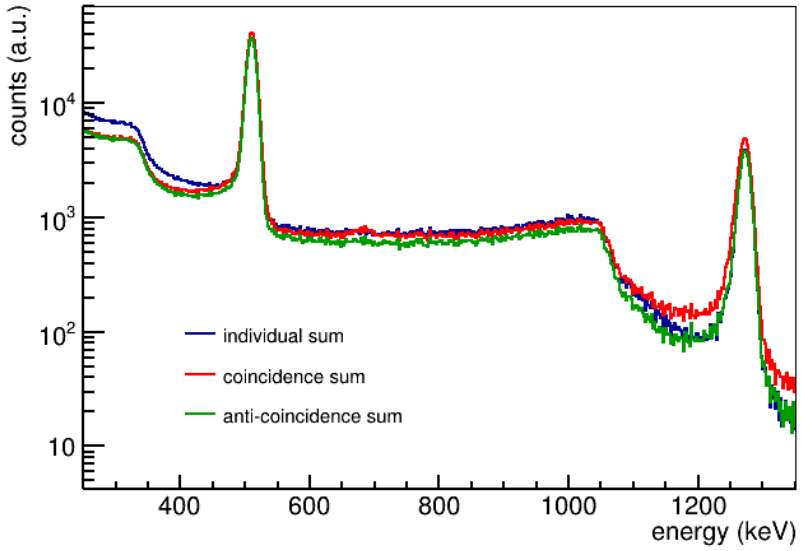

Figure 4.22.: Energy spectra of ^{22}Na in different summation modes for one qCPG detector at the LNGS [44]. Compared to the individual summation, the coincidence sum increases the peak entries, while the anti-coincidence sum improves the peak to background ratio.

The deposited energy in the bulk detector is obtained by combining the results of single sectors in different ways, as shown in Fig. 4.22. The "individual sum" is filled with all sectors' events without summation. The "coincidence sum" adds up the energy of coincident events within different sectors. These coincident events are mostly produced by γ-rays. This summation improves the full energy peak entries. Alternatively, the "anti-coincidence sum" rejects events that occur in coincidence. This mode reduces the full energy peak detection efficiency but improves the peak to background ratio, which is beneficial for double beta decay searches. For this summation, an energy resolution ranging from 1.40% to 2.70% at 1274.5 keV with an average of 1.83% has been achieved, considering all functional detectors. Also, the performance of a complete qCPG detector is comparable with that of single sectors.

The energy measured by the guard ring (GR) can be reconstructed independently from the CPGs. However, this is not possible for the data because the GR is not triggered simultaneously with the CPG channels as a consequence of the DAQ electronics' limitation. Besides, the GR signal is not implemented into MAnTiCORE and cannot be processed by the software yet. As for the physics data-taking, GR signals arise dominantly from backgrounds [69]. Therefore, it is reasonable not to add the GR signal into the total event reconstruction. Nevertheless, simulated pulses provide detailed information about the GR.

Fig. 4.23 shows the energy spectrum for ^{22}Na reconstructed from simulated GR pulses.

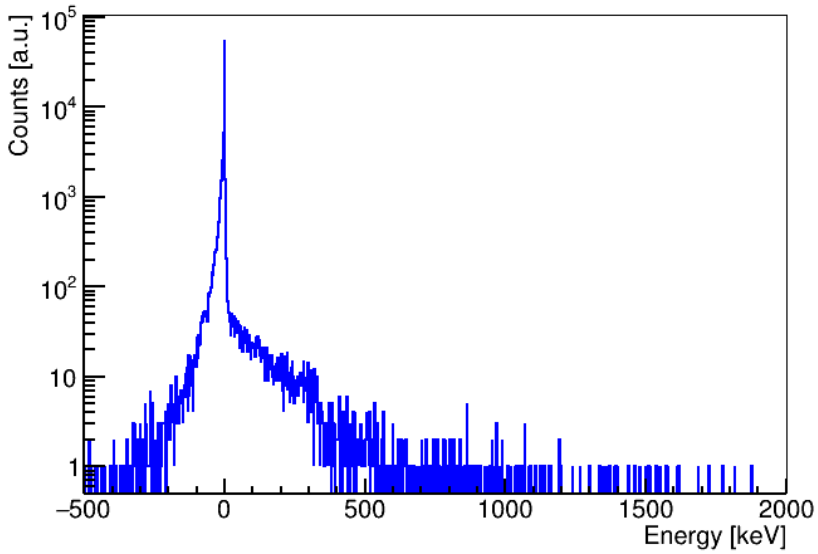

Figure 4.23.: Energy spectrum reconstructed from simulated GR pulses with a ^{22}Na source.

As can be seen, most GR signals are around zero or negative because the charge cloud is collected by CPGs. When the GR signal is above zero, the energy deposition on the GR is depth dependent, according to the weighting potential distribution in Fig. 4.10.

It is also possible to estimate the signal acceptance of the grounded GR from simulation. Previously, this was deduced from γ-ray measurements. However, the measurement leads to an efficiency with a significant uncertainty because the GR efficiency varies with the source and its position. For the $2\nu\beta\beta$ events of ^{116}Cd, the survived signal efficiency in the energy region above 1 MeV is (97.05±0.06)%. That is larger than the value of 89% estimated from the 661.7 keV γ-ray peak measured [43].

4.6.5. Energy threshold

An energy threshold defines the value that the pulse amplitude needs to exceed to trigger the DAQ system. In other words, a pulse can only be recorded if it is discernible above the random voltage fluctuations present in the system. A low threshold will be preferred, especially for low energy measurements, but should not overwhelm the disk space.

It has been proven that the CA-only triggering is robust against noise [39]. Every CA pulse exceeding a threshold will trigger the FADC readout. While the CA pulse height is constant at the trigger point, the absolute NCA pulse height decreases as a function of the interaction depth with the anode at $z = 0$ and the cathode at $z = 1$. As a result, the reconstructed energy threshold depends on the depth, showing a slope from 200 keV to 300 keV, as shown in Fig. 4.24.

This depth dependency causes a non-constant threshold. A threshold correction cut, E_{th},

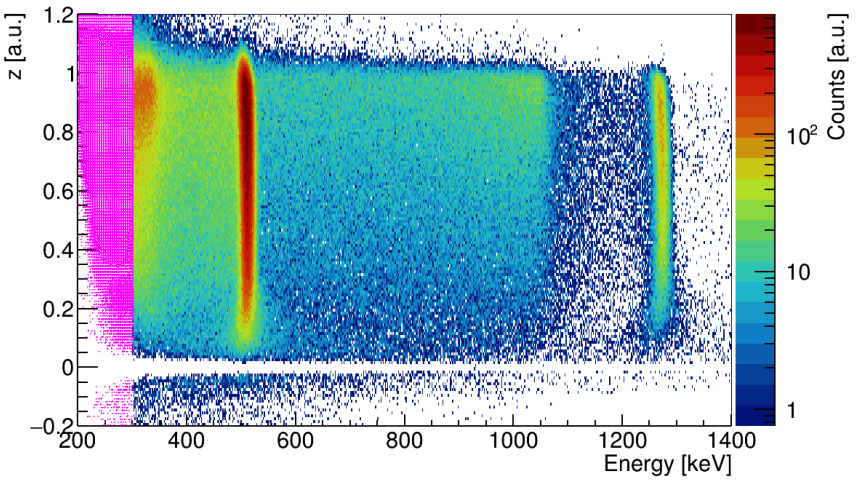

Figure 4.24.: Illustration of energy versus interaction depth for a qCPG detector with ^{22}Na calibrations. The energy threshold increases near the anode ($z = 0$) because of the CA-only triggering mode. The magenta shaded area at low energies indicates events that can be removed by the threshold correction cut E_{th}.

is thus developed to discard affected events. The E_{th} is defined as

$$E_{\mathrm{th}} = p_0 + p_1 \cdot (1 + \omega) \cdot \mathrm{CA}_{\mathrm{th}}, \tag{4.12}$$

where $\mathrm{CA}_{\mathrm{th}}$ is the threshold set on CA pulses. p_0 and p_1 are the offset and slope of the calibration function. ω is the weighting factor. Fig. 4.24 shows that the depth dependency of the low energy threshold is eliminated by removing events below the E_{th}. The resulting threshold ranges from 46.6 keV to 344.4 keV, depending on the noise level of each sector. The maximal E_{th} among the four sectors will be used for the complete detector.

Since the threshold varies by each run and detector, low energy channels will have different exposures. In order to unify the data exposure in the low energy region while maximizing the event number, an optimal threshold cut, E_{opt}, is developed to discard data runs with thresholds above the optimal value. The E_{opt} cut is adapted from Ref. [68]. It is based on the fourfold forbidden non-unique single β-decay of ^{113}Cd, which is the strongest signal at low energies. The decay goes directly into the ground state of the daughter nucleus $^{113}\mathrm{In}(\frac{9}{2}^+)$ with a Q-value of (322.2±1.2) keV. For further details about this decay, see Chapter 5.

Firstly, runs with a threshold energy over 200 keV are rejected to reduce statistical fluctuations. The total number of events is a function of the lifetime that is determined for each energy bin. The optimal threshold E_{opt} lies at the bin with maximum events. Considering the energy resolution, an additional offset of 15 keV is added.

Fig. 4.25 demonstrates the ^{113}Cd β-decay spectrum for one sector with its lifetime varying for different energies. An optimal threshold at 100.5 keV is found for this sector. Considering all functional sectors, an average optimal threshold of 107.5 keV is obtained, with a minimal threshold of 90.5 keV and a maximal of 130.5 keV.

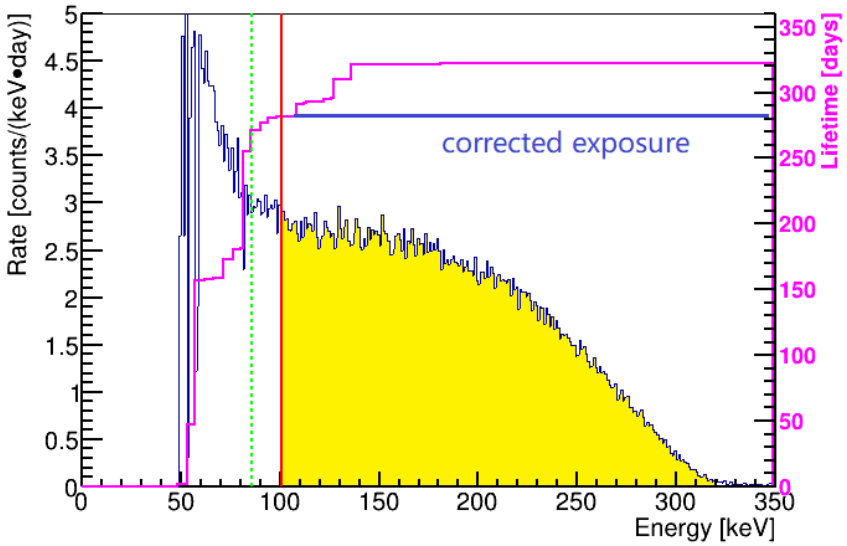

Figure 4.25.: The count rate of the ^{113}Cd β-decay for one sector and the corresponding lifetime per energy bin. The lifetime indicates operational duration and depends on the threshold at low energies. An optimal threshold E_{opt} in the red line at the 100.5 keV is determined for this sector. The green dashed line represents the threshold without considering the energy resolution. In order to have a constant lifetime, runs with energy thresholds higher than E_{opt} will be discarded. The corrected lifetime is shown in the blue line. Events within the yellow shaded area will be analyzed in Section 5.6.

4.7. Depth reconstruction

As mentioned in Section 3.2, the depth reconstruction is based on the fact that the cathode signal is linear with the depth and proportional to the deposited energy. The normalized depth, z, is mainly used to develop a fiducial cut that will be discussed in Section 6.4. A precise z-cut relies on the reconstruction accuracy.

COBRA has investigated the z reconstruction for 1 cm^3 CPG detectors [63] and a single sector of one qCPG prototype detector with a floating GR [107]. The adaption made for the XDEM detectors is verified in Section 4.4.3 with a simulation. This section will focus on the data, including electron trapping correction.

4.7.1. Zeroth-order depth reconstruction

In the case of a floating GR, the Q_{GR} term is omitted in Eq. 4.5. Assuming there is no electron trapping, z is obtained from

$$z = \frac{Q_{\text{CATH}}}{Q_{\text{DIFF}}} = \frac{\sum(Q^i_{\text{CA}} + Q^i_{\text{NCA}})}{Q_{\text{CA}} - Q_{\text{NCA}}}. \tag{4.13}$$

The cathode signal Q_{CATH} is reconstructed by adding up all anode signals. In the data, the summation usually adds the noise into Q_{CATH}, which is especially true for mirror pulses with very low amplitudes. To minimize the added noise, the cathode signal is smoothed by the moving average filter described in Section 6.1.1. Q_{DIFF} is the difference signal above a predefined threshold value. This measure ensures that only physical pulses with amplitudes above the noise level are considered.

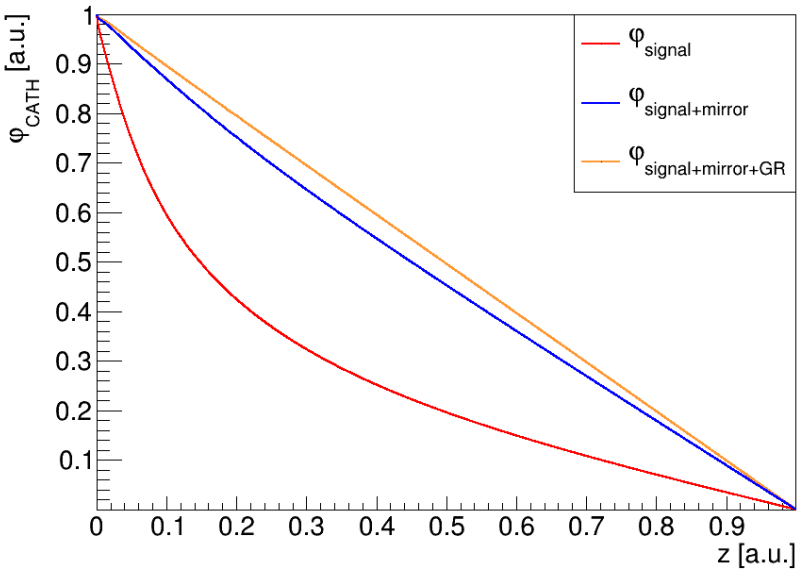

Figure 4.26.: The weighting potential of the cathode, φ_{CATH}, equivalent to different φ combinations of signal pulses, mirror pulses, and GR pulses along the depth. The anode is denoted at $z = 0$, while the cathode is at $z = 1$. The path is randomly chosen.

In terms of the grounded GR, in principle, the GR signal needs to be included in the cathode signal, as $Q_{\mathrm{CATH}} = \sum(Q^i_{\mathrm{CA}} + Q^i_{\mathrm{NCA}}) + Q_{\mathrm{GR}}$. However, it cannot be analyzed currently, as mentioned earlier. A consequence is seen in Fig. 4.26. The plot shows different combinations of the cathode weighting potential, φ_{CATH}, versus the depth. The relationship is linear when all pulses are added up. However, it is no longer linear if one only adds up signal pulses from the primary sector. Combining mirror pulses from neighboring sectors, φ_{CATH} also deviates from linearity. As shown in Fig. 4.27, the nonlinearity depends on the distance between the GR and the drift path of the charge cloud. If the trajectory is close to the GR, the GR-caused deviation is severe. Unfortunately, it is not possible to describe this deviation simply with a polynomial function.

A more direct comparison is shown with simulated data. Fig. 4.28 displays the depth distribution of simulated ^{22}Na events. The simulation is performed for the whole detector layer with the GR either floating or grounded. Simulated pulses are convolved with electronic responses and processed by MAnTiCORE as for the measured data. One can see that more events are positioned near the cathode ($z = 1$) than in other regions, as the calibration source is close to the cathode.

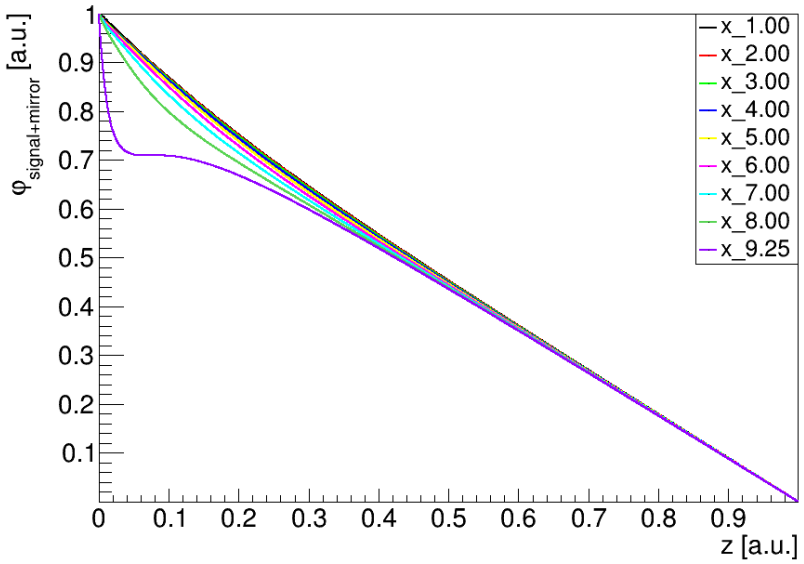

Figure 4.27.: $\varphi_{\text{signal+mirror}}$ distribution versus the normalized depth. The paths are at different distances from the GR. The closer to the GR with the x coordinate being larger, the $\varphi_{\text{signal+mirror}}$ deviates more from the linearity near the anodes ($z = 0$).

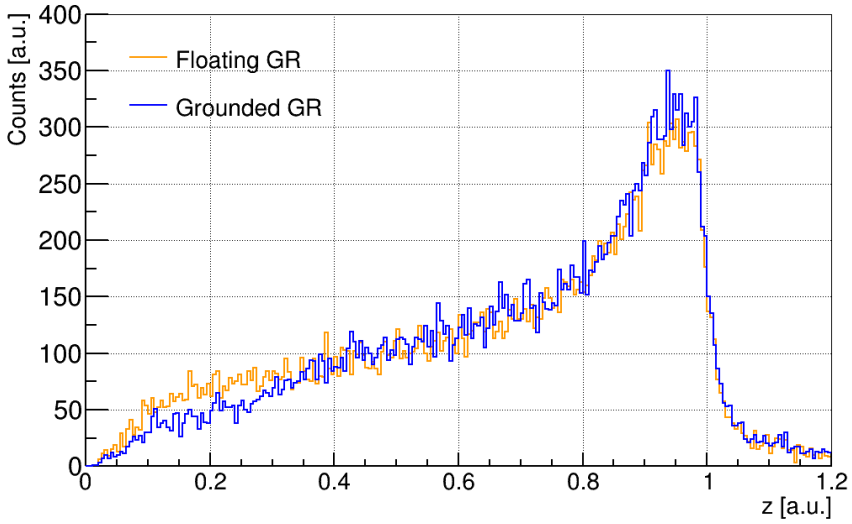

Figure 4.28.: Depth comparison with different GR configurations simulated, with the anode at $z = 0$ and the cathode at $z = 1$. The simulation was performed for the whole detector array with a ^{22}Na source. Simulated pulses are processed by MAnTiCORE. In the case of the grounded GR, the GR signal is not included in the cathode signal. As a result, part of the events is positioned at a depth value higher than the actual one, using Eq. 4.13. The spectra have the same number of entries.

Compared to the case of the floating GR, some low depth events are shifted to higher depth when the grounded GR signal is excluded from the reconstruction. This is because charges induced on the cathode are shared between the CPGs and the GR, and neglecting the GR signal will decrease φ_{CATH} around the periphery and lead the cathode signal to be larger than that in the center. This effect is more severe near the anodes and remains a systematic uncertainty. A direct readout of the cathode signal is expected to reduce this depth shift and will be investigated in the future.

It is worth noting that the depth distribution of the near cathode events does not peak at $z = 1$ but is slightly lower. A comparison among simulations and measured data is illustrated in Fig. A.3. It shows that the depth reconstructed from "clean" pulses actually shows a peak at $z = 1$. But for the simulated pulses which are convolved with electronics' response and processed by MAnTiCORE, z shifts to low values, as observed in the real data. It is suspected that this depth shift is caused by digital filters implemented in MAnTiCORE and will be included in the systematic uncertainty.

The depth reconstruction is tested with background events produced near the cathode. Only single-sector depositions with energies above 2 MeV are considered because they are mainly alpha particles from the decay products of ^{190}Pt contaminations in the electrode and from the naturally occurring ^{222}Rn decays. These α particles are likely to deposit energies on the detector surface due to their limited penetration power. Fig. 4.29 shows the depth spectrum with the centroid at around $z = 1$ for these events.

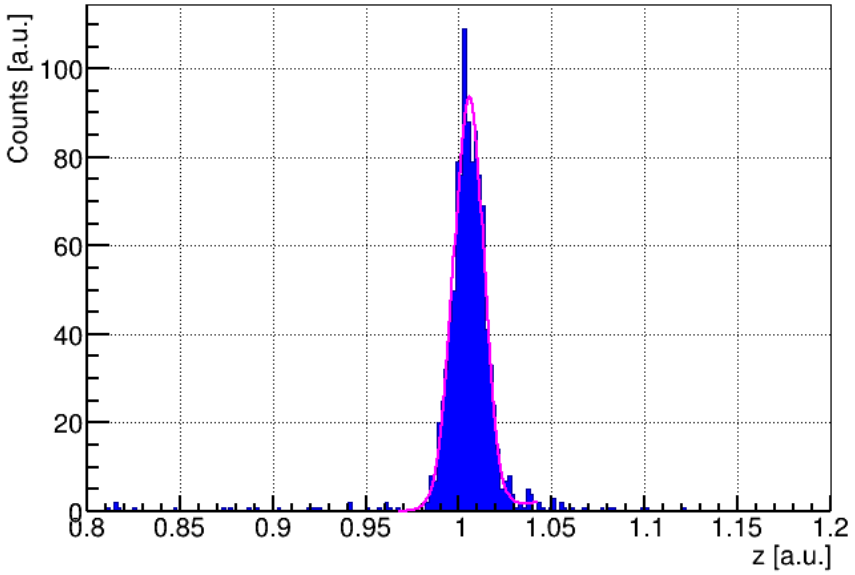

Figure 4.29.: Depth distribution of near cathode events collected from the XDEM array at the LNGS. Single sector events above 2 MeV are selected. The zeroth-order depth distribution is fitted with the two-sided Gaussian function described in Eq. 3.7.

The method mentioned above works only for events interacting in single sectors. However, for multi-sector events, the cathode-to-difference signal ratio cannot derive the individual

depths for each interaction site. Instead, the electron drift time measuring the time of the charge cloud moving from its origin to the anodes (see Section 6.7) can determine depth. However, this approach is currently limited by the time resolution.

4.7.2. Electron trapping correction

Electron trapping in CZT detectors also needs to be corrected in the depth reconstruction. When electrons are trapped in the crystal, due to the symmetrical weighting potential distribution in the 1 cm^3 single CPG detectors, the decrease of the CA signal nearly equals the increase of the NCA signal. For the summed cathode signal, the contributions of the electron trapping cancel each other. On the other hand, the difference signal is the subtraction of the anode signals, and Q_{DIFF} is thus reduced. Consequently, the depth is usually overestimated by the zeroth-order reconstruction in Eq. 4.13. However, the trapping corrected model successfully mitigates the overestimation [63].

For the XDEM detectors, it is only reasonable to correct the trapping effect by including the GR signal to the depth reconstruction when the GR is grounded. Otherwise, the correction will be inaccurate as the φ_{CATH} is not linear. Hence, the trapping correction is only investigated for the qCPG prototype detector with a floating GR.

According to the concept developed for single CPG detectors (Section 3.2.1), anode signals are deduced considering the trapping effect. The weighting potential of the CA and the NCA is assumed to be linear throughout the detector except near the anode. But this assumption fails for the single grids of the qCPG detector, as shown in Fig. 4.3. Therefore, the anode signals can not be derived for each sector separately. However, this nonlinearity is mitigated by adding all the signal and mirror pulses separately for the CA and the NCA. So, the summed CA constitutes all the CA recorded pulses, while the NCA consists of the NCA signal and mirror pulses.

Based on the previous assumptions, the charge transport is uniform within the entire detector volume [63, 108]. With a mean trapping length of around 10 cm, an exponential reduction of the electrons with the drift distance can be assumed [108]. Accordingly, the corrected z_{tc} for the qCPG detector is derived as

$$z_{\mathrm{tc}} = \lambda \cdot \ln\left(1 + \frac{1}{\lambda}\frac{Q_{\mathrm{CATH}}}{Q_{\mathrm{DIFF}}}\right), \tag{4.14}$$

which is the same as for the single CPG detectors. Q_{CATH} and Q_{CATH} are the same terms as Eq. 4.13. λ is the mean trapping length related to the weighting factor [43].

The weighting factor is extracted from the primary sector where an event deposits its energy. Variations arising from the weighting factors range from 0.70 to 1.15, which leads to a significant difference of λ even for the same detector. Such a difference explains why using a global λ can distort the event position.

Fig. 4.30 shows the depth reconstructed from the zeroth-order and the trapping corrected model using scanning data measured elsewhere [39]. The detector was irradiated with a ^{137}Cs along the z-dimensional. Each position is obtained from fitting the depth distribution of 661.7 keV γ-rays with a Gaussian plus polynomial functions. As a cross-check, the depth

distribution is also fitted with a Gaussian plus the Error function and a linear function. The mean values from the two fittings agree well.

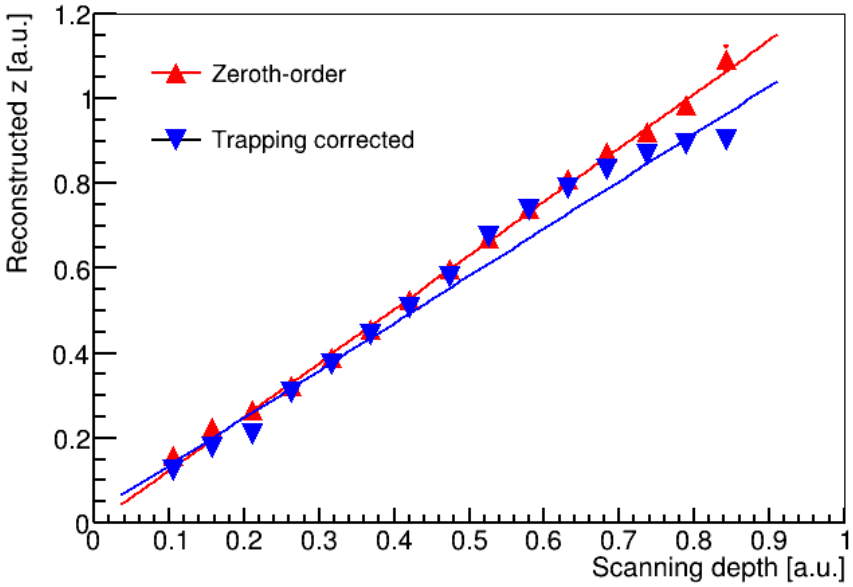

Figure 4.30.: Depth reconstructed by the zeroth-order formula (Eq. 4.13) and the trapping corrected model (Eq. 4.14) as a function of the scanned position are shown in red and blue triangles, respectively. Straight lines show the corresponding linear fits. Nonlinearity is observed for the trapping corrected depths. The data are taken by irradiating the detector with a floating GR in the z direction using a ^{137}Cs source.

As expected, the interaction depth with the trapping correction is shifted to low values for near cathode events, while it overlaps with the zeroth-order reconstructed position near the anode. However, a deviation from linearity is observed, especially for the trapping corrected depth. The deviation is expected to be associated with the charge transport properties and crystal quality. Trapping zones are probably not homogeneously distributed in the crystal, which contradicts the original assumption of uniform charge transport throughout the crystal. Due to the material quality variations, the idea of a constant mean trapping length over the entire bulk is too simplistic. Unfortunately, the model could not handle four mean trapping lengths at the same time. Furthermore, the holes' contribution is another challenge, as elaborated in Ref. [63].

At present, the trapping corrected depth reconstruction is not applied to the data. Nevertheless, this section provides the basis for further investigations that could model the trapping characteristics better.

4.8. x-y position

Additional information that can be obtained from the qCPG detector is the x and y positions, which will further help to improve the detector's performance by localizing its response. For instance, electron trapping can vary due to nonuniform material quality. By combining the z position discussed above, it is possible to correct the electron trapping in 3D by introducing multiple weighting factors.

As discussed in Section 4.4.4, mirror pulses are induced in neighboring sectors when electrons move towards the anode in the primary sector, where the event deposits its energy. If the trajectory of the charge cloud is near the border of neighboring sectors, its symmetrical paths in the neighboring sectors will also be close to the border.

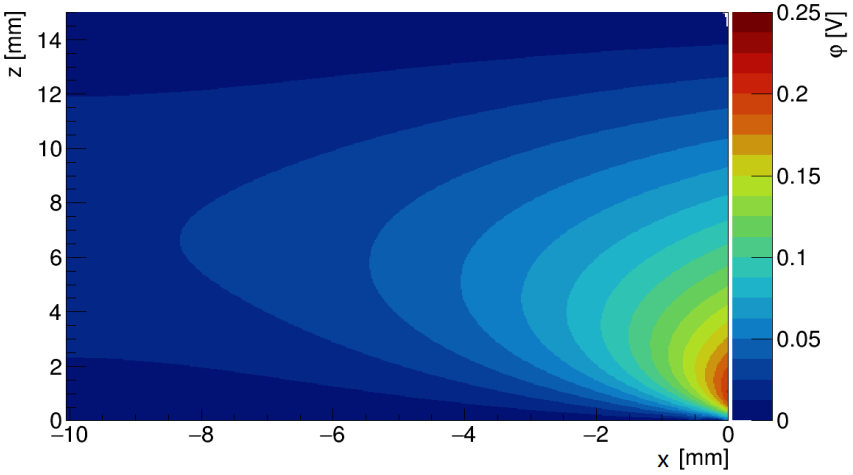

Figure 4.31.: The weighting potential φ in the x-neighbor sector projected on the 2D (xz) plane. The CA of the primary sector shown in Fig. 4.3 is set to a unit potential. The border to neighboring sectors is at $x = 0$, while $x =$ -10 mm is close to the outer guard ring.

Fig. 4.31 shows the weighting potential in the x-neighboring sector. Along the z path, the maximum weighting potential, $\varphi^{\max}$, changes with the interaction y position in the primary sector. The closer a trajectory is to the sector border, the larger $\varphi^{\max}$ is. This behavior also applies to the y-neighbor sector. As $\varphi^{\max}$ is usually located near the anode, the mirror pulses should include it for most events.

Firstly, we simulate the $\varphi^{\max}$ in neighboring sectors evolving with the interaction x and y positions in the primary sector. The 2D planes seen in Fig. 4.4 are considered for simplicity. For the maximal φ in the y-neighbor sector, $\varphi_y^{\max}$ is obtained by taking the amplitude of the mirrored CA pulse and normalizing it by the Q_{DIFF} of the primary sector, expressed as

$$\varphi^{\max} = \frac{Q_{\mathrm{CA}}^{\mathrm{neighbor}}(\max - \mathrm{postbaseline})}{Q_{\mathrm{DIFF}}^{\mathrm{primary}}}. \tag{4.15}$$

The amplitude of the mirror pulse is equal to its maximum minus the post-baseline. For each

$\varphi_y^{\max}$, there is a corresponding y. This calculation is repeated for the x-neighbor sector to get the x position.

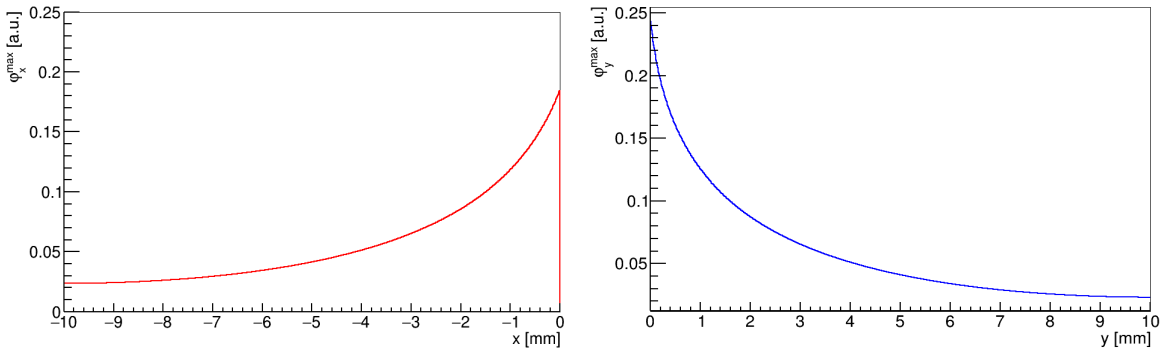

Figure 4.32.: Left: $\varphi_x^{\max}$ obtained from the x-neighbor sector versus x of the primary sector. Right: $\varphi_y^{\max}$ obtained from the y-neighbor sector versus y of the primary sector. The simulation is based on the setting illustrated in Fig. 4.3 projected on 2D planes.

Fig. 4.32 shows the $\varphi_x^{\max}$ obtained from the x-neighbor sector scaling with the x position of the primary sector. Likewise, $\varphi_y^{\max}$ from the y-neighbor sector depends on y. Based on this map, the combination of the two values corresponds to a unique x-y position. The mirror pulses' amplitudes are thus converted into the actual x and y coordinates.

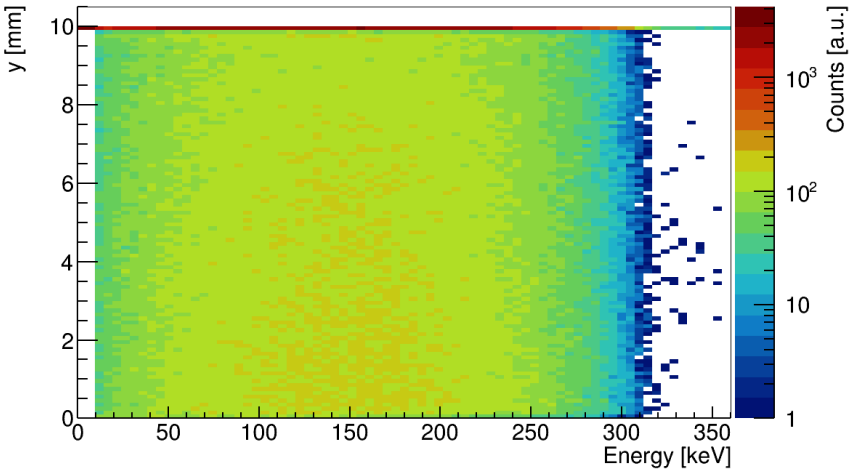

Figure 4.33.: Reconstructed y position versus energy deposition of the simulated ^{113}Cd β-decay events. $y = 0$ is the border with a neighboring sector, and $y = 10\,\text{mm}$ is the outer edge near the GR. As expected, events are uniformly distributed along the y-axis.

The simulated ^{113}Cd β-decay events are used to test the calculation mentioned above. As expected, Fig. 4.33 shows that events are evenly distributed along the reconstructed y of the primary sector. Due to the grounded GR near the edge, not many qCPG reconstructed events

are in that region.

A reconstruction artifact peaking in the periphery at $y = 10\,\mathrm{mm}$ is also observed. According to the relationship between $\varphi_y^{\max}$ and y shown in Fig. 4.32, the $\varphi_y^{\max}$ reduces to a value of around 0.024. However, $\varphi_y^{\max}$ values below the minimum are found for simulated events that end up on the outer edge and lead to this artifact. The artifact has very limited effects as it is independent of the energy deposition.

If one tries to apply this algorithm to real data, one obstacle is the difficulty in estimating the maximum value of the mirror pulse because of noise interferences. Many $\varphi^{\max}$ values are out of the range, leading to low statistics. It is also found that the initial rise structure is invisible for some mirror pulses. This invisibility is not related to the time response according to a simulation. Furthermore, the measurement has a smeared resolution and cannot accurately distinguish the small $\varphi^{\max}$ difference near the edge shown in Fig. 4.33. Nevertheless, Fig. A.8 shows the reconstructed y position in single sectors from data and simulation with ^{22}Na.

In principle, a xy scanning measurement is also helpful to verify the algorithm, but the results are not satisfying due to the current noise level. Further investigation with low-noise data is necessary. The other spatial parameter that can be obtained from pulse shapes is the x-y radial position, as discussed in Appendix A.5. It provides complementary information about the detector properties, particularly the charge induction uniformity [109].

This chapter describes the development of a pulse-shape simulation framework that is helpful to understand the detector response. Moreover, the event reconstruction is evaluated for the data. Although the non-uniform weighting potential distribution has posed challenges for the event reconstruction, the new detector allows for the reconstruction of the x and the y positions, apart from the z dimension.

5. XDEM setup performance

For detecting extremely rare events, the setup has to be stable over a long period underground. The detectors also need to have a good energy response. This chapter focuses on investigating the setup performance regarding the operating environment, the signal transmission, and the detector stability. These aspects will be elaborated in the following sections.

5.1. Data-taking

Data-taking is remotely controlled and is checked daily in case of unexpected interferences or sudden hardware failures. In these cases, data-taking has to restart. Each data file usually has a duration of four hours. The file size is optimized by adjusting the energy threshold from time to time. Otherwise, the maximum event rate that can be handled by the DAQ system could be exceeded.

The threshold is modified for each run to ensure the lowest possible energy threshold while keeping a reasonable event rate. It is adjusted based on the count rate of the fourfold forbidden non-unique single β-decay of ^{113}Cd. The decay has a long half-life of $(8.00\pm0.35)\times10^{15}$ yr [110], which should lead to a constant decay rate over time. This feature makes the decay an internal monitor evaluating the detector stability. Any deviations in the detected count rate would indicate an alteration of the detector properties. Since the detectors are made from natural Cadmium containing 12.22% of ^{113}Cd, the decay is the strongest signal detected in the low background environment [38, 68]. Assuming the detector mass is 36 g, and the detection efficiency is 100%, the expected decay rate will be about 100 per hour per detector. This number is a rough estimate of the trigger rate.

5.2. Temperature and humidity stability

Environmental conditions can affect the detector's performance and the electronics' functions. Several sensors are attached to the outer shielding to monitor the temperature and the humidity. Fig. 5.1 shows the temperature and humidity measured from different positions over a time scale of years. Near the preamplifiers, the temperature is lower than in other locations, as the cooling plates are placed closest to the preamplifier. When the cooling system is switched off due to on-site maintenance or a sudden power outage, the temperature increases dramatically. Besides these abnormal periods, the detectors are working at a roughly constant temperature of 12° C, as indicated by the temperature of the Lead castle in the plot.

The humidity level inside the Lead castle is adjusted by constantly filling it with Nitrogen. The Lead castle is sealed by the gas-tight Radon shield. The frequent oscillation is correlated with a bi-weekly Nitrogen filling cycle of the dewar where the liquid Nitrogen is stored. Broad

peaks indicate on-site activities of opening the outer shielding. There was also a short-term run without Nitrogen flushing in June 2019, which led to high humidities. In this case, the temperature is increased to avoid condensation.

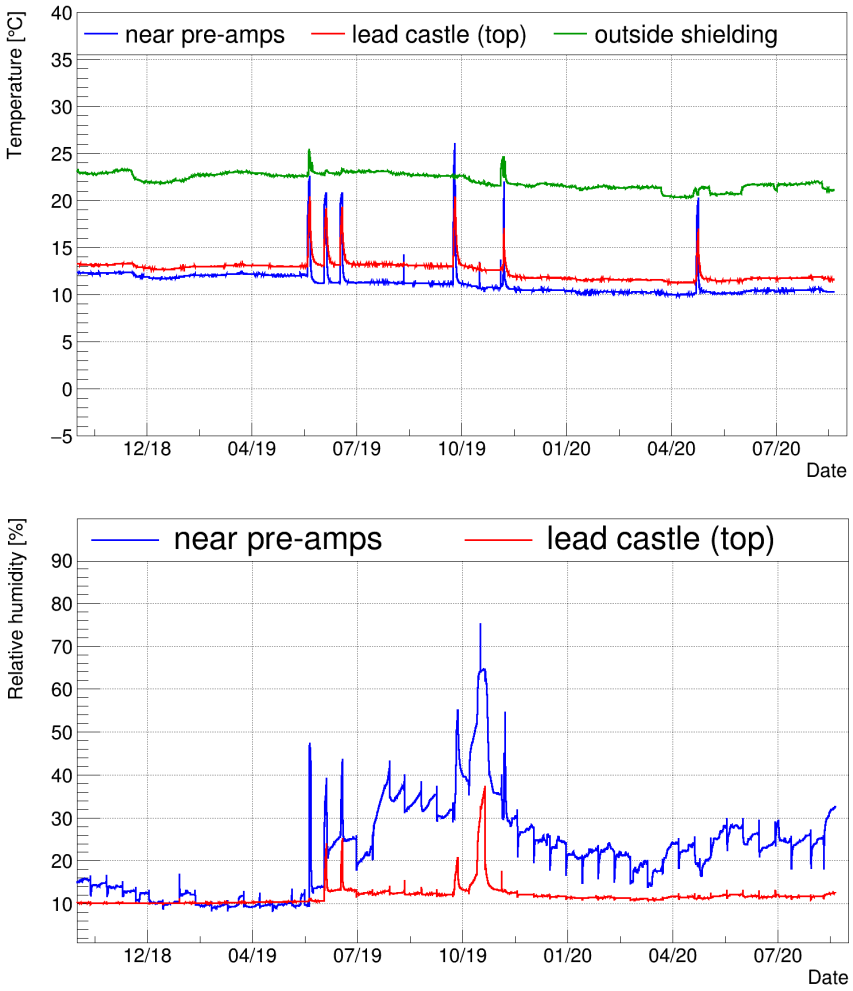

Figure 5.1.: Temperature (upper) and humidity (lower) measured at different locations during the operation of XDEM. Near the preamplifiers is where the cooling plates are placed. The Lead castle surrounding the Copper shield reflects the working temperature and humidity of the detectors. The temperature outside the shielding is also monitored, which is close to room temperature, as indicated by the green line.

When the detectors are exposed to thermal air and relatively high humidity, the thresholds are typically raised for several days. Only after the count rate is back to normal are thresholds lowered again.

5.3. Data acquisition electronics

Besides checking the operating environments, the electronic response of the DAQ is also monitored. This is done with the help of artificial pulses from a Berkley Nucleonics PB-5 precision pulse generator. As mentioned before, these pulses are regularly injected into the preamplifiers. The injected pulses are transmitted through the same electronic channels as signals detected by the detectors. Meanwhile, a TTL pulse from the pulse generator goes directly to the FADCs to discriminate the artificial pulses from physical events. Any electronic malfunction can be diagnosed by these injected pulses.

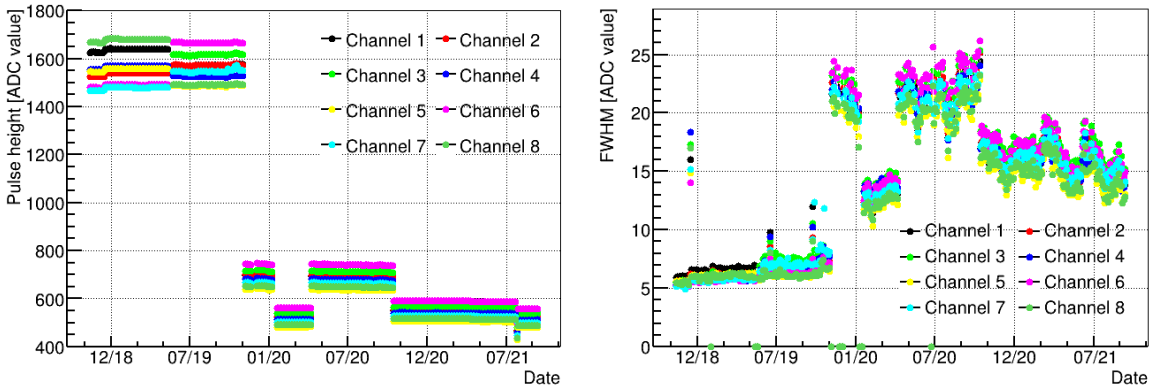

Figure 5.2.: Left: Pulse height of the injected pulses in ADC value versus time. The injected pulses are recorded from eight readout channels of one XDEM detector at the LNGS. Right: The FWHM of the pulse height distribution, representing the noise level, evolves with time.

The pulse height of these artificial events keeps track of the electronic stability with time. It should be constant if every component in the DAQ is stable. In order to show an evolution of the pulse height with time, injected pulses recorded every three days are analyzed to ensure enough statistics. Since the distribution of the overall noise is Gaussian, a constant signal amplitude superimposed on noisy baselines will yield a Gaussian peak whose mean value denotes the pulse height, and the FWHM represents the noise contribution.

Each data point in Fig. 5.2 corresponds to the mean value of a Gaussian fit. Even though the artificial pulse is distributed to each channel with an equal amplitude, the resulting pulse height differs from channel to channel. This variation is mainly caused by the amplification imbalances of the amplifier chips, and the corresponding correction is already discussed in Section 4.5.

It is found that the pulse height evolution is consistent with the operations performed on electronics. A slight transition at the beginning of 2019 coincides with the installation of the air-conditioning [43]. A 10° C decrease to the amplifiers has caused a fluctuation in the amplification, which leads to the transition. Till May 2019, the pulse height is nearly constant, followed by amplification shifts after replacing preamplifier chips as well as raising their low voltage supply. Around November 2019, the Demonstrator was disabled and the amplitude of injected pulses was adjusted, which explains the reduction of the pulse height. Following

an on-site maintenance shift, excessive noise has appeared on all the channels. Several test measurements were carried out to reduce the noise, which is why the pulse amplitude was changed in 2020.

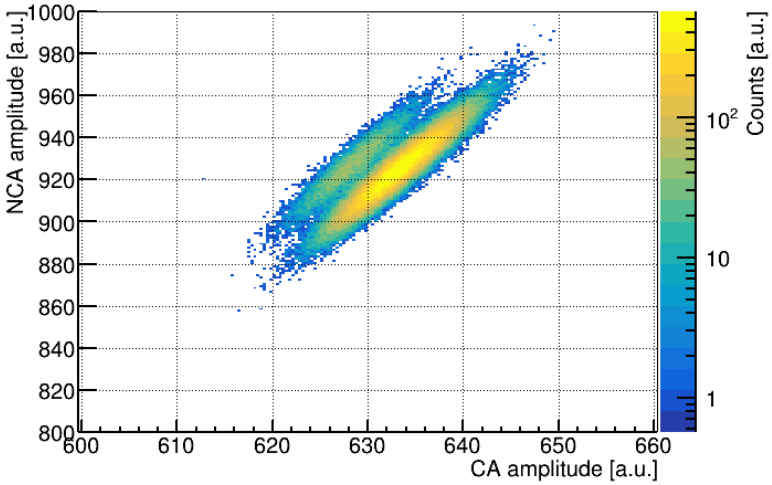

Figure 5.3.: The amplitude distribution of artificial pulses from the respective CA and NCA readout channels. The amplification is not consistent during the data-taking.

Sometimes, channels have changed their amplification during the data-taking. An example of such a change is shown in Fig. 5.3. This amplification shift is probably caused by a sudden power outage of the preamplifier. A direct consequence of the shift is showing double peaks at the full energy γ peak. Unfortunately, the affected datasets cannot be corrected and are discarded from post-processing.

Fig. 5.2 shows the FWHM for the pulse height distribution as a representative of the noise level, which hints at the noise origin and readout channels that shall be denoised. It has been dramatically increasing since November 2019. High-level noise is also observed when the detectors are exposed to heat or humidity after on-site maintenance.

Alternatively, the noise level can also be quantified as the root mean square (RMS) of the pulse baseline. The RMS estimation can include noise generated by the DAQ as well as detectors. Results are given in Appendix A.6 for all channels. In comparison, the electronic noise contribution in Fig. 5.2 agrees with 2.3548 times the baseline RMS. Possible noise sources will be discussed in the following section.

5.4. Noise sources and analysis

Noise can significantly affect the energy resolution or the obtainable detection threshold at low energies. These parameters are essential for rare decay searches. Hence, it is necessary to understand the origins and mechanisms of noise inherent to detectors and electronics. This knowledge can help to find an algorithm to minimize noise impacts on the detector performance.

5.4.1. Noise in CdZnTe detectors and electronics

Every component in a circuit can produce noise that arises intrinsically from fluctuations in the number and the velocity of charge carriers [111]. A flowing current i induced by n electrons moving with a velocity v depends on the space l of two electrodes. Following Ramo's theorem, the current is expressed as

$$i = \frac{nev}{l}. \tag{5.1}$$

The fluctuation of the current is the summation of differential n and v in quadrature

$$< di >^2 = \left(\frac{ev}{l} < dn >\right)^2 + \left(\frac{ne}{l} < dv >\right)^2. \tag{5.2}$$

The fluctuations related to the number of charge carriers, as indicated by the first term, can be caused by a current flow crossing a barrier. The current is referred to as the shot noise. Charge carrier trapping also causes number fluctuations. Impurities or defects in the material can trap charge carriers and release them after a certain lifetime, which leads to the frequency-dependent $1/f$ noise.

As for the second term, the velocity fluctuation originates mainly from thermal motions. Fluctuating velocities of individual charge carriers lead to an instantaneous random current, which depends on the device's resistance and increases with temperature.

Both the shot and thermal noise components cause the leakage current that can limit the spectral response of the detector. For a CZT detector, the actual magnitude of the leakage current depends on the physical characteristics of the detector, such as its area, thickness, material quality, operating temperature, the nature of the electrodes, applied voltages, and other factors. An exponential rise of the leakage current with voltage has been observed in the previous measurement [43]. The eV detectors have a larger leakage current than Redlen detectors as they require a higher voltage supply.

Besides the current noise as described in Eq. 5.2, the detector also acts as a capacitor, which generates the so-called voltage noise (or series noise). The overall detector noise is a quadratic sum of all contributions [64, 112].

Based on the discussion above, it is possible to find potential solutions to reduce the noise generated by detectors. For instance, cooling down the device decreases the thermal activation of charge carriers over a potential barrier. A mild cooling significantly improves the detector performance and lowers the energy threshold. Optimizing the fabrication technique can also reduce noise, especially surface treatments and electrode configurations.

The electronic noise from the preamplifier usually makes a noticeable contribution to the performance of the semiconductor detector. During the assembly of the XDEM preamplifier module, high-level noise was already present and could be reduced by cooling [113].

In addition to the intrinsic noise, external noise often limits the system's performance. There are many ways through which these undesired signals can enter the system. For instance, it is noticed that artificial pulses are usually followed by nonphysical waveforms. This is probably because after injecting artificial pulses, there is an accidental triggering in the DAQ system. The Piezo electrical effect or the ground loops[1] inside the preamplifier module may also

[1] Ground loops are formed wherever two or more circuits share a common current path. The shared track introduces voltage drops to the circuits.

contribute to the noise [113]. Like the intrinsic noise, external interferences also introduce baseline fluctuations that may trigger the FADCs. The exact origin and significance of external sources are beyond this work.

5.4.2. Frequency analyses of noise

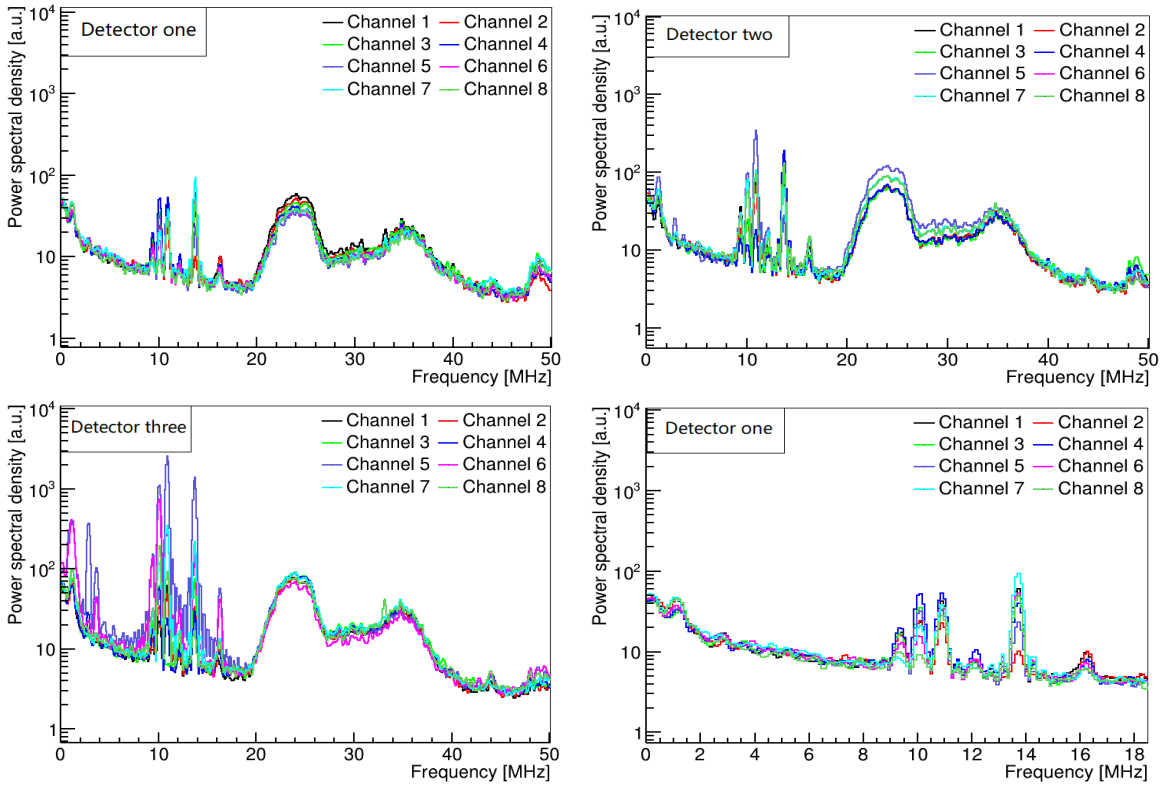

Figure 5.4.: The average noise power spectra of detector one (top left), two (top right), and three (bottom left) obtained from artificial pulses. Hundreds of artificial pulses are averaged to estimate the noise contribution from electronics. For each pulse, 256 samples of the pre-baseline are selected for the FFT. The power distribution of detector one is zoomed in and shown at the bottom right.

Several types of noise are usually superimposed on signals. Fourier analysis can help to identify different noise components. The FFT is explained in detail in Appendix C. If the FFT is applied, the signal will be decomposed into its sine and cosine functions and transformed from time to the frequency scale.

Each noise type has its characteristic frequency distribution. For example, transforming white noise to the frequency domain yields a constant distribution. The 1/f noise is dominant at low frequencies. Furthermore, periodic noise, seen as sinusoidal functions at the time scale, is shown as discrete frequency peaks. Spikes are typical of high frequency noise. These characteristic distributions may pinpoint the origin of unwanted noise or vibration.

Fig. 5.4 illustrates the noise's power spectral density for three detectors obtained from artificial pulses. The power spectral density represents the power of the noise (V^2/Hz) distributed over the frequency [114]. According to the previous knowledge of typical frequency features, different types of noise are identified. Apart from the 1/f and the white noise, there is also periodic noise with different frequencies. A 1 MHz peak, triple peaks around 10 MHz, and another one at 14 MHz are prominent in the low frequency region.

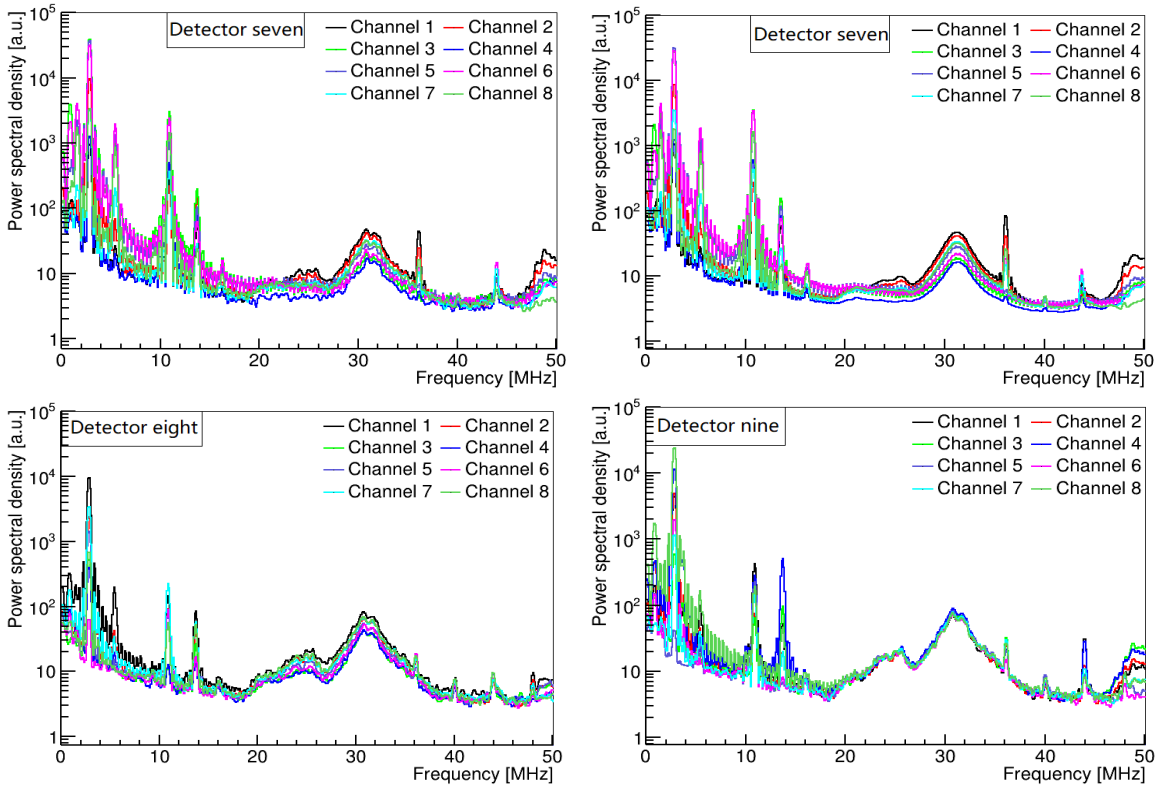

Figure 5.5.: The average noise power spectra deduced from the baseline of ^{22}Na calibration events (top left) and artificial pulses (top right) for detector seven. The pre-baseline with a length of 256 samples is chosen for the frequency analysis to avoid any rise structure of the signal pulses. Detector eight (bottom left) and nine (bottom right) are also shown.

The graphs depict that all channels of detectors one, two, and three show almost the same frequency distribution despite differing densities. This means that noise is not specific to one detector but common to all three detectors.

As a comparison, events taken from the Demonstrator are also analyzed with the FFT. The resulting frequency peaks differ from those of the XDEM. The prominent frequency bands in XDEM are not caused by external noise sources but by XDEM itself.

The pulse baseline of ^{22}Na calibration events is also analyzed and produces the same frequency bands as those obtained from the artificial pulses. The comparison is illustrated in the upper panel of Fig. 5.5. This agreement indicates that those frequency bands are likely

from the electronic system.

The averaged noise power spectra of detectors seven, eight, and nine are investigated. The three detectors display a similar pattern in the frequency domain, as demonstrated in Fig. 5.5. In addition, the frequency distributions of detectors four, five, and six displayed in Fig. C.2 are also similar to each other. Based on the detector and the preamplifier layout shown in Fig. 3.11, detectors from the respective preamplifier module have their own similarities in the frequency distribution. It can be concluded that noises generated from the preamplifier module have shaped the frequency distribution in a specific way.

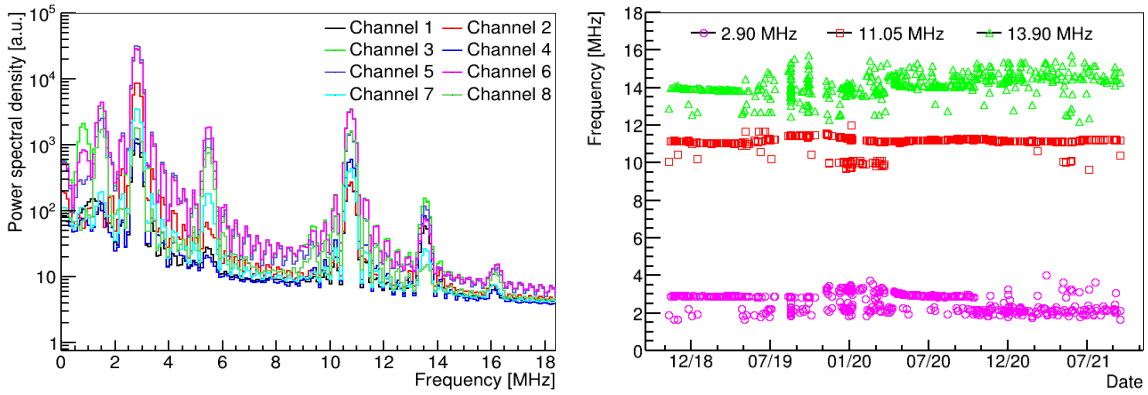

Figure 5.6.: Left: The average noise power spectra at low frequencies from physics events for detector seven. Right: The time evolution of characteristic bands at 2.90 MHz, 11.05 MHz, and 13.90 MHz for one of the eight readout channels. Each data point is obtained from a Gaussian fit plus a polynomial function. The other channels show the same pattern.

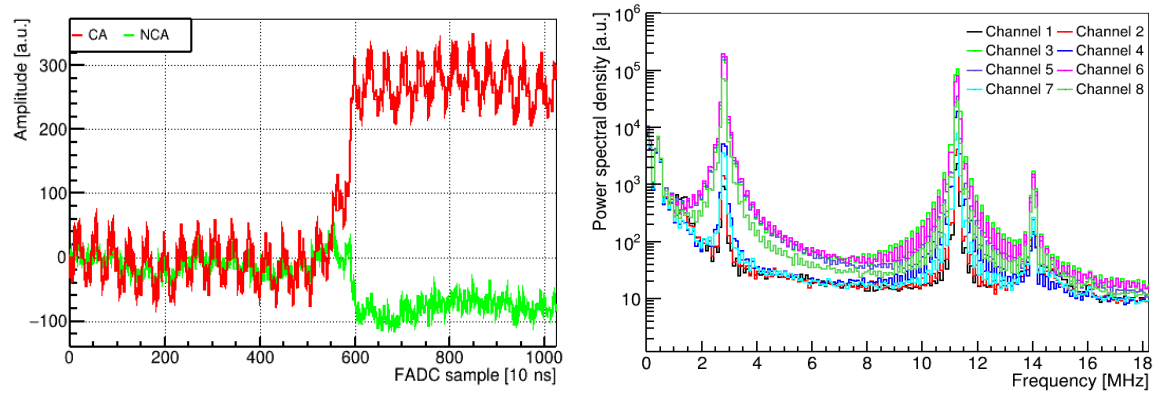

Figure 5.7.: Left: Signal pulses of one event with excessive noise from detector seven. Right: The average noise power spectrum at low frequencies obtained from the pre-baseline of injected pulses with 512 samples. A new peak at the 0.45 MHz is found.

These results suggest that there might be crosstalk inside the preamplifier modules. By analyzing the frequency distribution before and after exchanging preamplifier chips, the frequency

does not change. Therefore, the origin of the crosstalk is not connected to the preamplifier chip but could be related to the circuit connection.

Fig. 5.6 shows the time evolution of three prominent bands at low frequencies (2.90 MHz, 11.05 MHz, and 13.90 MHz) for detector seven. These bands are present the whole time with slight fluctuations. A common source of the periodic noise is electrical or electromechanical interference. However, the exact origin is unclear yet.

Based on the results gained from the Fourier analysis, the current electronics need to be modified or improved. However, custom-made electronics, as used in COBRA, have the shortcomings of not being replaced easily.

Pulses with excessive noise have been recorded for all detectors since November 2019, affecting the quality of the entire dataset. An example of such pulse shapes is given in Fig. 5.7. The averaged noise power spectrum of one detector is also provided. Compared with the frequency distribution shown in Fig. 5.6, similar frequency bands are observed but with higher intensity using the same sample number of pre-baseline. Additionally, a new peak at around 0.45 MHz is found in all channels. This means that there is a new noise source common to all detectors. After several tests, it is suspected that the interference is from a voltage supply unit. The power system supposed to supply low voltages to the preamplifier is probably not working properly. Electronic interferences may be coupled through the detector capacitance to the amplifier input and cause large pulse fluctuations.

The excessive noise is very undesirable for pulse shape analyses, which will be elaborated in detail in the following chapters. The affected dataset has to be dealt with differently. The later analyses will mainly focus on the data without the excessive noise.

5.5. Detector performance

To evaluate the detectors' performance, calibrations are carried out regularly in case dramatic changes occur during the data-taking. In addition, it has to be checked that the energy resolution is good enough so the detector is suitable for detecting rare signals.

Due to a high count rate of noise events in several readout channels and a failed electrical connection to some other channels, not all detectors are fully functional. Fig. 5.8 shows the energy resolution in percent at 2615 keV γ-line from ^{208}Tl for all sectors except those with degraded performance. An average energy resolution of (1.14±0.04)% is achieved.

Fig. 5.9 illustrates the obtained energy resolutions for one sector fitted with the function given in Eq. 3.9. Also shown is the parametrization from three contributions, including the corresponding uncertainties. It turns out that the extracted noise contribution is comparable with the value determined from injected pulses. It is also possible to estimate the contribution from the Poissonian term, which gives the FWHM of 14.07 keV at 2615 keV. The effect of the incomplete charge collection is rather small because the signal loss is minimized by applying an optimal working point and employing weighting factors. Therefore, the energy resolution is dominated by noise and statistical fluctuations.

The effective energy resolution of the XDEM detectors is determined from a combined energy spectrum of all functional detectors. Each detector is weighted with its corresponding exposure. The energy resolution function displayed in Fig. A.9 represents the overall setup

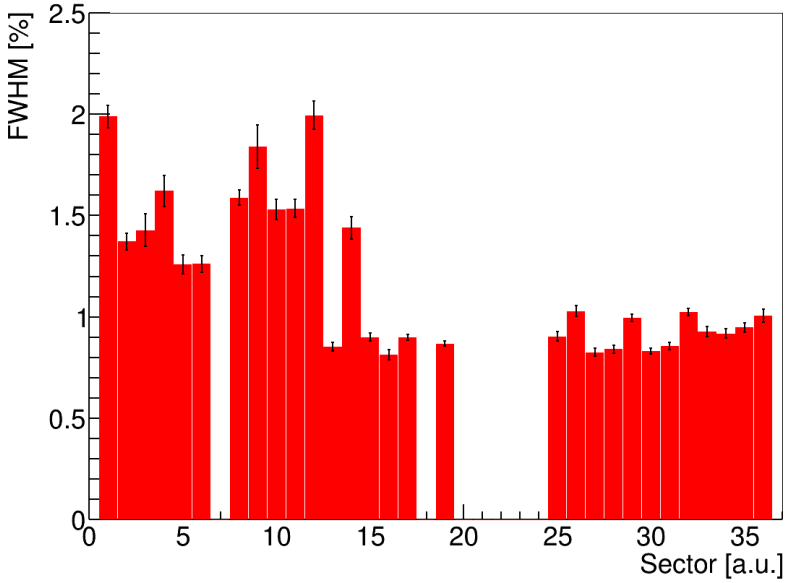

Figure 5.8.: The energy resolution at the 2615 keV γ-line emitted from ^{208}Tl. Sectors with a broad peak width, such as FWHM above 2.5%, are removed from further analysis. The FWHM variance is probably caused by the crystal quality.

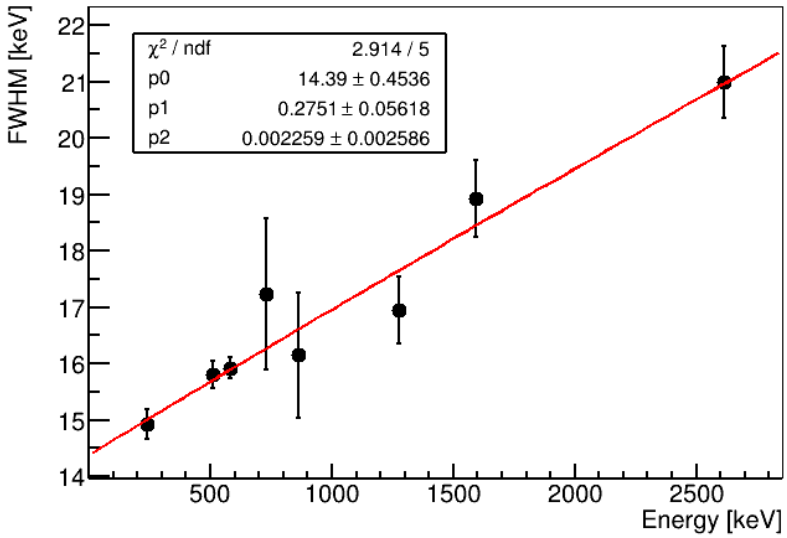

Figure 5.9.: The fitted energy resolution function for one sector (red line). ^{22}Na and ^{228}Th sources are used. $p0$ describes the constant noise. $p1$ accounts for the statistical fluctuation, and $p2$ is attributed to the instrumental effect.

performance.

5.6. Long-term detector stability

The XDEM has collected commissioning data with an exposure of 0.2 kg·yr during the last years, which allows us to probe the detector stability based on the internal monitor of the ^{113}Cd β-decay. The decay rate over one year is investigated.

The data are partitioned into time intervals of eight days for enough statistics. To ensure data quality, the following cuts are applied. The grounded GR intrinsically reduces signals originating from the lateral surfaces. The threshold cut E_{th} (Section 4.6.5) corrects for the depth dependency. Data runs with a threshold value higher than the optimal threshold E_{opt} (Section 4.6.5) are discarded to avoid large fluctuations. In addition, the data cleaning cuts (DCCs) (Section 6.3) can remove nonphysical events as well as signal events affected by noise. Furthermore, the interaction depth cut, z-cut (Section 6.4), is also employed to limit the fiducial volume to where energy and depth are reconstructed correctly. The surviving events are then normalized with the respective lifetime.

Fig. 5.10 shows the time evolution of the measured ^{113}Cd β-decay rate for detectors one and eight. The expected decay rate for each sector is shown in dashed lines. To compare the observed value to the expected, the cut efficiencies are taken into account. A signal acceptance of (95.13±0.06)% is estimated from a simulation for the grounded GR. The efficiency of the threshold cut highly depends on the energy and is also determined from the simulation considering the energy resolution. The efficiencies for the DCCs and z-cut are deduced from data and detailed in Chapter 6.

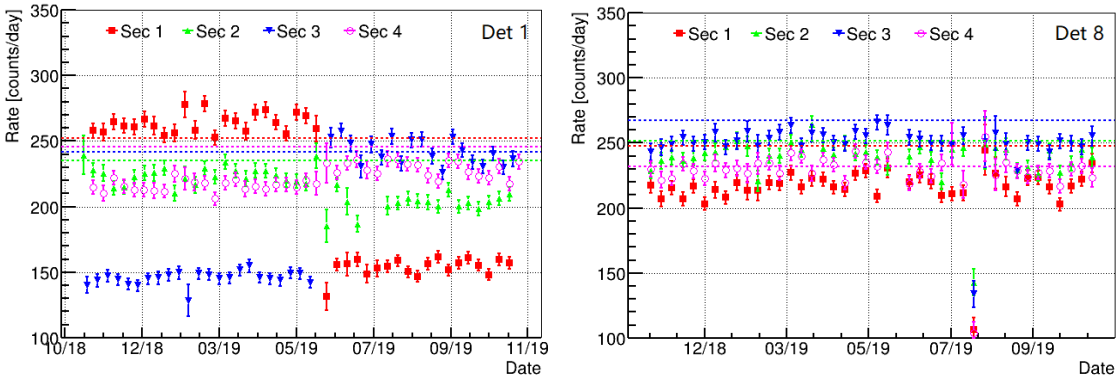

Figure 5.10.: The ^{113}Cd decay rate of detectors one (left) and eight (right) with corresponding statistical uncertainties versus time. The dashed lines show the expected rate of the ^{113}Cd β-decay above an optimal threshold. All the cut efficiencies are considered. The mass difference between the two detectors is also corrected for consistency. Deviations are observed for detector one, probably due to the increased bulk voltage.

Due to various optimal thresholds, the theoretically expected decay rate differs from one sector to another, and so is the measured rate. The measured decay rate is expected to be

constant over the operational period. However, deviations are observed for detector one and occur when the applied bulk voltage (BV) is increased to the optimal value, as indicated in Table. A.1. Before that, detectors were operated under a lower voltage, which is mainly limited by the capacity of the high voltage filter.

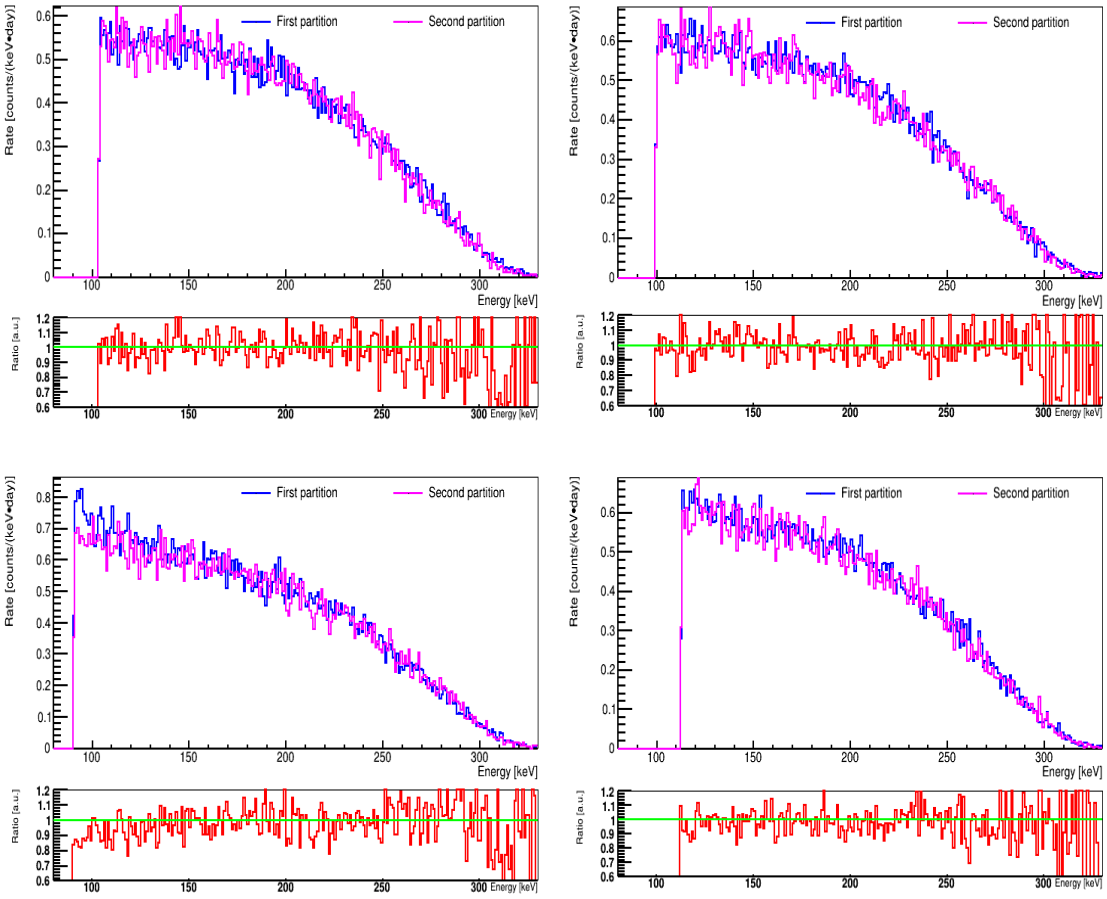

Figure 5.11.: The spectral shape of the ^{113}Cd β-decay for the four sectors of detector eight. The relative change between the two partitions is shown at the bottom.

In order to identify the cause of the deviation, all associated parameters are checked before and after applying the optimal voltage. It is found that the cut efficiencies at low energies do not vary much. Regarding changes in the DAQ system, the amplification does change but can be corrected by the g factor discussed in Section 4.5. A possible explanation would be that charge transport properties vary with voltage for this detector.

The measured decay rate of detector eight is nearly constant, which is also the case for the other detectors. An outlier, leading to a low count rate, is probably caused by the malfunction of the NIM crate at the time. Besides that, the theoretical expectation matches well with the measured rate except for sector one. One of the significant uncertainties is the

DCCs efficiency. It is estimated by applying an average energy threshold to all the data, even though the efficiency varies at low energies. The cut efficiency is also related to the noise level. Using a single threshold overestimates the efficiency for sectors with high-level noise, like sector one. That is why the expected count rate is higher than the measured. Furthermore, material uniformity also affects the decay rate.

To test whether the abrupt change in detector one is related to the operating voltages, the commissioning data is partitioned into two sets. The first dataset is measured when the detectors are applied with BV_1 given in Table A.1, while the second is collected when the optimal BV_2 is supplied. The spectral shape and the depth distribution of the decay are compared between two partitions. Fig. 5.11 shows the spectral shape from the four sectors of detector eight agrees well for the two periods, while detector one shows deviations (not shown here). Each partition is further divided into two shorter intervals to rule out the possibility of any deviation under the same voltage. The spectral shape stays the same.

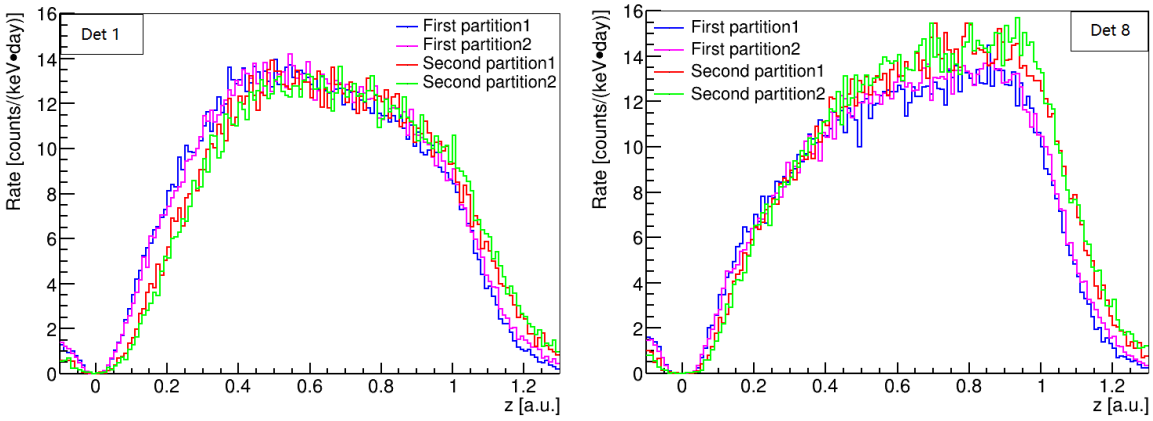

Figure 5.12.: Depth distribution of the ^{113}Cd β-decay for detector one (left) and eight (right), respectively. Each partition in Fig. 5.11 is split into two shorter intervals.

The depth distribution in Fig. 5.12 shows no shift for the two intervals within the respective partition. Compared to the first partition, the depth shifts to high z in the second, while the number of integral events remains the same. This is also observed for the other detectors. Adjusting the operating voltage has caused uncertainties in the long-term stability of this detector. The effect on the z-cut efficiency will be discussed in Section 6.4.

In conclusion, most functional detectors demonstrated excellent performance during the long-term operation. The following chapter will discuss the analysis cuts developed for the XDEM and the determination of signal acceptance and background rejection.

6. Pulse shape analyses

Although α contaminations on the detector surface are significantly reduced by the grounded GR, other background sources still pose a challenge to the XDEM despite the multi-layer shielding and radiopure construction materials. In order to achieve a low background level, pulse shape discrimination (PSD) is performed.

However, high-level noise can cause large uncertainties to the PSDs and even interfere with the physics interpretation, especially for low energy events. For this reason, noise reduction is often a preprocessing step. The other objective of denoising is to explore the possibility of not discarding the dataset strongly affected by noise.

The noise reductions based on the Fourier analysis and the Wavelet transform are investigated in sections 6.1 and 6.2. Section 6.3 discusses the basic data cleaning cuts applied, removing nonphysical pulses and signal pulses strongly interfered by noise. Then, a fiducial depth cut is developed in Section 6.4 to discard events near the electrodes. Section 6.5 presents different multi-site event cuts that enable further background suppression. Moreover, cut efficiencies are determined and cross-checked with the help of simulated pulses. Another multi-hit discrimination approach, the coincidence analysis, is explained in Section 6.6. Lastly, the drift time, whose determination is also based on the pulse shape analysis, is evaluated in Section 6.7.

6.1. Fourier transform denoising

The Fourier transform provides insights into the frequency content of noise by analyzing pulse baselines, as discussed in Section 5.4.2. One may wonder what the signal frequency would look like. As recorded pulses are usually coupled with noise, they cannot provide pure signal frequency. Instead, simulated pulses are evaluated.

Fig. 6.1 shows simulated pulses for one event of ^{228}Th and the corresponding frequencies. The frequency intensity decreases exponentially. Even though the frequency distribution varies by events, the signal always dominates at low frequencies, unlike the noise frequency showing multiple peaks, as illustrated in Fig. 5.4. With such a characteristic feature, Fourier-based noise reduction is performed to clean measured pulses.

The underlying philosophy of Fourier filtering is to reduce unnecessary Fourier coefficients that represent the noise component. The denoising procedure contains three steps: Fourier transform of the signal to the frequency domain, reduction of the unwanted Fourier coefficients, and inverse transform to the time domain. This procedure will be iterated through the following smoothing filters.

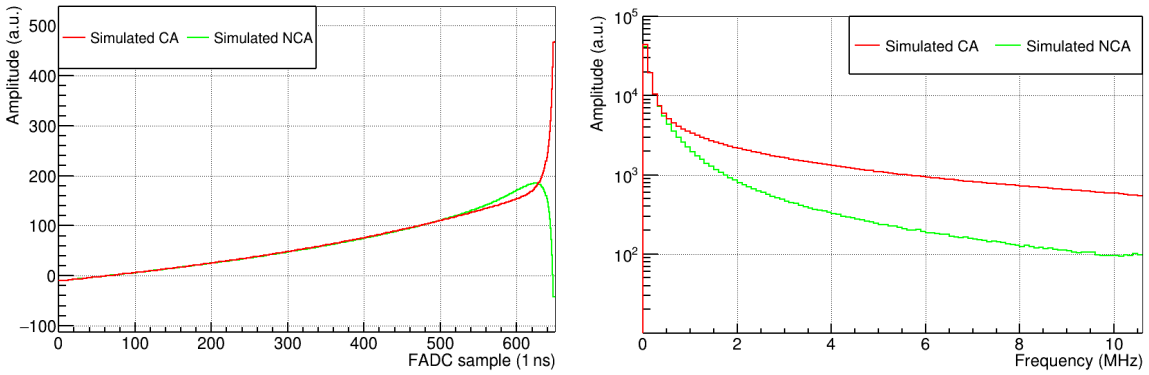

Figure 6.1.: Left: Simulated signal pulses of one event from ^{228}Th. Hardware responses are not included. Right: The frequency spectra for the same event zoomed in to 10 MHz.

6.1.1. Moving average filter

The moving average filter, or the moving average window, is viewed as a typical low pass filter in the signal processing. This filter employs a recursive algorithm to compute the average value of a set of samples within a predefined window. It is the fastest digital filter commonly used in time-series data, smoothing out short-term fluctuations.

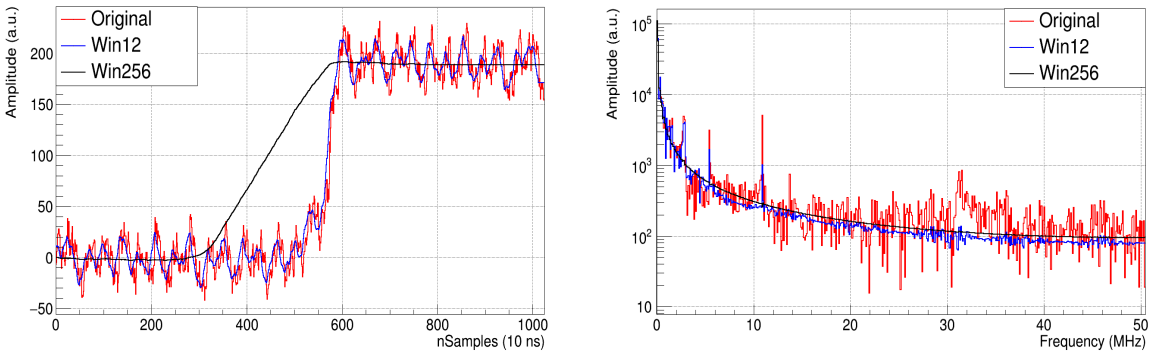

Figure 6.2.: Left: One CA pulse is filtered by moving average filters with the window size of 12 and 256 samples, respectively. The event is from a ^{22}Na calibration measurement at the LNGS. Right: The frequency distribution of the pulse before and after filter processing.

Fig. 6.2 shows one CA pulse and its frequency processed by the filter in two window sizes. The intensity of high frequency components is strongly suppressed, while the low frequency intensity remains nearly the same. A larger window smoothes out prominent frequency bands, especially those representing periodic noise, but at the expense of losing information. The rising slope of the original pulse has shifted dramatically. So, this filter is not beneficial for keeping the rising structure to which the pulse shape analysis is very sensitive.

For the COBRA usage, the moving average filter is applied to reduce noise interferences for an accurate pulse height determination, as mentioned before. Fig. 6.3 shows the filter

configuration in the time and frequency domains. Two windows, each with a size of 256 samples, are applied on the pre and post-baseline of the pulse, respectively. To preserve the information about the rising slope, the transient region where the abrupt change occurred is excluded from being filtered. However, the remaining high frequency components on the slope are not beneficial for the PSD.

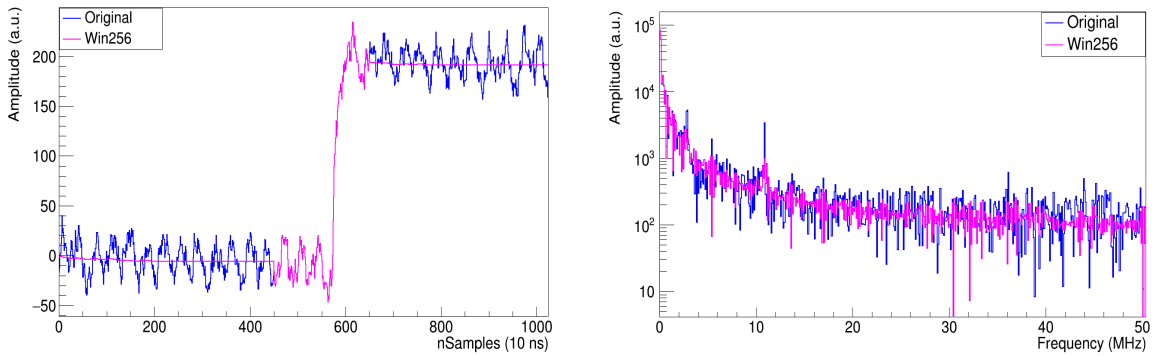

Figure 6.3.: Left: The pre and post-baseline of one difference pulse from ^{22}Na filtered by two moving average filters with a window size of 256 for each. Right: The frequency distribution of the pulse before and after applying the filter.

6.1.2. Optimal filter

In order to reduce noise interferences as well as preserve the pulse shape, an optimal filter is investigated based on the Fourier analysis. This filter can be defined in different ways. The basic concept is that the measured waveform in the frequency domain $y(\omega)$ is described as the summation of the signal frequency $s(\omega)$ and the average noise frequency $n(\omega)$,

$$y(\omega) = s(\omega) + n(\omega). \tag{6.1}$$

$n(\omega)$ is constructed for each readout channel using thousands of injected pulses. For each pulse, 512 samples are selected from the pre-baseline and are transformed to the frequency.

Simply speaking, the clean signal frequency $s(\omega)$ can be obtained by subtracting $n(\omega)$ from $y(\omega)$. However, the direct subtraction is quite conservative. By comparing the computed total signal frequency with the average noise frequency $n(\omega)$, it is possible to set a threshold to distinguish the signal frequency from the noise frequency. The first frequency at which the signal intensity is lower than that of the noise is assigned as the cutoff point [115]. The frequency above the cutoff point is dominated by noise and is either filled with zeros or suppressed in other ways.

Fig. 6.4 shows the denoising result obtained from filling zeros into the frequency component above the cutoff. The filtered pulses are cleaner than the original, and the rising slope is well preserved. However, the abrupt removal of all the Fourier coefficients beyond the cutoff point induces artifacts at the beginning and end of the pulse.

Instead of filling zeros, another approach is to smooth out high frequencies. This is done by a moving average filter with a window of 256 and an exponential function extrapolating the last 256 samples. Fig. 6.5 shows the smoothed pulses with the reduced artifacts.

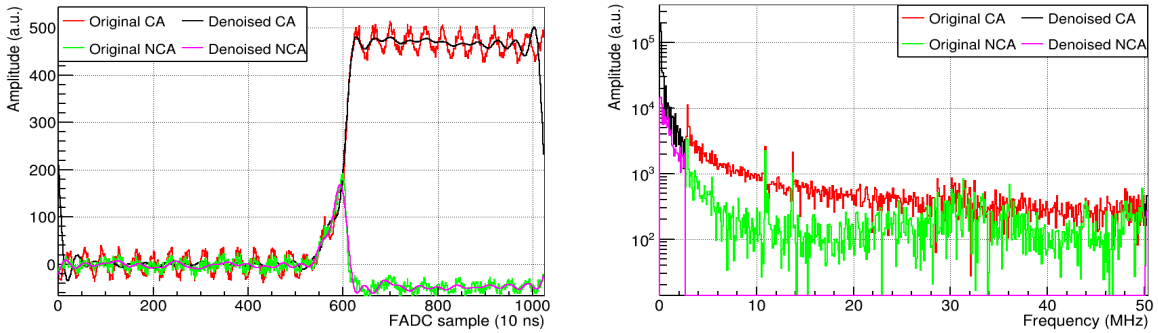

Figure 6.4.: Signal pulses (left) and frequency distribution (right) of one event from ^{22}Na before and after denoising. The frequency above the cutoff point is filled with zero.

It is worth noting that the optimal filter works well for the dataset without excessive noise. If there is excessive noise, visual inspections show inadequate noise removal and signal distortions for some resulting pulses. This is because the 0.45 MHz noise band located in the signal region is difficult to handle. Improvements can be made by measuring pure noise to estimate the noise frequency instead of using the pulse baseline only.

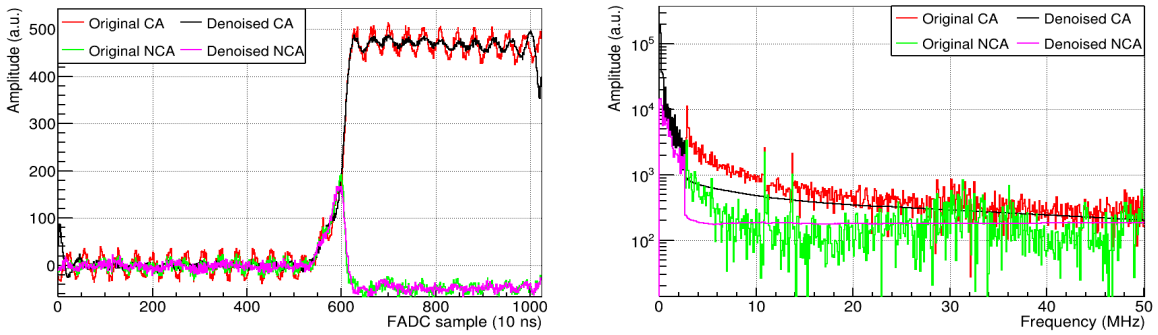

Figure 6.5.: Signal pulses (left) and frequency distribution (right) of the same event shown in Fig. 6.4 before and after denoising. Above the cutoff point, the frequency is smoothed out by a moving average filter.

6.2. Wavelet transform denoising

Since the decomposed sine and cosine functions of the Fourier transform are global in the time domain, the standard Fourier transform cannot provide local information about temporal changes. However, localized features can be identified by the wavelet transform through which

any function is decomposed into a set of wavelets. The wavelets are similar to the decomposed functions in the Fourier transform but are constructed to be local in space and frequency.

In addition, the nature of wavelets allows multi-resolution analysis, which decomposes a signal into scales with different time and frequency resolutions. In other words, average features and details of the signal are characterized at multiple levels, with each level divided by a factor of two. Appendix D contains more details about the Wavelet Transform (WT).

The WT is efficient for data compression, fast computation, and noise reduction [116–118]. The WT-based noise removal has been used in other double beta decay experiments [119, 120]. It is effective in denoising pulses with transient features. The basic idea is to choose a threshold and remove the wavelet coefficients below this threshold. These removed coefficients represent small details of signals that do not substantially affect the main features of the signal and are mostly noise components. Appropriate threshold values will be crucial to the filter performance. The filtered coefficients are then used in the inverse wavelet transform to reconstruct the denoised signals.

6.2.1. Thresholding method optimization

In the wavelet domain, the signal only resides in several high magnitude coefficients. The noise, however, is represented by many coefficients with small magnitudes. This sparsity is exploited by thresholding the coefficients to separate signal from noise.

Several approaches are available to select thresholds [121, 122]:

- Global threshold: The entire set of wavelet coefficients below one preselected global value are discarded as they contain mostly noise. The method gives limited improvement for the current dataset.
- Channel-dependent threshold: This method compensates for noise levels of readout channels, as opposed to the global threshold. The noise variance is estimated by the standard deviation of the pulse baseline, as mentioned in Section 5.3. The resulting noise levels are shown in Appendix A.6.
- Level-dependent threshold: Based on the multi-resolution analysis, the thresholds can be set for each decomposition level. The last two or three levels usually remain intact as they have frequency components valuable to the signals. This approach is preferred for data with a sparse representation in the wavelet domain.

The wavelet coefficients can be modified in several ways, Hard, Soft, and Garrote [115]. Hard thresholding sets all the wavelet coefficients below a particular threshold t to zero as

$$\tilde{d}_i = \begin{cases} 0, & |d_i| \leq t \\ d_i, & |d_i| > t \end{cases} \tag{6.2}$$

where $\tilde{d}_i$ and d_i are the denoised and original coefficients at the i^{th} decomposition level, respectively. Hard thresholding ensures that the signal wavelet coefficients are not tampered with thresholds. Soft thresholding, on the other hand, tends to over-smooth sharp peaks and

stretch rise structures. So, it will not be used for further tests. Garrote thresholding shrinks large coefficients by a nonlinear function and removes values below the threshold

$$\tilde{d}_i = \begin{cases} 0, & |d_i| \leq t \\ d_i - t^2/d_i, & |d_i| > t. \end{cases} \tag{6.3}$$

This method moderates the limitation of Hard and Soft thresholding.

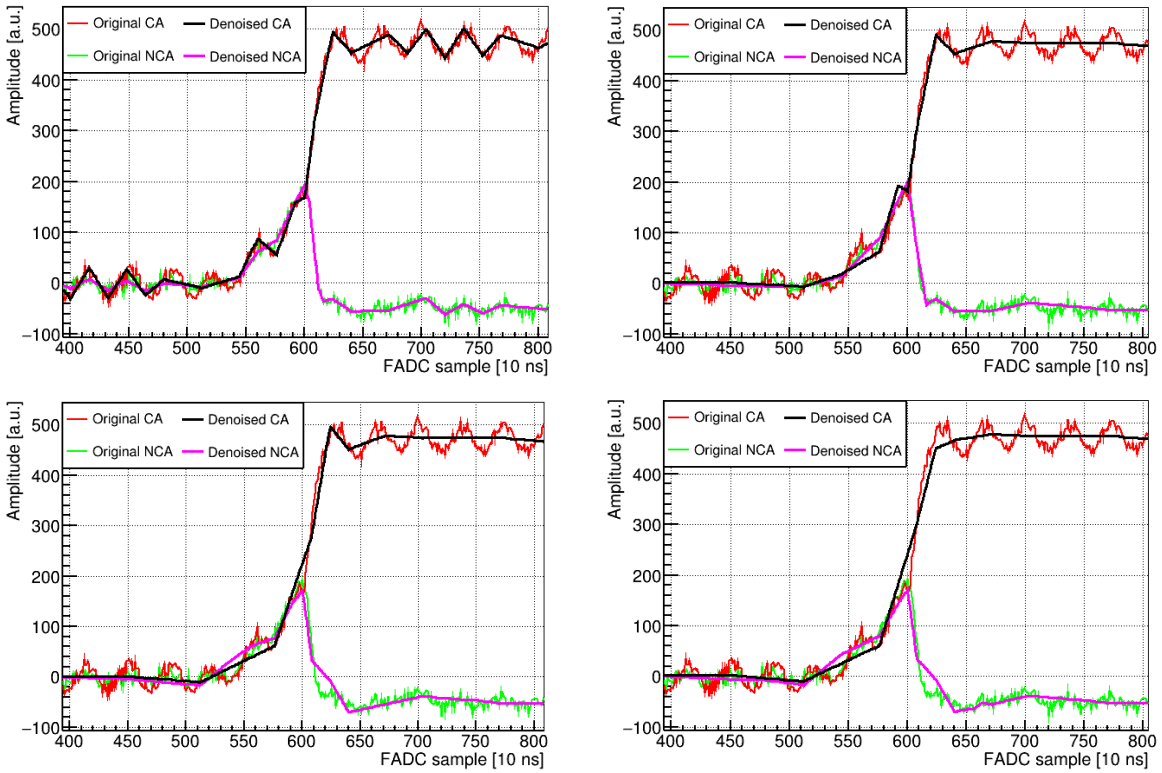

Figure 6.6.: Performance comparison of four combined thresholding methods with anode pulses of one event from ^{22}Na measured at the LNGS. Pulses are zoomed in to the transient region with rising and decreasing slopes. Top left: Channel-dependent Hard thresholding method. Top right: Level-dependent Hard thresholding. Bottom left: Channel-dependent Garrote thresholding. Bottom right: Level-dependent Garrote thresholding.

Hard and Garrote thresholding combined with the channel-dependent and the level-dependent thresholds are applied to the wavelet coefficients at each decomposition level, except for the last three. Fig. 6.6 shows an example of the denoising performance for the four methods. Garrote thresholding smooths spikes and removes periodic noise but does not produce desirable results in the rising slope. Pulses denoised with the channel-dependent Hard thresholding still show fluctuations on the baseline. In contrast, the level-dependent Hard thresholding method smooths out fluctuations without modifying the pulse shape.

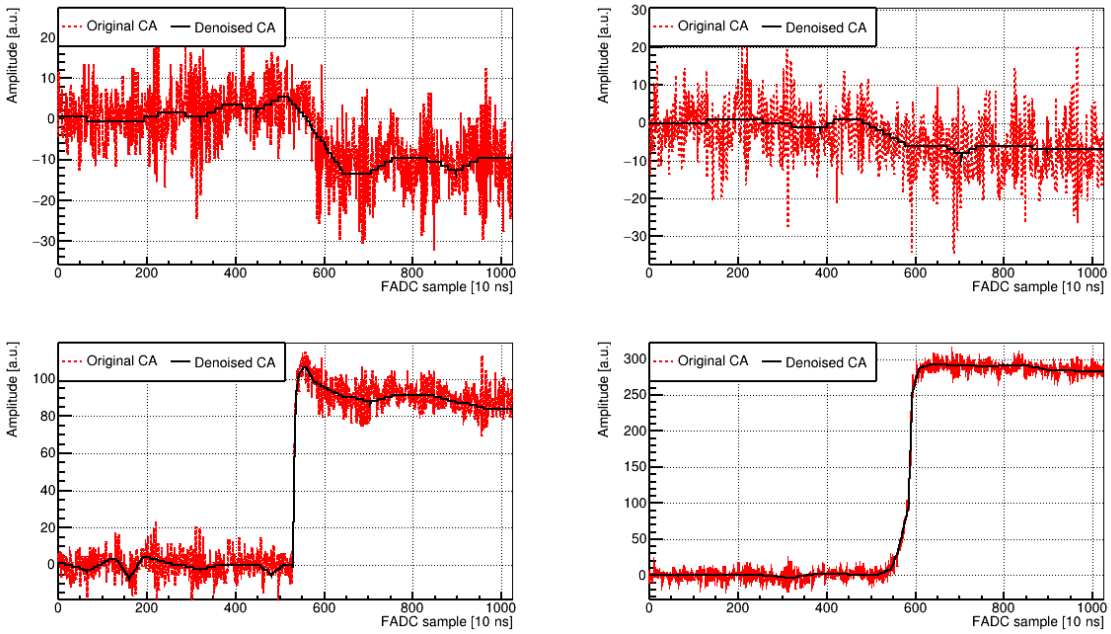

Figure 6.7.: Denoising the CA pulses of one event from ^{22}Na.

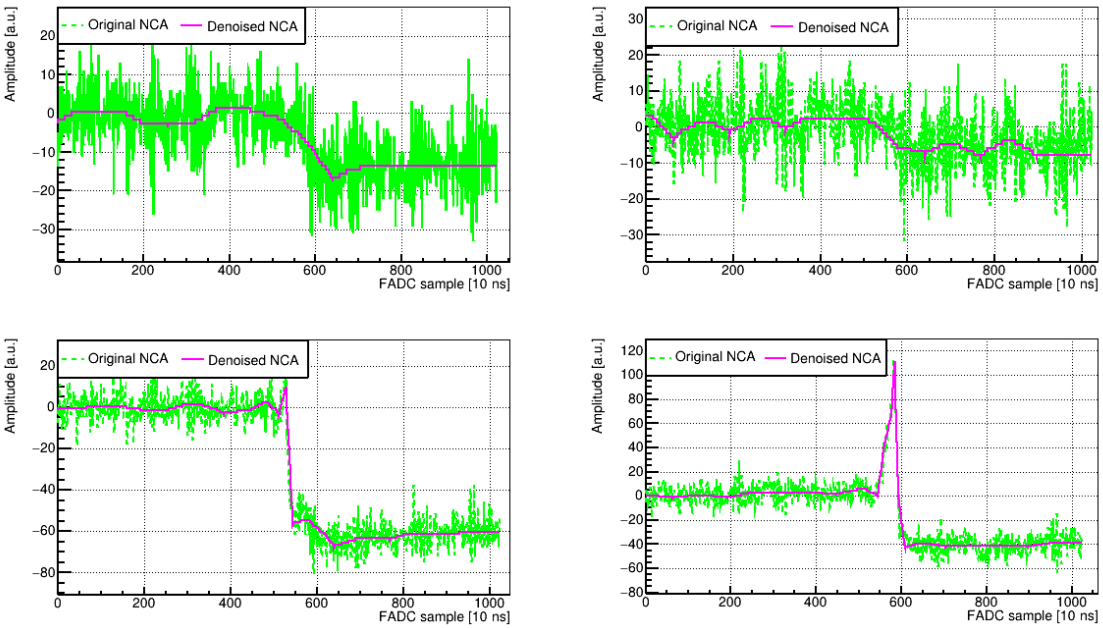

Figure 6.8.: Denoising the NCA pulses of the same event shown in Fig. 6.7.

In conclusion, the level-dependent Hard thresholding will be applied for wavelet denoising. Fig. 6.7 and Fig. 6.8 show the method applied to CA and NCA pulses for another event of ^{22}Na. While most noise components are suppressed, the pulse shapes are maintained.

However, this wavelet-based denoising is limited in retrieving weak signals, especially for mirror pulses with amplitudes close to the noise amplitude. Also, applying the denoising to the dataset with excessive noise does not remove the periodic noise at 0.45 MHz, as shown in Fig. D.4. A more efficient thresholding method could be investigated.

6.2.2. Denoising results

To evaluate the quality loss in the signal, the energy difference before and after the wavelet-based noise removal ΔE is introduced. This quantity should be constant with energy for an ideal filter. Fig. 6.9 demonstrates that ΔE is independent of the deposited energy.

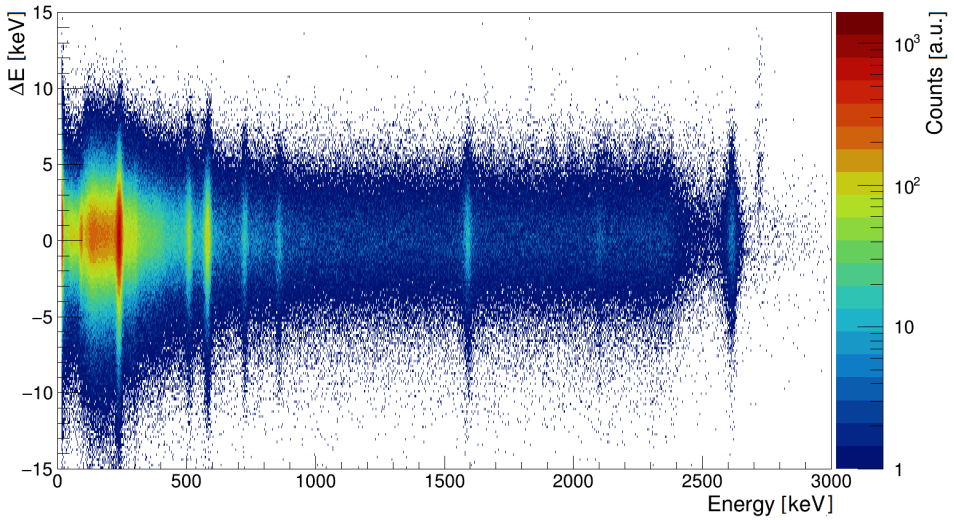

Figure 6.9.: The energy difference versus energy for the ^{228}Th decay events measured with all detectors at the LNGS. Raw data and denoised data use same calibration parameters.

The capability of noise reduction has shown great potential for improving data quality. Compared to the FFT, the essential advantage of the WT is its ability to extract local spectral and temporal information. As further investigation of the denoising method is needed, the denoised dataset is only used to cross-check the analysis cuts discussed in the following sections but not for searches of rare decays.

6.3. Data cleaning cuts

As mentioned in Section 5.4, there is noise originating from hardware abnormalities or electromagnetic interferences. These transient and irregular events contaminate the energy spectrum

at low energies and may lead to misleading data interpretation. However, the data quality can be assured by tagging those events via the data cleaning cuts (DCCs).

6.3.1. Selection criteria

The DCCs select physical events, and only those with good quality are kept. The selection criteria are defined based on the CPG working principle since nonphysical events do not follow this concept. These criteria have been proven effective for the Demonstrator [39]. As the pulse features of qCPG detectors differ from those of small detectors, corresponding quantities characterizing the signal shape for the XDEM need to be modified. Table 6.1 lists all the conditions used for the two types of detectors. Details are explained as follows.

Table 6.1.: Selection rules of the DCCs for the Demonstrator and the XDEM. Corresponding parameters are adjusted. The last two selections discriminate mirror pulses.

Selection criteria	Demonstrator	XDEM
trace length	$N_{\text{samples}} < 1024$	$N_{\text{samples}} < 1024$
high CA range	$\text{Ph}^{\text{ca}}_{\text{max-min}} > \text{Ph}_{\text{ca}} + 180$	$\text{Ph}^{\text{ca}}_{\text{max-min}} > \text{Ph}_{\text{ca}} + 230$
high NCA range	$\text{Ph}^{\text{nca}}_{\text{max-min}} > 1.05{\cdot}\text{Ph}_{\text{ca}} + 130$	$\text{Ph}^{\text{nca}}_{\text{max-min}} > 0.80{\cdot}\text{Ph}_{\text{ca}} + 250$
low NCA range	$< \text{Ph}_{\text{ca}}/4.0$	$< \text{Ph}_{\text{ca}}/6.67 + 20$
high CA RMS	$\text{RMS}_{\text{ca}} > 10.0{\cdot}\text{Ph}_{\text{ca}}$ > 200	$\text{RMS}_{\text{ca}} > 10.0{\cdot}\text{Ph}_{\text{ca}}$ > 200
high Diff change	$\text{MaxChange}_{\text{Diff}} > 4.0{\cdot}\text{Ph}_{\text{Diff}}$	$\text{MaxChange}_{\text{Diff}} > 4.0{\cdot}\text{Ph}_{\text{Diff}}$
low CA change	$\text{MaxChange}_{\text{ca}} < \text{Ph}_{\text{ca}}/4.0$	$\text{MaxChange}_{\text{ca}} < \text{Ph}_{\text{ca}}/7.0$
low NCA height	$\text{Ph}_{\text{nca}} <$ -1.05·Ph_{ca}	$\text{Ph}_{\text{nca}} <$ -1.05·Ph_{ca}
high NCA height	$\text{Ph}_{\text{nca}} > 0.5{\cdot}\text{Ph}_{\text{ca}}$	$\text{Ph}_{\text{nca}} > 0.5{\cdot}\text{Ph}_{\text{ca}}$
low Diff	$\frac{\text{Ph(ca-nca)}}{\text{Ph}_{\text{Diff}}} < 0.93$ $< 0.815 + 1{\times}10^{-3}{\cdot}\text{Ph}_{\text{Diff}}$	$\frac{\text{Ph(ca-nca)}}{\text{Ph}_{\text{Diff}}} < 0.93$ $< 0.815 + 9{\times}10^{-4}{\cdot}\text{Ph}_{\text{Diff}}$
high Diff	$\frac{\text{Ph(ca-nca)}}{\text{Ph}_{\text{Diff}}} > 1.02$ > 1.06 - $2{\times}10^{-4}{\cdot}\text{Ph}_{\text{Diff}}$	$\frac{\text{Ph(ca-nca)}}{\text{Ph}_{\text{Diff}}} > 1.02$ > 1.06 - $2{\times}10^{-4}{\cdot}\text{Ph}_{\text{Diff}}$
CA slope down	not applied	$\text{Ph}_{\text{ca}} <$ -2.0·RMS_{ca} $\text{RMS}_{\text{ca}} < 100$
CA slope up down	not applied	$\text{MaxChange}_{\text{ca}} < 10{\cdot}\text{abs}(\text{Ph}_{\text{ca}})$ $> 1.0{\cdot}\text{abs}(\text{Ph}_{\text{ca}})$

Firstly, the trace length counts the sample number. Each signal pulse should contain 1024

samples. As opposed to the signal, nonphysical waveforms usually have random numbers. This criterion is mainly to distinguish events caused by electronic disturbances.

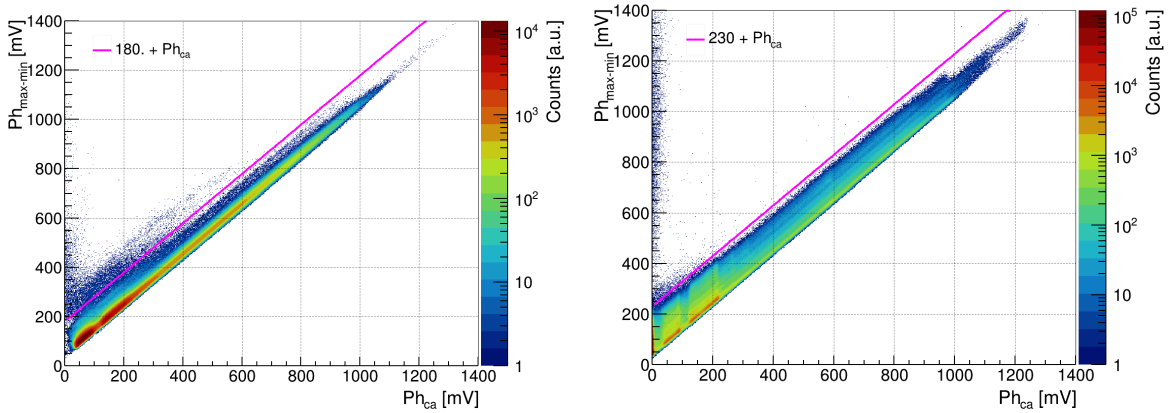

Figure 6.10.: The CA pulse range, $\mathrm{Ph}_{\mathrm{max-min}}$, versus the pulse height, $\mathrm{Ph}_{\mathrm{ca}}$, of ^{22}Na data for the Demonstrator (left) and the XDEM (right). Both are set with a conservative offset.

The second category identifies spikes coupled on pulses by evaluating the relationship between the maximal range and the height of CA pulses, $\mathrm{Ph}_{\mathrm{max-min}}$ and $\mathrm{Ph}_{\mathrm{ca}}$, with Ph denoting the pulse height. Fig. 6.10 shows the correlation between these two variables for the Demonstrator and XDEM detectors, respectively. For pure signals, the two quantities should be almost identical, but noise levels smear the linearity. Thus, a conservative threshold is set to reject outliers. Likewise, the NCA pulse range is also constrained.

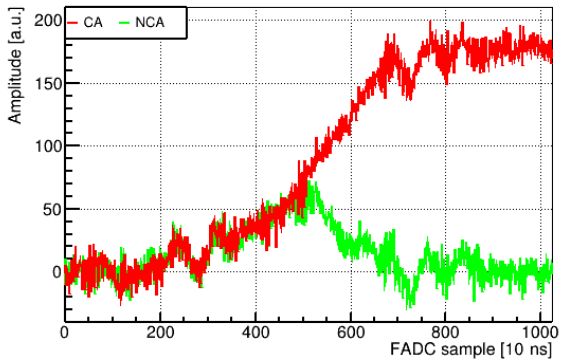

Figure 6.11.: Signal pulses exhibit flatter slopes than regular waveforms shown in Fig. 4.16. This event is discriminated by the low CA range criterion, the low Diff and high Diff selections.

As shown before in Fig. 3.3, the diverging point of the CA and NCA weighting potential is at $\varphi_{\mathrm{d}} = \frac{1}{2}$ for the small detectors and gets lower for the qCPG detector. Thus, the minimal NCA range has changed from a fraction of $\frac{1}{4}$ of the CA pulse range to $\frac{1}{6.67}$, half of the φ_{d}. An additional offset is included.

The third category compares the post-baseline RMS of the CA pulse with the pulse height. It also analyzes the maximal change of the difference pulse deduced from two samples with a 15-sample-wide gap in between. This category reduces noise or affected signal events dominant at low energies.

The following criterion, the low CA change, evaluates the maximum change of CA pulses. Apart from rejecting noise, this criterion also discards pulses typically with a rounding-off feature during the signal rise. Regular waveforms have a maximal rise time of about 1 µs. But the event shown in Fig. 6.11 takes much longer, which is probably related to the charge transport. These events degrade the detector's performance and are thus rejected.

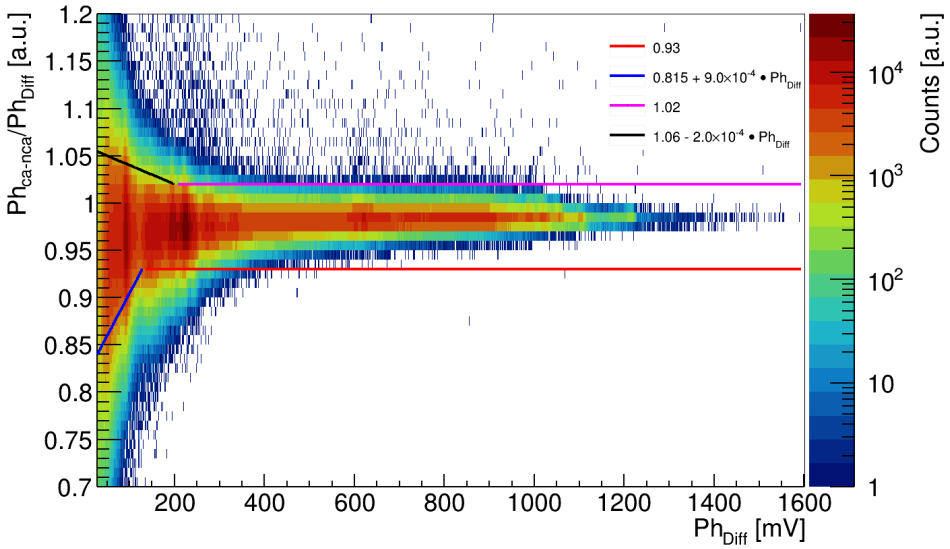

Figure 6.12.: The ratio of the CA and NCA pulse heights' subtraction, $\mathrm{Ph_{ca-nca}}$ to the difference pulse height, $\mathrm{Ph_{Diff}}$, versus the $\mathrm{Ph_{Diff}}$. The ^{228}Th calibration data taken with all detectors are analyzed. Outliers outside the four color-coded boundaries are rejected.

Furthermore, nonphysical events like the NCA recording waveforms similar to CA pulses are rejected. This is done by comparing the pulse height between the CA and the NCA. Note that mirror pulses are also categorized as nonphysical events by this selection.

The following two selections analyze the ratio of $\mathrm{Ph_{ca-nca}}$ to $\mathrm{Ph_{Diff}}$. This ratio should be one if the signal is clean and no filter is applied. However, due to the noise impact and the application of the moving average filter, the resulting values from the ^{228}Th calibration in Fig. 6.12 show that the distribution is not symmetrical at 1.0 but shifts to small ratios. At high energies, restrictions are within the range (0.93, 1.02) as established for the Demonstrator. The boundary condition of $(0.815{+}9.0{\times}10^{-4}{\cdot}\mathrm{Ph_{Diff}}, 1.06{-}2.0{\times}10^{-4}{\cdot}\mathrm{Ph_{Diff}})$ is slightly changed to limit the low energy events. The influence of the new value is compared with that of the old one, and a difference of 1% is minor. These two criteria flag most events with poor quality, and overlapping with other selections is expected.

As some selection criteria are sensitive to mirror pulses, the last two selections are thus

defined to distinguish the mirror pulses from the flagged events. However, identifying mirror pulses is easily affected by noise due to their low amplitudes. Hence, for a qCPG detector, excluding the primary sectors with an energy deposition, the rest sectors are seen as recording mirror pulses without additional selections.

All the criteria are tested with different datasets. Simulated pulses are also used to cross-check the cut validity. It turns out that pure signal pulses, without including hardware responses, are not flagged by these DCCs criteria, which implies that these selections can accurately characterize the signal shape.

6.3.2. Efficiency determination

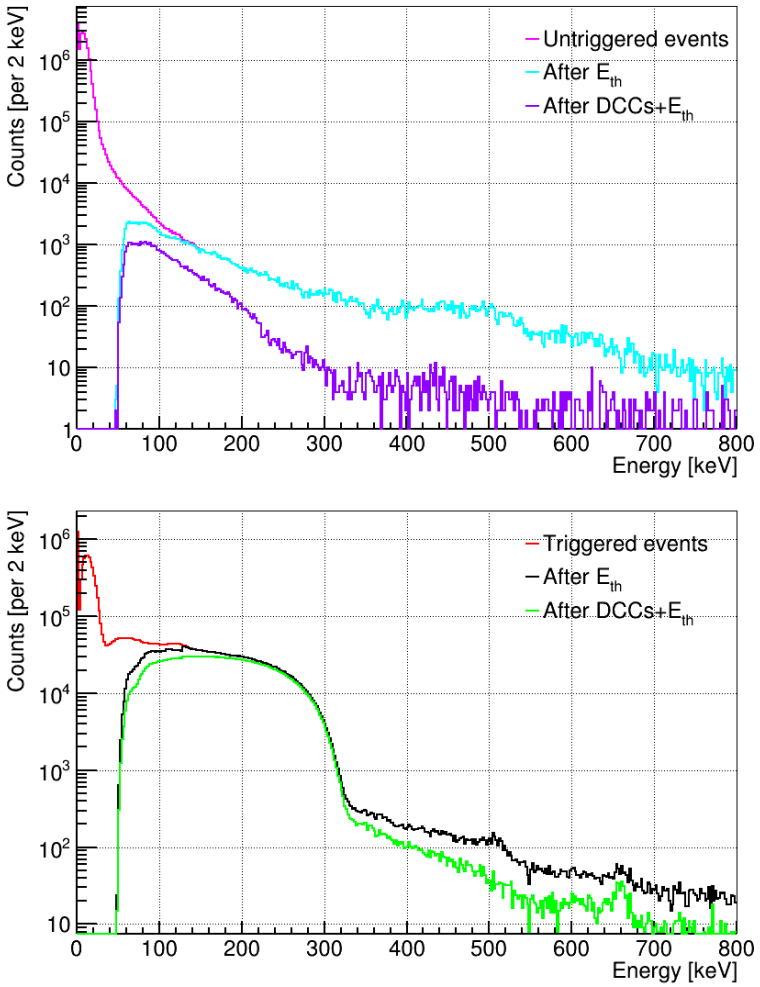

Figure 6.13.: Upper: Energy spectra for untriggered events before and after applying the threshold correction cut E_{th} (Section 4.6.5) and DCCs applied. Bottom: triggered events with E_{th} and DCCs. The non-unique single β-decay of ^{113}Cd dominates the spectrum.

It is essential to know the cut efficiency to quantify the surviving signals as well as the rejected background. This estimation is firstly done with the measured data. The trigger of a FADC is set to record pulses from all channels if one of the channels is triggered. The untriggered events, mostly noise and mirror pulses, are treated as random events that should be flagged by DCCs. These events help to determine the background rejection, the fraction of untriggered events discarded by the cut. On the other hand, the triggered events include mostly signals. But random events are also triggered sometimes.

Fig. 6.13 shows the spectra of untriggered and triggered events without and with the DCCs. Data runs with a threshold above 200 keV are discarded to reduce statistical fluctuations. The E_{th} and DCCs effectively reject random events dominant at low energies. In the energy range of 107 keV to 322.3 keV where the β-decay of ^{113}Cd lies, (99.99±0.22)% of the untriggered events are removed. The signal efficiency, the ratio of survived signal events to the total number of triggered events, is (84.53±0.06)% in the same energy range. However, this value is biased because some cut criteria are not effective in distinguishing signals from noise at low energies. As a result, the cuts are less sensitive to low energy signal events.

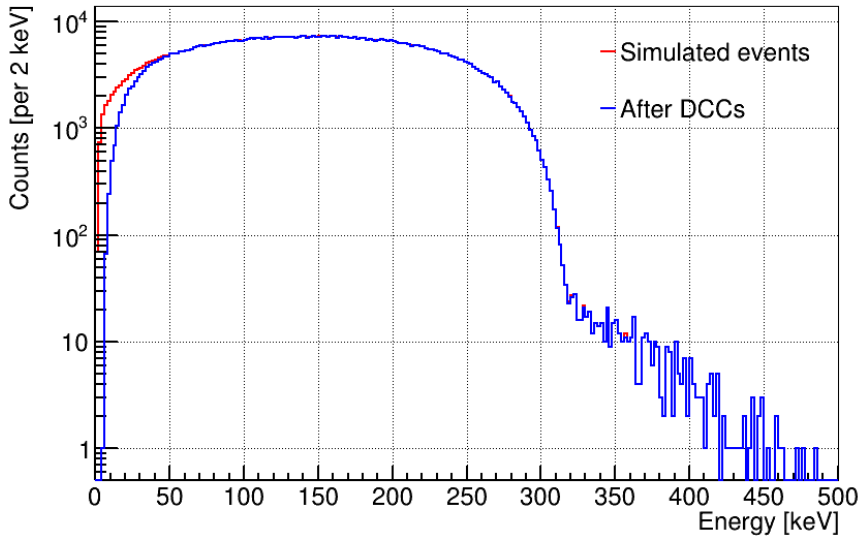

Figure 6.14.: Energy spectra for the simulated ^{113}Cd β-decay before and after applying the DCCs. Pulses are convolved with noise extracted from the pre-baseline of injected pulses recorded by all functional channels. Low energy events are reduced after applying the cut.

Depending on the operational conditions, noise events or signals with poor qualities can be recorded frequently. These events are all counted as signals for this estimation, which leads to an underestimated signal acceptance. This underestimation affects the measured decay rate of ^{113}Cd. Therefore, the signal efficiency is estimated via a simulation.

The simulated pulses are convolved with digital filters and electronic noise, as discussed in Section 4.4.4, to mimic the hardware response and the overall noise level. The electronic noise is extracted from injected pulses. Fig. 6.14 shows the simulated energy spectra for the

^{113}Cd β-decay. It can be seen that low energy events are suppressed by the cut, while higher energies are not affected. A signal efficiency of (99.99±0.51)% is obtained over an energy range of 107 keV to 322.3 keV.

Calibration data usually have a low count rate for random noise due to the relatively high radioactivity of calibration sources. Various γ peaks can help evaluate the cut efficiency at different energies and check the systematic uncertainty. A signal acceptance of (94.26±0.08)% is obtained from the γ peak of ^{152}Eu at the 344.3 keV. Fig. 6.15 shows the measured ^{228}Th energy spectra with events survived from and rejected by the DCCs. The signal acceptance at the low energy peak of 238.6 keV is (93.03±0.04)% lower than the value determined from the simulation. The difference of around 6% will be considered as the systematic uncertainty. The efficiency variation with the two mentioned γ lines indicates the energy dependence of the cut at low energies.

High energetic γ lines at 583.3 keV, 1592.5 keV and 2674.5 keV reach a signal acceptance of (99.0±0.04)%, (99.±0.10)%, (99.9±0.15)%, respectively, which are comparable with the efficiencies determined from the simulation. There is no significant variation among different channels.

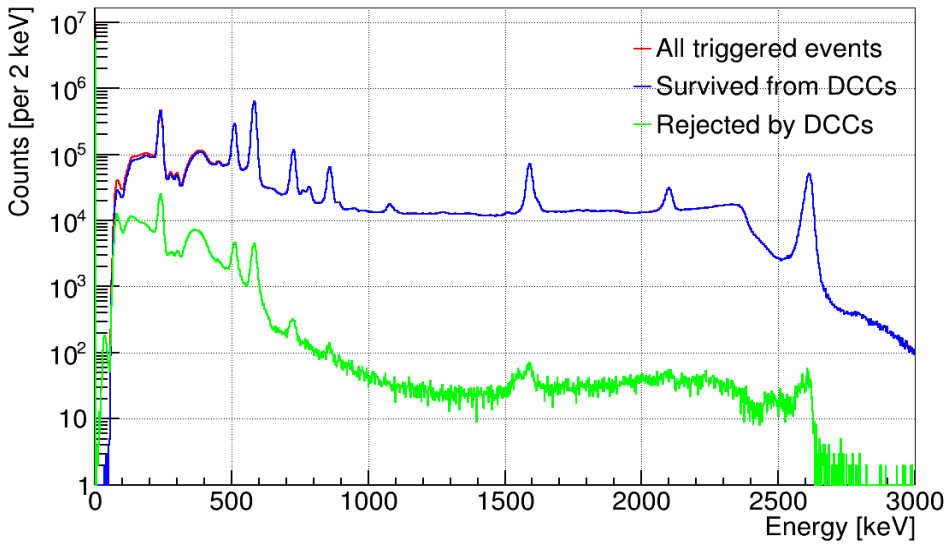

Figure 6.15.: The energy spectra for ^{228}Th before and after applying the DCCs.

6.4. Interaction depth cut

As known from the Demonstrator, the interaction depth is mainly used as a fiducial cut to remove contaminations on the electrode surface and the reconstruction artifacts near the anode originating from the CPG readout. Given the two detector types, the same criteria cannot be directly applied to the XDEM. Hence, the cut definitions are modified accordingly.

6.4.1. Cut definition

As discussed in Chapter 4, the interaction depth is reconstructed without including the guard ring (GR) signal and correcting the electron trapping effect. For developing a cut, the absence of the GR signal and trapping correction will be counted into the systematic uncertainty that can be quantified with simulated pulses.

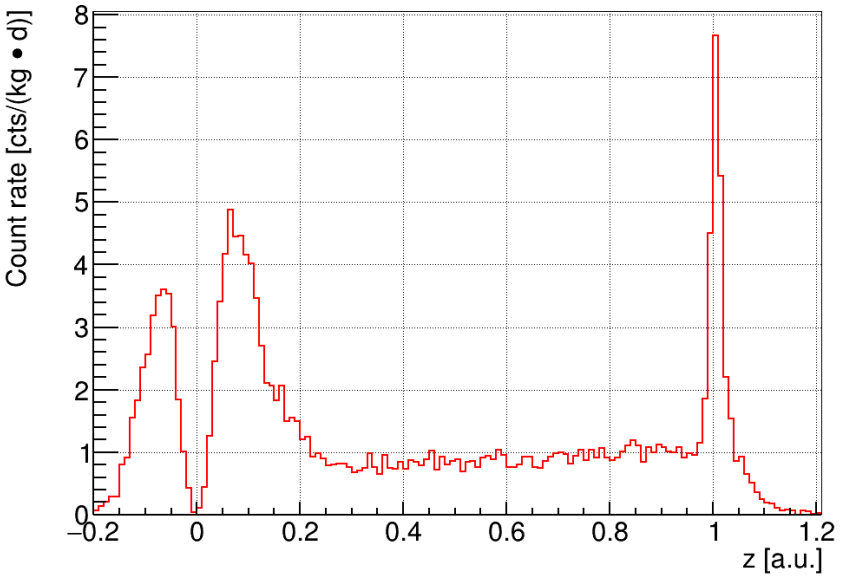

Figure 6.16.: Depth distribution of events above the ^{113}Cd β-decay. The DCCs are applied. A double peak distribution originating from the weighting potential distortions is found near the anode at $z = 0$, while near cathode contaminations are close to $z = 1$.

The depth cut is set in two regions, as seen in Fig. 6.16. For the high z region, α particles emitted from electrode contaminations and Radon decays are deposited on the detector surface as these particles cannot penetrate deep into the detector. The depth distribution of these events is modeled by a two-sided Gaussian function, as illustrated in Fig. 4.29. A mean value of 1.0056 and a standard deviation of 0.0081 are obtained from the fit. Events with a depth above the $\mu - 3\sigma$, as $z \geq 0.98$, are removed.

For the low z region, reconstruction artifacts, as a consequence of the inhomogeneity of the CA and NCA weighting potentials, limit the sensitive detector volume. One can see a double peak distribution near the anode in Fig. 6.16. Due to the neglected GR signal in the depth reconstruction, events from the same vertical position can end up with different z values. According to the φ_{CATH} distribution in Fig. 4.27, z will shift to higher values for events from the detector edges. Compared to small detectors, higher z regions will be affected by reconstruction artifacts.

Fig. 6.17 shows the relative FWHM of three γ peaks as a function of the depth. A thin depth layer with an interval of 0.06 is chosen except for the first layer with 0.15, as described for the depth-sensing in Section 4.6.2. Since the weighting potential inhomogeneity near the

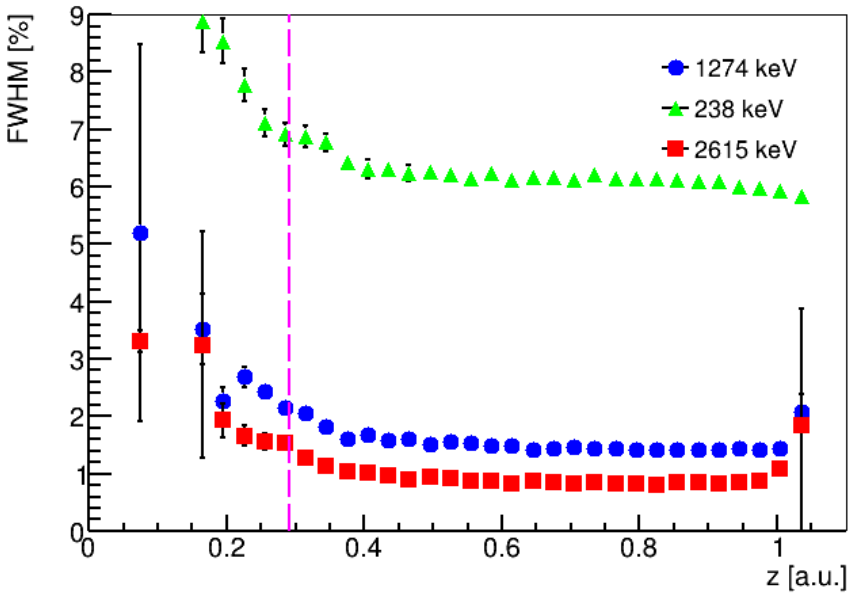

Figure 6.17.: Relative energy resolution as a function of the depth. Three γ lines at 1274 keV (^{22}Na), 238 keV (^{228}Th) and 2615 keV (^{228}Th) are shown. Data from all detectors are combined. The anode lies at $z = 0$, while the cathode is at $z = 1$. The magenta line indicates the depth cut at $z = 0.29$ near the anode.

anode is independent of the energy, the three curves show similar evolutions. In fact, a low energy tail is found near the anode, as displayed in Fig. A.10. The cut threshold at $z = 0.29$ is selected to reject the region with degraded performance.

6.4.2. Efficiency determination

While the z-cut removes mainly backgrounds, it also partially discards signals. Depending on the source and its position, the cut efficiency varies. The exact fraction of surviving signals will be needed when we set a half-life (or limit) on rare decays.

For $\beta\beta$-decay signals, the cut efficiency cannot be estimated experimentally. Instead, the homogeneously distributed ^{113}Cd β-decay in Fig. 4.13 is representative for approximating the efficiency of the $\beta\beta$-decay. It is noticed that the measured depth distribution for the ^{113}Cd β-decay shown in Fig. 6.18 is not constant but has fewer counts at low depths.

As discussed in Section 5.3, adjusting operating voltages causes fluctuations in the depth distribution. The dataset is thus partitioned into two sets, before and after the voltage adjustment, to test whether the fluctuation influences the cut efficiency. According to Table 6.2, the obtained values are rather comparable among different datasets and detectors.

The experimental result is compared to the efficiency calculated from a simulation. Table 6.3 lists the z-cut efficiency deduced from the simulated ^{113}Cd β-decay with different GR configurations. These values are calculated with clean pulses or MAnTiCORE. Clean pulses refer to simulated pulses without including any hardware effects. MAnTiCORE processes full

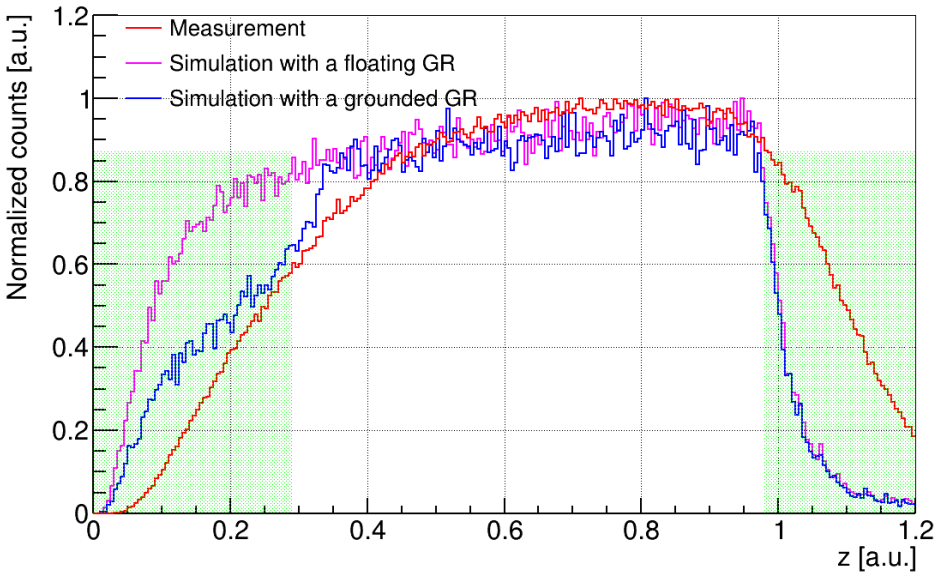

Figure 6.18.: Depth distribution of the ^{113}Cd β-decay events collected from the XDEM array (red line) and reconstructed from simulated pulses. The magenta line shows the depth with the floating GR in the simulation, and the blue line does not consider the GR signal. Events in the energy region of 107.5 keV to 340 keV are selected with the energy resolution taken into account. The shaded area indicates the cut values at $z > 0.29$ near the anodes and $z < 0.98$ close to the cathode. The dropping slope towards $z = 1.2$ in the measurement is presumably from electron trapping.

Table 6.2.: Deduced efficiency for the z-cut (0.29, 0.98) based on the measured ^{113}Cd β-decay taken from all the fully functional detectors at different operational periods (Section 5.6). Single detectors one and eight are also studied. The efficiency is defined by the ratio of the integral events in the selected area of Fig. 6.18 to the total number of events.

runs	detectors	efficiency [%]
first partition	all	78.44±0.74
second partition	all	78.86±0.78
combined	all	78.68±0.73
combined	1	78.83±1.35
combined	8	78.00±1.38

pulses convolved with digital filters and electronic noise. As can be seen, neglecting the GR signal overestimates the cut efficiency. This is because excluding the GR signal leads to a high z shift, as observed in Fig. 6.18. The depth distribution also agrees with that obtained from the data at low depths. At high depths, the measurement shows a slow drop near the cathode, probably caused by electron trapping.

Table 6.3.: The z-cut (0.29, 0.98) efficiency deduced from the ^{113}Cd β-decay simulated with the XDEM array. The detectors are assumed to employ the grounded GR or the floating GR. The data are collected with the grounded GR, but the GR signal is not used to reconstruct z. The statistical fluctuation is quoted as the uncertainty.

simulations	analysis methods	efficiency [%]
floating GR	clean pulses	70.85±0.25
grounded GR	clean pulses	69.54±0.25
grounded GR, no GR signal	clean pulses	78.61±0.26
floating GR	MAnTiCORE	73.60±0.26
grounded GR, no GR signal	MAnTiCORE	80.16±0.27

The systematic uncertainty is estimated from the efficiency variance between the simulation and the real data of the ^{113}Cd β-decay. It reaches 10% by including the GR signal in the simulation. Possible sources are the neglected GR signal, the actual distribution of ^{113}Cd atoms, as well as the convoluted hardware responses for simulated pulses. The electron trapping effect also contributes to the uncertainty. If the GR signal is excluded, the systematic uncertainty is reduced to 1.51%. The uncertainty associated with the geometry is studied by simulating either single detectors or the whole array, and no obvious deviation is seen. With the available pulse shape simulation framework, the cut efficiency for $\beta\beta$ signals can also be deduced. For more details, see Section 7.3.

6.5. Multi-site events identification

The previous analysis cuts reject nonphysical events and electrode α contaminations. γ photons are also known to be present in the setup and likely originate from the surrounding materials of the detector. Depending on the photon energy and the crystal size, high energetic γ photons can liberate electrons in two or more locations inside the detector via multiple Compton scattering or pair production, creating typical multi-site events. On the other hand, single-site events deposit all their energy in a single spot. The fraction of the multi-site event (MSE) is expected to increase for the XDEM detectors as multiple scattering is more likely to happen within a large volume.

According to simulations, $\beta\beta$-decays usually have the single-site event (SSE) character. The total energy carried by the two electrons is deposited in a single-site position. Hence, identifying MSEs helps to suppress the γ background and improve the background level.

6.5.1. Event signatures in CdZnTe detectors

The SSE and the MSE leave different signatures on pulses. A SSE produces a single charge cloud in the detector, which induces a current peak whose amplitude only depends on the deposited energy. Hence, SSEs have approximately the same shape as the left Fig. 6.19 shows. The current signal is obtained from the derivative of the charge pulse or the difference pulse

$$\mathrm{deriv}[i] = \sum_{j=i-n_{\mathrm{sm}}}^{i+n_{\mathrm{sm}}-1} \frac{\mathrm{Diff}[j-n_{\mathrm{sm}}] - \mathrm{Diff}[j+n_{\mathrm{sm}}]}{2 \cdot n_{\mathrm{sm}}}. \tag{6.4}$$

j and i are the sample number of pulses. High-level noise can lead to unreliable results. A smoothing window is thus applied to reduce noise interference. The optimization of the window size n_{sm} will be discussed in Section 6.5.3.

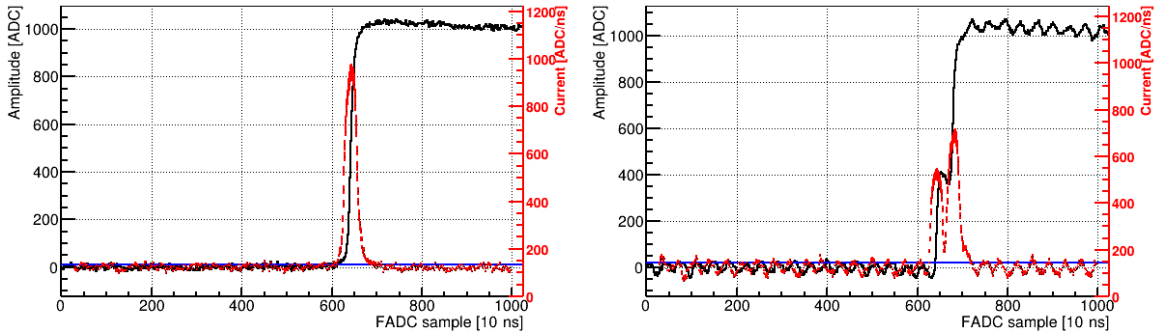

Figure 6.19.: Charge and current pulses formed by a SSE (left) and a MSE (right) in one qCPG detector. The two events are from the 2615 keV γ-line of ^{208}Tl. The charge pulses are in black solid lines. A current estimator performs derivative calculations on charge pulses with a smoothing window of 14. The current pulses are indicated by red dashed lines. Blue lines are the RMS of the current pulse's baseline.

When an event's energy is deposited at multiple locations, at least two charge clouds are created. If the arrival time of the charge clouds at the anode differs, the sum of the waveforms induced by individual clouds will result in a step-like shape on the rise structure of the difference pulse, as shown on the right Fig. 6.19. The current signal exhibits more than one peak and has a suppressed maximum amplitude.

Based on these signatures, a MSE cut is developed to discriminate the SSEs from MSEs. In order to evaluate how effective the cut is, two key parameters will be considered: the signal efficiency and the background rejection. A library of pure signal and background events is thus required to determine the two quantities.

Based on the mechanism of energetic γ-rays interacting with detectors via pair production, two 511 keV photons are produced by positron-electron annihilation. If both photons escape the detector, one interaction position is left in the detector, creating a double escape peak (DEP). A single escape peak (SEP) is characterized by one escaped 511 keV photon, resulting in two interaction locations and having a double-site event. The DEP of the 2615 keV γ-line

from ^{208}Tl predominantly constitutes SSEs at 2103 keV and is used as the repository for signal events. In contrast, events within the SEP at 1593 keV are dominantly MSEs.

Fig. 6.20 shows the selected peaks, each defined as $E_\gamma \pm \mathrm{FWHM}(E_\gamma)$, along with two sidebands (SBs) placed symmetrically around the peak with an energy shift of 30 keV. The SBs are used to control the underlying Compton background. The number of entries within the peak is expressed as

$$N_{\mathrm{peak}} = N_{\mathrm{ROI}} - N_{\mathrm{SB}}. \tag{6.5}$$

N_{ROI} is the total events in the ROI, and N_{SB} denotes the entry number in the SBs.

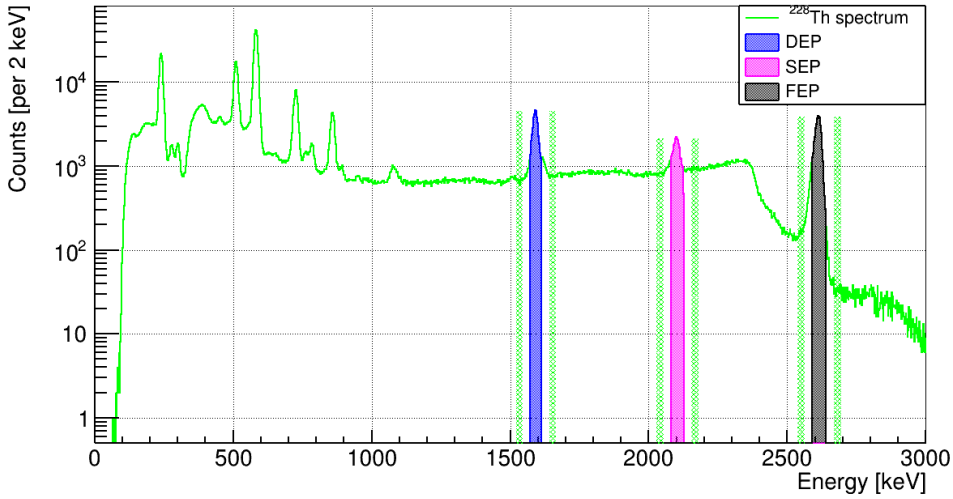

Figure 6.20.: Energy spectrum for the ^{228}Th measured with one detector at the LNGS. The data cleaning cuts (see Section 6.3) and z-cut (see Section 6.4) are applied. The ROIs shown in different colors highlight the double escape peak (DEP) at 1593 keV, single escape peak (SEP) at 2103 keV and full energy peak (FEP) at 2615 keV from ^{208}Tl γ-line. The sidebands (SBs) indicated in green are 30 keV away from the ROI.

The signal acceptance, $\varepsilon_{\mathrm{sig}}^{\mathrm{acc}}$, is then calculated by the survival efficiency of DEP events, while the background rejection, $\varepsilon_{\mathrm{bg}}^{\mathrm{rej}}$, is determined by the fraction of rejected events in the SEP, which are formulated as

$$\varepsilon_{\mathrm{sig}}^{\mathrm{acc}} = \frac{N_{\mathrm{DEP,sig}}}{N_{\mathrm{DEP,ref}}}, \quad \varepsilon_{\mathrm{bg}}^{\mathrm{rej}} = \frac{N_{\mathrm{SEP,bg}}}{N_{\mathrm{SEP,ref}}}, \tag{6.6}$$

where $N_{\mathrm{DEP,sig}}$ is the remaining events after the MSE cut, and $N_{\mathrm{SEP,bg}}$ is the number of rejected events. The reference spectrum contains all the events without applying the cut. An optimal cut should keep the most DEP events and discard as many SEP events as possible. The following sections discuss algorithms used for the XDEM.

6.5.2. *AvsE* cut

The so-called *AvsE* cut was first developed for HPGe detectors [123]. The parameter *AvsE* compares the maximum amplitude of the current pulse (A) to the energy deposition (E). The energy dependence of A is taken into account, which is assumed to be a second-order polynomial. The *AvsE* is thus expressed as

$$AvsE = -1(A \cdot E/E_{\mathrm{unc}} - p_0 - p_1 \cdot E - p_2 \cdot E^2)/j, \tag{6.7}$$

where E and E_{unc} are the calibrated and uncalibrated energy, respectively. A is multiplied by the gain shift E/E_{unc} to be consistent with the calibrated E. p_0, p_1, and p_2 are the parameters describing the energy dependence. j sets the cut value.

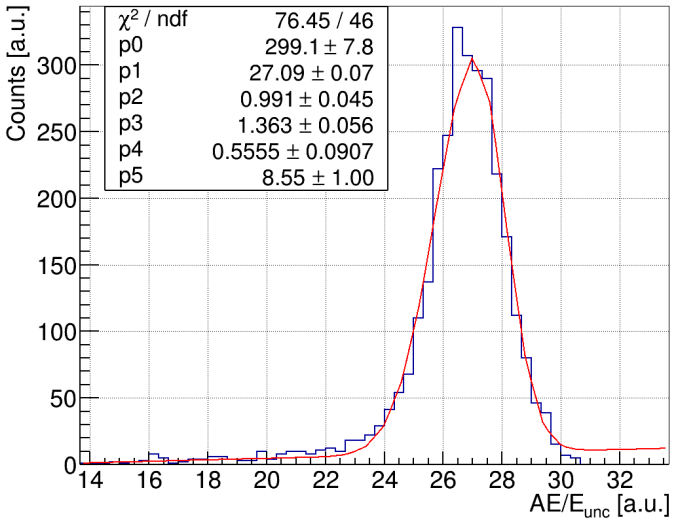

Figure 6.21.: Fitting the maximum current amplitude (AE/E_{unc}) with a two-sided Gaussian function given in Eq. 3.7. $p0$ gives the maximal amplitude. $p1$ is the mean value of the Gaussian peak. $p2$ and $p3$ represent the standard deviation on the left and right sides. $p4$ and $p5$ accounts for the underlying background.

All the parameters in Eq. 6.7 are determined to adapt the approach to the CZT detectors. Firstly, events from 22 distinct regions of the Compton continuum from the ^{228}Th calibration are selected, ranging from 200 keV to 2300 keV. These regions contain dominantly SSEs but mixed with MSEs. Each energy band has a width of 25 keV to ensure enough statistics. The AE/E_{unc} distribution is obtained for each region and fitted with a two-sided Gaussian function. One example is shown in Fig. 6.21.

Fig. 6.22 shows a second-order polynomial function modeling the curve of AE/E_{unc} versus E. A negative quadratic term quantifies the nonlinear energy dependence of the corrected maximum amplitude of current pulses (AE/E_{unc}). The nonlinearity is associated with spatial energy deposition. For example, high energetic βs have a long range and create a wide charge cloud distribution. Space charge effects and electronic responses also contribute to the nonlinearity.

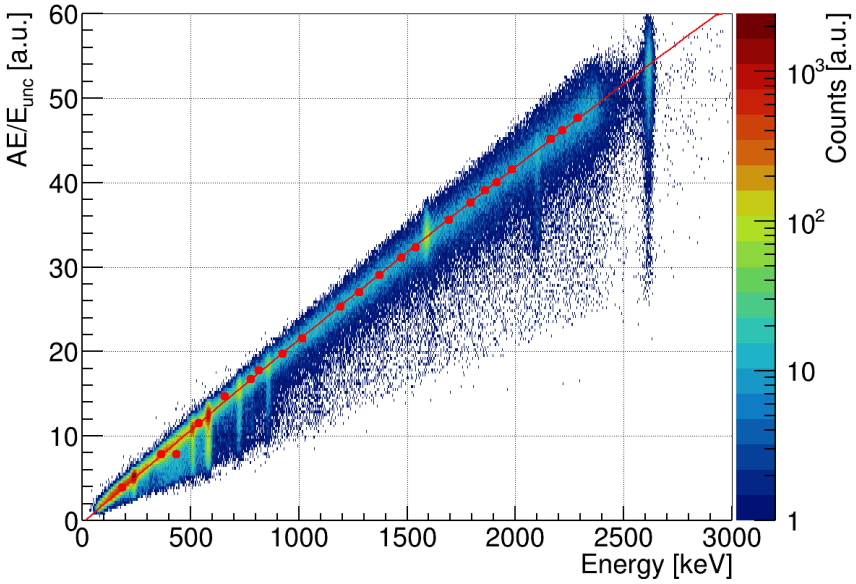

Figure 6.22.: Distribution of the maximum current amplitude (AE/E_{unc}) shown in red dots versus energy (E) for one detector. Each red dot is the mean value of the fitting function, like an example displayed in Fig. 6.21. The red line is the quadratic polynomial fit with AE/E_{unc} = -6.0×10^{-2} + 2.20×10^{-2} · E − 2.13×10^{-7} · E^2.

The distribution of the *AvsE* versus energy in Fig. 6.23 shows that the *AvsE* shifts to lower values at the full energy γ peak due to the increased fraction of multiple scattering. In comparison, the distribution in the Compton continuum is rather flat. Also, events within the DEP at 1593 keV have larger *AvsE* than the SEP events at 2103 keV. The cut value j is adjusted so that the signal acceptance for the DEP reaches 90% at $AvsE > -1$.

The cut may perform differently with two definitions of charge pulses. One definition is the Diff, obtained from the subtraction of the CA and NCA pulses, as $Q_{\mathrm{DIFF}} = Q_{\mathrm{CA}} - Q_{\mathrm{NCA}}$. The other is ADiff with the weighting factor included, as $Q_{\mathrm{ADIFF}} = Q_{\mathrm{CA}} - \omega \cdot Q_{\mathrm{NCA}}$. Fig. 6.24 shows the cut efficiency for each sector obtained from the charge pulses in two definitions. Due to the statistical uncertainty, the signal acceptance slightly deviates from 90%. As opposed to nearly constant signal acceptance, the background rejection varies with the sector. This is because different physical characteristics of sectors and their electronics lead to variations in the charge trapping or rise time and impact the current amplitude distribution. The cut value is tuned for each sector to produce the uniform DEP survival efficiency, which inevitably results in the nonuniform background rejection efficiency.

It can be seen that using the Diff pulse shows slightly better background rejection than the ADiff. Note that the cut is inefficient for several sectors, leading to background rejections much below the average. After removing these sectors, $\varepsilon_{\mathrm{sig}}^{\mathrm{acc}}$ is averaged to be (90.24 ± 0.22)%, while $\varepsilon_{\mathrm{bg}}^{\mathrm{rej}}$ reaches (66.28 ± 0.31)%. The wavelet-based denoised dataset (Section 6.2) produces comparable efficiencies.

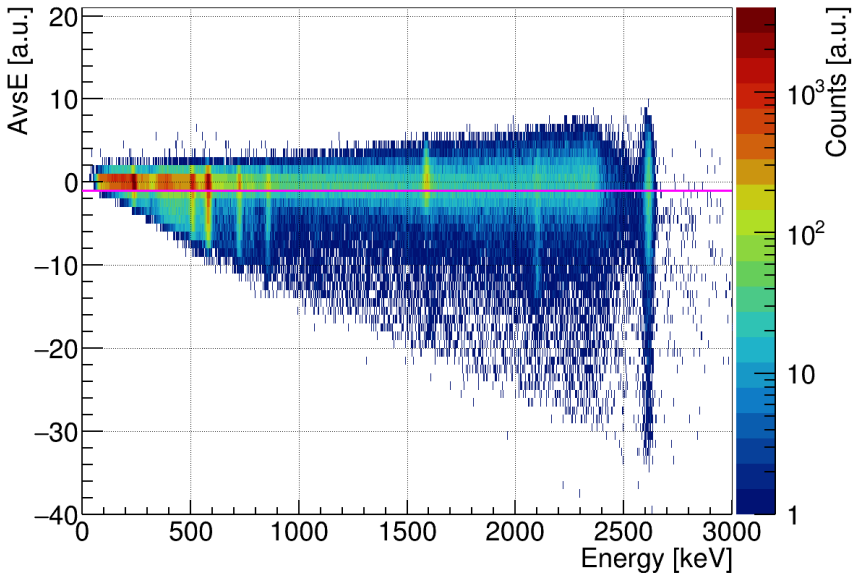

Figure 6.23.: *AvsE* versus energy with the cut discarding events below the magenta line with *AvsE* = -1.

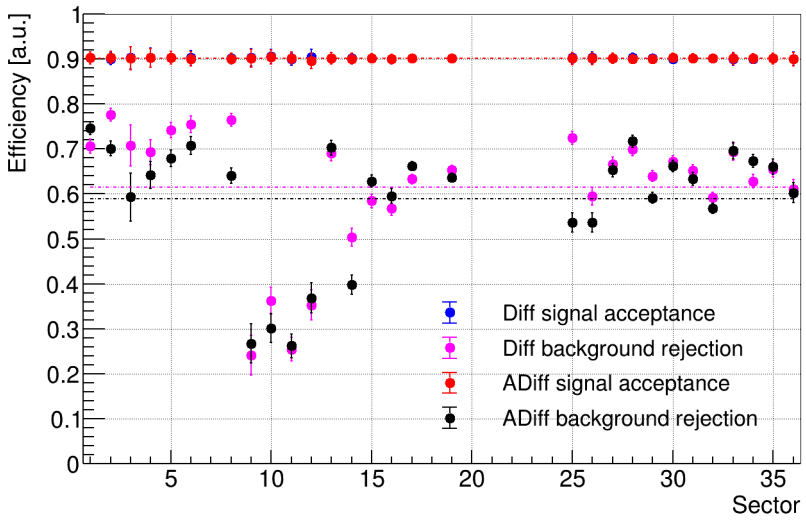

Figure 6.24.: The *AvsE* cut performance. The signal acceptance of the DEP of 2615 keV γ-line is fixed to 90%, with blue dots for Diff and red dots for ADiff overlapped with each other. The dashed lines indicate the efficiency averaged over all functional sectors. The magenta and black dots represent the background rejection of the SEP for Diff and ADiff, which varies significantly with sectors. An average background rejection efficiency reaches around 60%. The cut is inefficient for sectors 9, 10, 11, 12 and 14.

6.5.3. A/E cut

The so-called A/E cut is similar to the $AvsE$ cut. It characterizes MSEs by the ratio of the maximum amplitude of the current pulse (A) to the height of the charge pulse (E) like the name stated [124]. Unlike the $AvsE$ cut, E is not calibrated here. A previous work adapted the cut to the Demonstrator data [125]. This section will reevaluate the cut for the XDEM.

Based on the cut definition, an event with a low A/E is identified as a MSE. An optimal cut value should ensure a high signal acceptance and background rejection. Fig. 6.25 shows the cut efficiency as a function of A/E for one sector. The resulting A/E values at 90% of signal acceptance, $(A/E)_{90\%}$, together with the maximal product of $\varepsilon_{\text{sig}}^{\text{acc}} \cdot \varepsilon_{\text{bg}}^{\text{rej}}$ are close. A fixed signal acceptance simplifies the efficiency calculation. Therefore, the A/E at 90% of signal acceptance will be the cut value.

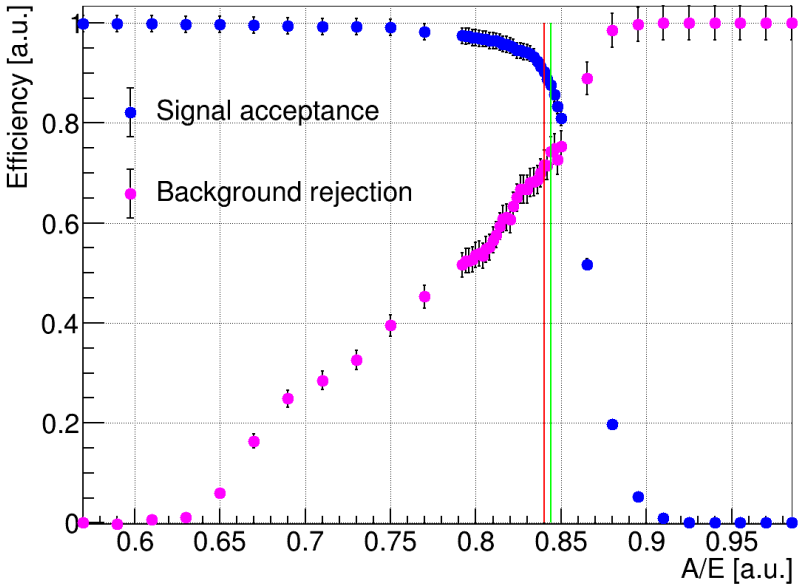

Figure 6.25.: A/E optimization based on the efficiencies deduced from the DEP and SEP events. The red vertical line denotes $(A/E)_{90\%} = 0.84$ with $\varepsilon_{\text{sig}}^{\text{acc}}$ at 90%. The green line represents $(A/E)_{\text{opt}}$ lying at 0.8442 when the product of $\varepsilon_{\text{sig}}^{\text{acc}}$ (0.8764) $\cdot$ $\varepsilon_{\text{bg}}^{\text{rej}}$ (0.7424) reaches a maximum.

As used for the $AvsE$, a smoothing window is also applied here to reduce noise disturbances. According to Figure 6.26, the background rejection reaches the maximum at a window size of 12, with the signal acceptance fixed at 90%. As pointed out in Ref. [125], the A/E distribution for the DEP events can be modeled by a two-sided Gaussian function. However, with a window size of 12, two sectors still show an abnormal A/E distribution. This abnormality is corrected by setting the final window size to 14.

Apart from the smoothing window, the noise interferences on the cut accuracy are checked with denoised datasets produced in Section 6.1 and 6.2. It turns out that the DEP and SEP

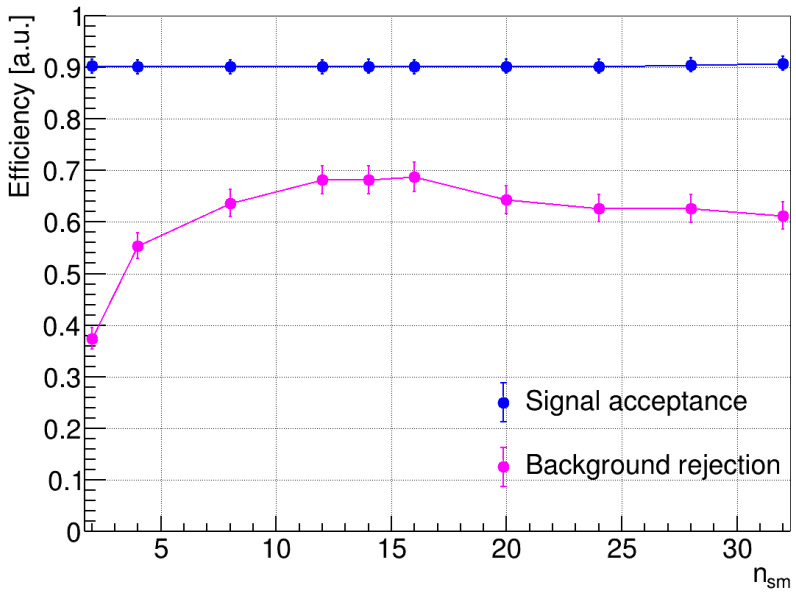

Figure 6.26.: The cut efficiency versus the smoothing window size (n_{sm}) for single sectors. The signal acceptance is tuned to 90%. An optimal window size of 14 is chosen.

events of 2615 keV γ-rays are not distinct in the A/E distribution for the FFT-based denoised data, which implies that the MSE features are likely smoothed out by the filter. As for the wavelet denoised data, the cut efficiency is comparable with the value shown above.

Similar to the $AvsE$ cut, the A/E distribution of individual sectors also varies in position and width. Defining a cut for every sector at each run is a tedious process. Thus, A/E calibration is performed to accommodate the differences as well as to develop a global cut. For this purpose, an arbitrary Gaussian function is defined as a reference, for instance, with a mean value of $\mu = 1.0$ and a standard deviation of $\sigma = 0.1$. After calibration, the A/E of different sectors will display the same distribution as the reference based on [125],

$$(A/E)_{\text{cal}} = \frac{\sigma}{\sigma_{A/E}}((A/E) - \mu_{A/E}) + \mu, \tag{6.8}$$

The calibration parameters, including the mean $\mu_{A/E}$ and the standard deviation $\sigma_{A/E}$, are extracted from the fit with the A/E distribution of DEP events.

The optimal $(A/E)_{90\%}$ determined for all the functional sectors are shown in Fig. 6.27. After the calibration, the distribution is more compact and shows a Gaussian fluctuation. Below the average $(A/E)_{90\%}$ of 0.863, events are recognized as MSEs and will be discarded for $\beta\beta$ searches. A signal acceptance of 90% with a background rejection of 65% is achieved.

Fig. 6.28 shows the energy spectra for ^{228}Th applied with the $AvsE$ and the A/E separately, besides the data cleaning cuts and z-cut. As can be seen, the two cuts perform similarly at high energies, strongly suppressing the SEP events while keeping most of the DEP events. The difference is prominent at low energies, however. The $AvsE$ cut is more accurate because

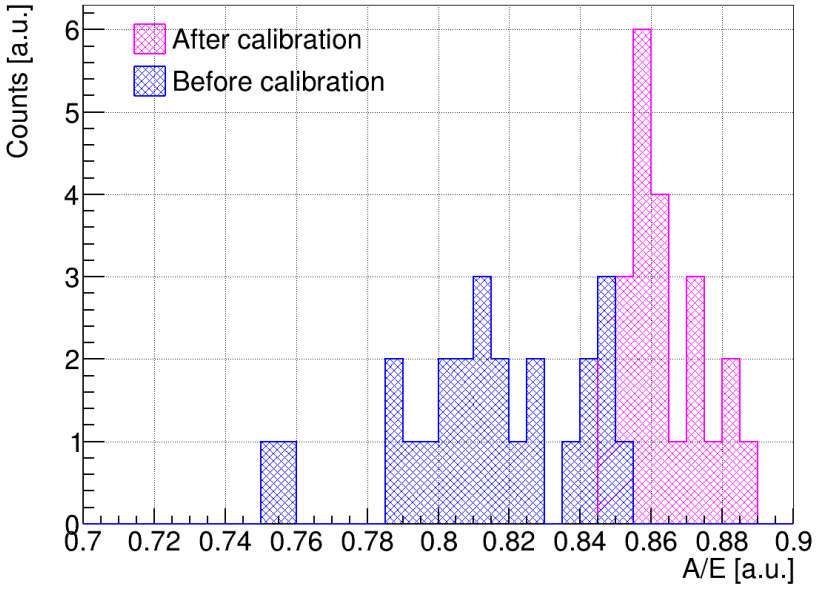

Figure 6.27.: Distribution of the A/E at 90% of the signal acceptance for all functional sectors before and after the calibration. It is wider before the calibration.

it is independent of energy. On the other hand, the uncorrected energy dependence of the A/E cut leads to a widened A/E distribution and degrades the cut performance. Nevertheless, a constant cut performance can be ensured in the ROI of the ^{116}Cd $\beta\beta$-decay. Since implementing $AvsE$ into MAnTiCORE would require four inputs, while the A/E only needs two, the A/E cut is used for the XDEM.

Finally, simulated pulses are used to verify the A/E cut and estimate the systematic difference. As shown in Fig. 6.29, the DEP and SEP entries are distinguishable from the A/E like data. With a cut value of μ-1.282σ, a signal acceptance of 90.74% and a background rejection of 78.42% are achieved. The μ and σ are obtained from the two-sided Gaussian function fit. The A/E cut performance evaluated with the simulation agrees with that of the real data. The difference in the background rejection between data and simulation is around 10% and can be treated as a systematic uncertainty.

6.6. Coincident events

The A/E cut discards MSEs in the sensitive volume of single sectors. What if an event deposits its energy in more than one sector? In this case, the detector granularity allows us to identify a multi-sector event. A multiplicity cut is developed based on this. A single-sector event has a multiplicity of one, and the multiplicity is two if an event is registered in two sectors. Like MSEs, most multi-sector events are caused by multiple scattering of γ-rays. According to a Monte Carlo simulation, the cut can remove around 4.7% of the $2\nu\beta\beta$-decay events of ^{116}Cd.

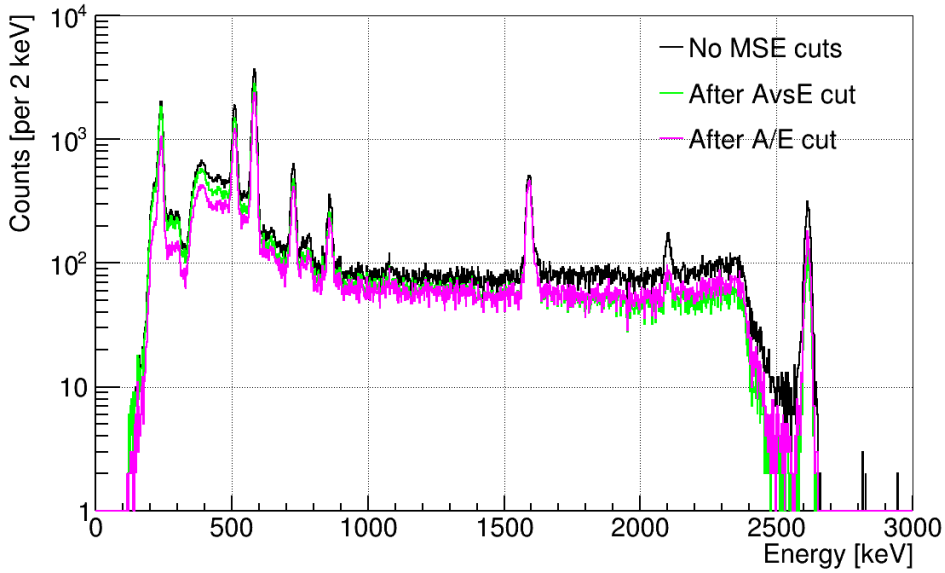

Figure 6.28.: Comparison of the $AvsE$ and A/E cuts applied to the ^{228}Th decay events in addition to the data cleaning cuts and z-cut.

However, the multiplicity cut can only be applied to single detectors. If a γ photon leaves partial energy inside a detector and the scattered photon deposits the remaining energy in neighboring detectors, at least two or more CZT crystals will measure energy depositions simultaneously. In order to distinguish events with more than one detector hit, a coincidence analysis can be performed.

6.6.1. Data synchronization

For the coincidence analysis, reliable time information that ensures events are recorded in the correct time order is necessary to identify coincident events. In reality, the internal clock for each FADC has its own speed. The difference can cause a time shift for the two simultaneous hits registered in different FADCs. To synchronize all the readout channels, an external master clock was installed. Unfortunately, it is not compatible with the data analysis software at the moment. Alternatively, artificial pulses injected into the DAQ system provide a reference time and allow for high-precision data synchronization. The synchronizing tool developed for the Demonstrator is used here [126].

The speed variations and the time delays of internal clocks in the FADCs are adjusted by regularly injected pulses. It is found that the time drift of FADCs shows complex patterns and has to be simplified to be linear. In this way, the offset and slope of each FADC are corrected according to a global time and speed. The time accuracy of this synchronization is 0.1 ms. After eliminating the time drift, it is possible to identify multi-detector hits.

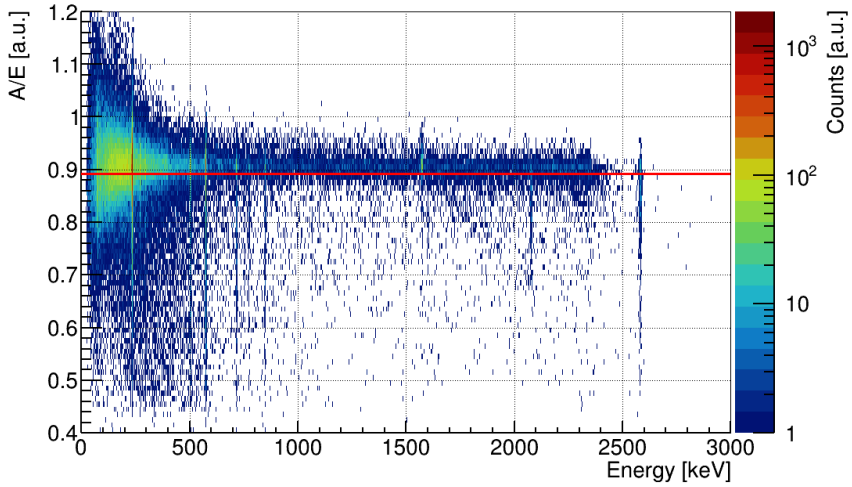

Figure 6.29.: A/E versus energy deposition for the simulated ^{228}Th calibration. The z-cut is applied. Hardware responses are convolved, including noise extracted from injected pulses. The cut value at 0.8925 is indicated in the red line.

6.6.2. Coincidence analysis

A small time window is specified to select coincident events in the synchronized dataset. If the time difference between the two neighboring events is smaller than the time window of 2 ms, the two events are coincident. Fig. 6.30 shows the energy spectra of synchronized data with an exposure of 0.13 kg·yr. Only events above the sector's energy threshold are taken into account. Besides, nonphysical events are also discarded. The coincidence cut is applied to veto multi-sector as well as multi-crystal events. One can see that the reduction of the prominent γ lines at 662 keV from the ^{137}Cs decay, and 1461 keV from the decay of ^{40}K is not obvious. This is because the total number of coincident events is limited.

It turns out that the coincidence analysis is not that powerful in rejecting γ backgrounds as the MSE cut but at the expense of losing the data exposure. Therefore, only the multiplicity cut and the A/E cut will be applied. Nevertheless, data synchronization with all functional detectors included will allow us to study coincidences and distinguish multiple-site energy depositions at full potential. This capability is essential to search for the double beta decay into excited states, as the decay is accompanied by the emission of characteristic γ-lines. For more details, see Section 7.4.

6.7. Drift time and mobility determination

The last section of the pulse shape analyses investigates the drift time and the electron mobility. These are intrinsic parameters reflecting charge transport properties and can help to cross-check detector characterizations. The two quantities are also closely related to the work discussed previously regarding the weighting factor determination (Section 4.6.3), the pulse shape simulations (Section 4.4), and the depth reconstruction (Section 4.7).

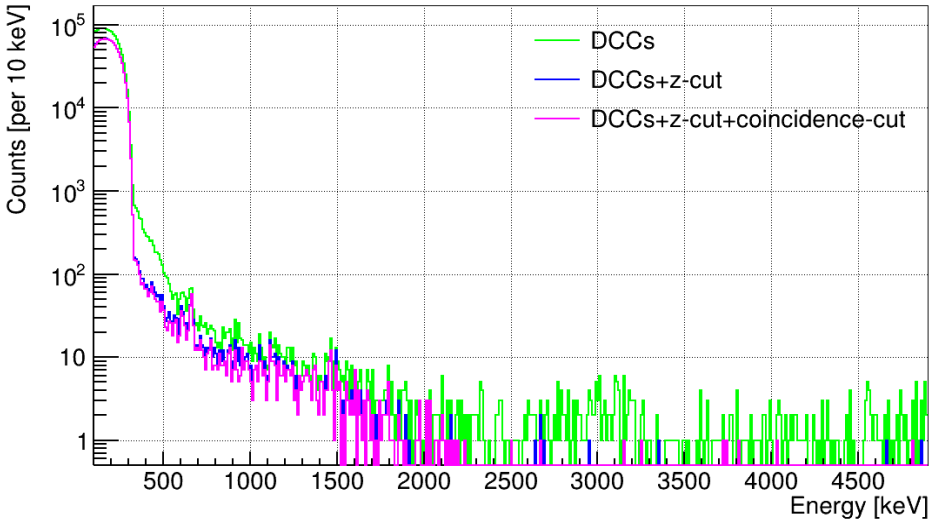

Figure 6.30.: The energy spectra measured at the LNGS applied with the data cleaning cuts and z-cut, and a coincidence cut. With the coincidence cut, if two signals occur within a time window of 2 ms, the events will not be filled into the histogram.

6.7.1. Drift time evaluation

The rising slope of raw pulses carries time information of the charge clouds. Previously, the drift time was determined by measuring the common electron drift towards the two anodes, starting from the end of the pre-baseline till the maximum of the NCA pulse [41, 89]. However, the NCA pulse is easily affected by noise due to its low amplitude, especially at the maximum. The CA pulse is less influenced by noise as one can always average its nearly constant tail. But the CA pulse contains slow-rising components from moving holes or detrapped electrons that degrade the time resolution [127, 128].

Besides anode pulses, the cathode pulse is also sensitive to the charge carriers' drift [128, 129]. However, the strong impact of noise from the sum of all anode pulses deteriorates the time resolution. Instead, the denoised cathode pulse is used, as illustrated in Fig. 6.31. To further reduce the effects of noise, only the percentage of the pulse height from 20% to 80% is used to extract the time difference that is then extrapolated to the full drift time. For low energy events, the precision of the exact fraction is low and worsens the time accuracy. Nevertheless, the reconstructed cathode pulse is a good option for estimating the drift time compared to the CA pulse, as shown in Fig. A.12.

The maximal drift time is how long it takes electrons to travel from the cathode to the anode, and it can be determined by analyzing near cathode events. The rise time distribution of these events taken from a ^{22}Na calibration is nearly symmetrical, as demonstrated in Fig. 6.32. A Gaussian fit is thus performed. The centroid is extrapolated to be around 1 µs, comparable to the maximal drift time of small detectors in the range of 0.86 µs to 1.03 µs [129]. However, it is expected that the value slightly deviates from the actual time. One reason for this is the absent GR signal affecting the cathode pulses and causing uncertainties to the rise time for

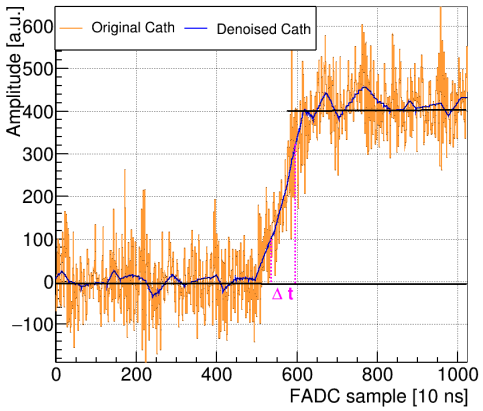

Figure 6.31.: Determining the drift time of one event from its denoised cathode pulse. The black lines are the pre and post-baseline, respectively. The subtraction of the two quantities represents the pulse height. The magenta dashed lines, ranging from 20% to 80% of the pulse height, are used to estimate their time difference Δt.

events close to the GR.

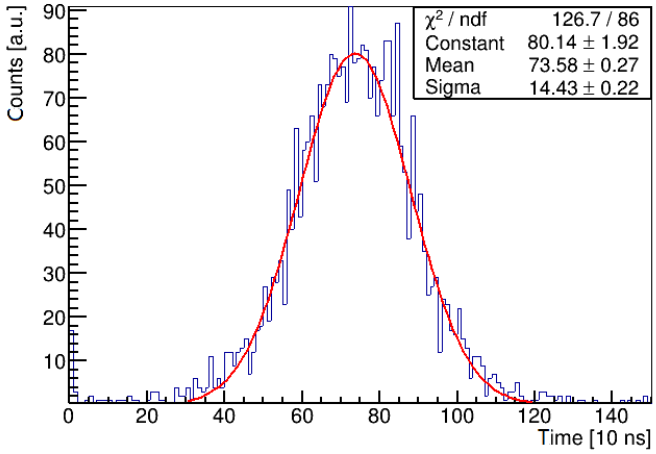

Figure 6.32.: The mean value obtained from a Gaussian fit will be extrapolated, which corresponds to the maximal drift time for events originating near the cathode.

As the CZT detector has a relatively broad time range for the signal rise, the interplay between the charge collection time in a detector and the time constant of an amplifier may cause the so-called ballistic deficit[1], leading to a pulse amplitude loss and an energy resolution deterioration [130–134]. However, given the maximal rise time and the decay time constant of

[1]The ballistic deficit is a difference in pulse height caused by electronics' shaping time constant. In principle, the longer the signal rise time is, the more serious it can be. A small CR time constant also causes a grown ballistic deficit.

the preamplifier of 140 µs, the amplitude deficit is negligible according to the peak attenuation law described in Ref. [128]. Details are referred to Appendix A.7.

6.7.2. Mobility estimation

The signal's drift time in the CZT detector depends on the electrons' velocity. When charge carriers move through the crystal driven by the electric field, the electrons' moving speed gained from the electric field may be reduced by electrons colliding with lattice atoms. Eventually, the velocity saturates under a high electric field as $v = \mu_e E$. The electron mobility μ_e depends on the electric field, material qualities, temperature as well as electron-hole concentrations. It is possible to estimate μ_e directly from a measurement. For this, the mobility-lifetime product $\mu_e\tau_e$ associated with charge transport properties is measured and compared with theoretical calculations.

The direct measurement for $\mu_e\tau_e$ is related to a photopeak shift observed from events near the cathode and the anode [135]. The expression is formulated as

$$\mu_e\tau_e = \frac{L^2}{V_{\text{bulk}}\ln(N_c/N_a)}, \tag{6.9}$$

where L is the detector thickness, V_{bulk} is the applied voltage between the anode and the cathode, $V_{\text{BV}} - \frac{1}{2}V_{\text{GB}}$. In this work, N_c and N_a are the photopeak centroid at the 1274 keV of ^{22}Na obtained from the cathode and anode, respectively.

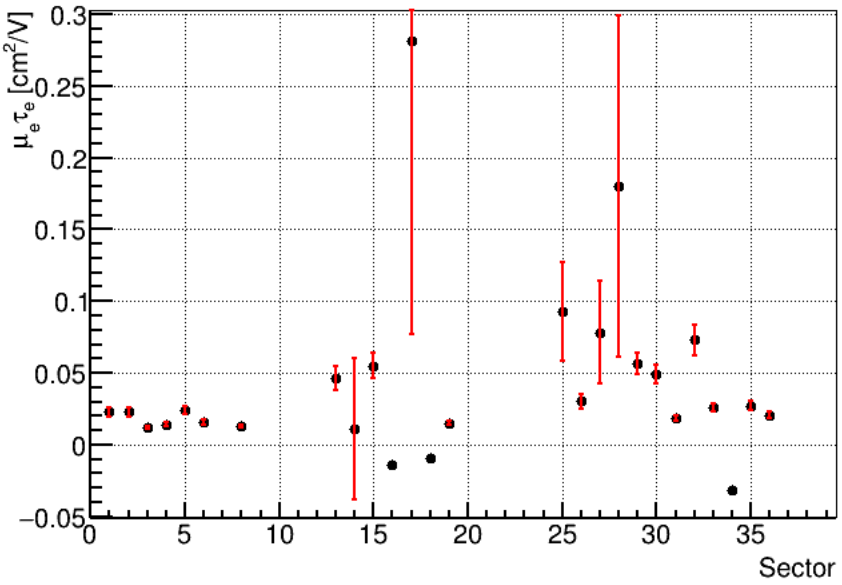

Figure 6.33.: The electron mobility-lifetime product $\mu_e\tau_e$ determined from one ^{22}Na calibration run for each sector. Error bars are shown in the red line.

Events originating from the anodes are affected by reconstruction artifacts and are excluded. L and V_{bulk} are corrected accordingly. As trapping occurs across the entire detector volume,

the electron loss might be underestimated. The uncertainty from the detector thickness, voltage fluctuations, and the measured photopeak centroid is estimated by applying error propagations to Eq. 6.9.

Fig. 6.33 shows $\mu_e\tau_e$ deduced from one ^{22}Na calibration taken at the LNGS. The majority of values fall between 1×10^{-2} and 9×10^{-2}, which is in good agreement with previous measurements in which different methods were used [107, 136]. However, a negative $\mu_e\tau_e$ is observed in three sectors. These sectors all have a weighting factor larger than one, such as the example seen in Fig. A.5. Possible explanations are related to material qualities, weighting potential distribution, and repopulating electrons [137].

Alternatively, $\mu_e\tau_e$ can also be determined from the mean trapping length λ. The expression is described as [63]

$$\mu_e\tau_e = \frac{L^2\lambda}{V_{\text{bulk}}}, \tag{6.10}$$

where λ is estimated empirically from the weighting factor ω via $\lambda = \frac{1+\omega}{1-\omega}$. So, μ_e is

$$\mu_e = \frac{L^2}{\tau_{\text{max}} \cdot V_{\text{bulk}}}. \tag{6.11}$$

τ_{max} is the maximal drift time discussed in the previous section.

Table 6.4.: Results of $\mu_e\tau_e$, λ_ω, λ_{m}, τ_{max} and μ_e for each sector based on ^{22}Na calibrations. λ_ω is deduced from the weighting factor, and λ_{m} is calculated via Eq. 6.9. μ_e is derived from Eq. 6.11. Detector one from eV Products and detector eight from Redlen are shown.

Det.	BV [V]	$\mu_e\tau_e$ [10^{-2} $\frac{\text{cm}^2}{\text{V}}$]	λ_ω [cm]	λ_{m} [cm]	τ_{max} [µs]	μ_e [$\frac{\text{cm}^2}{\text{Vs}}$]
1	2560	2.30±0.32	25.88	31.33±3.34	0.83±0.073	1049.84±71.58
	2560	2.29±0.30	19.66	31.25±3.04	0.93±0.097	935.26±62.44
	2560	1.18±0.12	8.40	16.15±0.66	1.07±0.03	821.29±54.77
	2560	1.41±0.14	10.51	19.30±0.81	0.92±0.04	948.47±63.25
8	1770	5.65±0.74	32.73	53.31±5.06	1.31±0.19	968.97±64.61
	1770	4.91±0.62	38.22	46.35±4.05	1.28±0.18	989.90±66.02
	1770	1.85±0.18	9.93	17.43±0.70	1.22±0.17	1038.74±69.27
	1770	7.29±1.05	63.10	68.84±7.67	1.32±0.20	960.33±64.04

The calculated results summarized in Table 6.4 are for two representative detectors belonging to different manufacturers. It is found the electron mobility μ_e of the eV detector is smaller than that of the Redlen detector. This comparison indicates a higher concentration of impurities in the eV detector, which is also why a higher voltage supply is needed for this batch. It is reported that $\mu_e\tau_e$ reaches its maximum when the energy resolution is the best [138, 139]. Indeed, the Redlen detectors perform slightly better than the detectors of eV Products regarding energy resolution, which agrees with the listed $\mu_e\tau_e$.

Besides the effects discussed above, the $\mu_e\tau_e$ variation is also associated with temperature. When the temperature is lowered, vibrations in the crystal structure decrease, resulting

in greater electron mobility due to less scattering. However, once a critical temperature is reached, the electron lifetime reduces, indicating that the electrons travel only a short distance before being trapped. Therefore, decreasing the temperature further will degrade the detector's performance.

It is also worth noting that the calculated μ_e is consistent with the literature value of $1000\,\mathrm{cm}^2/(\mathrm{V{\cdot}s})$, as used in the pulse shape simulation. The maximum drift time of around $0.9\,\mu\mathrm{s}$ obtained from the simulation is also comparable to measured values.

Fig. 6.34 compares the mean trapping length λ_ω deduced from the weighting factor and λ_m estimated from the measurement via Eq. 6.10. Despite slightly larger values from the direct measurement, the two agree well for most sectors. This comparison also validates the weighting factors.

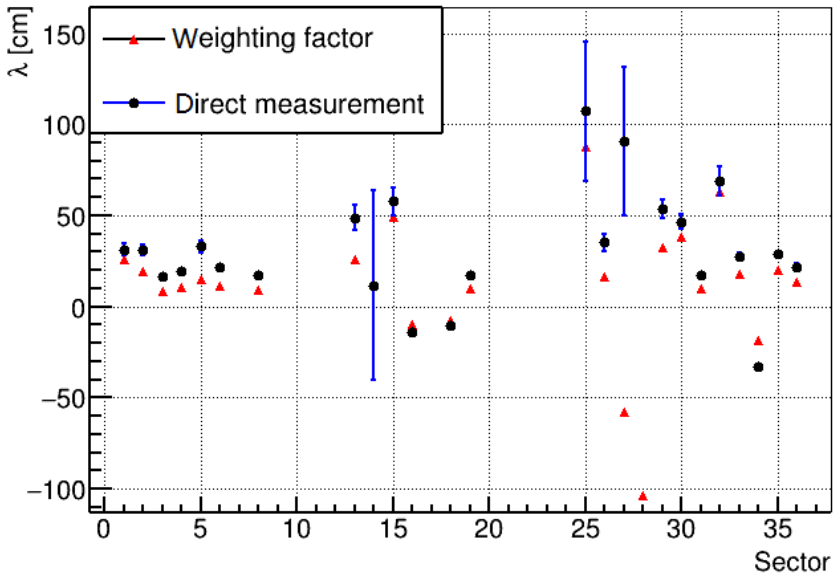

Figure 6.34.: The mean trapping length λ deduced from the weighting factor and direct measurement for each sector based on one ^{22}Na calibration.

In conclusion, pulse shape analyses are developed for the XDEM to reduce backgrounds. The following chapters will discuss searches for rare decays.

7. Investigating the $2\nu\beta\beta$-decay of ^{116}Cd

Measuring the $2\nu\beta\beta$-decay can help test theoretical model calculations. In particular, a precise $2\nu\beta\beta$-decay rate may constrain the axial vector coupling strength g_{A} and give information about the 1^+ Gamow-Teller nuclear matrix elements, which are crucial for the $0\nu\beta\beta$-decay. Furthermore, the spectral shape of the $2\nu\beta\beta$-decay might pinpoint the underlying decay mechanism for the $0\nu\beta\beta$-decay [7, 50, 140].

The $2\nu\beta\beta$-decay of ^{116}Cd to ^{116}Sn with a Q-value of 2814 keV was already measured by several experiments. The first observation with a half-life of $2.6^{+0.9}_{-0.5}\times10^{19}$ yr is from the ELEGANT V experiment using drift chambers and plastic scintillators. Some other experiments have used enriched $^{116}CdWO_4$ scintillators and tracking detectors. The most precise value provided by the NEMO-3 experiment is $(2.74\pm0.04(\mathrm{stat})\pm0.18(\mathrm{sys}))\times10^{19}$ yr and by the Auora experiment is $(2.6\pm0.04(\mathrm{stat})^{+0.11}_{-0.12}(\mathrm{sys}))\times10^{19}$ yr. However, semiconductor detectors have not been used yet. With a better energy resolution than the detectors used before, it would be worthwhile using COBRA CZT detectors. This chapter focuses on the investigation of this decay based on an exposure of 0.18 kg·yr data. The excited state transition of the decay is also explored.

7.1. Data selection

The data-taking conditions and setup stability of XDEM were discussed in Chapter 5. An exposure of 0.50 kg·yr has been collected in total. All the data runs are carefully inspected. Files with exceptionally high count rates, which is probably caused by electromagnetic interferences, are rejected. Files suffering from instabilities of the readout system are also excluded. Moreover, the dataset with an exposure of 0.30 kg·yr is coupled with excessive noise and will not be used for the following analysis.

During its operation, the setup has suffered from Nitrogen flushing failures several times. This leads to an increased Radon exposure. The dominant Radon-induced background is from ^{222}Rn, which belongs to the natural decay chain of ^{238}U. The ^{222}Rn decay has a half-life of 3.8 d. The isotopes ^{220}Rn and ^{219}Rn from the decay chains of ^{232}Th and ^{235}U have much shorter half-lives of 56 s and 4 s, respectively. Therefore, their contamination to detectors is comparatively minor.

Fig. 7.1 compares the energy spectra with and without Nitrogen flushing. It can be seen that the count rate is higher when the Nitrogen flushing fails. For high energetic events, α particles from ^{222}Rn (5.49 MeV) and its radioactive daughter nuclei ^{218}Po (6.09 MeV), ^{214}Po (7.69 MeV), and ^{210}Po (5.30 MeV) are dominant. As mentioned before, α contaminations on the lateral detector surfaces are suppressed by the grounded guard ring (GR). On the cathode, α particles need to pass through a Gold and a Platinum layer before entering the detector.

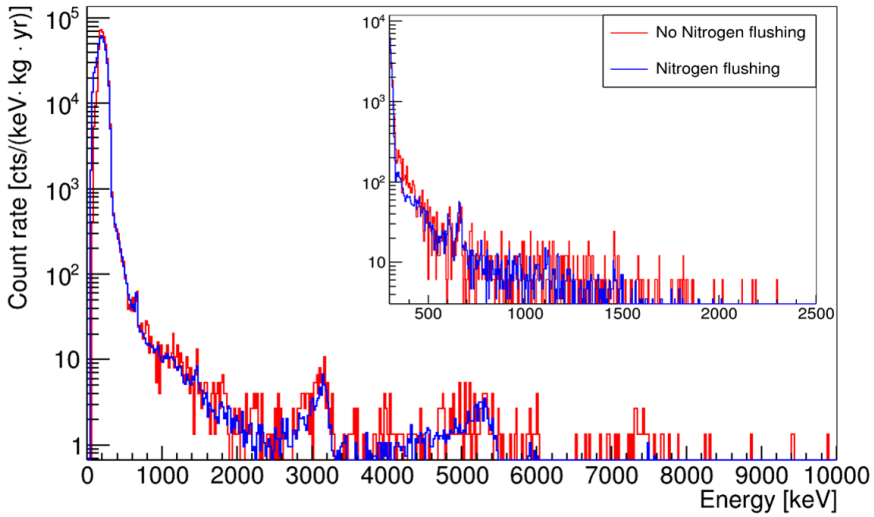

Figure 7.1.: Energy spectra combined from all sectors for the period with and without Nitrogen flushing. The data cleaning cuts are applied. α peaks at high energies are slightly higher for the spectrum taken without Nitrogen flushing. Also, the intensity of γ-lines highlighted in the inlet is higher in the case of failed Nitrogen flushing.

According to Ref. [39], the low energy tail of α peaks becomes prominent for layers with a certain thickness, but for thinner layers, this tailing effect is minor. For the data, the exact reason for the peak tailing needs further investigation as the actual thickness of the electrode layer is not well characterized yet.

Additionally, β-decays and de-excitation γ-lines from the Radon decay chain are present, as also shown in Fig. 7.1. The visible γ lines from the short-living ^{222}Rn decay daughters are at 351.9 keV (^{214}Pb) as well as at 609 keV and at 1120 keV (^{214}Bi). Since these decay products of ^{222}Rn cause background, the data files taken without Nitrogen flushing are discarded. Furthermore, several sectors not sensitive to the A/E cut, as stated in Section 6.7, are also removed. The data selection results in an exposure of 0.18 kg·yr.

7.2. Background identification and preliminary simulations

Although intensive shieldings and radiopure materials prevent the background from entering the setup, materials surrounding the detectors contain irreducible radionuclides, including natural radioactivity and cosmogenic activation. Some of these backgrounds contaminate the signal region of the $2\nu\beta\beta$-decay of ^{116}Cd. The prominent background sources are highlighted in Fig. 7.2. Most of the components identified in the XDEM are also present in the Demonstrator.

In order to quantify the background contribution from each component, a preliminary background description is developed in this section. Starting the simulation on the high energy side is beneficial as background sources are well known there. In contrast, the low

energy region does not show many distinguishable features except several visible γ lines.

At high energies, the α-decay of ^{190}Pt at 3.2 MeV is seen on the cathode surface as Platinum is part of the electrode material. According to the manufacturer, the electrodes of the Redlen detectors contain less ^{190}Pt compared to the batch from the eV Products. The other peak at 5.3 MeV belongs to ^{210}Po from the ^{222}Rn decay chain. As shown in Table B.1, ^{210}Po has a relatively long half-life of about 140 d compared to the other Polonium radioactive isotopes ^{218}Po and ^{214}Po. Its grandmother nuclide ^{210}Pb has a long half-life of 22.3 yr for the β-decay. It is reported that Radon decay daughters are originally positively charged [102]. This means that ^{210}Pb can be absorbed on the cathode by a negative bulk voltage, and ^{210}Po may gradually accumulate.

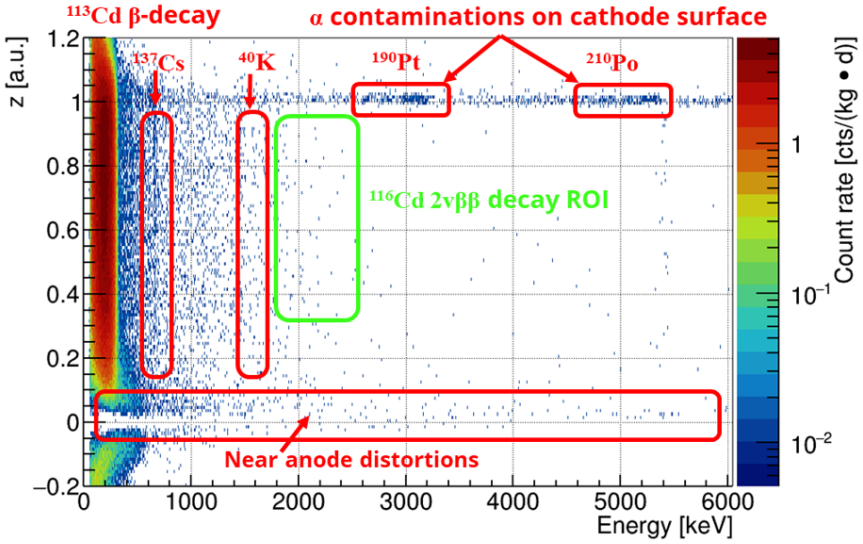

Figure 7.2.: Prominent background sources are identified via the 2D depth and energy spectrum. The anode lies at $z = 0$, while the cathode at $z = 1$. Only the data cleaning cuts are applied. The strongest signal is the β-decay of ^{113}Cd on the low energy side. α emitters are found on the cathode. The vertical lines indicate γ-rays from different radioactive nuclides. Near the anode, reconstruction artifacts are identified.

However, modeling the contribution of the α-decay via a Monte Carlo simulation is quite challenging. This is because its spectral shape is affected by several factors. As pointed out in Ref. [39], it is possible to model the thickness of the Platinum layer via the α spectrum shape of ^{190}Pt. However, the XDEM data show less than 30 events within this peak. Besides a lack of knowledge of the exact electrode thickness, the α peak also highly depends on the diffused volume of Radon gas and unknown energy resolutions for α particles. Another difficulty is that the grounded GR also smears the shape of α peaks.

As described in Section 4.3.2, VENOM already has most parts of the XDEM geometry implemented. Several details regarding the near detector components are added to VENOM so that background sources interacting with these materials can be simulated. Event generators in VENOM are available to produce primary particles for a single radionuclide. The decay

chain generator, *chaingen*, is used to simulate decay chains, like ^{222}Rn decays. For each source, $1{\times}10^6$ events are generated and confined to materials near the detectors. The CZT crystal can be assumed as radiopure [102].

In this study, several assumptions are made to simplify the procedure and to be conservative. For instance, the default thickness of 45 nm for the Platinum layer is used. In the first step of the simulation, the radioisotope ^{190}Pt is confined within the layer. The simulated α spectrum is smeared with the energy resolution function determined from γ peaks. Then, the smeared template is scaled with the measured spectrum by choosing an interval of $E_\alpha \pm \mathrm{FWHM}(E_\gamma)$. Following the χ^2 method, the scaling factor k needs to reduce

$$\chi^2 = \sum_{i=1} \frac{(N_{\mathrm{data},i} - k \cdot N_{\mathrm{sim},i})^2}{N_{\mathrm{data},i}} \tag{7.1}$$

where $N_{\mathrm{data},i}$ is the measured entries in the bin i, and $N_{\mathrm{sim},i}$ is the simulated entries.

The simulation only considers single-sector events as the measured data does. Events with a multiplicity above one are rejected. This multiplicity cut is especially important for modeling γ sources.

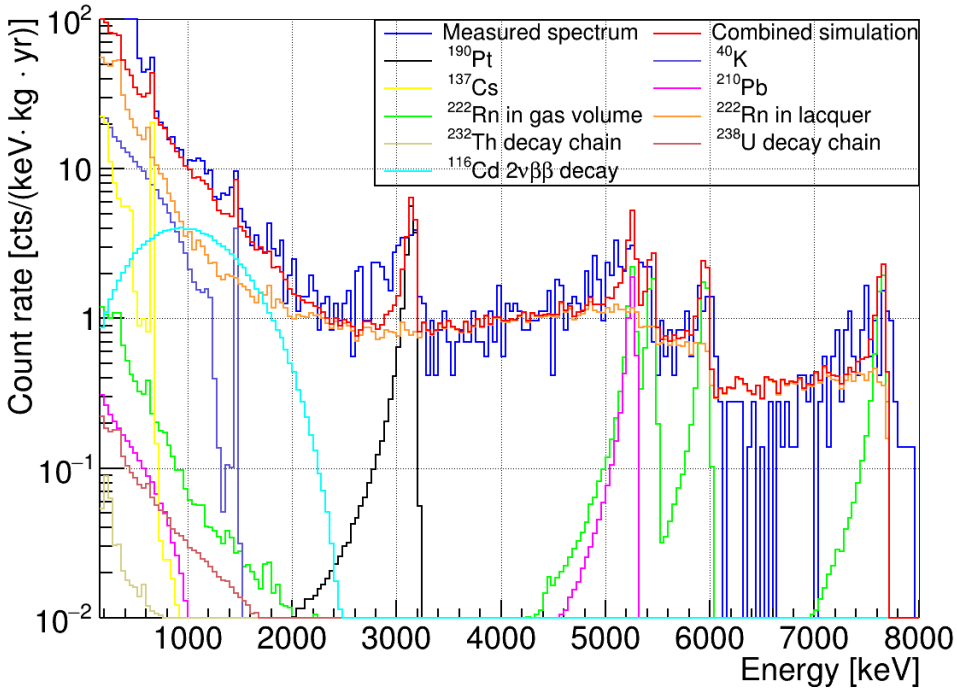

Figure 7.3.: Preliminary background characterizations in the ROI for the total XDEM spectrum based on modeling peak features and measured activities listed in Ref. [43]. The $2\nu\beta\beta$-decay of ^{116}Cd with a half-life of $2.63{\times}10^{19}$ yr is also included [50].

The presence of alpha peaks makes the decay of ^{222}Rn the second important step for modeling background radiation. The source is confined to the gas volume inside the Copper

shield surrounding the detectors. Note that possibly varying lacquer thickness on the lateral sides of the detectors has little impact on the α peaks due to the grounded GR, but may affect the interactions of β particles or γ-rays. As for the β particles emitted from the Radon decay chain, their distribution may also be affected by the grounded GR, whose rejection power to beta particles is not yet known. However, for simplicity, the same scaling procedure used for the ^{190}Pt is applied to determine the contribution of ^{222}Rn by modeling the alpha peak at 6.0 MeV.

The background contributed by the ^{222}Rn and ^{190}Pt decay is subtracted from the measured spectrum. The remaining events are used to model the ^{210}Pb contaminant accumulated on the cathode. The α peak produced by its daughter nucleus is affected by the thickness of the electrode layer, but it is not taken into account in this analysis.

To account for the effect of the thickness variation of the Platinum layer as well as the GR instrumentation, the ^{222}Rn decay is distributed on the lacquer surface as an approximation. The lacquer thickness is in the order of 10 µm and is not uniform, which can cause low energy tails for α peaks. One can see that the structure of α peaks matches better than the case without this component, as illustrated in Fig. 7.3. Simulated pulses are expected to model these effects more accurately and can be investigated in the future.

The background components from primordial decay chains are also important to know. But these long decay chains do not show any distinctive features. Therefore, the radiopurity measurements that were previously carried out with the CZT crystals and the construction materials, as given in Ref. [43], are used to estimate the contribution of ^{232}Th and ^{238}U decay chains according to the measured contamination level or specific activity.

For simplicity, the source of the decay chains is only constrained to one material. As the lacquer contains most of the portion, it is chosen as the source volume. The specific activity is obtained by adding up the measured specific activity of all the near-detector materials to be conservative, which results in a total specific activity of 20.14 mBq/kg for ^{238}U and 20.14 mBq/kg for ^{232}Th. Compared to the Demonstrator, the XDEM has used materials with higher radiopurity to construct the setup [43]. Assuming the decay chain is in equilibrium, the scaling factor is deduced using the following equation

$$k = \frac{N_{\text{exp}}}{N_{\text{sim}}} = \frac{amt}{N_{\text{sim}}}. \tag{7.2}$$

N_{exp} represents the expected number of events from the measured specific activity a. m is the mass of the source, and t is the measurement time. N_{sim} denotes the number of simulated events.

Prominent γ lines like the 1461 keV γ-line emitted after the EC of ^{40}K are also modeled. The ^{40}K source is originally confined within lacquer. It turns out that its contribution to the overall background is overestimated. This is because the lacquer is very close to the detectors, and the emitted β particles can travel to the detectors, increasing the count rate at low energies. Instead, the source is specified to the Delrin holder that is used to frame the detectors.

Another prominent γ-line at the 662 keV from ^{137}Cs is detected by detectors one, two, three, and four. This source is presumably contaminated on the Delrin surface.

This work provides a preliminary and conservative background simulation, even though the model does not match the data perfectly. Various source origins also affect the spectrum shape and thus lead to different contributions. Other background sources like cosmogenic activation could also be considered, as described in Ref. [43], and their fraction relies on descriptions for other background sources.

The signal's distribution is also simulated. The event generator, *Decay0*, can produce primary $2\nu\beta\beta$-decays of ^{116}Cd [103], which are distributed homogeneously in the detectors. The detector measures the two electrons' energy. Fig. 7.3 also shows the continuous energy spectrum of the decay with an endpoint at the Q-value of 2814 keV. At high energies, the event rate drops significantly.

7.3. Signal cut efficiency and data analysis

In order to improve the signal to background ratio (S/B), the cuts discussed in Chapter 6 are applied to reject unwanted backgrounds accordingly. Fig. 7.4 shows the corresponding energy spectra with respective cuts applied, including the grounded GR, data cleaning cuts (s), z-cut, and A/E cut. The signal efficiency is required to determine the half-life of the decay and is calculated from the intrinsic detection efficiency and the cut efficiency. The intrinsic detection efficiency ε_{int}, the proportion of detected events to the total events, is deduced from the Monte Carlo simulation.

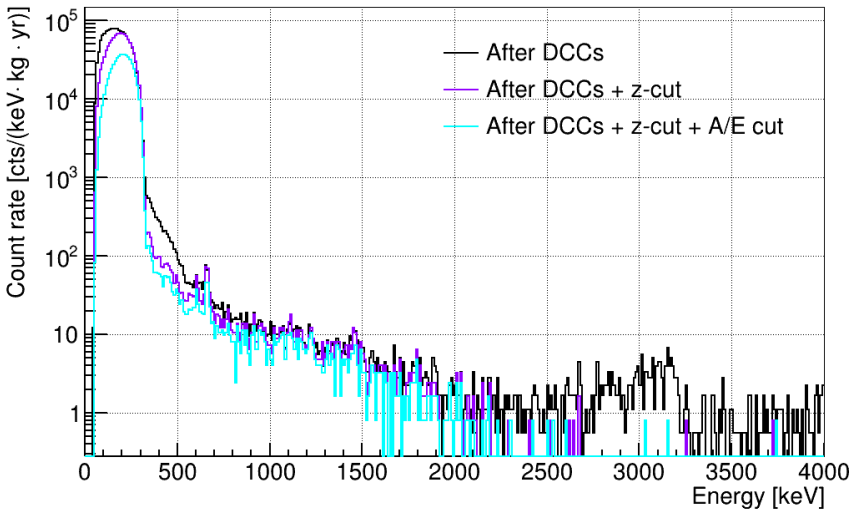

Figure 7.4.: Energy spectra with corresponding cuts applied, including data cleaning cuts, z-cut, and A/E cut.

The cut efficiency is derived from the number of surviving events divided by the total number of events in the energy range from 1500 keV to 2400 keV. This energy window is chosen to avoid the 1461 keV γ-line of ^{40}K and also due to a low signal rate above 2400 keV. Since the signal acceptance of the GR and z-cut cannot be determined directly from measurements,

simulated pulses of $2\nu\beta\beta$-decay of ^{116}Cd are used.

The cut efficiencies are summarized as follows:

- The efficiency of the grounded GR, $\varepsilon_{\mathrm{GR}}$, is determined to be (96.15±0.13)%.
- The z-cut efficiency, ε_{z}, is (79.36±0.33)% deduced from events surviving the GR.
- After applying the GR and the z-cut, the A/E cut performance is expected to be constant in the ROI and has a signal acceptance of (90.94±0.10)%.

The quoted uncertainties are attributed to statistical fluctuations. The DCCs do not affect events in the ROI, as mentioned in Section 6.3. The total efficiency $\varepsilon_{\mathrm{tot}}$ is the product of $\varepsilon_{\mathrm{int}}$ and the cut efficiencies,

$$\varepsilon_{\mathrm{tot}} = \varepsilon_{\mathrm{int}} \cdot \varepsilon_{\mathrm{GR}} \cdot \varepsilon_{\mathrm{DCCs}} \cdot \varepsilon_{\mathrm{z}} \cdot \varepsilon_{\mathrm{A/E}}, \tag{7.3}$$

which results in a total efficiency of (68.25±0.37)%.

However, these cuts cannot remove all the background. The relevant spectra still need to be modeled by background simulations with the effect of cuts taken into account. This modeling is no trivial work and is dependent on the model built for the total energy spectrum. In this work, only background components showing distinct features are included, which are basically γ sources.

The potential γ sources listed in Table 7.1 are simulated, and the template spectra are scaled to the remaining events based on the respective γ peak. For the Radon decay, multiple γ peaks are expected, as listed in Table B.1. The 609 keV γ-line is an appropriate choice as other peaks do not show a very clear feature. For instance, the low energy 351.9 keV γ-line is not well separated from an exponentially decreasing background despite a higher intensity. The event rate within the energy region of E_γ±FWHM(E_γ) is calculated from fitting the γ peak using a two-sided Gaussian function and a linear background.

Fig. 7.5 shows the background modeling and the simulated signal spectrum that is scaled with the total detection efficiency discussed in Section 7.3 and previously measured half-life [50]. It can be seen that the combined simulation underestimates the overall background, especially at low energies. Other background sources are expected.

Table 7.1.: Prominent γ sources identified in XDEM are confined in the volume that has the dominant background contribution. The count rate, R, is estimated from the energy range of E_γ±FWHM(E_γ) using the fit function in Eq. 3.7.

nuclides	energy [keV]	origins	R [cts/(kg·keV·yr)]
^{214}Bi	609.3	gas volume	98.47±8.92
^{137}Cs	662	Delrin holder	137.12±7.98
^{40}K	1461	Delrin holder	15.80±3.74

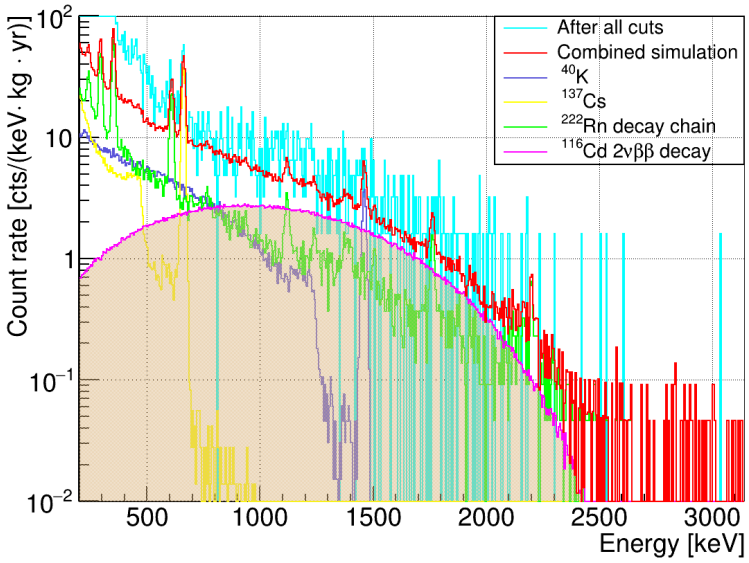

Figure 7.5.: Events surviving all the cuts indicated in Fig. 7.4 and the contribution of prominent γ backgrounds. The background simulation associated with γ-rays is also shown. The expected $2\nu\beta\beta$ spectrum of ^{116}Cd is shaded, considering a half-life of 2.63×10^{19} yr and the signal cut efficiency determined in this work [50]. The combined simulation includes the signal from the $2\nu\beta\beta$-decay of ^{116}Cd and the simulated backgrounds.

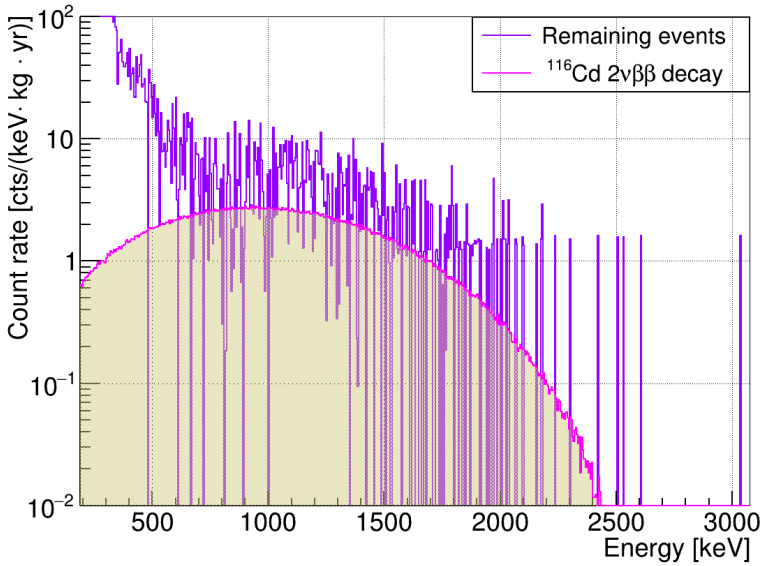

Figure 7.6.: Events remained from subtracting the simulated contributions of prominent γ backgrounds indicated in Fig. 7.5. The expected $2\nu\beta\beta$ spectrum of ^{116}Cd is shaded, considering a half-life of 2.63×10^{19} yr and the signal cut efficiency shown earlier [50].

Most of the $2\nu\beta\beta$ events are registered in the energy region where the background is relatively high. In the defined ROI, 121 events are found, and 61 events are expected from the signal. This corresponds to a S/B of 1.00±0.14. After subtracting the simulated γ background from the data shown in Fig. 7.5, the remaining events are shown in Fig. 7.6. There are still underlying background events not characterized by γ sources.

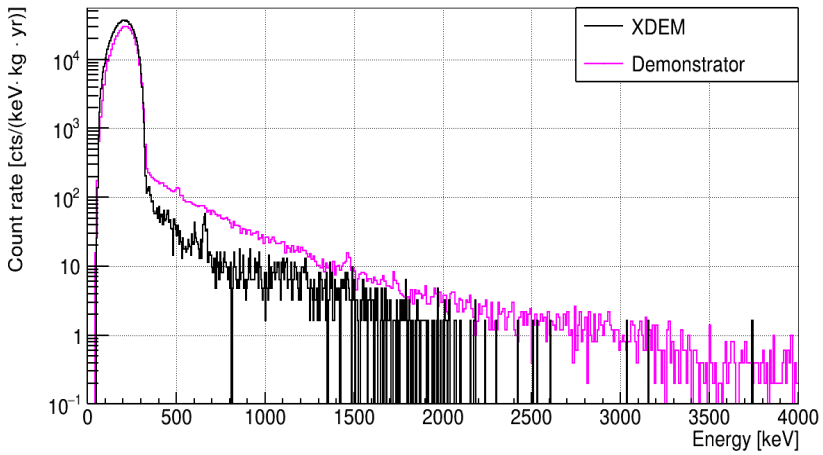

Figure 7.7.: The energy spectra of XDEM and Demonstrator after applying all the analysis cuts. The background level in the ROI has significantly improved with the XDEM.

Fig. 7.7 compares the energy spectra of the XDEM and the Demonstrator with all the cuts applied. The background level in cts/(keV·kg·yr) is defined in the energy range of $(Q_{\beta\beta}\pm300)$ keV for the $0\nu\beta\beta$-decay of ^{116}Cd, and a value of (0.053±0.031) is obtained for the XDEM. This value has improved by a factor of 23 compared to the Demonstrator.

In summary, the first attempt of modeling the XDEM γ background is made. However, a lack of a complete background description makes the half-life limit extraction difficult.

7.4. Potential for excited state searches

Besides the ground state transition, the $\beta\beta$-decay can also go to various excited states of daughter nuclei. Studies of the $2\nu\beta\beta$ transition to the excited states allow to obtain supplementary information about the $\beta\beta$-decay as well as to test nuclear structure calculations. Compared to the ground state transition, the smaller transition energy leads to a substantially suppressed decay rate for excited state transitions. This is because the phase space factor scales with $Q^{11}_{\beta\beta}$ for the $2\nu\beta\beta$-decay. Besides the reduced phase space, decaying to the excited state also depends on the nuclear spin of nuclei.

Fortunately, excited state transitions are accompanied by the emission of characteristic γ-rays from the de-excitation of the daughter nucleus. While the two electrons of the $\beta\beta$-decay remain in the source detector, those γ-rays may escape and fully or partially deposit energies in another detector. Therefore, a coincidence analysis can be used, which provides a clearer experimental signature than a continuous electron spectrum in the case of g.s. $\rightarrow$ g.s. decays.

This section studies the potential of finding the signal of the ^{116}Cd $2\nu\beta\beta$-decay to the excited states of ^{116}Sn based on Monte Carlo simulations.

7.4.1. Event signature

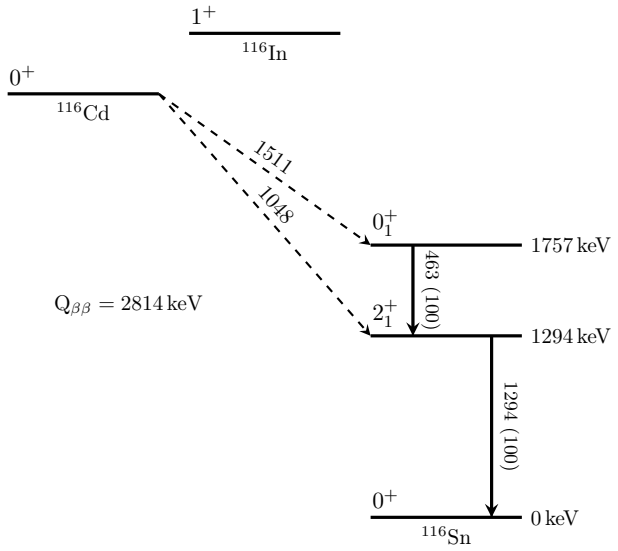

Figure 7.8.: Decay scheme of the ^{116}Cd $2\nu\beta\beta$-decay into excited states of ^{116}Sn. Only energy levels of interest for this work are shown [50].

Fig. 7.8 illustrates the decay scheme of excited state transitions of the ^{116}Cd $2\nu\beta\beta$-decay. The first excited state of the daughter nucleus is a 2^+_1 state that decays to the ground state by emitting one γ-ray with an energy of 1294 keV. In this case, a spin of 0^+ for the ground state of ^{116}Cd to the first excited state of ^{116}Sn with a spin of 2^+ is not favored [141]. Instead, a decay to the second excited state with a 0^+ spin configuration would be preferred. The second exited state 0^+_1 usually transits via the 2^+_1 state into the 0^+_{gs} while producing γ cascades [142]. Thus, an additional γ-line with energy of 463 keV is emitted in coincidence to the 1294 keV γ-line. Table 7.2 lists excited state transitions and the emitted γ-rays. The branching ratio is also shown.

Table 7.2.: Q-value of the ^{116}Cd $2\nu\beta\beta$-decay into excited states of ^{116}Sn. The de-excitation energy and the branching ratio are also given.

decay mode	$Q_{\beta\beta}$ [keV]	E_γ [keV]	Br [%]
$0^+_{g.s.} \rightarrow 2^+_1$	1511	1294	100
$0^+_{g.s.} \rightarrow 0^+_1$	1048	463	100
		1294	100

The excited state transitions of ^{116}Cd are simulated with XDEM using VENOM. Primary particles for the electrons and the γ-rays are generated by *Decay*0. For each decay mode, 10^7 events are randomly distributed in each detector, corresponding to $9{\times}10^7$ events in total. Fig. 7.9 shows the fraction of detecting M1, M2, and M3 events for the $0^+_{\text{g.s.}} \rightarrow 0^+_1$ decay in the XDEM. As mentioned in Section 6.6, M1 indicates a multiplicity of one sector hit. M2 denotes a multiplicity of two-sector hits that occurred simultaneously, and so on.

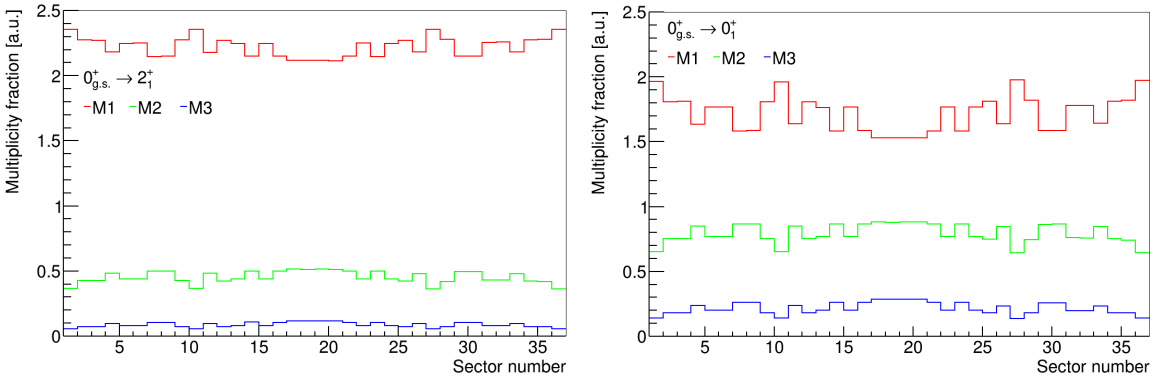

Figure 7.9.: The fraction of the $0^+_{\text{g.s.}} \rightarrow 2^+_1$ decay (left) and the $0^+_{\text{g.s.}} \rightarrow 0^+_1$ decay (right) that are detected as the M1, M2, or M3 events for each sector.

The fraction of M2 events depends on the detector size. Small detectors increase the probability of M2 events because of the reduced self-absorption for γ-rays. Table 7.3 lists the total multiplicity fraction deduced from the simulation for each decay mode. Even though the M1 events make up a large fraction of all decay modes, the excited state transitions feature an increased amount of M $>$ 1 events. Due to the high detector granularity of XDEM, the M2 fraction of excited state transitions has increased by around 10% compared to the Demonstrator. One can also see that investigating M2 events can help disentangle irreducible backgrounds from the $2\nu\beta\beta$-decay of ^{116}Cd into the ground state as $0^+_{\text{gs}} \rightarrow 0^+_{\text{gs}}$. Events with a higher multiplicity only constitute a smaller fraction of the simulated events. In comparison, these events will contribute less to the signal and will not be considered in the following analysis.

The energies of simulated events are smeared with the average energy resolution function given in Section 5.5. As only coincident events classified as M2 are of interest for this analysis, events with energy deposition in a single sector or more than two sectors are not considered. Fig. 7.10 shows the two dimensional spectra of M2 events for the $0^+_{\text{g.s.}} \rightarrow 2^+_1$ and the $0^+_{\text{g.s.}} \rightarrow 0^+_1$ decay modes, respectively.

The full energy deposition of γ-rays can be found in those horizontal and vertical lines. These γ-lines are the ROI for searching the excited state transitions. Along these lines lies the continuous β spectrum of the $2\nu\beta\beta$-decay superimposed with partial energy depositions of γ-rays. There is only one single γ line at the 1294 keV for the $0^+_{\text{g.s.}} \rightarrow 2^+_1$ decay mode. For the $0^+_{\text{g.s.}} \rightarrow 0^+_1$ decay mode, double lines corresponding to γ peaks at 463 keV and 1294 keV are visible. The summation peak of the two γ lines can also be seen. One thing to notice is

Table 7.3.: Multiplicity fraction for the decay modes of ^{116}Cd $2\nu\beta\beta$-decay into excited states and the ground state of ^{116}Sn.

decay mode	M1 [%]	M2 [%]	M3 [%]
$0^+_{\text{g.s.}} \rightarrow 2^+_1$	80.18	16.22	3.07
$0^+_{\text{g.s.}} \rightarrow 0^+_1$	62.32	28.38	7.57
$0^+_{\text{g.s.}} \rightarrow 0^+_{\text{g.s.}}$	95.28	4.43	0.21

that the backscattering peak of the de-excitation γ-rays interacting with the shielding is also present at around 200 keV.

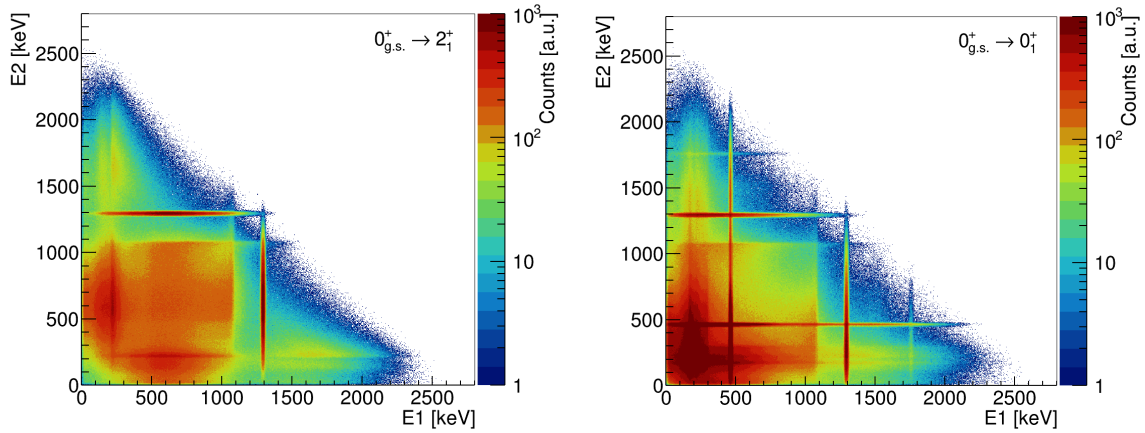

Figure 7.10.: Simulated M2 events. The energy of one sector hit versus the other sector for the two decay modes, $0^+_{\text{g.s.}} \rightarrow 2^+_1$ (left) and $0^+_{\text{g.s.}} \rightarrow 0^+_1$ (right).

7.4.2. Analysis cut optimization

As the synchronized experimental data have suffered a significant exposure loss due to non-functional FADCs, only the simulated data are used to estimate the experiment's sensitivity to the excited state transitions. An energy threshold of 100 keV is applied to the simulated M2 events on both channels. This value is approximated as the threshold set for the real data. The choice of the threshold affects the multiplicity. A high energy threshold degrades high multiplicity events to low multiplicities and vice versa. Optimizing the energy threshold will be explained later. Taking the recent half-life limits into account [50], the normalized M2 events are shown in Fig. 7.11 for the two decay modes. Considering only M2 events is equivalent to applying a coincidence cut.

The optimization of cuts is purely based on the simulation because a background model for M2 events is not available yet. In the neutrino accompanied decay mode, the continuous energy spectrum of the electrons from the $0^+_{\text{gs}} \rightarrow 0^+_{\text{gs}}$ decay poses an irreducible background

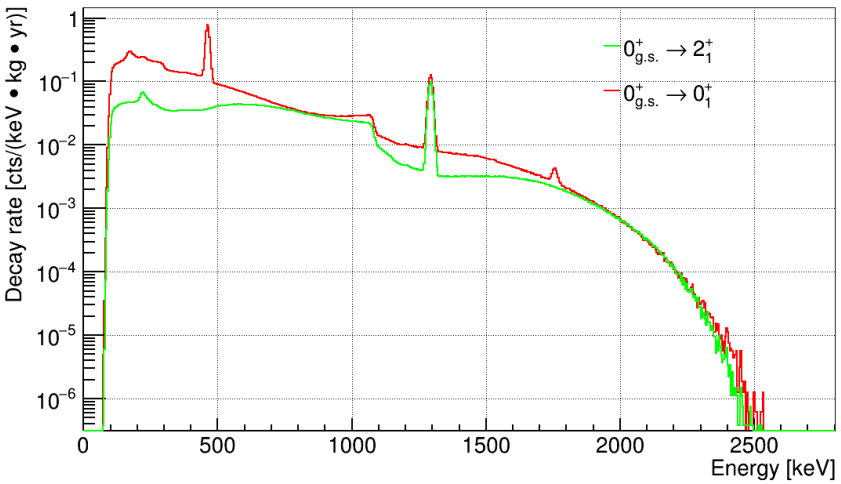

Figure 7.11.: Signal spectra of the simulated $0^+_{g.s.} \rightarrow 0^+_1$ and $0^+_{g.s.} \rightarrow 2^+_1$ decays normalized with a half-life limit of 5.9×10^{20} yr and 9.8×10^{20} yr, respectively. The half-life limits are taken from the Aurora experiment [50]. The spectra are smeared with the energy resolution.

to the excited state decay modes. In this work, only this background source is considered.

Based on the event signature of each decay mode, the energy window in the ROI is optimized. For the $0^+_{g.s.} \rightarrow 2^+_1$ decay, the energy deposition of either detector has to be within an energy window that covers the γ peak at 1274 keV. The signal cut of the $0^+_{g.s.} \rightarrow 0^+_1$ decay requires the energy deposition in one detector to either be within the ROI of 463 keV or 1294 keV. The summation peak at 1757 keV is also used. The energy deposition in the second detector can occupy any value in the range between the low energy threshold and the high energy end. Before optimization, the window width is set to a default value of $E_\gamma \pm 2 \cdot \mathrm{FWHM}(E_\gamma)$.

Each decay mode is evaluated separately. This is a valid approach for now because the ratio of the decay rates is unknown. As the background and signal vary with energy, the low energy threshold, the high energy end, and the energy window for defining the ROI are optimized to improve the sensitivity of the signal search. The significance $\bar{Z}$, representing the signal strength relative to the background, is expressed as [143],

$$\bar{Z} = \sqrt{2\left((s+b)\ln\left(1+\frac{s}{b}\right)-s\right)} \tag{7.4}$$

with s and b denoting the number of events for signal and background in the ROI. The formula was developed according to a profile Likelihood function. It accounts for the scenario that the expected signal strength is comparable with or stronger than the background [126]. This formula is suitable to optimize all the cut parameters and thus increase the sensitivity.

The low energy threshold ranges from 100 keV to 440 keV, in steps of 20 keV. The maximal 440 keV is chosen to avoid the signal region at 463 keV. The threshold with the highest $\bar{Z}$ is chosen as the optimized cut for low energies. Depending on the decay mode, optimal values of 420 keV and 100 keV are obtained for the $0^+_{g.s.} \rightarrow 2^+_1$ and $0^+_{g.s.} \rightarrow 0^+_1$ transition, respectively.

Similarly, the high energy limit is scanned from 1500 keV to 2500 keV, in steps of 50 keV. The high energy cutoff is given by the maximal energy indicated by Fig. 7.10. An optimal value of 2500 keV is found for both $0^+_{\text{g.s.}} \rightarrow 2^+_1$ and $0^+_{\text{g.s.}} \rightarrow 0^+_1$ transitions.

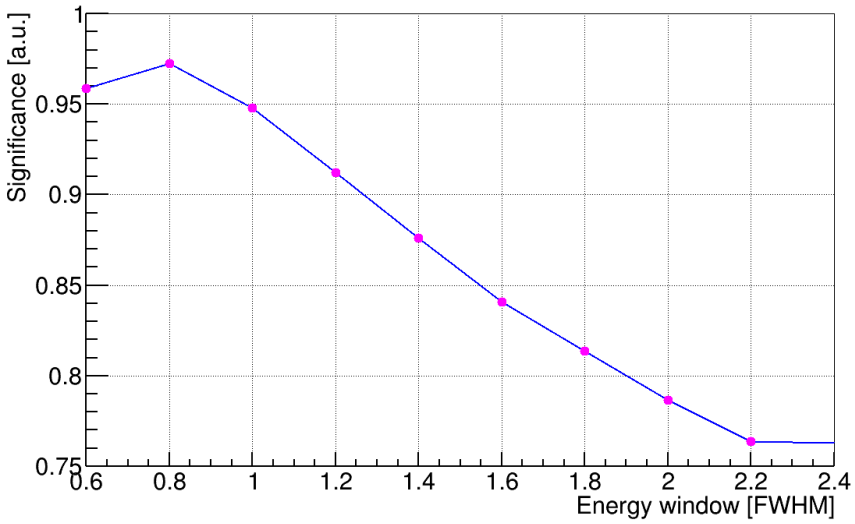

Figure 7.12.: Optimization of the energy window for the $0^+_{\text{g.s.}} \rightarrow 2^+_1$ transition, assuming that only the ground state transition of the $2\nu\beta\beta$-decay contributes to the background.

Depending on the underlying background level, an optimal energy window for selecting signals is expected. The window width is varied from 0.6·FWHM to 2.4·FWHM in steps of 0.2·FWHM. Fig. 7.12 shows the optimization curve obtained for the $0^+_{\text{g.s.}} \rightarrow 2^+_1$ decay mode. The optimal value of 0.8·FWHM is found for both decay modes. With the optimized cuts, the obtained S/B is 5.46, increased by a factor of 4.2 for the $0^+_{\text{g.s.}} \rightarrow 2^+_1$ decay mode compared to the Demonstrator. The $0^+_{\text{g.s.}} \rightarrow 0^+_1$ transition has reached 4.25 and 2.81, improved by 3.6 and 2.4 for 1294 keV and 463 keV, respectively.

An optimal arrangement of the detector granularity is beneficial for searching for coincident events. Depending on the detector position, the contribution of each sector pair to the signal efficiency and background is different. Neighboring sectors usually have a high probability of observing a full energy deposition of γ-rays because of less absorbing materials. On the other hand, some pairs can add more background than contribute to the signal. Excluding such pairs will increase the total signal sensitivity. However, after normalizing M2 events with the corresponding half-life limit, pair optimization is strongly limited by statistics. For more details, see in Appendix B.2.

8. Charge non-conserving decay of ^{113}Cd

Electric charge conservation is one of the fundamental laws of the Standard Model, which results from the gauge invariance of electromagnetic fields. However, in the framework of the Grand Unified Theory that merges the electromagnetic, weak, and strong forces, the conservation of electric charge may break down. This possibility and its implications have been extensively discussed in Refs. [144–146]. Several models are proposed to understand the underlying theory of the charge non-conservation but encounter difficulties. Although a self-consistent theoretical framework for describing the violation of charge conservation does not exist yet, experimental efforts to search for a charge non-conserving (CNC) decay have been ongoing for several decades [147].

The CNC decay can be tested by decays of electrons and nucleons. One way is to search for γ-rays of 255.5 keV following the decay of an electron $e^- \rightarrow \nu_e\gamma$. No signals have ever been observed for this decay mode. Experimentalists have also been looking for a CNC β-decay. In particular, if a single neutron in the parent nucleus undergoes the decay $n \rightarrow p + \nu_e + \bar{\nu_e}$, no electron will be emitted in the final state, but instead a nearly massless neutral particle, namely the electron neutrino. In this case, the additional 511 keV allow for a decay to an energy level of the daughter nucleus that is energetically forbidden for the typical, charge conserving β-decay. Previous experiments have restrained a stringent limit on this decay's half-life of $T_{1/2} > 2.4{\times}10^{26}$ yr (68% C.L.) for nuclei like ^{71}Ga [147].

^{113}Cd is one of the candidates being investigated. However, so far, only a low half-life limit of $T_{1/2} > 1.4{\times}10^{18}$ yr (90% C.L.) has been reported [148]. The COBRA CdZnTe (CZT) detector is a good choice for the investigation of the ^{113}Cd decay with the ultra-low background operation and good inherent detection efficiency. This chapter focuses on searching for the CNC β-decay of ^{113}Cd using the available Demonstrator and XDEM data, respectively.

8.1. Event signature of the decay

As mentioned earlier, ^{113}Cd undergoes the fourfold forbidden non-unique single β-decay to the ground state of ^{113}In, as $^{113}\mathrm{Cd}\ ^{(\frac{1}{2}+)} \rightarrow {}^{113}\mathrm{In}^{(\frac{9}{2}+)}$. The decay to the isomeric state of $^{113\mathrm{m}}$In is energetically forbidden if charge conservation is exact. If the electron is not produced in the final state, the emission of neutral particles as $^{113}\mathrm{Cd} \rightarrow {}^{113\mathrm{m}}\mathrm{In} + \nu_e + \bar{\nu}_e$ would be allowed, as displayed in Fig. 8.1. The de-excitation of the isomeric state of $^{113\mathrm{m}}$In would produce either an electron via internal conversion or a γ-line at 391.7 keV. The exact fraction depends on the electron conversion coefficient.

The previous experiment has searched for the coincidence of the K-conversion electrons from the isomeric transition of $^{113\mathrm{m}}$In and the subsequent X-rays emission using $CdCl_2$ samples. However, the chemical procedures applied in the experiment have limited the number of the

source atoms despite reducing most of the background.

The detection of the γ-line would also indicate the existence of the CNC decay, which is what this work will present. As there is no theoretical prediction about the branching ratio of the decay to the isomer state, a value of 100% is assumed.

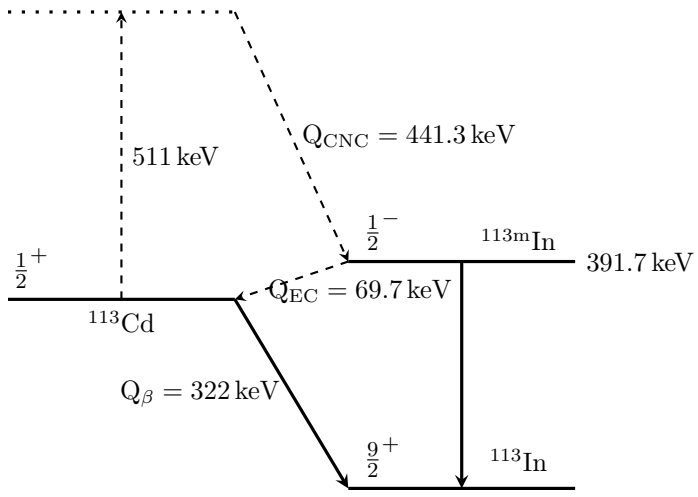

Figure 8.1.: Decay scheme of the CNC β-decay of ^{113}Cd.

A preliminary search for the γ-rays has set a limit of $T_{1/2} > 1.47{\times}10^{19}$ yr (90% C.L.) with the COBRA Prototype. The Prototype comprised of 2×2 CZT detectors and was operated at the LNGS in the last decade [149]. As more data exposure and advanced analysis methods are available, the limit will be updated here.

8.2. Data sets

As already discussed, the accumulated exposure at low energies is affected by changing trigger thresholds from time to time. To ensure a consistent exposure for events above a threshold, an optimal threshold cut (see Section 4.6.5) has been implemented. For the XDEM, runs with a threshold above 367.48 keV are rejected. The energy threshold is also to avoid the contamination from the low energy γ-line at 351.9 keV from the de-excitation of ^{214}Pb by considering the FWHM at 391.7 keV and 351.9 keV. Likewise, a threshold of 370 keV is obtained for the Demonstrator data.

As mentioned in Section 5.3, several sectors of the XDEM show deviations in the spectral shape of ^{113}Cd β-decay. Detectors with unstable operating conditions are discarded in this analysis. The data selection results in an exposure of 0.18 kg·yr. As for the Demonstrator, three detectors have suffered from electrical contacting issues, leading to abnormal voltage supplies. After excluding these detectors, the resulting data exposure is 1.25 kg·yr.

To improve the signal to background ratio, analysis cuts are applied. These cuts are referred to as the data cleaning cuts (Section 6.3) removing nonphysical events, a bad period cut

(Section 7.1) suppressing Radon decays, and a z-cut (Section 6.4) reducing surface contaminations as well as reconstruction artifacts. For the XDEM, an additional cut with the guard ring (Section 4.6.1) is intrinsically applied, discarding α particles on the lateral surfaces. For setting a new $T_{1/2}$ limit, the percentage of surviving signals from all the cuts is required.

8.3. Monte Carlo simulation

It is not possible to deduce the signal cut efficiency using the experimental data because there is no calibration source emitting a prominent γ-line at this energy. Instead, a Monte Carlo simulation is performed to estimate the cut efficiency as well as the intrinsic detection efficiency. VENOM simulates the interaction of the 391.7 keV γ-rays with the detectors of the XDEM and Demonstrator, separately. For each setup, 10^6 mono-energetic γ photons at 391.7 keV are randomly distributed in the detector volumes. In order to derive the cut efficiency, simulated pulses are processed with the same analysis framework as the measured events. All the efficiencies are summarized as follows,

- The full energy peak detection efficiency describes the probability of depositing the full energy of the photons inside the sensitive detector volume. This efficiency, $\varepsilon_{\mathrm{int}}$, is derived via the simulation and has a value of (11.30±0.04)% for the whole XDEM array and (14.49±0.038)% for the total Demonstrator setup. According to a database provided in Refs [150, 151], the mean free path of 392 keV γ photons in the CdZnTe is 1.7 cm. The detector array of the Demonstrator has a relatively large geometry, which explains the high probability of stopping γ-rays.

- The $\varepsilon_{\mathrm{GR}}$ is associated with the guard ring (GR). It is calculated by the number of the full energy peak events detected by the four CPGs relative to the total number.

- With the GR applied, the $\varepsilon_{\mathrm{DCCs}}$ represents the survival probability of gamma photons within the full energy peak after the data cleaning cuts.

- With the GR and the data cleaning cuts applied, the ε_{z} denotes the fraction of the remaining signal events after the z-cut.

The cut efficiencies for the XDEM and Demonstrator are listed in Table 8.1.

8.4. Data analysis and results for the XDEM

Due to differing detector characteristics and background features, the datasets from the two setups are analyzed separately. For the XDEM, data collected from all detectors are combined due to limited statistics.

The analysis is based on an optimized window counting method, as described in Appendix E.3. First, the energy window of the ROI is set to default values. These are optimized to maximize the sensitivity, which involves the signal efficiency and the expected background. More details will be discussed in the following analysis.

Table 8.1.: Determined efficiency for the data cleaning cuts, z-cut, and the grounded GR with simulated 391.7 keV γ-rays. The uncertainties are statistical fluctuations stemming from the simulation.

analysis cuts	XDEM	Demonstrator
$\varepsilon_{\mathrm{GR}}$ [%]	99.68±0.35	-
$\varepsilon_{\mathrm{DCCs}}$ [%]	99.60±0.53	99.39±1.12
ε_{z} [%]	83.74±0.72	85.88±0.45

8.4.1. Signal efficiency

The efficiency determinations for the γ peak have been discussed in the previous section. The detection efficiency, $\varepsilon_{\mathrm{det}}$, is related to the intrinsic efficiency $\varepsilon_{\mathrm{int}}$ and the efficiency of the applied cuts,

$$\varepsilon_{\mathrm{det}} = \varepsilon_{\mathrm{int}} \cdot \varepsilon_{\mathrm{GR}} \cdot \varepsilon_{\mathrm{DCCs}} \cdot \varepsilon_{\mathrm{z}}. \tag{8.1}$$

A wide energy window contains more signal events. Therefore, an energy cut is applied. For the efficiency of the energy cut or the ROI interval, $\varepsilon_{\mathrm{ROI}}$, a normalized signal response function or the signal shape $\rho(E)$ is specified so that

$$\varepsilon_{\mathrm{ROI}} = \int_{E_{\mathrm{l}}}^{E_{\mathrm{r}}} \rho(E)\, dE, \tag{8.2}$$

where $\rho(E)$ is defined as a Gaussian function for the γ peak,

$$\rho(E) = \frac{1}{\sigma\sqrt{2\pi}} \mathrm{e}^{-\frac{(E-E_\gamma)^2}{2\sigma^2}}. \tag{8.3}$$

The standard deviation, σ, is obtained from the average energy resolution function discussed in Section 5.5.

The total detection efficiency, $\varepsilon_{\mathrm{tot}}$, is correlated with the window width of the ROI. It is expressed as the product of the overall detection efficiency in Eq. 8.1, and the energy cut efficiency $\varepsilon_{\mathrm{ROI}}$,

$$\varepsilon_{\mathrm{tot}}(E_{\mathrm{l}}, E_{\mathrm{r}}) = \varepsilon_{\mathrm{det}} \cdot \varepsilon_{\mathrm{ROI}}, \tag{8.4}$$

where E_{l} and E_{r} are the left and right boundaries of the window, respectively.

8.4.2. Background estimation

The choice of the energy window also depends on the background events that need to be estimated after applying the analysis cuts. Since a detailed background model is not available, the background distribution is approximated by an exponential function,

$$\beta(E) = \beta_0 \mathrm{e}^{-\lambda E}, \tag{8.5}$$

where β_0 in cts/(keV·kg·yr) stands for the normalized amplitude of the function, and λ in keV^{-1} denotes the decreasing rate of the background with energy. As illustrated in Fig. 8.2, there are no visible peaks in the ROI, and the background suffices to account for the events.

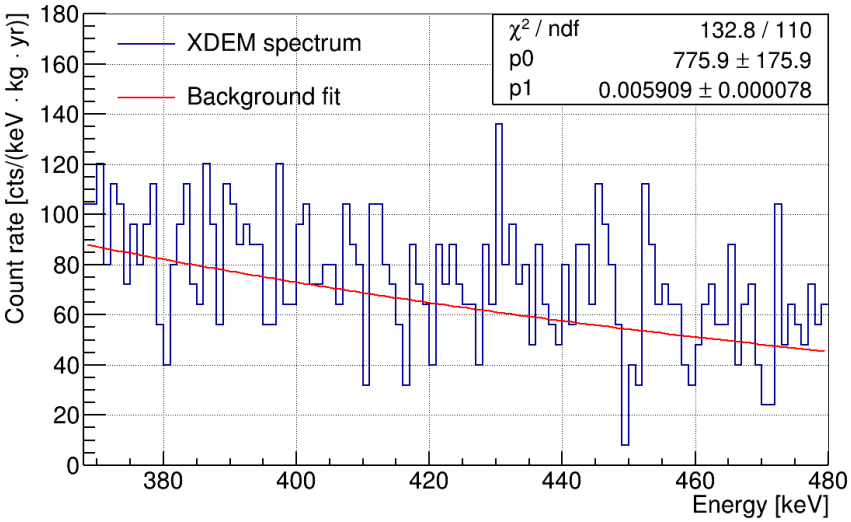

Figure 8.2.: The energy spectrum of the XDEM fitted with an exponential function with $p0$ and $p1$ denoting β_0 and λ, respectively.

With the known background shape $\beta(E)$, the number of expected background events, $\bar{b}$, is extracted from the integral of $\beta(E)$ over the given ROI of (E_l, E_r) and multiplied by the accumulated exposure mt in kg·yr,

$$\bar{b} = mt \int_{E_\mathrm{l}}^{E_\mathrm{r}} \beta_0 \mathrm{e}^{-\lambda E}\, \mathrm{d}E. \tag{8.6}$$

8.4.3. New half-life limit

According to Fig. 8.2, there is no sign of signal events. The Feldman-Cousins method considers the statistical nature of a decay process and provides a conservative upper limit for the signal sensitivity, as explained in Appendix E.1 [152]. Based on this statistical analysis approach, a lower $T_{1/2}$ limit on the decay is set.

Following the radioactive decay law, the half-life for rare nuclear decays can be deduced [153]. The $T_{1/2}$ for the investigating decay process is given by the following expression

$$T_{1/2} = \frac{\ln(2) N_A a}{M} \frac{mt\varepsilon}{S(\bar{b})} Br\, \alpha. \tag{8.7}$$

The first term contains the Avogadro constant N_A, the molar mass of the isotope M, and the natural abundance a. With these constants, the number of ^{113}Cd source atoms per kilogram is estimated to be $2.81{\times}10^{23}$. In the second term, ε is the ROI dependent detection efficiency ε_tot. $S(\bar{b})$ is the observed signal strength. The branching ratio, Br, as mentioned earlier, is

assumed to be 100%. α is the probability of the ^{113m}In de-excitation. It is deduced from an electron conversion coefficient of 0.55 [154] and has a value of 0.645.

The signal strength $S(\bar{b})$ represents a weighted sum of minimal detectable signals reported by an ensemble of identical experiments. For getting $S(\bar{b})$, all the upper limits and the corresponding probabilities are obtained from an expected background $\bar{b}$ and the predefined confidence level. The TFeldmanCousins class implemented in ROOT is used in this work.

As stated in Eq. 8.7, introducing $\varepsilon_{\mathrm{ROI}}$ to the total efficiency $\varepsilon_{\mathrm{tot}}$ can be seen as modifying the fraction of the data exposure mt and the signal strength $S(\bar{b})$ included in the analysis. The remaining question is how to find the optimal E_{l} and E_{r} to keep as many signal events as possible and discard most background events, resulting in the maximal $T_{1/2}$ sensitivity. The solution is to solve the following derivative equations

$$\frac{\partial T_{1/2}(E_{\mathrm{l}}, E_{\mathrm{r}})}{\partial E_{\mathrm{l}}} = 0, \quad \frac{\partial T_{1/2}(E_{\mathrm{l}}, E_{\mathrm{r}})}{\partial E_{\mathrm{r}}} = 0. \tag{8.8}$$

Detailed deductions are performed in Ref. [153] and summarized in Appendix E.3. It is possible to reduce the number of free variables to only one variable, ρ/β. The parameters ρ and β are associated with the signal shape and the background model, as mentioned in previous sections. This simplification is especially helpful for the Demonstrator data analysis discussed in the following section. This variable should take the same value for both the left and the right boundary of the ROI to satisfy the best ROI conditions as $\rho(E_{\mathrm{l}})/\beta(E_{\mathrm{l}}) = \rho(E_{\mathrm{r}})/\beta(E_{\mathrm{r}})$. For each ρ/β, the window width varies, and a $T_{1/2}$ sensitivity is computed with the expected number of events and the background.

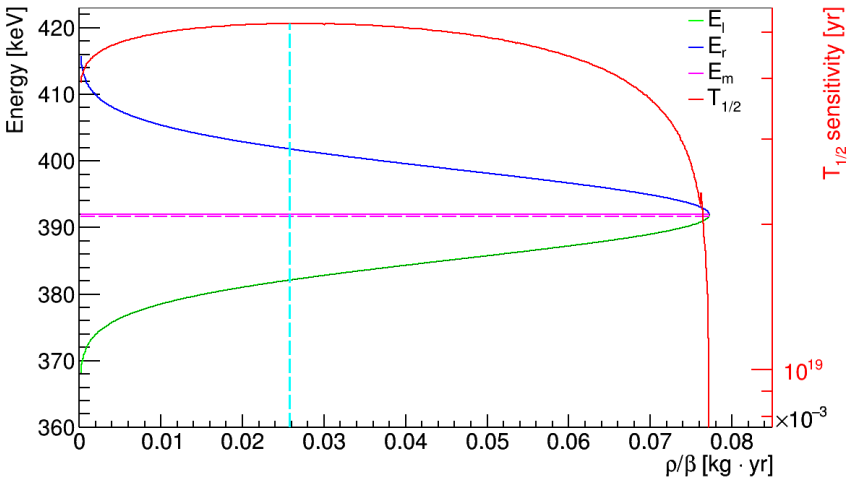

Figure 8.3.: The optimization of the ROI in dependence of ρ/β. The corresponding $T_{1/2}$ sensitivity is the red curve. The left boundary E_{l} is shown in blue color, and the right boundary E_{r} is in green. The maximum sensitivity is indicated by the dashed line in light blue and lies at 2.58×10^{-5} kg·yr. The solid magenta line shows the mean energy of the ROI at 392 keV, while the dashed line indicates the γ-line energy at 391.7 keV.

Fig. 8.3 illustrates the optimization for the ROI along with the obtained $T_{1/2}$ sensitivity

as a function of ρ/β. The best ROI is marked by the dashed blue line, crossing the optimal left and right endpoints. The optimal window is found in the energy range from 382 keV to 402 keV at a ρ/β of 2.58×10^{-5} kg·yr. The highest $T_{1/2}$ sensitivity reaches 5.21×10^{19} yr at 90% C.L. with an expected background count of 180.40.

One can see that the centered energy of the optimal ROI is slightly above the Q-value. This is preferred as the signal shape is assumed to be a Gaussian distribution symmetrical at Q-value, while the background is exponentially decreasing with energy, the signal to background ratio will thus be improved at the high energy side. The optimal interval tends to be the one with a relatively small background contribution.

8.5. Data analysis and results from the Demonstrator

A similar analysis is performed with the Demonstrator data. One major difference is that the Demonstrator dataset is partitioned by detector numbers, resulting in 61 partitions after rejecting three nonfunctional detectors. The data partitioning is to distinguish variations in detector qualities, performances, and backgrounds. Finer partitions are not made due to the statistics.

Compared to the XDEM, the Demonstrator has a relatively high background level. Sources of the background have already been discussed in Ref. [39]. In the ROI, the background is mainly contributed by surface contaminations of detectors and radioactive sources in surrounding materials. Fig. 8.4 shows the total energy spectrum of the Demonstrator applied with analysis cuts. The prominent γ-line at the 351.9 keV originates from the decay of ^{214}Pb, short-lived Radon decay products. This is because there were short periods when the Nitrogen flushing failed, leading to an increased Radon exposure. To remove data with high Radon exposure, the so-called bad period cut was applied. Each partition is individually fitted with an exponential function to describe the background distribution. The signal shape is modeled according to the energy resolution function of each detector.

Taking individual partitions into account, the resulting $T_{1/2}$ is expressed by

$$T_{1/2} = \frac{\ln(2) N_A a}{M} \frac{\sum_{n=1}^{n=61} m_{\mathrm{n}} t_{\mathrm{n}} \varepsilon_{\mathrm{n}} \int_{E_{\mathrm{l}}^n}^{E_{\mathrm{r}}^n} \rho_{\mathrm{n}}(E)\, dE}{S(\sum_{n=1}^{n=61} m_{\mathrm{n}} t_{\mathrm{n}} \int_{E_{\mathrm{l}}^n}^{E_{\mathrm{r}}^n} \beta_{\mathrm{n}}(E)\, dE)} Br\, \alpha. \tag{8.9}$$

n is the index of the partition. All the parameters depend on the partition. For each partition, an optimal interval is found so that the total $T_{1/2}$ limit reaches a maximum. Similar to the previous analysis for the XDEM, ρ/β is used to simplify Eq. 8.9 in order to find the left boundary E_{l} and the right boundary E_{r} for each data partition.

Fig. 8.5 shows that at a ρ/β of 5.85×10^{-6} kg·yr, the maximal half-life limit is 6.70×10^{19} yr with an expected number of background events of 6875. It can be also seen that some partitions have windows closed early to improve the final half-life limit. This is automatically done by the algorithm. When the window closes, $E_{\mathrm{l}} = E_{\mathrm{r}}$, the resulting ρ/β is

$$\rho/\beta = \frac{\varepsilon}{\beta_0 \sigma \sqrt{2\pi}} e^{\lambda(\frac{\lambda\sigma^2}{2} + E_\gamma)} \equiv q. \tag{8.10}$$

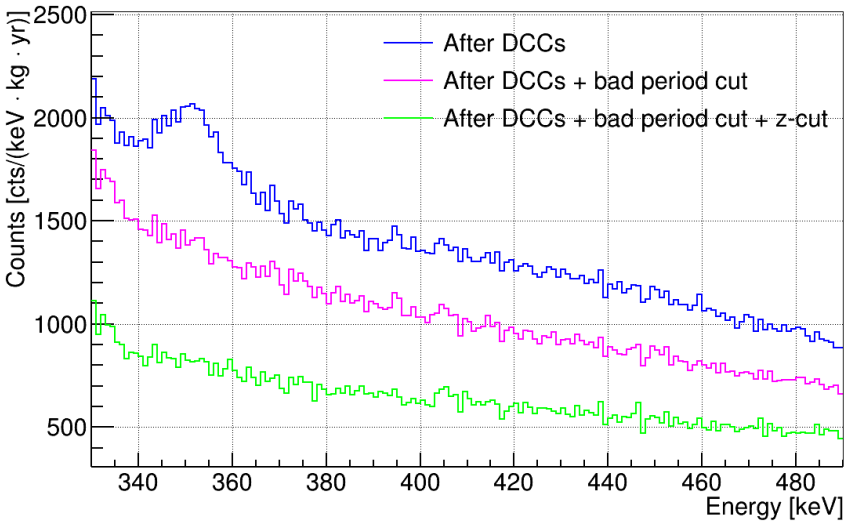

Figure 8.4.: The energy spectrum of the Demonstrator in the ROI applied with the data cleaning cuts, bad period cut, and z-cut. A significant reduction of the background is seen.

The parameter q represents the partition quality. Partitions with high quality contribute in a wider range than low quality partitions.

Even with a comparatively large exposure, the sensitivity improvement compared to the XDEM is inhibited due to a significant increase in the background of the Demonstrator. Apart from surface contaminations, it is suspected that the detector layers of the Demonstrator were contaminated with dust near the cathode. The dust may contain natural decay chains and emit energetic α and β particles, which can enter the detector and cause more events deposited near the cathode. The β-decay of ^{214}Bi with a Q-value of 3269 keV is one of the dominant sources. In addition, the Compton scattering of γ lines contributes to the low energy background. One prominent line is the 511 keV annihilation line, partly from a possible ^{22}Na contamination. Another γ-line is produced by ^{40}K probably stemming from the coating material.

The possible option to improve the sensitivity is investigated by excluding detectors from the analysis. When applying a stricter z-cut, $0.2 < z < 0.6$, the background level is reduced, but the sacrifice of the signal efficiency is also significant with a value of (43.14±0.32)% left. Overall, the sensitivity does not improve. Instead, only for highly contaminated detectors, the stricter z-cut is employed. Furthermore, detectors with a high count rate in the ROI are also removed. A sensitivity of 6.65×10^{19} yr is expected employing those additional cuts, which is comparable to the value mentioned above.

8.6. Discussion and conclusion

The TFeldmanCousins does not take uncertainties into account. This section will discuss contributions to the systematic uncertainty. The final result will be physically interpreted.

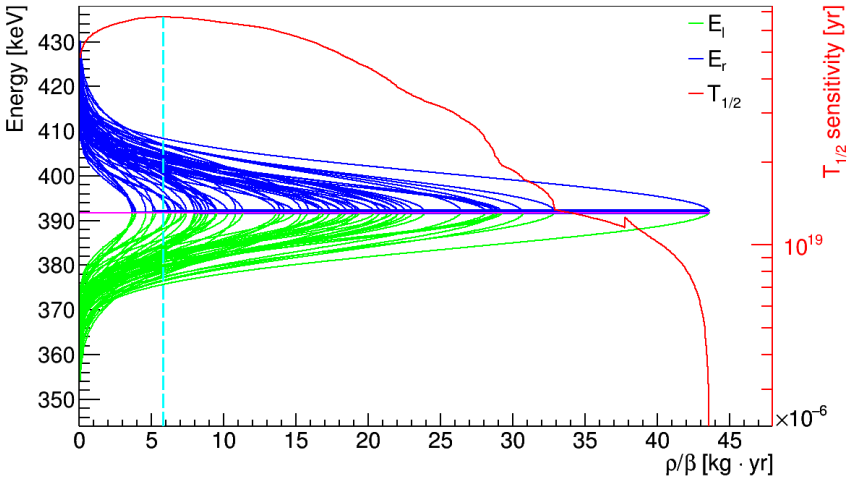

Figure 8.5.: The optimization of the ROI as a function of ρ/β. The $T_{1/2}$ sensitivity in the red curve is for all partitions. The maximal $T_{1/2}$ sensitivity is indicated by the blue dashed line. The left and right boundaries are shown in blue and green, respectively.

8.6.1. Systematic uncertainties

The obtained limit should be adjusted to account for experimental uncertainties of the signal efficiency and the background level. For this purpose, the TRolke class based on the profile likelihood method, as explained in Appendix E.2, is used to incorporate these nuisance parameters [155]. The resulting limit is also frequentist.

Uncertainties related to the signal expectation are referred to as nuisance parameters of the signal detection efficiency. Each systematic effect on the signal efficiency is evaluated separately. This is done by modifying the respective parameter while keeping the other parameters at their default values and re-calculating the efficiency. The difference between the altered efficiencies represents the associated systematic uncertainty. The main sources and their contributions to the signal efficiency are listed in Table 8.2. The systematic uncertainty of the cut efficiency is dealt with differently. A discussion of the calculation follows.

The number of source atoms directly affects the efficiency by affecting the number of signal decays. The exact content of Zinc in the $Cd_xZn_{1-x}Te$ detector (a typical x of 0.9) is an issue as Zinc is not uniformly distributed during the crystal growth. Adding Zinc to the CdTe increases the band gap and reduces the number of defects. The amount of Zinc directly affects the atom number of Cadmium isotopes as the Zinc to Cadmium ratio can be controlled. Previous works have discussed the uncertainties in detail for the XDEM and the Demonstrator detectors [43, 89]. Since the Zinc fraction varies among manufacturers and crystals, an average systematic uncertainty is cited. This value is directly added to the efficiency uncertainty.

The signal shape is defined based on the energy resolution, which varies with detectors. A broad peak within a certain energy range has less signal events compared to a sharp peak. This systematic difference can be quantified by convolving the simulated spectra with the energy resolution varied by a certain amount and repeating the efficiency calculation.

Table 8.2.: Sources of the systematic uncertainty and their contributions to the signal efficiency in percent. The uncorrelated factors are summed quadratically, while the correlated ones are combined linearly.

sources	XDEM [%]	Demonstrator [%]
Cd content	0.98	2.00
energy resolution	0.02	1.5
energy calibration	0.003	0.03
DCCs	5.45	4.00
GR	10.00	-
z-cut	9.62	10.00

The uncertainty estimation is handled differently for the XDEM and the Demonstrator. For the XDEM, the data are combined from all detectors, and the uncertainty of an average energy resolution function is propagated to the efficiency calculation. For the Demonstrator, individual detectors are analyzed due to data partition, and thus the best and worst energy resolutions are used to recalculate the efficiency. The systematic difference between the two extreme cases accounts for the uncertainty.

Similar to the influence of the energy resolution, due to the uncertainty of the energy calibration, the peak position has an intrinsic error of 0.42 keV for XDEM, which is evaluated by the shift of the γ line of ^{152}Eu at 344.28 keV with respect to the literature values. This γ-line is chosen because it is close to the ROI. For the Demonstrator, a conservative peak shift of 1.9 keV is quoted from a previous work [37]. Based on the energy shift, the efficiency uncertainty is calculated as the systematic difference between the low and high energy shifted ranges.

For the uncertainty of the cut efficiency, the systematic difference between the simulation and the measurement is evaluated accordingly. The systematic uncertainty of the DCCs is related to the detector performance and the DAQ electronics. According to the simulation, all signal events within the ROI of the γ peak should survive the DCCs. In the real data, the cut efficiency is deduced from the same energy range of calibration data. The same procedure is performed for the Demonstrator.

The GR related systematic uncertainty is extracted from the γ peak of ^{137}Cs at 662 keV, as it is the only measurement associated with the GR available now. In the simulation, the ^{137}Cs source is located 2 cm away from a single detector. The difference in the deduced signal efficiency of the full energy peak entries between the simulation and the measurement in Ref. [43] accounts for the systematic uncertainty.

Furthermore, the associated systematic uncertainty of the z-cut is deduced from the dif-

ference between the simulated and measured ^{113}Cd β-decay events. Details are discussed in Section 6.4 for the XDEM and in Ref. [37] for the Demonstrator.

The dominant contributions to the systematic uncertainty are attributed to the analysis cuts. Other factors like the varying detector mass have a negligible effect on the intrinsic efficiency ϵ_{int}, as it has been measured with a precision of milligrams. With a relatively large number of signals, the statistical uncertainty of the signal efficiency in the simulation also plays a minor role.

A final uncertainty value is obtained by adding the individual values from the Cd content, energy resolution, energy calibration, and cuts quadratically, assuming no correlations among them. As the cuts are correlated, a linear summation combines the uncertainties from the DCCs, GR, and z-cut. The total uncertainties are 25.09% for the XDEM and 14.71% for the Demonstrator.

The uncertainty on the background fit is investigated by fitting the event distribution with a second-order polynomial for comparison. A background fluctuation of 12.56% is treated as a systematic uncertainty for the XDEM. For the Demonstrator, a global fit is done by grouping all the detectors. The difference between the global fit and the summed individual fits is extracted.

In summary, systematic uncertainties on the signal efficiency are estimated with the help of Monte Carlo simulations and combined into a single value. The background uncertainty is obtained from different models. After considering the systematic effect, the final half-life limits at 90% C.L. are 4.86×10^{19} yr for the XDEM, and 6.85×10^{19} yr for the Demonstrator. Underestimating the background tends to weaken the result. A better background estimation is expected to improve the limit.

8.6.2. Discussion of the results

Although current theories can not constrain the CNC-decay parameters, the obtained experimental half-life limits provide the relative strength of the CNC process to the corresponding charge-conserving process.

According to Bahcall's theory, by including a small CNC component in the weak interactions with the usual form and a neutrino replacing the electron in the lepton current [156], the relative strength of the CNC process related to the neutron decay branching ratio ϵ^2 can be expressed as

$$\epsilon^2 = \frac{\Gamma(n \to p + \nu_e + \bar{\nu_e})}{\Gamma(n \to p + e^- + \bar{\nu_e})} = \frac{\tau_n}{\tau_{\text{CNC}}} \left[\left(\frac{W(n)}{W(^{113\text{m}}\text{In})} \right)^5 \frac{ft(^{113\text{m}}\text{In})}{ft(n)} \right] \tag{8.11}$$

where $\tau(n)$ is the mean life of free neutron (877.75 s) [157], τ_{CNC} stands for the mean life of the CNC decay of the nuclide. $W(n)$ is the $n-p$ mass difference (1.293 MeV) [158], and W($^{113\text{m}}$In) is the nuclear mass difference between ^{113}Cd and $^{113\text{m}}$In in the CNC decay, which is around 0.838 MeV [159]. The $ft(n)$ product, or comparative half-life, is 1043 s for neutron. Here f, the phase space factor, takes the kinematic constraints into account and corrects all half-lives to a comparable basis [160]. $ft(^{113\text{m}}\text{In})$ is the comparative half-life of the EC of

^{113m}In to ^{113}Cd, and its value is quoted from Ref. [148]. These terms result in a branching ratio of $\epsilon^2 \leq 1.08\times10^{-20}$ at 90% C.L. for the Demonstrator that has a higher half-life limit.

New limits have been obtained for the CNC-decay of ^{113}Cd using 0.18 kg·yr of XDEM and the 1.25 kg·yr of Demonstrator data. This analysis is based on a peak searching method with sensitivity optimization. Compared to the previous work, the new limit has improved by more than one order of magnitude. Due to the dominant backgrounds, the Demonstrator does not improve significantly compared to the XDEM in sensitivity despite the higher exposure, which also demonstrates the great potential of the XDEM for rare event searches. An exposure of 1 kg·yr would increase the sensitivity by a factor of 2.4.

9. Summary and outlook

The COBRA extended Demonstrator (XDEM) was newly upgraded, aiming to improve the sensitivity for double beta decays while keeping a low background level. The present work has covered various aspects of the experiment, from detector characterizations and background reductions to sensitivity studies for rare nuclear decays.

The new CZT detector employs a novel readout, a quad-coplanar grid (qCPG) surrounded by a guard ring, which is beneficial in background suppression and spectral performance. However, its non-uniform weighting potential distribution poses challenges to event reconstruction. For this reason, a simulation framework based on COMSOL and Geant4 has been developed to model pulse shapes for the CZT detectors. The pulse simulation has allowed us to gain a good understanding of the detector response under different electrode configurations.

As opposed to the simulation where hardware can be perfect, in the real data, there are electronic imperfections and electron trapping that have to be corrected for in order to achieve an optimal detector performance. For this purpose, the methods for calculating the gain factor and the weighting factor have been refined significantly. In addition to the reconstruction of the energy deposition and the interaction depth z, the qCPG detector also allows for the determination of the x, y position by analyzing the non-uniform weighting potentials.

Various procedures are used to ensure the integrity of the measured data. First of all, data-taking is monitored based on thorough checks with a special focus on environmental conditions and the electronic stability. Subsequent analyses are performed to distinguish between well functional and problematic channels. The non-unique single β-decay of ^{113}Cd, which is intrinsic to the detectors, is used to monitor the long-term detector stability. A constant decay rate has proved that most detectors show excellent stability over one year.

The two detector batches from different manufacturers show slight differences in their physical properties and performances. An average energy resolution of (1.14±0.04)% at 2615 keV is achieved for all the functional detectors.

One major issue for COBRA is the background level. There are different ways to reduce backgrounds as much as possible. Firstly, the new qCPG detector has the intrinsic capabilities of vetoing γ-rays and rejecting the dominant surface contaminations through its guard ring, which was not possible in the previous Demonstrator. Secondly, the new setup is shielded by multi-layer shielding from natural backgrounds and has been constructed to be as radiopure as possible to reduce potential contaminations. Furthermore, a pulse shape analysis is developed based on the knowledge gained from the Demonstrator to further suppress any remaining backgrounds.

The precision of the pulse shape discrimination relies on the noise level of the system. Hence, several noise reduction techniques have been investigated. This study has provided clean datasets for pulse shape discriminations. The other motivation for developing denoising

methods is to be able to retrieve the data strongly affected by noise. This part was not as successful as expected. However, this work leads to an analytic tool for further studies.

Analysis cuts are established for the XDEM based on the pulse properties related to the charge carrier transport and physical parameters such as interaction depth. These cuts are optimized to remove random noise, surface contaminations, and γ-rays. Simulated pulses have been proven useful for estimating the signal cut efficiencies for double beta decays and other rare nuclear decays that cannot be investigated experimentally. After applying these cuts, the prominent backgrounds are effectively suppressed. A background index of $(0.053\pm0.031)\,\mathrm{cts/(keV{\cdot}kg{\cdot}yr)}$ is achieved in the ROI of the $0\nu\beta\beta$-decay of ^{116}Cd, while the background level of the Demonstrator is $1.2\,\mathrm{cts/(keV{\cdot}kg{\cdot}yr)}$ for the same energy region.

Measuring the half-life of the ^{116}Cd $2\nu\beta\beta$-decay is challenging because of its continuous spectrum. A preliminary background model with the commissioning data is developed based on Monte Carlo simulations to understand potential background sources and their contribution in the ROI. For setting a half-life (limit) on the decay, a more detailed background description with a larger data exposure is necessary. The potential of finding excited state transitions of the decay is investigated with simulation data, assuming that only the $2\nu\beta\beta$-decay to the ground state is present as the background. The investigation has shown an improvement in the signal sensitivity compared to the Demonstrator's study and also has provided a basic optimization analysis for future studies.

A dedicated investigation of the charge non-conserving decay of ^{113}Cd has been carried out for both the XDEM and the Demonstrator. This search is based on a peak searching analysis. The signal region is optimized to increase the sensitivity and remove bias in choosing the energy window. Under the assumption of no signal being found in the ROI of the 391.7 keV γ-rays, the half-life limit is updated. The half-life limit has been improved by more than one order of magnitude compared to previous work and helps constrain the branching ratio of the neutron decay.

This work demonstrates the great potential of the XDEM in searches for rare events and the feasibility of using qCPG CZT detectors in a double beta decay experiment. It is planned to transfer all the detectors from LNGS to Felsenkeller Shallow Underground Laboratory and install them. For the upcoming setup, several improvements could be made. One persistent issue at the LNGS is the high-level noise caused by analog electronics, which is identified in this work using Fourier analysis. Reducing noise means a lower energy threshold can be applied, which would be interesting for measuring low energy signal events, like the ^{113}Cd β-decay spectrum. To decrease the noise level, integrated readout electronics with low noise could be considered. Moreover, the noise reduction technique could be further optimized and applied to digital signal processing.

In the shallow underground laboratory, the muon-induced background will be prominent. Therefore, it is necessary to have an active shielding layer like a muon panel to veto muons besides using the old shielding and radiopure materials. Meanwhile, dedicated α measurements would be helpful for the background description. Furthermore, the detector could be used for coincidence measurements. Lastly, regarding the pulse shape simulation, it is possible to implement the charge cloud diffusion model to further investigate particle identification with α and β particles.

Bibliography

[1] K. Zuber, "COBRA—double beta decay searches using CdTe detectors", Physics Letters B **519**, 1 (2001) DOI: 10.1016/S0370-2693(01)01056-5.

[2] K. C. Wang, "A suggestion on the detection of the neutrino", Physical Review **61**, 97 (1942) DOI: 10.1103/PhysRev.61.97.

[3] J. S. Allen, "Experimental evidence for the existence of a neutrino", Physical Review **61**, 692 (1942) DOI: 10.1103/PhysRev.61.692.

[4] C. L. Cowan Jr, F. Reines, F. Harrison, and et al., "Detection of the free neutrino: a confirmation", Science **124**, 103 (1956) DOI: 10.1126/science.124.3212.103.

[5] K. Zuber, *Neutrino physics* (Taylor & Francis, 2020), DOI: 10.1201/9781315195612.

[6] Z. Xing and S. Zhou, *Neutrinos in particle physics, astronomy and cosmology* (Springer Science & Business Media, 2011), DOI: 10.1007/978-3-642-17560-2.

[7] H. Ejiri, J. Suhonen, and K. Zuber, "Neutrino–nuclear responses for astro-neutrinos, single beta decays and double beta decays", Physics Reports **797**, 1 (2019) DOI: 10.1016/j.physrep.2018.12.001.

[8] K. Zuber, "The discovery of neutrino oscillations", Annalen der Physik **528**, 452 (2016) DOI: 10.1002/andp.201600097.

[9] D. Akimov, J. Albert, P. An, and et al., "Observation of coherent elastic neutrino-nucleus scattering", Science **357**, 1123 (2017) DOI: 10.1126/science.aao0990.

[10] A. Taroni, "Nobel prize 2015: kajita and mcdonald", Nature Physics **11**, 891 (2015) DOI: 10.1038/nphys3543.

[11] G. Bellini, L. Ludhova, G. Ranucci, and et al., "Neutrino oscillations", Advances in High Energy Physics **2014** (2014) DOI: 10.1155/2014/191960.

[12] T. Kajita, "Nobel lecture: discovery of atmospheric neutrino oscillations", Reviews of Modern Physics **88**, 030501 (2016) DOI: 10.1103/RevModPhys.88.030501.

[13] Y. Suzuki, "The super-kamiokande experiment", The European Physical Journal C **79**, 1 (2019) DOI: 10.1140/epjc/s10052-019-6796-2.

[14] M. Decowski, K. Collaboration, et al., "Kamland's precision neutrino oscillation measurements", Nuclear Physics B **908**, 52 (2016) DOI: 10.1016/j.nuclphysb.2016.04.014.

[15] A. Abusleme, T. Adam, S. Ahmad, and et al., "JUNO physics and detector", arXiv preprint arXiv:2104.02565 (2021) DOI: 10.48550/arXiv.2104.02565.

[16] B. Jamieson, "Future neutrino experiments", arXiv preprint arXiv:2207.05044 (2022) DOI: 10.48550/arXiv.2207.05044.

[17] Y. Cai, T. Han, T. Li, and et al., "Lepton number violation: seesaw models and their collider tests", Frontiers in Physics **6**, 40 (2018) DOI: 10.3389/fphy.2018.00040.

[18] T. K. Collaboration, "Direct neutrino-mass measurement with sub-electronvolt sensitivity", Nature Physics **18**, 160 (2022) DOI: 10.1038/s41567-021-01463-1.

[19] C. Velte, F. Ahrens, A. Barth, and et al., "High-resolution and low-background 163Ho spectrum: interpretation of the resonance tails", The European Physical Journal C **79**, 1 (2019) DOI: 10.1140/epjc/s10052-019-7513-x.

[20] M. De Gerone, B. Alpert, M. Balata, and et al., "Status of the HOLMES experiment", Journal of Low Temperature Physics, 1 (2022) DOI: 10.1007/s10909-022-02895-6.

[21] T. P. Collaboration, "Planck 2018 results-VI. cosmological parameters", Astronomy & Astrophysics **641**, A6 (2020) DOI: 10.1051/0004-6361/201833910e.

[22] A. Zolotarova, "Bolometric double beta decay experiments: review and prospects", Symmetry **13**, 2255 (2021) DOI: 10.3390/sym13122255.

[23] M. Goeppert-Mayer, "Double beta-disintegration", Physical Review **48**, 512 (1935) DOI: 10.1103/PhysRev.48.512.

[24] V. I. Tretyak and Y. G. Zdesenko, "Tables of double beta decay data—an update", Atomic Data and Nuclear Data Tables **80**, 83 (2002) DOI: 10.1006/adnd.2001.0873.

[25] S. Stoica and M. Mirea, "Phase space factors for double-beta decays", Frontiers in Physics **7**, 12 (2019) DOI: 10.3389/fphy.2019.00012.

[26] H. Ejiri, "Nuclear matrix elements for β and $\beta\beta$ decays and quenching of the weak coupling gA in QRPA", Frontiers in Physics **7**, 30 (2019) DOI: 10.3389/fphy.2019.00030.

[27] P. Vogel, "Nuclear structure and double beta decay", Journal of Physics G: Nuclear and Particle Physics **39**, 124002 (2012) DOI: 10.1088/0954-3899/39/12/124002.

[28] S. Dell'Oro, S. Marcocci, M. Viel, and et al., "Neutrinoless double beta decay: 2015 review", Advances in High Energy Physics **2016**, 1 (2016) DOI: 10.1155/2016/2162659.

[29] M. Agostini, G. Araujo, A. Bakalyarov, and et al., "Final results of GERDA on the search for neutrinoless double-β decay", Physical review letters **125**, 252502 (2020) DOI: 10.1103/PhysRevLett.125.252502.

[30] S. Alvis, I. Arnquist, F. Avignone III, and et al., "Search for neutrinoless double-β decay in 76Ge with 26 kg yr of exposure from the Majorana Demonstrator", Physical Review C **100**, 025501 (2019) DOI: 10.1103/PhysRevC.100.025501.

[31] V. Albanese, R. Alves, M. Anderson, and et al., "The SNO+ experiment", Journal of Instrumentation **16**, P08059 (2021) DOI: 10.1088/1748-0221/16/08/P08059.

[32] A. Jeremie, "The SuperNEMO demonstrator double beta experiment", Nuclear Instruments and Methods in Physics Research Section A: Accelerators, Spectrometers, Detectors and Associated Equipment **958**, 162115 (2020) DOI: 10.1016/j.nima.2019.04.069.

[33] D. Adams, C. Alduino, K. Alfonso, and et al., "Search for double-beta decay of 130Te to the 0+ states of 130Xe with CUORE", The European Physical Journal C **81**, 567 (2021) DOI: 10.1140/epjc/s10052-021-09317-z.

[34] J. Albert, P. Barbeau, D. Beck, and et al., "Measurement of the drift velocity and transverse diffusion of electrons in liquid xenon with the EXO-200 detector", Physical Review C **95**, 025502 (2017) DOI: 10.1103/PhysRevC.95.025502.

[35] W. Armstrong, "CUPID pre-CDR", arXiv. org Repository **2019** (2019) DOI: 10.48550/arXiv.1907.09376.

[36] K. Alfonso, A. Armatol, C. Augier, and et al., "CUPID: the next-generation neutrinoless double beta decay experiment", Journal of Low Temperature Physics, 1 (2022) DOI: 10.1007/s10909-022-02909-3.

[37] J. Ebert, M. Fritts, D. Gehre, and et al., "Results of a search for neutrinoless double-β decay using the COBRA demonstrator", Physical Review C **94**, 024603 (2016) DOI: 10.1103/PhysRevC.94.024603.

[38] L. Bodenstein-Dresler, Y. Chu, D. Gehre, and et al., "Quenching of gA deduced from the β-spectrum shape of 113Cd measured with the C0BRA experiment", Physics Letters B **800**, 135092 (2020) DOI: 10.1016/j.physletb.2019.135092.

[39] S. Zatschler, "Pulse-shape studies with coplanar grid CdZnTe detectors and searches for rare nuclear decays with the C0BRA experiment", PhD thesis (TU Dresden, Dresden, 2020), DOI: https://nbn-resolving.org/urn:nbn:de:bsz:14-qucosa2-724352.

[40] G. Bellini, J. Benziger, D. Bick, and et al., "Cosmic-muon flux and annual modulation in Borexino at 3800 m water-equivalent depth", Journal of Cosmology and Astroparticle Physics **2012**, 015 (2012) DOI: 10.1088/1475-7516/2012/05/015.

[41] J. Tebrügge, "Commissioning of the COBRA demonstrator and investigation of surface events as its main background", PhD thesis (TU Dortmund, Dortmund, 2016), DOI: 10.17877/DE290R-17197.

[42] J. Ebert, M. Fritts, D. Gehre, and et al., "The COBRA demonstrator at the LNGS underground laboratory", Nuclear Instruments and Methods in Physics Research Section A: Accelerators, Spectrometers, Detectors and Associated Equipment **807**, 114 (2016) DOI: 10.1016/j.nima.2015.10.079.

[43] R. Temminghoff, "The C0BRA extended demonstrator-conception, characterization, commissioning", PhD thesis (TU Dortmund, Dortmund, 2019), DOI: 10.17877/DE290R-20430.

[44] J.-H. Arling, L. Bodenstein-Dresler, Y. Chu, and et al., "Commissioning of the C0BRA extended demonstrator at the LNGS", Nuclear Instruments and Methods in Physics Research Section A: Accelerators, Spectrometers, Detectors and Associated Equipment, 165524 (2021) DOI: 10.1016/j.nima.2021.165524.

[45] O. Azzolini, J. Beeman, F. Bellini, and et al., "Search for neutrinoless double beta decay of 64Zn and 70Zn with CUPID-0", The European Physical Journal C **80**, 1 (2020) DOI: 10.1140/epjc/s10052-020-8280-4.

[46] F. Bellini, M. Beretta, L. Cardani, and et al., "Search for double β-decay modes of 64Zn using purified zinc", The European Physical Journal C **81**, 1 (2021) DOI: 10.1140/epjc/s10052-021-08918-y.

[47] V. Tretyak, P. Belli, R. Bernabei, and et al., "First results of the experiment to search for 2β decay of 106Cd with 106CdWO4 crystal scintillator in coincidence with four crystals HPGe detector", in Epj web of conferences, Vol. 65 (EDP Sciences, 2014), p. 01004, DOI: 10.1051/epjconf/20136501004.

[48] P. Belli, R. Bernabei, V. Brudanin, and et al., "Search for double beta decay in 106Cd in the DAMA/CRYS setup", in Aip conference proceedings, Vol. 1894, 1 (AIP Publishing LLC, 2017), p. 020005, DOI: 10.1063/1.5007630.

[49] P. Belli, R. Bernabei, F. Cappella, and et al., "Search for double-β decay processes in 108Cd and 114Cd with the help of the low-background CdWO4 crystal scintillator", The European Physical Journal A **36**, 167 (2008) DOI: 10.1140/epja/i2008-10593-6.

[50] A. Barabash, P. Belli, R. Bernabei, and et al., "Final results of the aurora experiment to study 2β decay of 116Cd with enriched $CdWO_4$ crystal scintillators", Physical Review D **98**, 092007 (2018) DOI: 10.1103/PhysRevD.98.092007.

[51] D. Adams, C. Alduino, K. Alfonso, and et al., "Search for neutrinoless $\beta+$ EC decay of 120Te with CUORE", Physical Review C (2022) DOI: 10.1103/PhysRevC.97.055502.

[52] A. Barabash, F. Hubert, P. Hubert, and et al., "New limits on the $\beta+$ EC and ECEC processes in 120Te", Journal of Physics G: Nuclear and Particle Physics **34**, 1721 (2007) DOI: 10.1088/0954-3899/34/7/012.

[53] V. Dompè, D. Adams, C. Alduino, and et al., "Expected sensitivity to 128Te neutrinoless double beta decay with the CUORE TeO2 cryogenic bolometers", Journal of Low Temperature Physics, 1 (2022) DOI: 10.1007/s10909-022-02738-4.

[54] "Search for Majorana neutrinos exploiting millikelvin cryogenics with CUORE", Nature **604**, 53 (2022) DOI: 10.1038/s41586-022-04497-4.

[55] Z. He, "Review of the Shockley–Ramo theorem and its application in semiconductor gamma-ray detectors", Nuclear Instruments and Methods in Physics Research Section A: Accelerators, Spectrometers, Detectors and Associated Equipment **463**, 250 (2001) DOI: 10.1016/S0168-9002(01)00223-6.

[56] F. Zhang, Z. He, D. Xu, and et al., "Improved resolution for 3-D position sensitive CdZnTe spectrometers", IEEE Transactions on Nuclear Science **51**, 2427 (2004) DOI: 10.1109/TNS.2004.835635.

[57] A. Bolotnikov, N. M. Abdul-Jabbar, S. Babalola, and et al., "Optimization of virtual Frisch-grid CdZnTe detector designs for imaging and spectroscopy of gamma rays", in Hard x-ray and gamma-ray detector physics ix, Vol. 6706 (International Society for Optics and Photonics, 2007), p. 670603, DOI: 10.1117/12.736654.

[58] P. N. Luke, "Single-polarity charge sensing in ionization detectors using coplanar electrodes", Applied Physics Letters **65**, 2884 (1994) DOI: 10.1063/1.112523.

[59] P. Luke, "Unipolar charge sensing with coplanar electrodes-application to semiconductor detectors", IEEE Transactions on Nuclear Science **42**, 207 (1995) DOI: 10.1109/23.467848.

[60] J. H. Arling, "Characterization of coplanar grid CdZnTe detectors and instrumentation of the guardring for the cobra experiment", MA thesis (TU Dortmund, Dortmund, 2016).

[61] W. Shockley, "Currents to conductors induced by a moving point charge", Journal of applied physics **9**, 635 (1938) DOI: 10.1063/1.1710367.

[62] S. Ramo, "Currents induced by electron motion", Proceedings of the IRE **27**, 584 (1939) DOI: 10.1109/JRPROC.1939.228757.

[63] M. Fritts, J. Durst, T. Göpfert, and et al., "Analytical model for event reconstruction in coplanar grid CdZnTe detectors", Nuclear Instruments and Methods in Physics Research Section A: Accelerators, Spectrometers, Detectors and Associated Equipment **708**, 1 (2013) DOI: 10.1016/j.nima.2013.01.004.

[64] P. N. Luke, M. Amman, and J. S. Lee, "Factors affecting energy resolution of coplanar-grid CdZnTe detectors", IEEE Transactions on Nuclear Science **51**, 1199 (2004) DOI: 10.1109/TNS.2004.829441.

[65] T. Wester, "Characterization of CdZnTe coplanar grid detectors and pulse shape analysis for the C0BRA experiment", MA thesis (TU Dresden, Dresden, 2012).

[66] P. Luke, M. Amman, T. Prettyman, and et al., "Electrode design for coplanar-grid detectors", IEEE Transactions on Nuclear Science **44**, 713 (1997) DOI: 10.1109/23.603739.

[67] Z. He, G. Knoll, D. Wehe, and et al., "Coplanar grid patterns and their effect on energy resolution of CdZnTe detectors", Nuclear Instruments and Methods in Physics Research Section A: Accelerators, Spectrometers, Detectors and Associated Equipment **411**, 107 (1998) DOI: 10.1016/S0168-9002(98)00285-X.

[68] J. Ebert, C. Gößling, D. Gehre, and et al., "Long-term stability of underground operated CZT detectors based on the analysis of intrinsic 113Cd β–decay", Nuclear Instruments and Methods in Physics Research Section A: Accelerators, Spectrometers, Detectors and Associated Equipment **821**, 109 (2016) DOI: 10.1016/j.nima.2016.03.012.

[69] J.-H. Arling, M. Gerhardt, C. Gößling, and et al., "Suppression of alpha-induced lateral surface events in the COBRA experiment using CdZnTe detectors with an instrumented guard-ring electrode", Journal of Instrumentation **12**, P11025 (2017) DOI: 10.1088/1748-0221/12/11/P11025.

[70] S. Agostinelli, J. Allison, K. a. Amako, and et al., "Geant4—a simulation toolkit", Nuclear instruments and methods in physics research section A: Accelerators, Spectrometers, Detectors and Associated Equipment **506**, 250 (2003) DOI: 10.1016/S0168-9002(03)01368-8.

[71] J. Pérez, Z. He, D. Wehe, and et al., "Estimate of large CZT detector absolute efficiency", IEEE Transactions on Nuclear Science **49**, 2010 (2002) DOI: 10.1109/TNS.2002.801512.

[72] Z. He, B. W. Sturm, and E. Rhodes, "Investigation of a large volume multi-pair coplanar grid CdZnTe detector for improved detection efficiency", in Ieee nuclear science symposium conference record, 2005, Vol. 2 (IEEE, 2005), pp. 1159–1162, DOI: 10.1109/NSSMIC.2005.1596456.

[73] A. Bolotnikov, S. Babalola, G. Camarda, and et al., "Performance of a large volume 20 ×20× 15 mm3 CPG detector", IEEE Transactions on Nuclear Science **58**, 3167 (2011) DOI: 10.1109/TNS.2011.2167984.

[74] M. Amman, P. Luke, and J. Lee, "CdZnTe material uniformity and coplanar-grid gamma-ray detector performance", in 1999 ieee nuclear science symposium. conference record. 1999 nuclear science symposium and medical imaging conference (cat. no. 99ch37019), Vol. 1 (IEEE, 1999), pp. 182–189, DOI: 10.1109/NSSMIC.1999.842472.

[75] A. Bolotnikov, G. Camarda, G. Carini, and et al., "Performance-limiting defects in CdZnTe detectors", IEEE Transactions on Nuclear Science **54**, 821 (2007) DOI: 10.1109/TNS.2007.894555.

[76] A. E. Bolotnikov, S. O. Babalola, G. S. Camarda, and et al., "Extended defects in CdZnTe radiation detectors", IEEE Transactions on Nuclear Science **56**, 1775 (2009) DOI: 10.1109/TNS.2009.2019960.

[77] A. Bolotnikov, G. Camarda, G. Carini, and et al., "Cumulative effects of te precipitates in CdZnTe radiation detectors", Nuclear Instruments and Methods in Physics Research Section A: Accelerators, Spectrometers, Detectors and Associated Equipment **571**, 687 (2007) DOI: 10.1016/j.nima.2006.11.023.

[78] A. Bolotnikov, G. Camarda, E. Chen, and et al., "CdZnTe position-sensitive drift detectors with thicknesses up to 5 cm", Applied Physics Letters **108**, 093504 (2016) DOI: 10.1063/1.4943161.

[79] M. Amman, J. S. Lee, and P. N. Luke, "Temperature study of CdZnTe coplanar-grid detectors", IEEE transactions on nuclear science **53**, 3035 (2006) DOI: 10.1109/TNS.2006.879909.

[80] A. Bolotnikov, G. Camarda, Y. Cui, and et al., "Internal electric-field-lines distribution in CdZnTe detectors measured using X-ray mapping", IEEE Transactions on nuclear science **56**, 791 (2009) DOI: 10.1109/TNS.2008.2007904.

[81] G. Yang, A. E. Bolotnik, G. Camarda, and et al., "Opto-electrical characterization and X-ray mapping of large-volume cadmium zinc telluride radiation detectors", MRS Online Proceedings Library (OPL) **1164** (2009) DOI: 10.1557/PROC-1164-L10-07.

[82] H. Chen, S. Awadalla, K. Iniewski, and et al., "Characterization of large CdZnTe crystals grown by traveling heater method", Journal of Applied Physics **103**, 014903 (2008) DOI: 10.1063/1.2828170.

[83] M. Amman, J. S. Lee, P. N. Luke, and et al., "Evaluation of THM-grown CdZnTe material for large-volume gamma-ray detector applications", IEEE Transactions on Nuclear Science **56**, 795 (2009) DOI: 10.1109/TNS.2008.2010402.

[84] S. Awadalla, J. Mackenzie, H. Chen, and et al., "Characterization of detector-grade CdZnTe crystals grown by traveling heater method (THM)", Journal of Crystal Growth **312**, 507 (2010) DOI: 10.1016/j.jcrysgro.2009.11.007.

[85] A. Owens, T. Buslaps, V. Gostilo, and et al., "Hard X- and γ-ray measurements with a large volume coplanar grid CdZnTe detector", Nuclear Instruments and Methods in Physics Research Section A: Accelerators, Spectrometers, Detectors and Associated Equipment **563**, 242 (2006) DOI: 10.1016/j.nima.2006.01.120.

[86] B. W. Sturm, "Gamma-ray spectroscopy using depth-sensing coplanar grid CdZnTe semiconductor detectors", PhD thesis (Citeseer, 2006).

[87] Y. Ma, S. Xiao, G. Yang, and et al., "Design and study of a coplanar grid array CdZnTe detector for improved spatial resolution", Applied Radiation and Isotopes **94**, 314 (2014) DOI: 10.1016/j.apradiso.2014.09.003.

[88] R. Theinert and C. collaboration, "Characterization of a large CdZnTe detector with a coplanar quad-grid design", Nuclear Instruments and Methods in Physics Research Section A: Accelerators, Spectrometers, Detectors and Associated Equipment **845**, 181 (2017) DOI: 10.1016/j.nima.2016.06.018.

[89] D. Gehre, "Investigations on CdZnTe semiconductor-detectors for the search of the neutrinoless double beta decay", PhD thesis (TU Dresden, Dresden, 2017), DOI: http://tud.qucosa.de/api/qucosa%3A31119/attachment/ATT-0/.

[90] G. S. Camarda, A. E. Bolotnikov, Y. Cui, and et al., "Polarization studies of CdZnTe detectors using synchrotron X-ray radiation", IEEE Transactions on Nuclear Science **55**, 3725 (2008) DOI: 10.1109/NSSMIC.2007.4436508.

[91] K. Rohatsch, "Charakterisierung von großvolumigen CdZnTe-Detektoren mit segmentierter CPG-Anodenkonfiguration für das COBRA Experiment", MA thesis (TU Dresden, Dresden, 2016).

[92] M. C. Schlarb, "Simulation and real-time analysis of pulse shapes from segmented HPGe-detectors", PhD thesis (TU Muechen, Muechen, 2009), DOI: 21317703.

[93] A. Pandey, D. Singh, and V. Singh, "Pulse shape simulation of p-type point contact germanium detector for the Majorana Demonstrator experiment", arXiv preprint arXiv:2103.09679 (2021) DOI: 10.48550/arXiv.2103.09679.

[94] H. Wilsenach, "Long live alpha decay", PhD thesis (TU Dresden, Dresden, 2021), DOI: https://www.tib.eu/de/suchen/id/TIBKAT:1758251352/Long-live-alpha-decay?cHash=a0f76a7dcbca67f539487d49a152e7ae.

[95] *COMSOL*, (2021) https://www.comsol.com/ (visited on 09/13/2021).

[96] *AutoCAD*, (2023) https://www.autodesk.com/ (visited on 01/06/2023).

[97] T. Prettyman, C. Cooper, P. Luke, and et al., "Physics-based generation of gamma-ray response functions for CdZnTe detectors", Journal of radioanalytical and nuclear chemistry **233**, 257 (1998) DOI: 10.1007/BF02389681.

[98] C. Canali, M. Martini, G. Ottaviani, and et al., "Transport properties of CdTe", Physical Review B **4**, 422 (1971) DOI: 10.1103/PhysRevB.4.422.

[99] J. Fink, H. Krueger, P. Lodomez, and et al., "Characterization of charge collection in CdTe and CZT using the transient current technique", Nuclear Instruments and Methods in Physics Research Section A: Accelerators, Spectrometers, Detectors and Associated Equipment **560**, 435 (2006) DOI: 10.1016/j.nima.2006.01.072.

[100] H. Rebber, "Discrimination of alpha particles in CdZnTe detectors with coplanar grid", MA thesis (Uni Hamburg, Hamburg, 2015).

[101] *ROOT*, (2021) https://root.cern.ch/root/ (visited on 04/13/2021).

[102] N. Heidrich, "Monte Carlo-based development of a shield and total background estimation for the COBRA experiment", PhD thesis (Universität Hamburg, Hamburg, 2014), DOI: 10.3204/PUBDB-2014-04120.

[103] *DECAY0*, (2022) https://github.com/BxCppDev/bxdecay0 (visited on 01/10/2022).

[104] C. Herrmann, "Monte-Carlo based studies of potential background in the XDEM-phase of the C0BRA experiment", MA thesis (TU Dortmund, Dortmund, 2018).

[105] *GDML*, (2023) https://physics.nist.gov/cgi-bin/Xcom/xcom2 (visited on 06/28/2021).

[106] O. Schulz, "Exploration of new data acquisition and background reduction techniques for the cobra experiment", PhD thesis (TU Dortmund, Dortmund, 2011).

[107] R. Temminghoff, "Investigation of the depth reconstruction and search for local performance variations with a large coplanar-quad-grid CdZnTe detector", IEEE Transactions on Nuclear Science **64**, 1934 (2017) DOI: 10.1109/TNS.2017.2711922.

[108] P. N. Luke and M. Amman, "Room-temperature replacement for Ge detectors—Are we there yet?", IEEE Transactions on nuclear science **54**, 834 (2007) DOI: 10.1109/TNS.2007.903184.

[109] Z. He and B. W. Sturm, "Characteristics of depth-sensing coplanar grid CdZnTe detectors", Nuclear Instruments and Methods in Physics Research Section A: Accelerators, Spectrometers, Detectors and Associated Equipment **554**, 291 (2005) DOI: 10.1016/j.nima.2005.06.064.

[110] J. Dawson, C. Montag, C. Reeve, and et al., "An investigation on cooling of CZT coplanar grid detectors", Nuclear Instruments and Methods in Physics Research Section A: Accelerators, Spectrometers, Detectors and Associated Equipment **599**, 209 (2009) DOI: 10.1016/j.nima.2008.11.013.

[111] H. Spieler, "Analog and digital electronics for detectors", Proceedings of the 2003 ICFA School on Instrumentation, Itacuruca, Brazil (2003) DOI: https://www-physics.lbl.gov/~spieler/ICFA_Rio_2003/index.html.

[112] P. Luke, M. Amman, J. Lee, and et al., "Noise in CdZnTe detectors", in 2000 ieee nuclear science symposium. conference record (cat. no. 00ch37149), Vol. 1 (IEEE, 2000), pp. 4–25, DOI: 10.1109/NSSMIC.2000.949041.

[113] L. Bodenstein-Dresler, "Preparation for the C0BRA XDEM phase including design of mechanical parts, tests of electronics and measurement of β-suppression", MA thesis (TU Dortmund, Dortmund, 2018).

[114] *Power spectral density*, (2021) https://blog.endaq.com/vibration-analysis-fft-psd-and-spectrogram#psd (visited on 03/10/2022).

[115] C. Cai and P. d. B. Harrington, "Different discrete wavelet transforms applied to denoising analytical data", Journal of chemical information and computer sciences **38**, 1161 (1998) DOI: 10.1021/ci980210j.

[116] A. Graps, "An introduction to wavelets", IEEE computational science and engineering **2**, 50 (1995) DOI: 10.1109/99.388960.

[117] A. Bruce, D. Donoho, and H.-Y. Gao, "Wavelet analysis for signal processing", IEEE spectrum **33**, 26 (1996) DOI: 10.1109/6.540087.

[118] B. K. Alsberg, A. M. Woodward, and D. B. Kell, "An introduction to wavelet transforms for chemometricians: a time-frequency approach", Chemometrics and intelligent laboratory systems **37**, 215 (1997) DOI: 10.1016/S0169-7439(97)00029-4.

[119] Matthew P. Green, *Majorana Demonstrator status and background characterization*, URL: http://www-kam2.icrr.u-tokyo.ac.jp/indico/event/3/session/16/contribution/346/material/slides/0.pdf, Sept. 2019.

[120] M. Walter, "Background reduction techniques for the GERDA experiment", PhD thesis (University of Zurich, Zurich, 2015).

[121] D. L. Donoho, "Nonlinear wavelet methods for recovery of signals, densities, and spectra from indirect and noisy data", in In proceedings of symposia in applied mathematics (Citeseer, 1993), DOI: 10.1090/psapm/047/1268002.

[122] D. L. Donoho and I. M. Johnstone, "Adapting to unknown smoothness via wavelet shrinkage", Journal of the american statistical association **90**, 1200 (1995) DOI: 10.1080/01621459.1995.10476626.

[123] S. Alvis, I. Arnquist, F. Avignone III, and et al., "Multisite event discrimination for the Majorana Demonstrator", Physical Review C **99**, 065501 (2019) DOI: 10.1103/PhysRevC.99.065501.

[124] M. Agostini, M. Allardt, E. Andreotti, and et al., "Pulse shape discrimination for GERDA phase I data", The European Physical Journal C **73**, 1 (2013) DOI: 10.1140/epjc/s10052-013-2583-7.

[125] J. Küttler, "Investigation of the $2\nu2\beta$-spectrum of 116Cd with the C0BRA experiment", MA thesis (TU Dresden, Dresden, 2019).

[126] J. Volkmer, "Prospects of the investigation of ec/beta+ decays with the C0BRA experiment", MA thesis (TU Dresden, Dresden, 2018).

[127] W. Mengesha, C. E. Aalseth, D. S. Barnett, and et al., "Pulse shape analysis for electron mobility study in CdZnTe gamma-ray detectors", in 2003 ieee nuclear science symposium. conference record (ieee cat. no. 03ch37515), Vol. 5 (IEEE, 2003), pp. 3498–3502, DOI: 10.1109/NSSMIC.2003.1352665.

[128] P. Födisch, M. Berthel, B. Lange, and et al., "Charge-sensitive front-end electronics with operational amplifiers for CdZnTe detectors", Journal of Instrumentation **11**, T09001 (2016) DOI: 10.1088/1748-0221/11/09/T09001.

[129] S. Zatschler, "Identification of multi-site events in coplanar-grid CdZnTe detectors for the COBRA experiment", MA thesis (TU Dresden, Dresden, 2014).

[130] F. Goulding and D. Landis, "Ballistic deficit correction in semiconductor detector spectrometers", IEEE Transactions on Nuclear Science **35**, 119 (1988) DOI: 10.1109/23.12687.

[131] B. W. Loo, F. S. Goulding, and D. Gao, "Ballistic deficits in pulse shaping amplifiers", IEEE Transactions on Nuclear Science **35**, 114 (1988) DOI: 10.1109/23.12686.

[132] F. Goulding, D. Landis, and S. Hinshaw, "Large coaxial germanium detectors-correction for ballistic deficit and trapping losses", IEEE transactions on nuclear science **37**, 417 (1990) DOI: 10.1109/23.106655.

[133] M. Moszyński and G. Duchêne, "Ballistic deficit correction methods for large Ge detectors", Nuclear Instruments and Methods in Physics Research Section A: Accelerators, Spectrometers, Detectors and Associated Equipment **308**, 557 (1991) DOI: 10.1016/0168-9002(91)90068-2.

[134] C.-Y. Xiong, M.-Z. Liu, Z. Zuo, and et al., "Ballistic deficit compensation method for a large-volume HPGe detector at high count rates", Nuclear Science and Techniques **27**, 67 (2016) DOI: 10.1007/s41365-016-0063-0.

[135] Z. He, G. F. Knoll, and D. K. Wehe, "Direct measurement of product of the electron mobility and mean free drift time of CdZnTe semiconductors using position sensitive single polarity charge sensing detectors", Journal of Applied Physics **84**, 5566 (1998) DOI: 10.1063/1.368601.

[136] V. Gostilo, Z. He, V. Ivanov, and et al., "Preliminary results of large volume multi-pair coplanar grid CdZnTe detector fabrication", in Ieee nuclear science symposium conference record, 2005, Vol. 3 (IEEE, 2005), pp. 1402–1407, DOI: 10.1109/NSSMIC.2005.1596582.

[137] J. Isberg, M. Gabrysch, S. Majdi, and et al., "Negative electron mobility in diamond", Applied Physics Letters **100**, 172103 (2012) DOI: 10.1063/1.4705434.

[138] B. W. Sturm, Z. He, T. H. Zurbuchen, and et al., "Investigation of the asymmetric characteristics and temperature effects of CdZnTe detectors", IEEE Transactions on Nuclear Science **52**, 2068 (2005) DOI: 10.1109/TNS.2005.856728.

[139] W. Li, Y. Du, B. D. Yanoff, and et al., "Impact of temperature variation on the energy resolution of 3D position sensitive CZT gamma-ray spectrometers", in 2007 ieee nuclear science symposium conference record, Vol. 3 (IEEE, 2007), pp. 1809–1815, DOI: 10.1109/NSSMIC.2007.4436510.

[140] J. D. Vergados, H. Ejiri, and F. Šimkovic, "Neutrinoless double beta decay and neutrino mass", International Journal of Modern Physics E **25**, 1630007 (2016) DOI: 10.1142/S0218301316300071.

[141] A. Piepke, M. Beck, J. Bockholt, and et al., "Investigation of the $\beta\beta$ decay of 116Cd into excited states of 116Sn", Nuclear Physics A **577**, 493 (1994) DOI: 10.1016/0375-9474(94)90930-X.

[142] B. Lehnert, "Excited state transitions in double beta decay: a brief review", in Epj web of conferences, Vol. 93 (EDP Sciences, 2015), p. 01025, DOI: 10.1051/epjconf/20159301025.

[143] G. Cowan, "Discovery sensitivity for a counting experiment with background uncertainty", en. In, 8 (2012).

[144] G. Feinberg and M. Goldhaber, "Microscopic tests of symmetry principles", Proceedings of the National Academy of Sciences **45**, 1301 (1959) DOI: 10.1073/pnas.45.8.1301.

[145] M. Visser, "Charge-nonconserving decays in ordinary matter", Physical Review D **24**, 2542 (1981) DOI: 10.1103/PhysRevD.24.2542.

[146] S. Nussinov, "Charge-nonconserving decays", Physical Review Letters **59**, 2401 (1987) DOI: 10.1103/PhysRevLett.59.2401.

[147] A. Klimenko, S. Osetrov, A. Smolnikov, and et al., "Experimental limit on the charge non-conserving β decay of 73Ge", Physics Letters B **535**, 77 (2002) DOI: 10.1016/S0370-2693(02)01724-0.

[148] A. Roy, S. Vaidya, D. Ephraim, and et al., "Further experimental test of nucleon charge conservation through the reaction 113Cd to 113m+In neutrals", Physical Review D **28**, 1770 (1983) DOI: 10.1103/PhysRevD.28.1770.

[149] H. Kiel, "Determination of the half lives of rare decays of Cd, Te and Zn isotopes for the COBRA experiment", PhD thesis (TU Dortmund, Dortmund, 2005), DOI: https://d-nb.info/998025291/34.

[150] C. E. Moss, K. D. Ianakiev, T. H. Prettyman, and et al., "Performance of multielement CdZnTe detectors", in Hard x-ray, gamma-ray, and neutron detector physics, Vol. 3768 (SPIE, 1999), pp. 320–329, DOI: 10.1117/12.366597.

[151] *XCOM*, (2023) https://physics.nist.gov/cgi-bin/Xcom/xcom2 (visited on 06/28/2023).

[152] G. J. Feldman and R. D. Cousins, "Unified approach to the classical statistical analysis of small signals", Physical review D **57**, 3873 (1998) DOI: 10.1103/PhysRevD.57.3873.

[153] M. Petro, "Calculation of sensitivity to neutrinoless double beta-decay for C0BRA demonstrator", MA thesis (IEAP CTU, Prague, 2021).

[154] *Live Chart*, (2023) https://www-nds.iaea.org/relnsd/vcharthtml/VChartHTML.html (visited on 11/20/2023).

[155] W. A. Rolke, A. M. López, and J. Conrad, "Limits and confidence intervals in the presence of nuisance parameters", Nuclear Instruments and Methods in Physics Research Section A: Accelerators, Spectrometers, Detectors and Associated Equipment **551**, 493 (2005) DOI: 10.1016/j.nima.2005.05.068.

[156] J. N. Bahcall, "Solar neutrino experiments", Reviews of Modern Physics **50**, 881 (1978) DOI: 10.1103/RevModPhys.50.881.

[157] F. M. Gonzalez, E. M. Fries, C. Cude-Woods, and et al., "Improved neutron lifetime measurement with UCNτ", Phys. Rev. Lett. **127**, 162501 (2021) DOI: 10.1103/PhysRevLett.127.162501.

[158] *Nist*, (2023) https://physics.nist.gov/cgi-bin/cuu/Value?mnmmpc2mev (visited on 08/09/2023).

[159] *Internetchemie*, (2023) https://www.internetchemie.info/ (visited on 08/09/2023).

[160] J. Byrne, "An overview of neutron decay", Heidelberg, 21 (2002) DOI: hep-ph/0312124.

[161] *Fast Fourier transform introduction*, (2021) https://community.sw.siemens.com/s/article/what-is-the-fourier-transform (visited on 04/13/2021).

[162] *MATLAB*, (2021) https://de.mathworks.com/products/matlab.html (visited on 02/13/2021).

[163] *Fast Fourier transform*, (2021) https://rosettacode.org/wiki/Fast_Fourier_transform (visited on 09/24/2018).

[164] *Wavelet transform introduction*, (2023) https://builtin.com/data-science/wavelet-transform (visited on 09/13/2023).

[165] G. Uytterhoeven, D. Roose, A. Bultheel, and M. Moonen, "Applying integer wavelet transforms", Wavelet analysis: a new tool in signal and image processing, 1 (1996) DOI: lirias1945734.

[166] B. Walczak and D. Massart, "Noise suppression and signal compression using the wavelet packet transform", Chemometrics and Intelligent Laboratory Systems **36**, 81 (1997) DOI: 10.1016/S0169-7439(96)00077-9.

[167] W. Sweldens, "The lifting scheme: a custom-design construction of biorthogonal wavelets", Applied and computational harmonic analysis **3**, 186 (1996) DOI: 10.1006/acha.1996.0015.

[168] A. la Cour-Harbo and A. Jensen, "Wavelets and the lifting scheme", (2007) DOI: 10.1007/978-0-387-30440-3_588.

[169] A. M. Gavrovska, M. P. Paskaš, and I. S. Reljin, "Wavelet denoising within the lifting scheme framework", Telfor Journal **4**, 101 (2012) DOI: 1821-32511202101G.

[170] O. Schulz, *Blitzwave C++ wavelet library*, (2011) http://blitzwave.sourceforge.net (visited on 02/27/2021).

[171] R. D. Cousins, "Why isn't every physicist a Bayesian?", American Journal of Physics **63**, 398 (1995) DOI: 10.1119/1.17901.

[172] S. Yellin, "Finding an upper limit in the presence of an unknown background", Physical Review D **66**, 032005 (2002) DOI: 10.1103/PhysRevD.66.032005.

[173] *Half-life limits from LNGS data*, (2014) https://www.cobra-experiment.org/ (visited on 07/01/2023).

Appendices

A. XDEM detector characterizations

A.1. Experimental setup at the LNGS

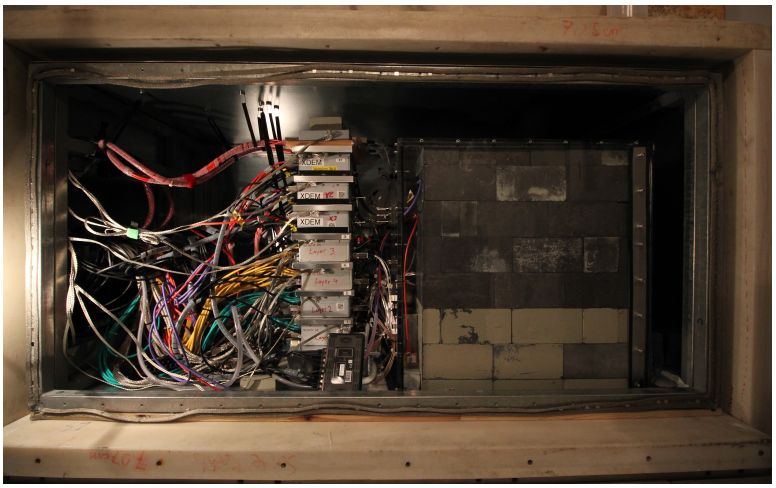

Figure A.1.: Picture for the experimental setup at the LNGS.

Table A.1.: Operating voltages (BV_1, GB) and optimal working points (BV_2, GB) for detectors from two manufacturers. The (BV_2, GB) has been applied since 24-05-2019.

detector	BV_1 [V]	BV_2 [V]	GB [V]
eV			
1	2200	2600	80
2	2200	2600	80
3	2200	2600	80
4	2000	2000	60
Redlen			
5	2200	2200	80
6	1800	1800	60/30
7	2200	2200	60
8	1800	1800	60
9	2000	2000	60

A.2. Simulated detector response

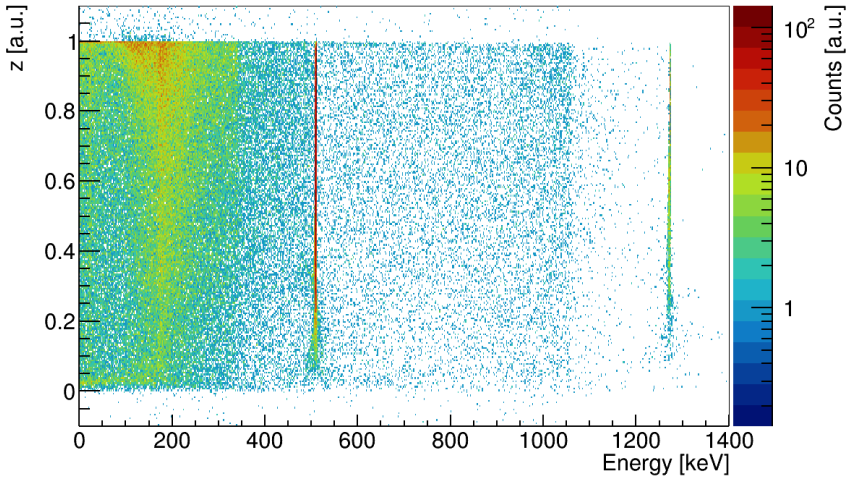

Figure A.2.: The energy versus depth distribution. Both quantities are reconstructed from simulated pulses of ^{22}Na for the XDEM. The energy is not smeared.

A.3. Gain factor stability

The plot is shown below in Fig. A.4.

A.4. Electron trapping corrected energy reconstruction

Table A.2.: Comparison of different energy reconstructions and their impact on the achievable energy resolution at the 1274.5 keV γ-line for all four sectors of detector four. The corresponding ω is in agreement with the trapping curve for the four sectors, whereas ω for sector four is no longer less than unity. The difference in the CPG performances is mainly attributed to the varying material quality [64]. According to Tab. A.3, sector two has the worst performance despite a low noise level.

sector	zeroth order [%]	depth-sensing [%]	differential gain [%]	ω
1	2.12±0.05	1.42±0.03	1.49±0.03	0.93
2	2.27±0.05	2.02±0.04	2.03±0.05	0.95
3	1.76±0.03	1.47±0.02	1.53±0.03	0.96
4	3.57±0.07	1.79±0.04	1.43±0.03	1.23

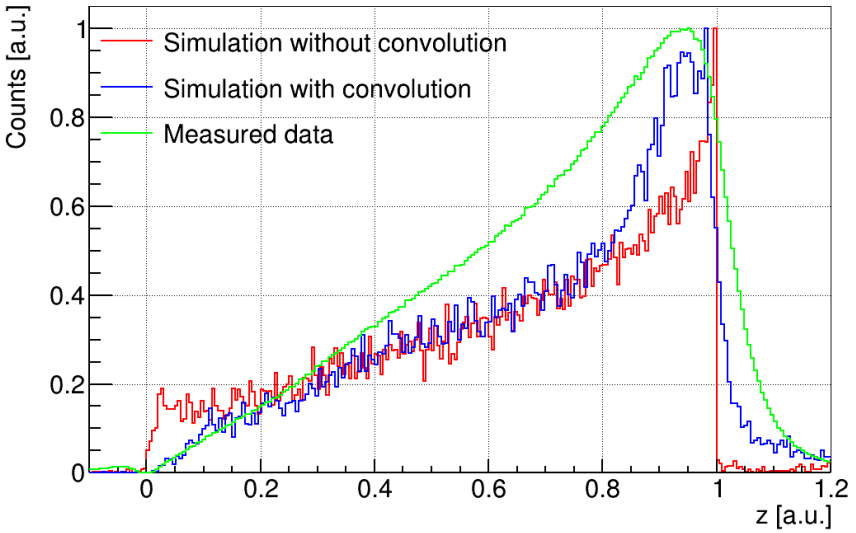

Figure A.3.: Depth comparison among simulations and real data for the whole array with ^{22}Na. The anode is $z = 0$ and the cathode at $z = 1$. Simulated pulses with hardware convolution are processed by MAnTiCORE. Without convolution, "clean" pulses are used.

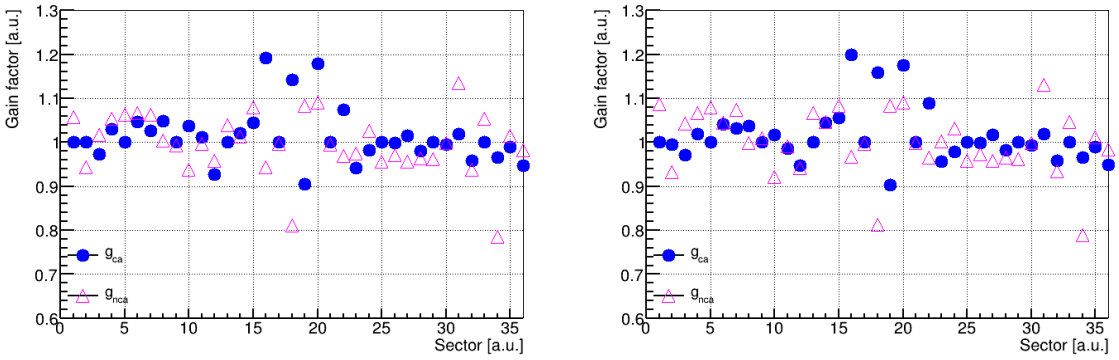

Figure A.4.: The gain distribution of the second calibration period (left) and the third period (right). The gain values are extracted from the artificial pulses injected into the preamplifier during data-taking. The g_{ca} factor is the value to correct the amplifications among all sectors, and the g_{nca} corrects the imbalance between the CA and NCA for the respective sector. Statistical uncertainties are too small to be seen.

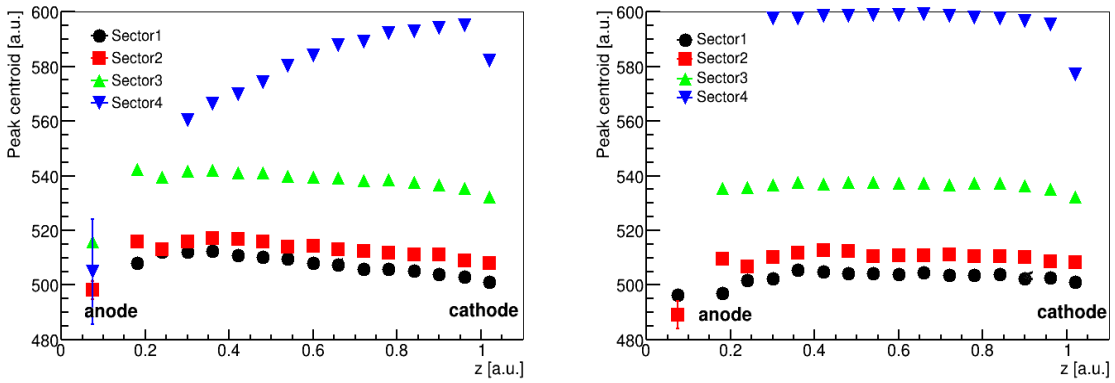

Figure A.5.: Left: Peak centroid reconstructed with the zeroth-order at the 1274.5 keV γ-line of ^{22}Na as versus depth for detector four (Redlen). Right: Corrected centroid with the differential gain method. The trapping curve of sector four shows its peak centroid shits to high values instead of a decreasing slope towards the cathode, probably due to the non-symmetric weighting potential of the CA and NCA before the diverging point.

A.5. Radial and x-y position reconstruction

Radial sensing depends on the anode geometry. With the GR being grounded, the anodes' weighting potential is forced to be zero along the periphery on the anode surface, which leads to a convex distribution of the weighting potential in the lateral direction near the anode. As a result, the anodes' φ in the center is higher than that along the periphery, especially the region close to neighboring sectors.

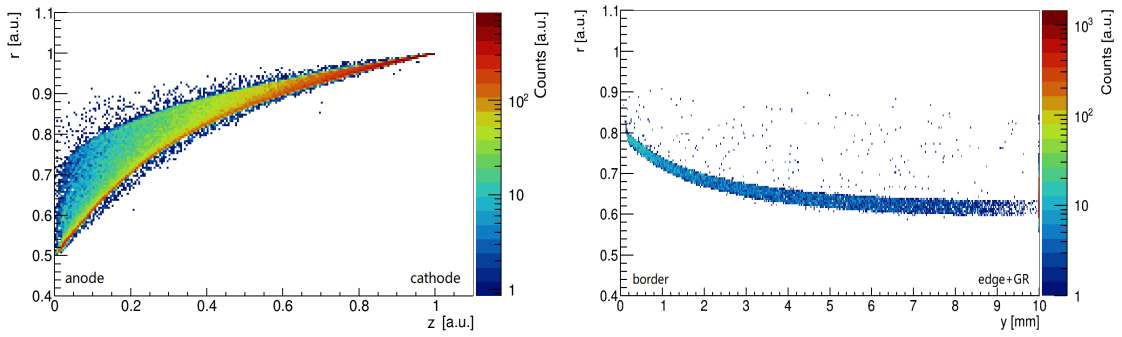

Figure A.6.: Left: The radial versus depth of simulated ^{113}Cd β-decay events. The widespread near the anodes is caused by the nonuniform weighting potential. Right: The radial position along y position (Section 4.8) at a depth layer of 0.1.

This variation is reflected on the signal and is used to reconstruct the radial position,

$$r = \frac{Q_{\mathrm{CA}}}{Q_{\mathrm{DIFF}}} = q\frac{\Delta\varphi_{\mathrm{CA}}}{\varphi_{\mathrm{DIFF}}} \tag{A.1}$$

with φ_{DIFF} known to be unity. q is the moving charge. The CA signal Q_{CA} for events starting from the edges will be larger than that of events from the center. Hence, the resulting r_{center} will be smaller than r_{edge}.

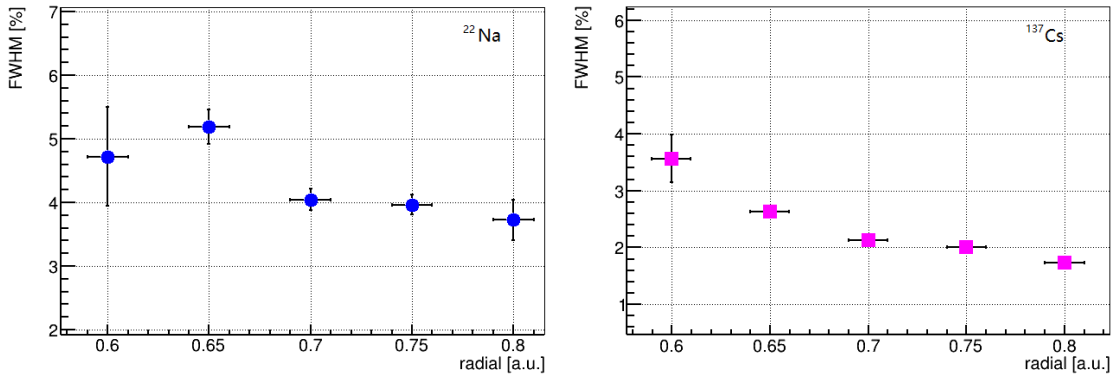

Figure A.7.: Left: The FWHM at 661.7 keV γ-line of ^{137}Cs versus the radial position at a depth layer of 0.18 to 0.28. Right: The FWHM at at 1274.5 keV of ^{22}Na versus the radial position at about the same depth. All datasets are combined for enough statistics. The FWHM at the FEP of ^{137}Cs and ^{22}Na does not worsen with the radial position.

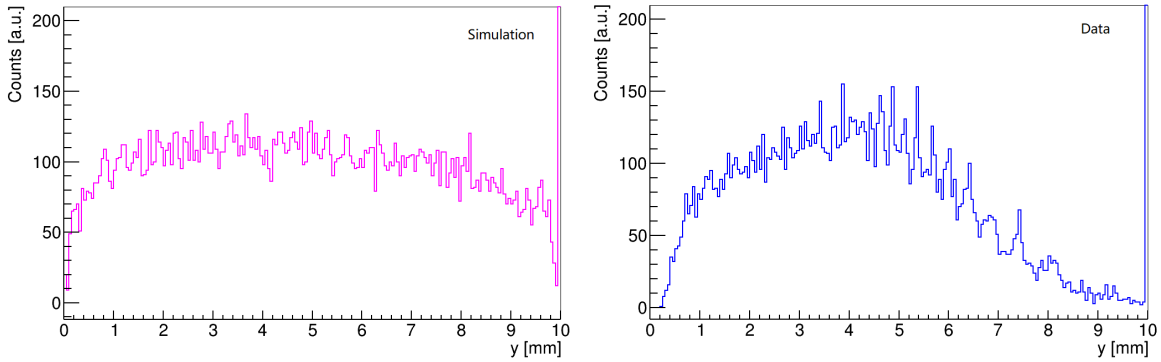

Figure A.8.: Reconstructed y position with 511 keV γ-rays from the simulated (top) and denoised (bottom) ^{22}Na in single sectors. The count decreases from the center to the edges due to the increased probability of Compton scattering and photons leaving the sector.

A.6. Detector noise level

The baseline RMS noise voltage has been calculated to estimate the noise level via

$$f_{\mathrm{RMS}} = \sqrt{\frac{1}{n}\sum_{i}^{n}(x_i - \bar{x})}. \tag{A.2}$$

Table A.3.: RMS as a measure of the noise level determined from the 2018-11-01 calibration.

detector	NCA_1	CA_1	NCA_2	CA_2	NCA_3	CA_3	NCA_4	CA_4
1	7.45	7.04	7.10	6.95	6.54	6.80	6.98	6.66
2	7.89	7.93	7.64	7.90	9.81	-	8.77	8.75
3	8.02	8.02	8.54	8.36	16.31	11.00	9.56	8.75
4	24.78	19.02	15.28	9.61	39.20	32.94	34.20	27.34
5	18.15	17.80	16.05	-	15.80	10.62	23.71	41.12
6	35.62	12.77	27.18	11.46	21.47	26.88	18.08	-
7	9.60	19.09	40.46	9.48	37.19	37.28	12.88	16.64
8	19.84	11.44	7.45	7.30	9.62	6.93	13.14	8.74
9	14.83	15.25	9.41	21.99	8.16	11.08	9.88	30.11

-: no physical signal recorded.

Table A.4.: RMS as a measure of the noise level determined from the 2019-05-16 calibration.

detector	NCA_1	CA_1	NCA_2	CA_2	NCA_3	CA_3	NCA_4	CA_4
1	7.35	7.03	7.03	6.87	6.51	6.77	7.11	6.70
2	7.50	7.66	7.39	7.62	9.63	-	8.37	8.35
3	8.11	7.92	8.42	8.06	19.25	15.54	10.03	9.15
4	24.68	19.94	14.78	11.07	36.20	32.42	31.38	25.40
5	18.38	17.60	15.53	-	14.50	10.19	22.12	42.05
6	38.16	13.02	26.43	10.99	20.51	25.80	18.67	-
7	10.96	18.65	36.38	9.86	35.27	36.96	13.28	15.34
8	20.77	12.10	7.55	7.50	9.82	7.04	12.71	8.91
9	15.56	15.94	9.34	21.92	8.24	11.49	10.01	30.50

Detector six is not usable due to the baseline distortion and large noise.

The averaged RMS of the pre- and post-baseline with 256 samples each is extracted from recorded pulses. The following tables give the results of each readout channel at each ^{22}Na calibration. The RMS noise levels agree well with the values calculated from the physics data. Based on this criterion, preliminary selections of the detectors are performed.

Most channels have an acceptable noise level, although high-level noise is present in some channels. Due to a failed electrical contact, one channel of detector two and one from detector six cannot record any physical signal. Another problematic channel belongs to detector five with signals not transmitted through the DAQ system. This issue was resolved by exchanging the cable connecting the detector to the preamplifier. Concerning detector six, most channels are noisy, and pulses show distorted shapes, which was partly fixed by decreasing high voltage and disabling noisy sectors. Detector three also records pulses with distorted baselines and remains nonfunctional due to broken preamplifiers.

A.7. Detector response in the measurement

Table A.5.: RMS as a measure of the noise level determined from the 2019-05-24 calibration.

detector	NCA_1	CA_1	NCA_2	CA_2	NCA_3	CA_3	NCA_4	CA_4
1	7.09	7.40	7.24	7.17	8.13	7.73	7.63	7.61
2	9.12	8.28	8.02	8.03	12.13	-	10.53	9.40
3	8.46	8.61	10.20	9.19	25.88	21.54	10.17	9.73
4	20.84	11.57	15.66	10.14	26.54	27.37	23.56	19.55
5	20.43	23.03	12.52	10.20	10.66	9.42	12.88	33.17
6	19.22	7.88	11.15	8.01	13.24	17.71	14.05	-
7	10.05	11.08	36.38	14.69	33.64	39.46	13.92	29.50
8	15.09	9.96	8.35	8.99	8.85	8.94	11.32	10.72
9	14.62	17.10	11.38	15.48	12.48	10.74	11.46	21.53

Detector six is partly functional with disabled sector three; detector five has improved

Table A.6.: RMS as a measure of the noise level determined from the 2019-11-05 calibration.

detector	NCA_1	CA_1	NCA_2	CA_2	NCA_3	CA_3	NCA_4	CA_4
1	7.29	7.45	8.11	7.61	8.29	8.16	7.72	7.80
2	8.82	8.46	8.21	8.25	13.25	-	11.08	9.82
3	10.01	9.74	11.20	9.67	30.23	30.27	12.54	12.58
4	30.44	18.01	18.38	18.51	24.77	24.25	22.04	19.96
5	16.60	19.00	12.36	10.27	10.68	9.99	12.88	27.49
6	18.93	9.03	10.57	8.64	16.18	15.88	14.71	-
7	24.30	17.51	36.07	16.91	38.11	40.22	16.33	30.38
8	13.94	10.07	8.72	9.64	9.02	8.88	10.81	10.62
9	17.48	16.67	12.27	17.68	12.52	10.85	11.70	20.10

Detector three: distortions in the pulse baseline related to the charge transport

Table A.7.: RMS as a measure of the noise level determined from the 2019-11-07 calibration.

detector	NCA_1	CA_1	NCA_2	CA_2	NCA_3	CA_3	NCA_4	CA_4
1	9.41	10.11	10.69	10.57	10.61	10.60	10.09	10.14
2	10.85	10.91	10.61	10.91	11.45	-	11.86	11.37
3	10.60	11.01	11.65	10.82	16.19	14.80	12.44	11.85
4	24.85	14.54	17.25	14.88	19.98	20.63	16.61	14.84
5	15.48	18.92	17.26	13.11	16.37	15.24	17.29	18.31
6	18.76	13.33	15.78	13.76	25.46	15.13	18.50	-
7	12.31	12.55	49.76	17.31	44.54	51.00	14.27	32.04
8	17.32	11.98	10.90	11.81	10.44	11.19	13.51	12.07
9	17.06	24.20	13.43	18.81	14.56	15.23	14.54	37.88

Large fluctuations on the baseline are observed for all detectors.

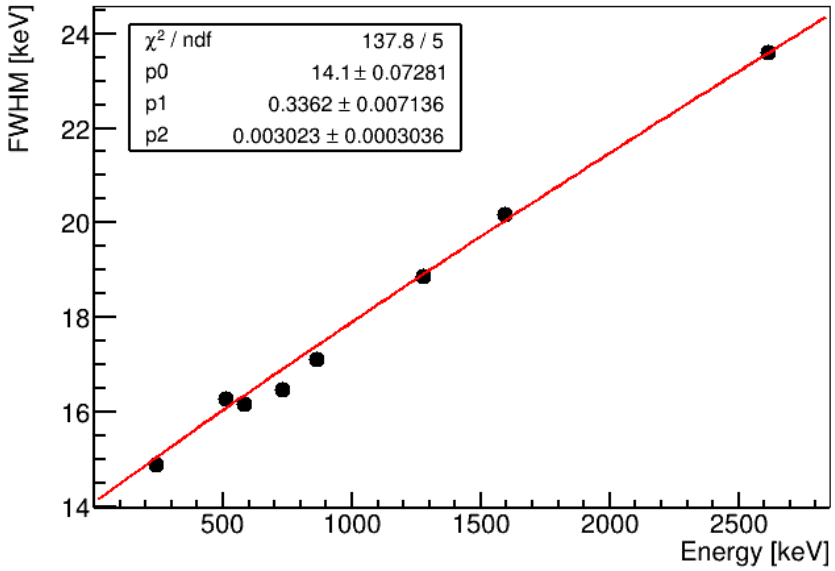

Figure A.9.: The average energy resolution function fitted with a combined XDEM dataset.

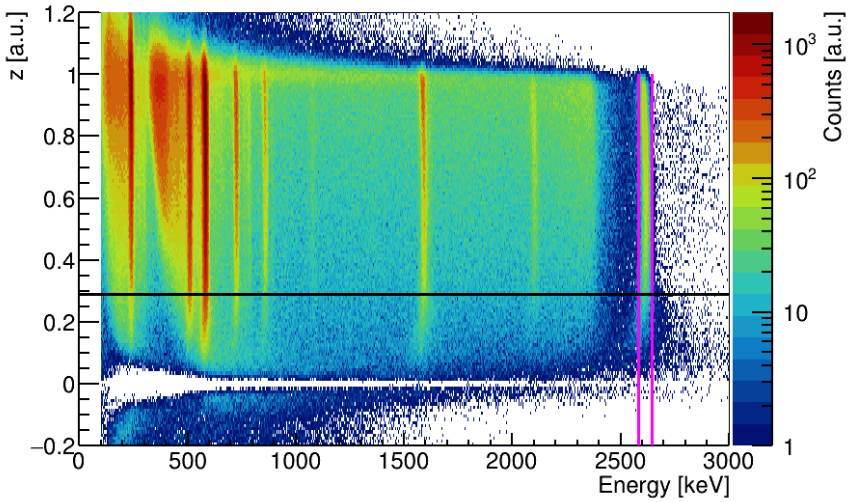

Figure A.10.: Depth distribution of ^{228}Th calibration events collected from the XDEM array. The magenta lines indicate the γ peak within $(2615\pm3\sigma)$ keV. The peak width at high energies is increased close to the anodes, as also shown from the simulation in Fig. A.2. The black line shows the depth cut at $z = 0.29$ near the anode.

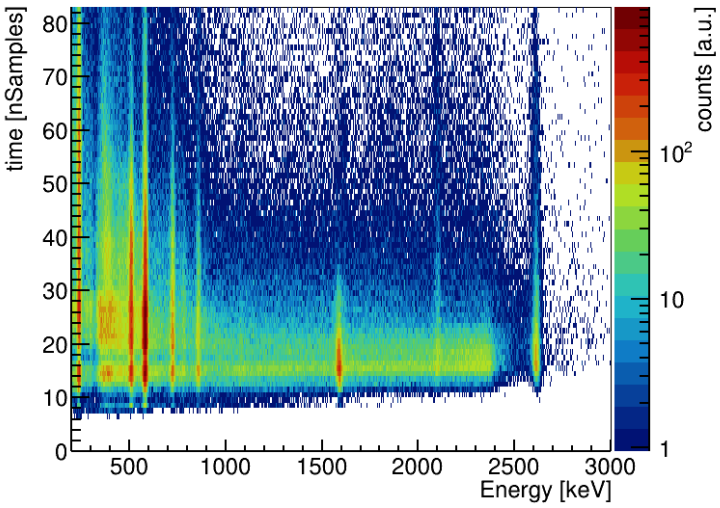

Figure A.11.: Time distribution for the ^{228}Th calibration with one detector. Near-anode events are rejected. The drift time is not extrapolated. As the γ peaks are not distorted, the shaping time constant of amplifiers should be large enough to allow full charge collection.

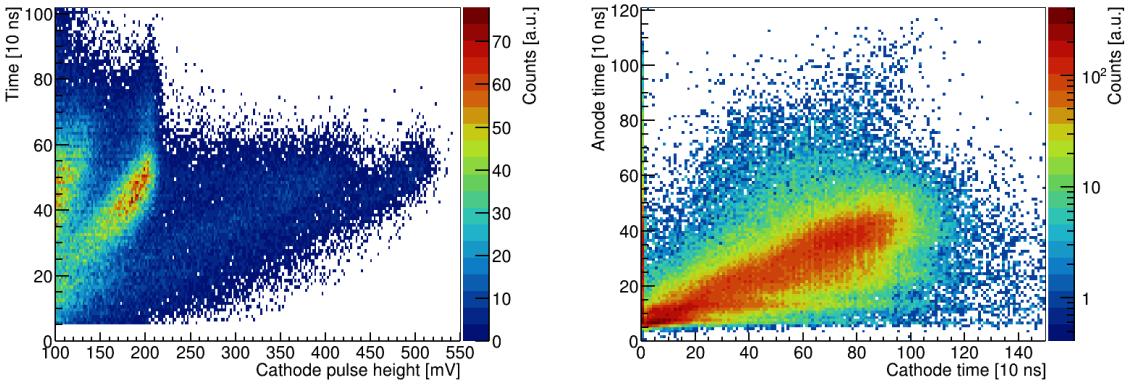

Figure A.12.: Left: The height of reconstructed cathode pulses from ^{22}Na versus the drift time that equals to the time difference between 20% and 80% of pulse heights. The pulse height is roughly linear along the 511 keV (200 mV) and 1274.5 keV (500 mV) photopeaks. Right: The correlation between the drift time of the cathode and the anode is not linear. Also, the nonlinear weighting potential of anodes results in inaccurate extrapolation.

B. The $2\nu\beta\beta$ decay of ^{116}Cd

B.1. Radon decay chain as background

Table B.1.: Decay products and corresponding decay modes listed for the ^{222}Rn decay chain. The energy of α and γ peaks are also given. The Q values and half-lives are cited from Ref. [154]. γ-rays with relative probability less than 3% are omitted.

nuclides	decay type	α energy [MeV]	Q-value [MeV]	half-life	γ energy [keV]	γ prob.
^{222}Rn	α	5.49	5.59	3.82 d		
^{218}Po	α	6.00	6.11	3.05 min		
^{214}Pb	β		1.02	27.06 min	241.99	7%
					295.22	18%
					351.93	36%
^{214}Bi	β		3.26	19.71 min	609	45%
					768	5%
					934	3%
					1120	15%
					1238	6%
					1378	4%
					1764	15%
					2204	5%
^{214}Po	α	7.69	7.83	164.30 µs		
^{210}Pb	β		0.06	22.20 yr	46.5	4%
^{210}Bi	β		1.16	5.01 d		
^{210}Po	α	5.30	5.41	138.40 d		
^{206}Pb						

B.2. Sector pair optimization for the excited state transition

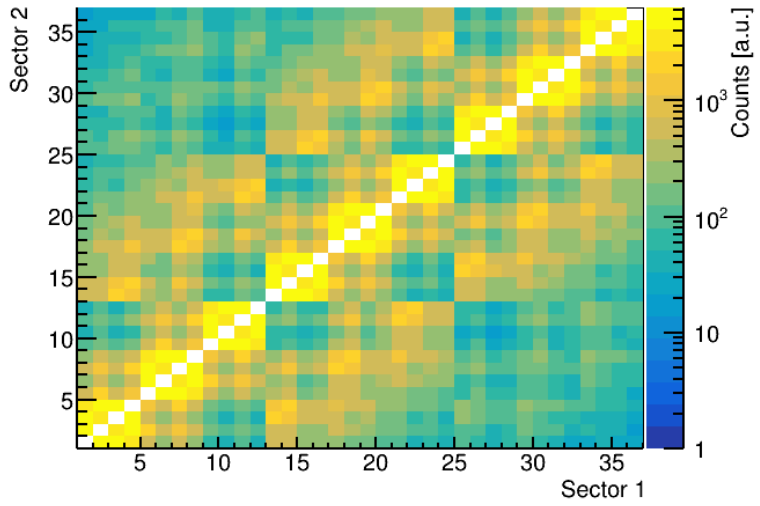

Figure B.1.: The M2 events selected in each sector pair for the $0^+_{\text{g.s.}} \rightarrow 2^+_1$ decay mode. The signal decay is in the first sector, and the γ-ray deposition is in the second sector.

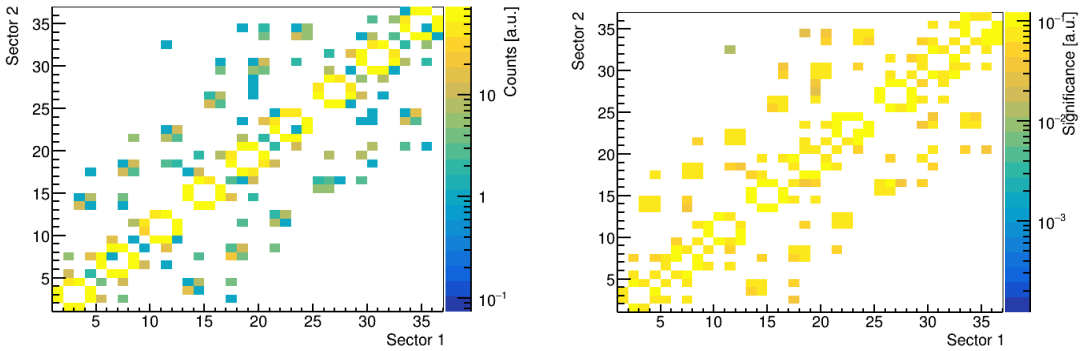

Figure B.2.: Left: M2 events for the $0^+_{\text{g.s.}} \rightarrow 0^+_{\text{g.s.}}$ decay mode. The signal decay is in the sector 1, and the γ-ray deposition is in the sector 2. Events are normalized by the corresponding half-life limit, which leads to sector pairs without a single entry. Right: Significance distribution for the $0^+_{\text{g.s.}} \rightarrow 2^+_1$ decay mode after selecting the sector pair. Due to statistics in the background, currently it is not realistic to select optimal sector pairs. With a complete background model, the significance can be reevaluated. Sector pairs with the high-ranked significance can be selected.

C. Fourier analysis

C.1. Fourier transform

Fourier Transform (FT) is the dominant analytical tool for frequency domain analysis. It shows that any signal can be treated as a superposition of sinusoids with different amplitudes, phases, and frequencies. One example is illustrated in Fig. C.1. A waveform is the sum of individual sine waves and is represented by three frequency components. The expression for the FT is

$$F(\omega) = \frac{1}{2\pi} \int_{-\infty}^{+\infty} f(t) \mathrm{e}^{-i\omega t}\, dt, \tag{C.1}$$

where f(t) is the input function, and ω denotes the frequency in radians per second. F(ω) is the output with a series of complex numbers that contain information about the amplitude and phase of the frequency components resulting from the original time signal. The lowest frequency is 0 Hz, the so-called direct current component. The highest frequency is the Nyquist frequency which is half the sampling rate.

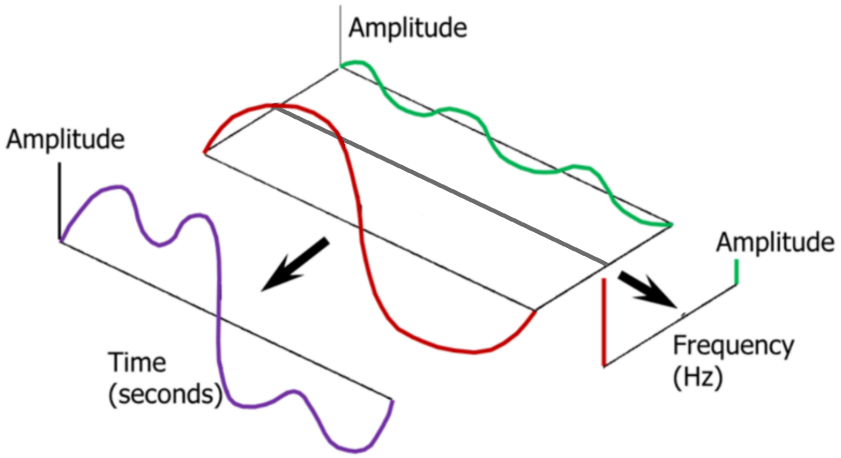

Figure C.1.: One waveform in the time domain decomposed into three frequency components in the frequency domain [161].

FFT determines the discrete FT of the input by computing even and odd indexed subsets concurrently, making it computationally efficient. The algorithm requires the number of samples to be a power of two. The Fourier matrix (n×n matrix) is factored into a product of just a few sparse matrices. An outer loop is executed logN times and calculates transformations

of the length 2, 4, 8, ..., N. For each stage of this process, the inner loops calculate the sum of the even-numbered and odd-numbered points. The total computation is then simplified to O(NlogN) times.

The inverse FT is to reconstruct the original signal using the preserved amplitude and phase in the frequency domain. It is the transpose of Eq. C.1,

$$f(t) = \frac{1}{2\pi} \int_0^{+\infty} F(\omega) \mathrm{e}^{i\omega t} \, d\omega. \tag{C.2}$$

FFT in this work is performed by the TVirtualFFT class provided by ROOT [101] and cross-checked with the Matlab [162] as well as a C++ program implemented with the Cooley–Tukey algorithm [163].

C.2. The frequency spectra of detectors four, five, and six

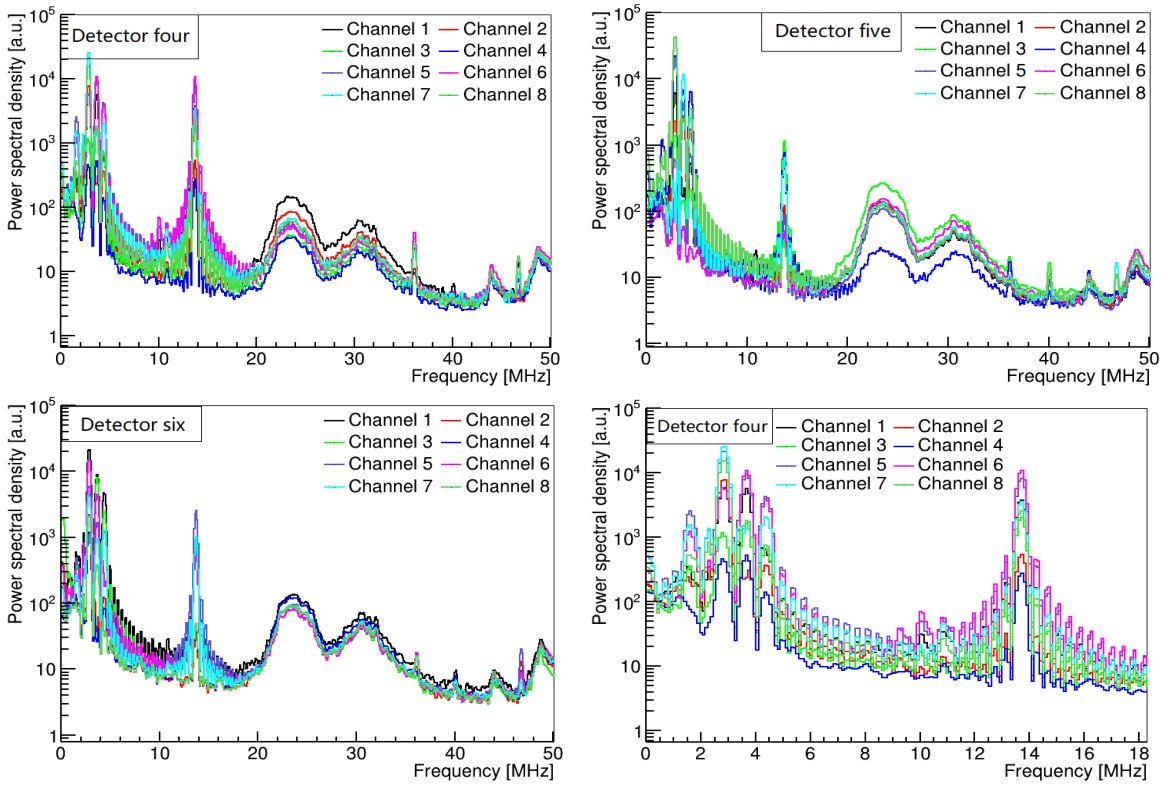

Figure C.2.: The average noise power spectra of detectors four (top left), five (top right), and six (bottom left), operated by the preamplifier module 3. The pre-baseline of injected pulses with 256 samples are analyzed. The three detectors show a similar pattern regardless of the intensity. The power distribution of detector four is zoomed in to 18 MHz. There are multiple peaks from 2 MHz to 5 MHz, and a peak dominant at 14 MHz.

D. Wavelet analysis

D.1. Wavelet transform and the lift scheme

The computation of the WT is similar to the FT. For the WT, a signal is multiplied by a transform matrix constructed with wavelets. The transformation is expressed by

$$F(a,b) = \int_{-\infty}^{+\infty} f(x)\Psi^*_{(a,b)}(x)\,dx, \tag{D.1}$$

where Ψ represents the wavelet series, and a, b are their dilation and translation factors. The dilation determines how stretched or squished a wavelet is. This property relates to the frequency as defined for waves. The translation defines the position of the wavelet in time or space. The wavelet coefficients *F(a,b)* essentially quantify the strength of the wavelets' contribution at a particular set of scales and locations.

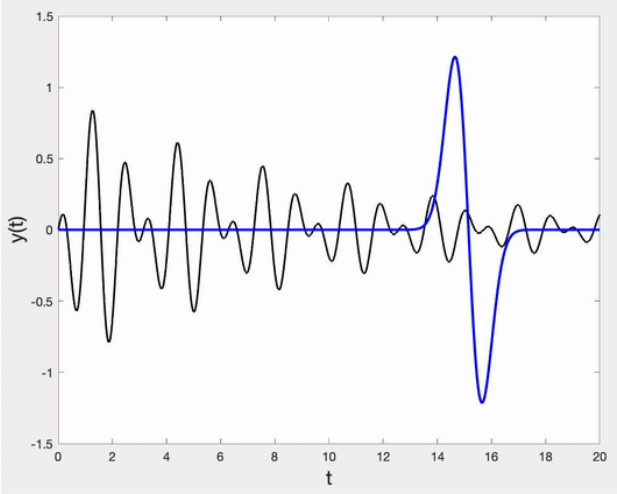

Figure D.1.: A wavelet in blue moving through the entire signal shown in black [164].

Fig. D.1 illustrates a wavelet of a particular scale sliding across the signal. At each time step, the multiplication product of the wavelet and the signal tells how much of the wavelet is in this signal. A series of coefficients for this wavelet can thus be obtained. This process is repeated for wavelets with a variety of scales.

The wavelet theory relies on multi-resolution analysis. The multi-resolution consists of a sequence of nested subspaces. Each resolution space is a subset of subspaces with a higher resolution. The subspace V_j can be written as $...V_{-2} \subset V_{-1} \subset V_0 \subset V_1 \subset V_2...$ [118]. At each

resolution level, the function f(x) in V_j is expressed as a linear combination of basis functions, ψ (wavelet function) and ϕ (scaling function),

$$f(x) = \sum_j d_{jk}\psi_{jk} + \sum_j s_{jk}\phi_{jk}. \tag{D.2}$$

d_{jk} and s_{jk} represent the wavelet coefficient and the scaling coefficient, respectively. At each resolution level, the scaling coefficients act as a smoothing filter, while the wavelet coefficient shows the signal's detail.

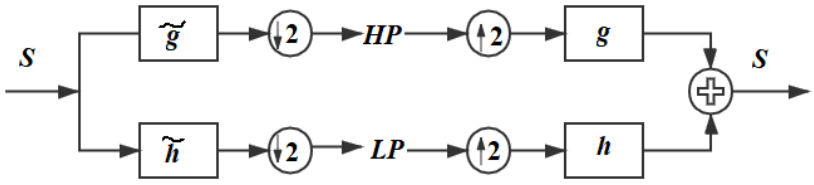

Figure D.2.: Working flow of the fast WT [165]. The idea is to apply the defined transformation matrix to data and generate detail coefficients and approximation coefficients at different levels from the high pass and low pass decomposition filters, $\widetilde{g}$ and $\widetilde{h}$. The inverse WT combines the results from the high pass and low pass reconstruction filters, g and h.

Fig. D.2 illustrates how the fast WT works. The signal input is split into a high pass band (corresponding to the wavelet function) and a low pass band (equivalent to the scaling function) by the applied matrix [166]. The outputs are detail coefficients and approximation coefficients, respectively. The approximation coefficients represent the global properties of the signal, which need to be saved. On the other hand, the detail coefficients reveal signal differences at different levels. A recursive algorithm is applied to the subsampled low pass band at the second resolution level. The high pass band is not used for further calculations. This process iterates till the last level. The algorithm thus offers a hierarchical, multi-resolution representation of the signal.

Compared to the standard algorithm, the lifting scheme proposed by Sweldens allows a faster and in-place calculation [116, 167–169]. This algorithm exploits the correlation structure of the neighboring data samples of the signal to speed up computations. The filter iteration is similar to the standard algorithm, as illustrated in Fig. D.3. It starts by splitting the signal into odd and even indexed samples. The predict step replaces the odd-numbered elements with the difference between the odd-numbered elements and the predict function. This difference reflects the high frequency components of the signal, basically the details. This process can be viewed as a high pass filter. The update step then replaces the even elements with a local average, approximating the signal. The resulting signal is smoother than the previous level. This step acts as a low pass filter.

A Blitzwave wavelet library is referenced to perform WT based on the lifting scheme [170]. The Demonstrator has used the CDF(2, 2) wavelet [106], a biorthogonal wavelet with a symmetric feature from the Cohen–Daubechies–Feauveau wavelets family. Given the similarities of pulse shapes, this wavelet is also employed for the XDEM.

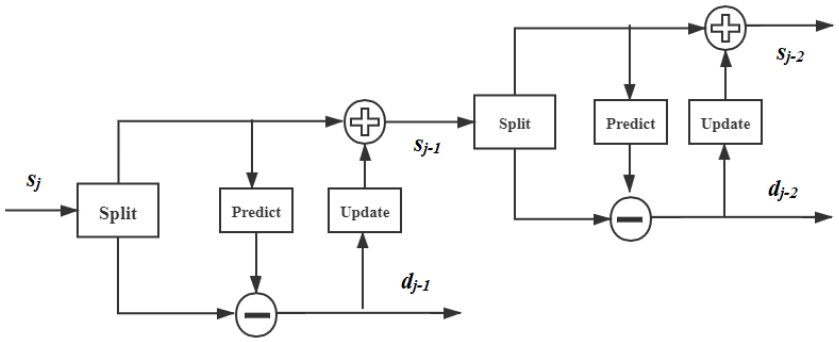

Figure D.3.: Working flow of the lifting scheme. In the first stage, data are split into two subsets. Secondly, one of the subsets is used to predict the other subset (wavelet subset) based on their correlations. Thirdly, the constructed wavelet subset is used to update the other. This procedure is iterated through the following levels.

D.2. Wavelet based denoising

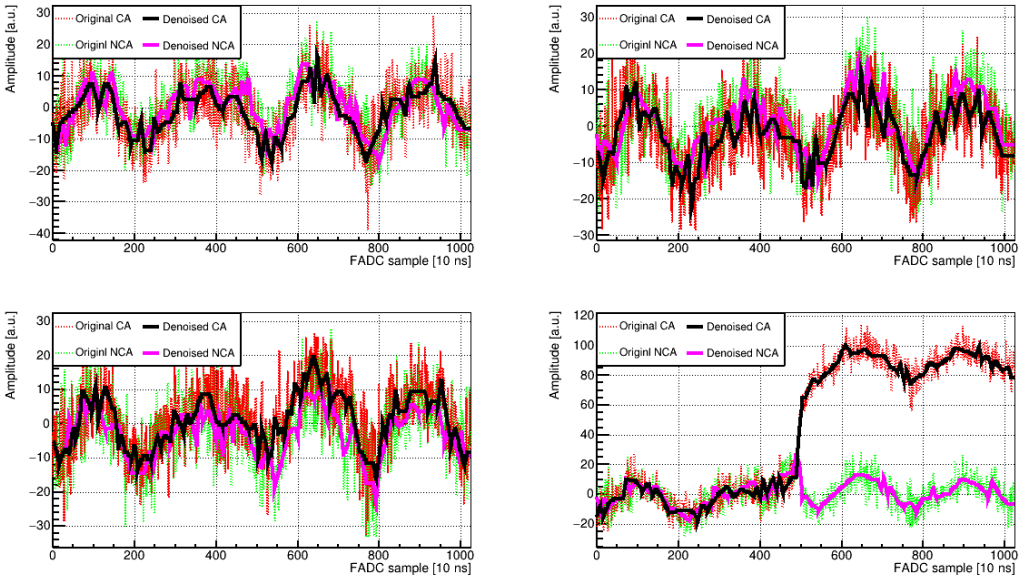

Figure D.4.: Denosing anode pulses of one event from ^{22}Na with excessive noise.

E. Statistical analysis

The radioactive decay is expected to follow a Poisson distribution. If one experiment has measured five events in total, and the expected background count is three, naively thinking, the signal count would be two. On the other hand, the Poisson distribution indicates that there are also other possibilities. For example, all the measured events can be attributed to backgrounds. This means that the signal strength cannot be a single value but a range of values with given probabilities, the so-called confidence interval. One way to obtain these values is to use the Feldman-Cousins method.

E.1. Feldman-Cousins approach

The method interprets the result of an experiment in a frequentist way. From an ensemble of identical experiments with the actual value of μ, multiple confidence intervals are obtained, of which a fraction of α intervals cover the μ. α is the confidence level of the interval as described by $P(\mu \in [\mu_1, \mu_2]) = \alpha$. Here μ_1 and μ_2 are functions of the measured quantity. $[\mu_1, \mu_2]$ refers to the multiple confidence intervals that contain all the fixed μ values in a fraction of α of experiments.

If the fraction of intervals covering the actual value is higher than α, intervals will overcover and are conservative. In this case, the frequentist confidence interval contains experiments' information. Otherwise, the intervals undercover for that μ, which will be a serious flaw. Compared to the Neyman method constructing the classical confidence intervals, the Feldman-Cousins method has overcome problems with the non-physical boundaries or the empty intervals and undercover by using the ordering principle [171].

The algorithm is briefly described here. For a Poisson process with backgrounds, the observable quantity x corresponds to the total number of observed events n that consist of signal events with a mean value, μ, and the known background b. The Poissonian probability for a mean of $\mu+b$ events with a variance of n can be calculated as

$$P(n|\mu) = (\mu + b)^n \exp[-(\mu + b)]/n! \ . \tag{E.1}$$

A ratio of likelihoods is then used in the ordering principle and dictates which n_i is added to the cumulative sum first. The summation is in decreasing order and finishes until the desired C.L. is fulfilled.

The choice of the order in which the individual components of the cumulative sum is expressed as

$$R = P(n|\mu)/P(n|\mu_{\text{best}}), \tag{E.2}$$

where R is the ratio of two likelihoods. $P(n|\mu)$ is the likelihood of obtaining the total observed events n given the mean signal μ, and $P(n|\mu_{\text{best}})$ is the likelihood of obtaining n given the

best-fit as well as physically allowed mean value $\mu_{\rm best}$ = max(0, n-b). The ordering principle avoids empty confidence intervals. Additionally, the transition from a one-sided to a two-sided limit is automatic, preventing the drawbacks of the Neyman construction.

For a given value of μ_j, the confidence interval is constructed by looking for the smallest number of observed events, $n_{\rm min}$ (lower limit), and the maximal number, $n_{\rm max}$ (upper limit). By applying the ordering principle, the cumulative sum of the interval [$n_{\rm min}$, $n_{\rm max}$] ends up a summed probability that meets the required C.L.,

$$CL(n,\mu) \leq \sum_{n_i=n_{\rm min}}^{n_i=n_{\rm max}} P(n_i, \mu_j + b). \tag{E.3}$$

Due to the discreteness of n, the obtained value is usually more than the defined C.L., which leads to conservative confidence intervals. This process is repeated for different μ.

If an experiment measures no signal, it is suggested that the sensitivity be reported. For an experiment expecting background counts of $\bar{b}$ and total observed events of n_i for a given C.L., the count sensitivity $S\left(\bar{b}\right)$ is given by the weighted sum of all the upper limits U

$$S\left(\bar{b}\right) = \sum_{n_i=0}^{\infty} P\left(n_i, \bar{b}\right) U\left(n_i, \bar{b}\right). \tag{E.4}$$

The weight P is the Poissonian probability that such an experiment would measure total events of n_i while expecting background of $\bar{b}$. If $\bar{b}$ is above a threshold of 329, as pointed out in Ref. [153], it is possible to use the Gaussian sensitivity to estimate the signal strength.

E.2. Profile likelihood method

The profile likelihood approach is also a frequentist method. It includes the experimental uncertainties as nuisance parameters. The construction of the confidence intervals is based on the likelihood ratio test statistic and shows good coverage [155].

In the context of nuisance parameters, the profile likelihood function is given by

$$\lambda(\mu|(x,y)) = \frac{L(\mu, \hat{\hat{b}}(\mu)|(n,b))}{L(\hat{\mu}, \hat{b}|(n,b))}, \tag{E.5}$$

with L denoting the probability model for the data, and also called the likelihood function. If a Possion distribution is assumed, L is given by the same expression as Eq. E.1. The resulting -2 logλ has approximately a chi-square distribution, which can be used to extract limits. The interval is found by starting from the minimum and then moving to the left and right to determine the points where the function increases by the corresponding percentile of the chi-square distribution with one degree of freedom. Special treatments are also made for cases when the distribution is not exactly chi-square.

E.3. Optimized window method

If the background is distributed differently from the expected signal, it is possible to take advantage of this difference to set a strong limit. The optimal interval method proposed in Ref. [172] depends on the choice of ROI, which can lead to non-optimal results. Therefore, it is motivated to find an optimal window within which as many as signal counts can be accepted while most background counts are rejected.

The concept was further developed in Ref. [153, 173] for the Demonstrator to set a new $T_{1/2}$ limit on the $0\nu\beta\beta$-decays. The overall test quantity is the maximal $T_{1/2}$ over all possibilities. For data each partition, an optimal ROI is estimated separately to set the strongest total $T_{1/2}$ limit. If we assume the signal follows a Gaussian distribution, ρ_n, and the background is described by an exponential function, β_n, the half-life is formulated as

$$T_{1/2} \geq \frac{\ln(2) N_A a}{M} \frac{\sum_{n=1}^{n=64} m_{\mathrm{n}} t_{\mathrm{n}} \varepsilon_{\mathrm{n}} \int_{E_{\mathrm{l}}^n}^{E_{\mathrm{r}}^n} \rho_{\mathrm{n}}(E)\, dE}{S(\sum_{n=1}^{n=64} m_{\mathrm{n}} t_{\mathrm{n}} \int_{E_{\mathrm{l}}^n}^{E_{\mathrm{r}}^n} \beta_{\mathrm{n}}(E)\, dE)}, \tag{E.6}$$

where n is the index of the data partition with 64 assumed. E_{l}^n and E_{r}^n are the left and right boundaries of the window for each partition, respectively.

To find the maximal value, the following equations need to be satisfied for the respective partition p,

$$\frac{\partial T_{1/2}(E_{\mathrm{l}}^n, E_{\mathrm{r}}^n)}{\partial E_{\mathrm{l}}^p} = 0, \quad \frac{\partial T_{1/2}(E_{\mathrm{l}}^n, E_{\mathrm{r}}^n)}{\partial E_{\mathrm{r}}^p} = 0. \tag{E.7}$$

Therefore, there will be 128 similar equations because of the 64 partitions. Detailed derivations are referred to Ref. [153]. The optimal ROI will fulfill

$$\frac{\rho_p(E_l^n)}{\beta_p(E_l^n)} = \frac{S'(\bar{b})}{S(\bar{b})} \sum_{n=1}^{n=64} m_{\mathrm{n}} t_{\mathrm{n}} \varepsilon_n(E_{\mathrm{l}}^n, E_{\mathrm{r}}^n) = \frac{\rho_p(E_r^n)}{\beta_p(E_r^n)} \equiv \left(\frac{\rho}{\beta}\right). \tag{E.8}$$

One can see that the $\frac{\rho_p(E)}{\beta_p(E)}$ is equal at the left and right endpoints of the optimal window. And the middle term is the same for each partition. A global parameter $\rho(E)/\beta(E)$ is thus used to simplify the computing procedure, reducing the 128 variables to one parameter. The variable is related to the signal and background shape and is formulated as

$$\rho(E)/\beta(E) = \frac{1}{\beta_0 \sigma \sqrt{2\pi}} \mathrm{e}^{\lambda E - \frac{(E-E_\gamma)^2}{2\sigma^2}}. \tag{E.9}$$

As (ρ/β) is the same on the boundaries of the optimal ROI, the left boundary E_{l} and the right boundary E_{r} of the ROI can be derived from,

$$E_{\mathrm{l,r}} = E_\gamma + \lambda\sigma^2 \pm \sigma \sqrt{(\lambda\sigma)^2 + 2\lambda E_\gamma - 2\ln\left(\frac{\beta_0 \sigma \sqrt{2\pi}}{\varepsilon}\right)\left(\frac{\rho}{\beta}\right)}. \tag{E.10}$$

For each (ρ/β), a window is obtained. By varying the (ρ/β) value, the window width changes accordingly, and so does the $T_{1/2}$ limit. If the term under the square root is equal to zero, the window closes. When the sensitivity is maximal, the corresponding (ρ/β) will give the optimal window.

Acronyms

0$\nu\beta\beta$ neutrinoless double beta

2$\nu\beta\beta$ two neutrino double beta

BV bulk voltage

CA collecting anode

CC charged current

C.L. confidence level

CNC charge non-conserving

COBRA Cadmium Zinc Telluride 0-Neutrino Double Beta Research Apparatus

CP charge parity

CPG coplanar grid

CZT CdZnTe

DAQ data acquisition

DCCs data cleaning cuts

DEP double escape peak

EC electron capture

EMI electromagnetic interferences

FADC Flash Analog to Digital Converter

FEP full energy peak

FT Fourier Transform

FWHM full width at half maximum

GB grid bias

GDML Geometry Description Markup Language

GR guard ring

GT Gamow-Teller

ICP-MS Inductively Coupled Plasma Mass Spectrometry

LNGS Laboratori Nazionali del Gran Sasso

MAnTiCORE Multiple-Analysis Toolkit for the COBRA Experiment

MSE multi-site event

MSW Mikheyev-Smirnov-Wolfenstein

NC neutral current

NCA non-collecting anode

OFHC oxygen-free high conductivity

PMNS Pontecorvo-Maki-Nakagawa-Sakata

PSD pulse shape discrimination

qCPG quad coplanar grid

RMS root mean square

ROI region of interest

SBs sidebands

SEP single escape peak

SSE single-site event

ULA ultra-low activity

UPS uninterruptible power supply

WT Wavelet Transform

XDEM eXtended DEMonstrator

Acknowledgements

Firstly, I would like to thank my supervisor Prof. Kai Zuber for leading me to this field and generously offering me the opportunity to work on this interesting experiment. Without his support, this work cannot be done.

Secondly, I am grateful to Prof. Daniel Bemmerer for his very kind financial support and for agreeing to be my first referee, as well as for writing the reference letter for me. I would also like to thank Dr. Ivan Stekl who kindly agreed to be my second referee. I appreciate Prof. Arno Straessner for inspiring me to work on detectors. I also want to thank Prof. Dominik Stoeckinger for his kind support and advice on referees.

A special thanks go to Andreas Jansen and Dr. Steffen Turkat who spent so much effort helping me with the funding.

I would also like to thank Dr. Stefan Zatschler for guiding me to the COBRA experiment with his incredible patience and the best knowledge. Without his help, I could not have moved this far. I appreciate that he squeezed time from his busy schedule to help improve this work, especially chapters one to five. I also want to thank Juliane Volkmer who made great efforts to proofread this work and provided a lot of comments and corrections. I am also grateful to Yuzhen and Michael who provide comments for individual chapters.

Former and current COBRA members who have indirectly contributed to this work are also acknowledged. I am specifically grateful to Stefan and Dr. Robert Temminghoff who have shared great experience in hardware and data analysis. I also want to thank Juliane, Dr. Miroslav Macko, Maros Petro, and Dr. Rastislav Hodak for their great collaborations.

I appreciate all the assistance from the IKTP administrators in IT and the secretary, especially Wolfgang, Rainer, Nicole, Birgit, Lisa, and Kristin.

I would also like to thank the neutrino group, Juliane, Stefan, Birgit, Mikko, Andreas, Steffen, Johann, Jan, Heinrich, Michael, Marie, Hans, Xianke, Christoph, Jonas, Antonio, and Bjoern. I benefited a lot from all the fruitful discussions with them regarding data analysis, simulations, and presenting results. This work would not be the same without them. Furthermore, a big thanks to Stefan for helping me with my exams. I am also thankful to Andi for his great advice in research and life, and for creating a very warm and laughing environment in the group. I also want to thank Michael, who gave me a lot of encouragement and kindly gave me several lectures on neutrino physics and mathematics.

I want to thank my friends Dr. Yuzhen Ma, Dr. Ningning Zhang, Dr. Xuan Yang, Yumeng Xue, Chang Hong, Xianke, and Jianan Yi who have given me so much support and advice in life. Also, I would like to mention Dr. Tianbing He and Dr. Chunxiang Guo who kindly offered me help when I was new in Germany.

I want to thank Prof. Giovanni Benato for his kind support on the postdoc position.

Last but not least, I would like to thank my family for their continuous support, especially my parents Xu Changqing and Chu Yanling, as well as my aunt Chu Yanmin. I also appreciate Xu Junmei's wholehearted support, especially in difficult times.

Not all names are listed here, of course. For the past years, I was financially supported by the China Scholarship Council (67%), Graduate Academy(4%), GFF (3%), DAAD (4%), personal savings (11%), IKTP (7%) and HZDR (4%).

Declaration

Herewith I declare that I have produced this work without the prohibited assistance of third parties and without making use of aids other than those specified notions taken over directly or indirectly from other sources have been identified as such. This paper has not previously been presented in identical or similar form to any other German or foreign examination board.

I further declare that no previous unsuccessful doctorate proceedings have been undertaken. The doctorate was obtained and carried out at the TU Dresden, at the Institute for Nuclear and Particle Physics under the supervision of Prof. Kai Zuber.

I accept the regulations for obtaining a doctoral degree of the TU Dresden School of Science (Bereich Mathematik und Naturwissenschaften) from February 23, 2011.

Place, Date Signature